UNIVERSITY OF SOUTHERN QUEENSLAND

Faculty of Engineering and Surveying

DEVELOPMENT AND APPLICATION OF ASSUMED STRAIN SMOOTHING FINITE ELEMENT TECHNIQUE FOR COMPOSITE PLATE/SHELL STRUCTURES

A dissertation submitted by

Hieu Nguyen-Van

B.Eng., Ho Chi Minh City University of Architecture, 1998

M.Eng. (Hon.), University of Liège, Belgium, 2000

For the award of

Doctor of Philosophy

July 2009 (revised on December 2009)

To my beloved parents, with love, respect, and gratitude

Abstract

The present study is mainly concerned with the development and application of simple, efficient and accurate finite element models for geometrically linear and nonlinear analysis of composite plates/shells. It is also demonstrated that the developed approach can be extended for analysis of functionally graded material (FGM) structures as well as coupled electric-structural piezoelectric systems.

The primary goal is achieved through the development of two novel four-node displacement-based C^0 quadrilateral flat elements, one with fictional drilling DOFs (MISQ20) and one with actual drilling DOFs (MISQ24) within the framework of the first-order shear deformation theory (FSDT). The developed elements are based on the incorporation of the strain smoothing technique of the stabilized conforming nodal integration (SCNI) mesh-free method into the four-node quadrilateral finite elements. The most distinguishing feature of the present elements is the evaluation of membrane, bending and geometric stiffness matrices by integration along the boundary of smoothing elements. It is observed that this assumed strain smoothing technique can yield more accurate solutions even with badly shaped elements or coarse discretization and reduce computational time when compared with domain integration approach. To accommodate small strain geometric nonlinearity with large deformations, the von-Karman's large deflection theory and the total Lagrangian approach are employed to formulate the present elements for geometrically nonlinear analysis. The present formulation is therefore applicable to moderately thick and thin plate/shell configurations, involving isotropic or composite material properties, with improved solutions in a wide range of geometrically linear and nonlinear problems. Extensive numerical verification is carried out with a set of demanding benchmark problems and the present results are

compared with analytical, experimental and numerical solutions in the literature. The comparative study does show the validity as well as the high-performance of the developed finite element models for laminated composite structures. The developed approach also performs very well in the analysis of FGM plate structures under thermo-mechanical loading.

The analysis of coupled mechanical-electrical behaviours of piezoelectric problems is accomplished by the normalization of both mechanical strains and electric potential fields using the smoothing constant function of the SCNI. Two novel piezoelectric elements for linear static and free vibration analysis of planar piezoelectric structures are proposed. The first one, the cell-based element (SPQ4), is based on the subdivision of original quadrilateral finite elements into smoothing cells. The second one, the node-based element (NSPE-T3 or NSPE-Q4), is created by transforming a triangular or quadrilateral mesh into a mesh of new smoothing cells associated with each of the nodes of the original mesh. The reliability and accuracy of the proposed formulations are demonstrated through various favourable comparisons with other existing elements and analytic solutions. The present models are attractive for coupled multifield problems owing to the following properties: (i) very good accuracy, (ii) insensitivity to mesh distortion, and (iii) simplicity of formulation.

Certification of Dissertation

I certify that the idea, experimental work, results and analyses, software and conclusions reported in this dissertation are entirely my own effort, except where otherwise acknowledged in the text. I also certify that the work is original and has not been previously submitted for any other award.

Hieu Nguyen-Van, Candidate	Date

ENDORSEMENT

Prof. Thanh Tran-Cong, Principal supervisor	Date
Dr. Nam Mai-Duy, Associate supervisor	Date

Acknowledgements

I would like to express my deepest gratitude to Professor Thanh Tran-Cong, my principal supervisor, not only for his valuable guidance throughout my research but also for his philosophical attitude which has inspired my own research interest. Undoubtedly, without his continuing support and devotion this thesis would not have been completed.

In addition, I wish to express my sincere thanks to Dr. Nam Mai-Duy for acting his role as associate supervisor; to Assoc Prof. David Buttsworth (Associate Dean–Research) and Mr. Dean Beliveau (Research Technologist) for their help and friendly support; to Prof. Hung Nguyen-Dang (my former Master's thesis advisor) for firstly introducing me to the world of Applied Mechanics and to many friends and people who I have not mentioned by name for their direct or indirect support during my course of study as well as the realization of this thesis.

I also would like to mention here my sincere acknowledgement of the support provided by the University of Southern Queensland. This thesis may not exist without the generous financial support provided by the Research Scholarship from the Faculty of Engineering and Surveying and by the Scholarship Supplement from the Computational Engineering and Science Research Centre (CESRC).

Lastly and most importantly, I am greatly indebted to my family, especially my mother, for much unconditional support, understanding and love in so many areas over the years and for endlessly encouraging me in academic pursuits.

Publications Arising from the Research

During the course of the research, a number of papers have been published based on the work presented in this thesis. They are listed here for reference.

Publications in Refereed Journals

1. Nguyen-Van H., Mai-Duy N. and Tran-Cong T. (2009). An improved quadrilateral flat element with drilling degrees of freedom for shell structural analysis. *CMES: Computer Modeling in Engineering & Sciences.* Vol. 49, No. 2, pp. 81–112.

2. Nguyen-Van H., Mai-Duy N. and Tran-Cong T. (2008c). A node-based element for analysis of planar piezoelectric structures. *CMES: Computer Modeling in Engineering & Sciences.* Vol. 36, No. 1, pp. 65–96.

3. Nguyen-Van H., Mai-Duy N. and Tran-Cong T. (2008b). Free vibration of laminated plate/shell structures based on FSDT with a stabilized nodal-integrated quadrilateral element. *Journal of Sound and Vibration.* Vol. 313, pp. 205–223.

4. Nguyen-Van H., Mai-Duy N. and Tran-Cong T. (2008a). A smoothed four-node piezoelectric element for analysis of two-dimensional smart structures. *CMES: Computer Modeling in Engineering & Sciences.* Vol. 23, No. 3, pp. 209–222.

5. Nguyen-Van H., Mai-Duy N. and Tran-Cong T. (2007b). A simple and

accurate four-node quadrilateral element using stabilized nodal integration for laminated plates. *CMC :Computer, Materials & Continua.* Vol. 6, No. 3, pp. 159–175.

Publications in International Conferences

6. Nguyen-Van H., Le Thong, Mai-Duy N. and Tran-Cong T. (2008e). Nodal integration finite element techniques for analysis of piezoelectric solids. *The International Conference on Computational Solid Mechanics (CSM2008), November 27-30, 2008, Ho Chi Minh City, Vietnam.*

7. Nguyen-Van H., Mai-Duy N. and Tran-Cong T. (2008d). Analysis of piezoelectric solids with an efficient node-based smoothing element. *The 8^{th} World Congress on Computational Mechanics (WCCM8), June 30–July 5, 2008, Venice, Italy.*

8. Nguyen-Van H., Mai-Duy N. and Tran-Cong T. (2007a). Analysis of laminated composite plate/shell structures using a stabilized nodal-integrated quadrilateral element. *The 1^{st} International Conference on Modern Design, Construction & Maintenance of Structures (MDCMS2007), 10-11 Dec 2007, Ha Noi, Vietnam.*

9. Nguyen-Van, Hieu and Khennane, Amar and Tran-Cong, Thanh (2006). Monte-Carlo simulation of the durability of glass fibre reinforced composite under environmental stress corrosion. *The International Conference on Nonlinear Analysis & Engineering Mechanics Today (NA-EMT2006), 11-14 Dec 2006, Ho Chi Minh City, Vietnam.*

Papers Submitted to Refereed Journals

10. Nguyen-Van H., Mai-Duy N. and Tran-Cong T. (2009a). Buckling analysis of laminated plate/shell structures based on a FSDT stabilized nodal-integrated quadrilateral element. *Submitted to Composite Structures.*

11. Nguyen-Van H., Mai-Duy N. and Tran-Cong T. (2009b). Geometrically nonlinear analysis of composite plate/shell structures via an assumed strain smoothing quadrilateral flat element. *Submitted to International Journal of Mechanical Sciences.*

Papers to Be Submitted

12. Nguyen-Van H., Mai-Duy N. and Tran-Cong T. (2009c). Vibration and buckling analysis of laminated plate/shell structures via a smoothed quadrilateral flat element with in-plane rotations. *(To be submitted)*

13. Nguyen-Van H., Mai-Duy N. and Tran-Cong T. (2009d). Thermoelastic analysis of functionally graded plates using a FSDT stabilized nodal-integrated quadrilateral element. *(To be submitted)*

14. Nguyen-Van H., Mai-Duy N. and Tran-Cong T. (2009e). A family of high-performance smoothed quadrilateral elements for geometrically linear and nonlinear analysis of composite plates. *(To be submitted)*

Table of Contents

Abstract i

Certification of Dissertation iii

Acknowledgements iv

Publications Arising from the Research v

List of Acronyms xiv

List of Tables xv

List of Figures xxiii

Chapter 1 Introduction 1

1.1 General aspects 1

1.2 A brief review of recent plate/shell finite elements based on the FSDT 6

1.3 Motivation and Objectives 8

1.4 Outline of the dissertation 11

1.5 Main contributions of the research 12

Chapter 2 Overview of Finite Element Formulations 14

2.1 Membrane elements 14

2.1.1 Isoparametric quadrilateral membrane element 14

2.1.2 Quadrilateral membrane element with drilling degrees of freedom 16

2.2 Shear deformable plate bending element 19

2.3 Flat shell element 21

2.4 Assumed strain smoothing technique 23

Chapter 3 Assumed Strain Smoothing Plate Finite Elements 25

3.1 Introduction 25

3.2 First-order shear deformation theory of laminated plates 27

3.2.1 Governing equations 27

3.2.2 Finite element formulations 32

3.3 Strain smoothing approach for laminated plate 34

3.3.1 Smoothed membrane strains 34

3.3.1.1 Smoothed isoparametric membrane element . . . 35

3.3.1.2 Smoothed membrane element with drilling degrees of freedom 36

3.3.2 Smoothed bending strains of the element 38

3.3.3 Transverse shear strains of the element 39

3.3.4 Smoothed element stiffness matrix 40

3.3.5 Smoothed element geometric stiffness matrix 41

3.4 Numerical examples: Static analysis 42

3.4.1 Patch tests 42

3.4.2 Cross-ply 3-layer symmetric $[0^0/90^0/0^0]$ and 2-layer unsymmetric $[0^0/90^0]$ laminates under uniformly distributed load 44

3.4.3 Angle-ply $[\theta^0/-\theta^0]$ square plate under uniformly distributed load 48

3.4.4 Antisymmetric angle-ply $[-45^0/45^0]$ and $[-45^0/45^0]_4$ square plate under a double sinusoidal load 53

3.4.5 Cross-ply 9-layer $[(0^0/90^0)_2/0]_s$ square plates under uniformly distributed load 56

3.4.6 Cross-ply $[0^0/90^0/0^0]$ and angle-ply $[45^0/-45^0/45^0]$ skew laminated plates under uniformly distributed load 59

3.4.7 Circular plate subjected to uniform pressure 61

3.4.8 Triangular plate subjected to uniform pressure 61

3.4.9 Thermo-mechanical analysis of functionally graded material (FGM) plates 63

3.4.9.1 Convergence study 65
3.4.9.2 Thermal-mechanical analysis 69
3.5 Numerical examples: Free vibration analysis 72
3.5.1 Square laminated plates 72
3.5.1.1 Convergence study and effect of modulus ratios . 73
3.5.1.2 Effect of mesh distortion 75
3.5.1.3 Effect of span-to-thickness ratio 77
3.5.1.4 Effect of lay-up sequence and fibre orientation . . 78
3.5.1.5 Effect of mixed boundaries and span-to-thickness ratio 79
3.5.2 Skew laminated plates 83
3.5.3 Circular laminated plates 86
3.5.4 Right-angle triangular laminated plates 89
3.6 Numerical examples: Buckling analysis 91
3.6.1 Cross-ply $[0^0/90^0/90^0/0^0]$ square plate under uniaxial compression 91
3.6.1.1 Convergence study and effect of modulus ratios . 91
3.6.1.2 Effect of mesh distortion 93
3.6.2 Symmetric/anti-symmetric cross-ply and angle-ply square plates under uniaxial compression 95
3.6.2.1 Effect of span-to-thickness ratio 95
3.6.2.2 Effect of mixed boundaries 99
3.6.3 Cross-ply skew plates with various skew angles and span-to-thickness ratios under uniaxial compression 102
3.6.4 Cross-ply square plates under biaxial compression 104
3.6.4.1 Effect of material anisotropy 104
3.6.4.2 Effect of mixed boundary conditions 104
3.7 Concluding remarks 105

Chapter 4 Assumed Strain Smoothing Flat Shell Finite Elements 108

4.1 Introduction 108
4.2 Assumed strain smoothing flat shell finite element formulations . . 110

4.3 Numerical examples: Static analysis . . . 113
4.3.1 Scordelis-lo (Barrel vault) roof . . . 115
4.3.2 Pinched cylinder with end diaphragms . . . 117
4.3.3 Pinched hemispherical shell with an 18^0 hole . . . 121
4.3.4 Shallow spherical shells . . . 123
4.3.5 A hypar shell . . . 126
4.3.6 Partly clamped hyperbolic paraboloid shells . . . 127
4.3.7 Pre-twisted cantilever beams . . . 129
4.4 Numerical examples: Free vibration and Buckling analysis . . . 135
4.4.1 Free vibration of cross-ply laminated cylindrical shells . . . 135
4.4.2 Free vibration of angle-ply laminated cylindrical shells . . . 136
4.4.3 Free vibration of cross-ply laminated spherical shells . . . 137
4.4.4 Uniaxial buckling of multi-layer cylindrical shallow shell panels . . . 140
4.4.4.1 Effect of span-to-thickness ratio . . . 140
4.4.4.2 Effect of the number of layers . . . 141
4.5 Concluding remarks . . . 142

Chapter 5 Geometrically Nonlinear Analysis of Plate/Shell Structures 144

5.1 Introduction . . . 144
5.2 Finite element formulation for geometrically nonlinear analysis . . . 146
5.2.1 Kinematic equations . . . 146
5.2.2 Total Lagrangian finite element formulation . . . 147
5.3 Strain smoothing formulation for geometrically nonlinear analysis 150
5.4 Numerical examples . . . 152
5.4.1 Clamped cross-ply 4-layer symmetric $[0^0/90^0/90^0/0^0]$ square plate under uniform pressure . . . 153
5.4.2 Simply supported unidirectional 8-layer $[0^0]_8$ square plate under uniform pressure . . . 156
5.4.3 Simply supported cross-ply 4-layer $[0^0/90^0/90^0/0^0]$ square plate under uniform pressure . . . 158

5.4.4 Clamped antisymmetric cross-ply and angle-ply square plates under uniform pressure . . . 162
5.4.5 Clamped isotropic circular plate under uniform pressure . 164
5.4.6 Clamped isotropic cylindrical shell . . . 167
5.4.7 Hinged antisymmetrical angle-ply cylindrical shell . . . 167
5.4.8 Simply supported cross-ply spherical shell . . . 169
5.4.9 Pinched semi-cylindrical cross-ply laminated shells . . . 170
5.5 Concluding remarks . . . 172

Chapter 6 Assumed Strain Smoothing Methods for Piezoelectric Materials 173

6.1 Introduction . . . 174
6.2 Linear piezoelectric constitutive relations . . . 176
6.3 Review of finite element formulations for 2D piezoelectric problems 178
6.4 Strain smoothing approach for piezoelectric finite element method 181
6.4.1 Cell-based strain smoothing approach . . . 181
6.4.2 Node-based strain smoothing approach . . . 185
6.4.2.1 Construction of linear shape functions . . . 188
6.4.2.2 Implementation procedure . . . 189
6.5 Numerical examples . . . 191
6.5.1 Patch tests . . . 192
6.5.2 Single-layer piezoelectric strip in tension . . . 195
6.5.3 Single-layer piezoelectric strip in shear deformation . . . 200
6.5.4 Single-layer piezoelectric strip in bending . . . 206
6.5.5 Parallel piezoelectric bimorph beam . . . 211
6.5.6 Piezoelectric Cook's membrane . . . 213
6.5.7 Double bimorph optical micro-scanner . . . 218
6.5.8 Infinite piezoelectric plate with a circular hole . . . 220
6.5.9 Free vibration of a piezoelectric transducer . . . 225
6.6 Concluding remarks . . . 229

Chapter 7 Conclusions 230

7.1 Summary and conclusion 230
7.2 Suggested work 233

Appendix A Determination of transverse shear stresses 234

Appendix B Assumed strain smoothing finite elements for FGM Reissner-Mindlin plates 237

B.1 Material properties and thermal analysis 237
B.2 Assumed strain smoothing finite element formulation for FGM Reissner-Mindlin plates 238

Bibliography 241

List of Acronyms

ESL	Equivalent Sigle-Layer
LW	Layer-wise
CLPT	Classical Laminated Plate Theory
FSDT	First-order Shear Deformation Theory
TSDT	Third-order Shear Deformation Theory
HSDT	Higher-order Shear Deformation Theory
FEM	Finite Element Method
SFEM	Smoothed Finite Element Method
MLSDQ	Moving Least Squares Differential Quadrature
RKPM	Reproducing Kernel Particle Method
RBF	Radial Basic Function
PCM	Point Collocation Method
PIM	Point Interpolation Method
RPIM	Radial Point Interpolation Method
SCNI	Stabilized Conforming Nodal Integration
ASS	Assumed Strain Smoothing
DOFs	Degrees of Freedom
SCFs	Shear Correction Factors
FGM	Functionally Graded Material
TL	Total Lagrangian
MISQ20	Mixed Integration Smoothed Quadrilateral Element
MISQ24	Mixed Integration Smoothed Quadrilateral Element with drilling DOFs
SPQ4	Smoothed Piezoelectric Quadrilateral Element
NSPE-Q4	Node-based Smoothed Piezoelectric Quadrilateral Element
NSPE-T3	Node-based Smoothed Piezoelectric Triangular Element

List of Tables

Table 3.1 Material properties. 42

Table 3.2 Results of patch test 43

Table 3.3 Simply supported cross-ply $[0^0/90^0]$ and $[0^0/90^0/0^0]$ square plate under uniform load: Convergence of normalized central deflection $w^* = 100E_2wh^3/(q_oa^4)$ and comparison with available literature. 46

Table 3.4 Simply supported 2-layer angle-ply $[\theta/-\theta]$ square plate under uniform load: Convergence of the normalized central deflection $w^* = 100E_2wh^3/(q_oa^4)$ with different fibre angles and comparison with available literature. 50

Table 3.5 Clamped 2-layer angle-ply $[\theta/-\theta]$ square plate under uniform load: Convergence of normalized central deflection $w^* = 100E_2wh^3/(q_oa^4)$ with different fibre angles and comparison with available literature. 51

Table 3.6 Simply supported 2-layer angle-ply $[-45^0/45^0]$ square plate under doubly sinusoidal loading: Comparison of normalized central deflection and normalized stresses. 54

Table 3.7 Simply supported 8-layer angle-ply $[-45^0/45^0]_4$ square plate under doubly sinusoidal loading: Comparison of normalized central deflection and normalized stresses. 55

Table 3.8 Clamped 9-layer cross-ply $[(0^0/90^0)_2/0]_s$ square plate under uniform load: Comparison of normalized central deflection $w^* = 1000E_2wh^3/(q_oa^4)$. 57

Table 3.9 Clamped 9-layer cross-ply $[(0^0/90^0)_2/0]_s$ square plate under uniform load: Comparison of normalized central moment resultant $M_x^* = 100E_2M_x/(q_oa^2)$. 57

Table 3.10 Simply supported 9-layer cross-ply $[(0^0/90^0)_2/0]_s$ square plate under uniform load: Comparison of normalized central deflection $w^* = 1000E_2wh^3/(q_oa^4)$. 58

Table 3.11 Simply supported 9-layer cross-ply $[(0^0/90^0)_2/0]_s$ square plate under uniform load: Comparison of normalized central moment resultant $M_x^* = 1000E_2M_x/(q_oa^2)$. 58

Table 3.12 Simply supported $[0^0/90^0/0^0]$ and $[45^0/-45^0/45^0]$ skew plate: Comparison of normalized central deflection and stress ($a/h = 100$). 60

Table 3.13 Clamped circular plate under uniform loading: Comparison of normalized central deflection $w^* = wD/(qR^4)$. 62

Table 3.14 Clamped triangular plate under uniform load: Comparison of normalized centroidal deflection $w_C^* = 1000E_2w_Ch^3/(q_oa^4)$. . . 63

Table 3.15 Material properties of the FGM components 64

Table 3.16 Square FGM Al/ZrO_2-1 plates: Convergence study of non-dimensional central deflections ($a/h = 10$, $D_0 = E_{Zr}h^3/(12(1-\nu_{Zr}^2))$, $w^* = 100wD_0/(q_0a^4)$). 65

Table 3.17 Simply supported cross-ply $[0^0/90^0/90^0/0^0]$ square plate: Convergence of normalized fundamental frequencies and comparison with other solutions ($\omega^* = (\omega a^2/h)\sqrt{\rho/E_2}, a/h = 5$). . . . 73

Table 3.18 Simply supported cross-ply $[0^0/90^0/90^0/0^0]$ square plate: Effect of mesh distortion on the normalized fundamental frequencies ($\omega^* = (\omega a^2/h)\sqrt{\rho/E_2},\ a/h = 5$). 76

Table 3.19 Simply supported cross-ply $[0^0/90^0/90^0/0^0]$ square plate with various a/h ratios: Convergence of normalized fundamental frequencies and comparison with other solutions ($E_1/E_2 = 40$, $\omega^* = (\omega a^2/h)\sqrt{\rho/E_2}$). 77

Table 3.20 Cross-ply $[0^0/90^0/0^0]$ square plate with various mixed boundaries and span-to-thickness ratios: Comparison of normalized fundamental frequencies with other solutions ($E_1/E_2 = 40$, $\omega^* = (\omega a^2/h)\sqrt{\rho/E_2}$). 80

Table 3.21 Clamped cross-ply $[0^0/90^0/0^0]$ square plate: Comparison of the first five natural frequencies with other solutions ($E_1/E_2 = 40$, $D_0 = E_2h^3/(12(1-\nu_{12}\nu_{21}))$, $\omega^* = (\omega a^2/\pi^2)\sqrt{\rho h/D_0}$). 81

Table 3.22 Simply supported cross-ply $[90^0/0^0/90^0/0^0/90^0]$ skew plate with various skew angles: Convergence of fundamental frequencies and comparison with other solutions ($E_1/E_2 = 40,\ a/h = 10$, $\omega^* = \omega a^2\sqrt{\rho/E_2}/(\pi^2 h)$). 84

Table 3.23 Clamped cross-ply $[90^0/0^0/90^0/0^0/90^0]$ skew plate with various skew angles: Convergence of fundamental frequencies and comparison with other solutions ($E_1/E_2 = 40,\ a/h = 10$, $\omega^* = \omega a^2\sqrt{\rho/E_2}/(\pi^2 h)$). 84

Table 3.24 Simply supported angle-ply $[45^0/-45^0/45^0/-45^0/45^0]$ skew plate with various skew angles: Convergence of fundamental frequencies and comparison with other solutions ($E_1/E_2 = 40$, $a/h = 10$, $\omega^* = \omega a^2\sqrt{\rho/E_2}/(\pi^2 h)$). 85

Table 3.25 Clamped angle-ply $[45^0/-45^0/45^0/-45^0/45^0]$ skew plate with various skew angles: Convergence of fundamental frequencies and comparison with other solutions ($E_1/E_2 = 40,\ a/h = 10$, $\omega^* = \omega a^2\sqrt{\rho/E_2}/(\pi^2 h)$). 85

Table 3.26 Circular 4-layer $[\theta/-\theta/-\theta/\theta]$ laminated plates with various boundary conditions and ply angles: Comparison of fundamental frequencies with other solutions ($\omega^* = (\omega a^2/h)\sqrt{\rho/E_2}$, $E_1/E_2 = 40,\ a/h = 10$). 87

Table 3.27 Clamped circular 4-layer $[\theta/-\theta/-\theta/\theta]$ laminated plate: Comparison of the normalized natural frequencies of the first six modes ($\omega^* = (\omega a^2/h)\sqrt{\rho/E_2}, E_1/E_2 = 40, a/h = 10$). 87

Table 3.28 Clamped right-angle triangular laminated plate: Comparison of the normalized natural frequencies of the first six modes ($\omega^* = (\omega a^2/h)\sqrt{\rho/E_2}, E_1/E_2 = 25, a/h = 100$). 89

Table 3.29 Simply supported cross-ply $[0^0/90^0/90^0/0^0]$ square plate: Convergence of normalized critical buckling loads with various E_1/E_2 ratios and comparison with other solutions ($\lambda^* = N_x a^2/(E_2 h^3)$, $a/h = 10$). 93

Table 3.30 Simply supported cross-ply $[0^0/90^0/90^0/0^0]$ square plate: Effect of mesh distortion on the normalized critical buckling loads ($\lambda^* = N_x a^2/(E_2 h^3),\ a/h = 10$). 95

Table 3.31 Simply supported symmetric cross-ply $[0^0/90^0/90^0/0^0]$ square plate with various a/h ratios: Convergence of normalized critical buckling loads and comparison with other solutions ($E_1/E_2 = 40,\ \lambda^* = N_x a^2/(E_2 h^3)$). 97

Table 3.32 Simply supported unsymmetric cross-ply $[0^0/90^0]$ square plate with various a/h ratios: Convergence of normalized critical buckling loads and comparison with other solutions ($E_1/E_2 = 40,\ \lambda^* = N_x a^2/(E_2 h^3)$). 97

Table 3.33 Simply supported angle-ply $[45^0/-45^0]$ square plate with various a/h ratios: Convergence of normalized critical buckling loads and comparison with other solutions ($E_1/E_2 = 25,\ \lambda^* = N_x a^2/(E_2 h^3)$). 98

Table 3.34 Simply supported angle-ply $[45^0/-45^0/45^0/-45^0]$ square plate with various a/h ratios: Convergence of normalized critical buckling loads and comparison with other solutions ($E_1/E_2 = 25,\ \lambda^* = N_x a^2/(E_2 h^3)$). 98

Table 3.35 Cross-ply $[0^0/90^0]$ square plate with various mixed boundaries: Comparison of normalized critical buckling loads with other solutions ($E_1/E_2 = 40,\ a/h = 10,\ \lambda^* = N_x a^2/(E_2 h^3)$). 99

Table 3.36 Cross-ply 10-layer $[0^0/90^0]_5$ square plate with various mixed boundaries: Comparison of normalized critical buckling loads with other solutions ($E_1/E_2 = 40,\ a/h = 10,\ \lambda^* = N_x a^2/(E_2 h^3)$).100

Table 3.37 Angle-ply $[45^0/-45^0]$ square plate with various mixed boundaries: Comparison of normalized critical buckling loads with other solutions ($E_1/E_2 = 40,\ a/h = 10,\ \lambda^* = N_x a^2/(E_2 h^3)$). . 100

Table 3.38 Angle-ply $[45^0/-45^0]_5$ square plate with various mixed boundaries: Comparison of normalized critical buckling loads with other solutions ($E_1/E_2 = 40,\ a/h = 10,\ \lambda^* = N_x a^2/(E_2 h^3)$). . 100

Table 3.39 Simply supported cross-ply $[90^0/0^0/0^0/90^0]$ skew plate with various skew angles and span-to-thickness ratios: Comparison of the critical buckling loads with other solutions ($\lambda^* = N_x a^2/(E_2 h^3)$). 103

Table 3.40 Simply supported cross-ply $[0^0/90^0/0^0]$ square plate with various modulus ratio: Comparison of the critical bi-axial buckling loads with other solutions ($\lambda^* = N_x a^2/(E_2 h^3)$). 105

Table 3.41 Cross-ply $[0^0/90^0/0^0]$ square plate with various mixed boundaries under biaxial compression: Comparison of normalized critical buckling loads with other solutions ($E_1/E_2 = 40,\ a/h = 10,\ \lambda^* = N_x a^2/(E_2 h^3)$). 105

Table 4.1 List of shell elements used for comparison in the present study. 114

Table 4.2 The Scordelis-Lo roof: displacements at point B, normalized by 0.3024. 116

Table 4.3 An isotropic pinched cylinder with end diaphragms: normalized displacements at point C. Normalized by: 1.8248×10^{-5} . . . 119

Table 4.4 A laminated composite pinched cylinder problem: normalized displacements at point C, $w_c^* = 10w_c(\frac{a}{2}, \frac{a}{2})E_1h^3/(PR^2)$ 120

Table 4.5 A hemispherical shell with an 18^0 hole: displacements at point A, normalized by 0.0940 122

Table 4.6 Isotropic shallow spherical shell: vertical deflection $w_A \times 10^3$ at the center point A with various thickness h. 124

Table 4.7 Laminated composite shallow spherical shells: Convergence of central deflection $w_A \times 10^{-3}$ at the center point A with various span-to-thickness a/h. 125

Table 4.8 A hypar shell: central deflection w_0 for different elements . . . 127

Table 4.9 A partly clamped hyperbolic paraboloid shell: deflection at point A with mesh refinement. 129

Table 4.10 A partly clamped hyperbolic paraboloid shell: strain energy with mesh refinement 129

Table 4.11 Isotropic pre-twisted cantilever beam: tip displacements, normalized by 5.424×10^{-2} for in-plane displacements and by 1.754×10^{-2} for out-of-plane displacements. 132

Table 4.12 Thick laminated pre-twisted beam: Convergence of tip displacements and comparison with other solutions. 133

Table 4.13 Thin laminated pre-twisted beam: Convergence of tip displacements and comparison with other solutions. 134

Table 4.14 Simply supported cross-ply cylindrical shells: Convergence of normalized fundamental frequencies $\omega^* = (\omega L^2/h)\sqrt{\rho/E_2}$ for doubly symmetric modes and comparison with other solutions. 136

Table 4.15 Simply supported angle-ply cylindrical shells: Convergence of normalized fundamental frequencies $\omega^* = (\omega L^2/h)\sqrt{\rho/E_2}$ for doubly symmetric modes and comparison with other solutions. 137

Table 4.16 Clamped 9-layer $[(0^0/90^0)_4/0^0]$ cross-ply spherical shell: Comparison of the normalized frequencies $\omega^* = (\omega a^2/h)\sqrt{\rho/E_2}$ with other solutions. 138

Table 4.17 Simply supported cross-ply $[0^0/90^0/0^0/90^0//0^0]$ cylindrical shell panel: Comparison of the normalized critical buckling loads with other solutions ($\lambda^* = N_x a^2/(E_2 h^3)$). 141

Table 4.18 Simply supported cross-ply $k-$layer $[0^0/90^0/...]_k$ cylindrical shallow shell: Comparison of normalized critical buckling loads ($\lambda^* = N_x/(E_2 h)$, $R/a = 2$, $a/b = 1$). 142

Table 5.1 A clamped cross-ply $[0^0/90^0/90^0/0^0]$ square plate: Central deflections under a uniformly distributed load q_0. 154

Table 5.2 A simply supported unidirectional $[0^0]_8$ square plate: Central deflections under a uniformly distributed load q_0. 157

Table 5.3 Simply supported cross-ply $[0^0/90^0/90^0/0^0]$ square plate with various span-to-thickness ratios L/h: Comparison of normalized central deflections $w^* = w/h$ with other solutions under uniformly distributed load. 159

Table 5.4 Clamped cross-ply $[0^0/90^0]$ and angle-ply $[45^0/-45^0]$ square plates: Effect of the span-to-thickness ratios on normalized central deflections. 165

Table 5.5 Clamped isotropic circular plate under uniformly distributed load: Comparison of normalized central deflections $w^* = w/h$ with other solutions. 166

Table 6.1 Results of the patch test 194

Table 6.2 Single-layer piezoelectric material properties, dimensions and other constants. 200

Table 6.3 Tip deflections of the bimorph beam and comparison with available literatures ($\times 10^{-8}$ m). 212

Table 6.4 Computed results of piezoelectric membrane and relative error in comparion with the best known results of Long et al. (2006). 215

Table 6.5 Tip deflection of the bimorph beam of the micro-scanner MEMS device. 220

Table 6.6 Computed eigenvalues of the transducer and comparison with other solutions. 227

List of Figures

Figure 1.1 Schematic modelling of laminate structures in equivalent single-layer or layer-wise theories. 2

Figure 1.2 Kinematics of deformation in various ESL theories 4

Figure 2.1 A 4-node isoparametric quadrilateral element. 15

Figure 2.2 A 4-node quadrilateral element with drilling degrees of freedom 16

Figure 2.3 A 4-node quadrilateral plate bending element 19

Figure 2.4 A 4-node quadrilateral flat shell element 21

Figure 2.5 The projection of a warped shell element into a flat mean plane 22

Figure 3.1 Coordinate systems and layer positions defined in a laminate 27

Figure 3.2 Undeformed and deformed geometries of an edge of a plate under the assumptions of the FSDT. 28

Figure 3.3 Orientation and positive direction of force and moment resultants on a flat plate element 31

Figure 3.4 Subdivision of elements into *nc* smoothing cells and the values of shape functions at nodes in the format (N_1, N_2, N_3, N_4). . 35

Figure 3.5 Mid-side points used to interpolate the transverse shear deformation. 39

Figure 3.6 Patch test geometry and mesh. Isotropic material properties: $E = 10^6,\ \nu = 0.25,\ h = 0.001$. 43

Figure 3.7 Meshes of a quarter of simply supported plate: (a) regular mesh 6×6; (b) irregular mesh 3×3; (c) irregular mesh 6×6; (d) irregular mesh 12×12. 44

Figure 3.8 Convergence behaviour of the normalized central deflection w^*: (a) antisymmetric cross-ply $[0^0/90^0]$ and (b) symmetric cross-ply $[0^0/90^0/0^0]$. 47

Figure 3.9 Finite element and geometry data for an unsymmetric angle-ply plate. 48

Figure 3.10 Angle-ply $[\theta^0/-\theta^0]$ square plates: The effect of θ on the accuracy of w^*: (a) simply supported edges and (b) clamped edges. 52

Figure 3.11 Geometry data for unsymmetric angle-ply square plate. . . . 53

Figure 3.12 Finite element and geometry data of skew plate. 59

Figure 3.13 Typical meshes of a circular laminated plate: (a) a mesh of 12 elements and (b) a mesh of 48 elements. 61

Figure 3.14 Finite element and geometry data for triangular plate. 62

Figure 3.15 Geometry and material distribution of the functionally graded plate. 64

Figure 3.16 Square FGM Al/ZrO_2–1 plates under uniform load: non-dimensional central deflections versus the span-to-thickness ratios for (a) simply supported edges and (b) fully clamped edges. 67

Figure 3.17 Square FGM Al/ZrO_2–1 plates under uniform load: non-dimensional central normal stress σ_x^* at the top surface versus the span-to-thickness ratios for (a) simply supported edges and (b) fully clamped edges. 68

Figure 3.18 Square FGM Al/ZrO_2–2 plates: non-dimensional central deflections versus load parameter P under (a) mechanical load and (b) thermo-mechanical load. 70

Figure 3.19 Square FGM Al/ZrO_2–2 plates: non-dimensional central normal stress profile through the thickness under (a) mechanical load and (b) thermo-mechanical load. 71

Figure 3.20 Geometry and discretization of square laminated plates . . . 72

Figure 3.21 Cross-ply $[0^0/90^0/90^0/0^0]$ square laminated plate: (a) convergence of the present method and (b) effect of modulus ratio on the accuracy of fundamental frequencies. 74

Figure 3.22 Typical irregular meshes of 14×14 with various distortion factor s. 75

Figure 3.23 Square cross-ply [0/90/90/0] laminated plate: Effect of mesh distortion on the accuracy of the fundamental frequency. . . 76

Figure 3.24 Effect of fibre orientation and stacking sequence on fundamental frequencies of square laminated plates. 78

Figure 3.25 Clamped cross-ply $[0^0/90^0/0^0]$ square plate ($E_1/E_2 = 40$, $a/h = 10$): the first six mode shapes. 82

Figure 3.26 Geometry and discretization of skew laminated plates 83

Figure 3.27 Geometry and discretization of a circular laminated plate . . 86

Figure 3.28 Clamped circular angle-ply $[45^0/-45^0/-45^0/45^0]$ laminated plate: the first six mode shapes. 88

Figure 3.29 Clamped cross-ply $[0^0/90^0/0^0]$ right-angle triangular plates: the first six mode shapes. 90

Figure 3.30 Cross-ply square laminated plate subjected to in-plane compression. 92

Figure 3.31 Effect of modulus ratios on the accuracy of critical buckling loads. 92

Figure 3.32 Typical irregular meshes of 16×16 with various distortion factor s. 94

Figure 3.33 Cross-ply $[0^0/90^0/90^0/0^0]$ square plate: Effect of mesh distortion on the accuracy of critical buckling load. 94

Figure 3.34 Geometry and discretization of square laminated plates. . . . 96

Figure 3.35 Fundamental buckling modes of cross-ply 10-layer $[0^0/90^0]_5$ square plate with various mixed boundaries: (a) SSSS; (b) SSFF; (c) SSCC; (d) SSSC; (e) SSFC and (f) SSFS. 101

Figure 3.36 Geometry and discretization of cross-ply skew plates. 102

Figure 3.37 Geometry and discretization of cross-ply square plates. . . . 104

Figure 4.1 The Scordelis-Lo roof: Geometry and material data. 115

Figure 4.2 The Scordelis-Lo roof: (a) typical regular mesh and (b) irregular mesh. 115

Figure 4.3 The Scordelis-Lo roof: Convergence behaviour of normalized displacements at point B. 117

Figure 4.4 A pinched cylinder with end diaphragms: Geometry and material data. 118

Figure 4.5 A pinched cylinder with end diaphragms: (a) typical regular mesh and (b) irregular mesh. 118

Figure 4.6 An isotropic pinched cylinder with end diaphragms: Convergence behaviour. 120

Figure 4.7 A pinched hemispherical shell with 18^0 hole: Geometry and material data. 121

Figure 4.8 A pinched hemispherical shell with an 18^0 hole: Convergence behaviour of radial displacements at point A. 122

Figure 4.9 A shallow spherical shell: Geometry and material data. . . . 123

Figure 4.10 Isotropic shallow spherical shell: effect of thickness on the accuracy of central deflection. 124

Figure 4.11 A hypar shell: Geometry and material data. 126

Figure 4.12 A hypar shell: normalized central deflections with mesh refinement. 127

Figure 4.13 A partly clamped hypar shell: Geometry and material data. . 128

Figure 4.14 A partly clamped hypar shell: Typical meshes (a) a mesh of 16×8 uniform elements and (b) a mesh of 32×16 uniform elements. 128

Figure 4.15 A partly clamped hypar shell: Convergence of the displacement at point A. 130

Figure 4.16 A partly clamped hypar shell: Convergence of the strain energy. 130

Figure 4.17 Pre-twisted cantilever beams: geometry and material data. . 131

Figure 4.18 The pre-twisted cantilever beam: (a) typical regular mesh of 2×6 elements and (b) 4×24 elements. 131

Figure 4.19 Geometry and discretization of laminated cylindrical shells. . 135

Figure 4.20 Geometry and discretization of a laminated spherical shell. . 138

Figure 4.21 Clamped 9-layer cross-ply $[(0^0/90^0)_4/0^0]$ spherical shell: the first six mode shapes. 139

Figure 4.22 Geometry data of a cylindrical shallow shell subjected to uniaxial compression. 140

Figure 5.1 Meshes of a quarter of a simply supported plate: (a) typical regular mesh 3×3; (b) irregular mesh 3×3; (c) irregular mesh 4×4; (d) irregular mesh 5×5. 153

Figure 5.2 Clamped cross-ply 4-layer [0/90/90/0] square plate: Load-deflection relationship curves. 155

Figure 5.3 Clamped cross-ply 4-layer [0/90/90/0] square plate: Effect of mesh distortion. 155

Figure 5.4 Simply supported unidirectional 8-layer $[0^0]_8$ square plate: (a) regular mesh and (b) irregular mesh. 156

Figure 5.5 Simply supported unidirectional 8-layer $[0^0]_8$ square plate: Load-deflection relationship curves. 157

Figure 5.6 Simply supported unidirectional 8-layer $[0^0]_8$ square plate: Effect of mesh distortion. 158

Figure 5.7 Simply supported cross-ply $[0^0/90^0/90^0/0^0]$ square plate: Load-deflection curves with (a) $L/h = 40$ and (b) $L/h = 20$ 160

Figure 5.8 Simply supported cross-ply $[0^0/90^0/90^0/0^0]$ square plate: Load-deflection curves with (a) $L/h = 10$ and (b) the effect of span-to-thickness ratios. 161

Figure 5.9 Effect of span-to-thickness ratio L/h on the central deflection of clamped two-layer square plates: (a) cross-ply lamination (b) angle-ply lamination. 163

Figure 5.10 Effect of span-to-thickness ratio L/h and lamination scheme on the central deflection of clamped antisymmetric cross-ply and angle-ply square plates. 164

Figure 5.11 A quadrant of a clamped isotropic circular plate under uniform pressure with a mesh of 27 elements. 164

Figure 5.12 Clamped isotropic circular plate under uniformly distributed load: Load-deflection relationship curve. 166

Figure 5.13 Clamped isotropic cylindrical shell under uniform pressure. . 167

Figure 5.14 Clamped isotropic circular plate under uniformly distributed load: Load-deflection relationship curve. 168

Figure 5.15 A free-hinged angle-ply cylindrical shell under a uniform pressure. 168

Figure 5.16 A free-hinged angle-ply cylindrical shell under a uniform pressure. 169

Figure 5.17 A cross-ply spherical shell: Geometry and material data. . . 169

Figure 5.18 A free-hinged angle-ply cylindrical shell under a uniform pressure. 170

Figure 5.19 Semi-cylindrical shell under an end pinching force: Geometry and material data. 171

Figure 5.20 Semi-cylindrical shell under an end pinching force: Load-deflection curves at point load. 171

Figure 6.1 Subdivision of an element into *nc* smoothing cells and the values of shape functions at nodes. 182

Figure 6.2 Node-based elements: Transformation of an original mesh into smoothing elements associated with nodes. The dashed lines are formed by connecting midside points with centroidal points of original elements and serve as new cell (element) boundaries. 186

Figure 6.3 Shape function values for a typical linear triangular and bilinear quadrilateral element. 189

Figure 6.4 Detail of a node-based element (smoothing cell) and values of shape functions at Gauss points (a,b,c,d,e,f,g,h) 190

Figure 6.5 Typical meshes of the patch test: (a) triangular mesh (NSPE-T3 elements); (b) quadrilateral mesh (SPQ4, NSPE-Q4 elements). 192

Figure 6.6 Piezo-strip subjected to a uniform tension stress. 195

Figure 6.7 Typical meshes of a piezo-strip in tension: (a) triangular mesh (NSPE-T3, FEM-T3 elements); (b) quadrilateral mesh (NSPE-Q4, SPQ4 elements). 196

Figure 6.8 Total deformation of a piezo-strip in tension (scale factor: 5×10^5): (a) triangular mesh; (b) quadrilateral mesh. 196

Figure 6.9 Piezo-strip in tension: Computed and exact $u-$displacements: (a) Distribution of u on the edge $z = 0$; (b) Comparison of the error in $u-$displacement 197

Figure 6.10 Piezo-strip in tension: Computed and exact $w-$displacements: (a) Distribution of w on the edge $x = 0$; (b) Comparison of the error in $w-$displacement 198

Figure 6.11 Piezo-strip in tension: Computed and exact electric potential ϕ: (a) Distribution of ϕ on the edge $x = 0$; (b) Comparison of the error in electric potential. 199

Figure 6.12 Piezo-strip subjected to a uniform stress and a voltage. . . . 200

Figure 6.13 Typical meshes of a piezo-strip in shear: (a) triangular mesh (NSPE-T3, FEM-T3 elements); (b) quadrilateral mesh (NSPE-Q4, SPQ4 elements). 201

Figure 6.14 Total deformation of the piezo-strip in shear (scale factor=70): (a) triangular mesh; (b) quadrilateral mesh 202

Figure 6.15 Piezo-strip in shear: Computed and exact $u-$displacements: (a) Distribution of u on the edge $z = -h$; (b) Comparison of the error of $u-$displacement. 203

Figure 6.16 Piezo-strip in shear: Computed and exact $w-$displacements: (a) Distribution of w on the edge $z = -h$; (b) Comparison of the error of $w-$displacement. 204

Figure 6.17 Piezo-strip in shear: Computed and exact electric potential ϕ: (a) Distribution of ϕ on the edge $z = -h$; (b) Comparison of the error of electric potential. 205

Figure 6.18 Piezo-strip subjected to a linear stress and a voltage. 206

Figure 6.19 Total deformation of the piezo-strip in bending (scale factor=70): (a) triangular mesh; (b) quadrilateral mesh 207

Figure 6.20 Piezo-strip in bending: Computed and exact $u-$displacements: (a) Distribution of u on the edge $x = L$; (b) Comparison of the error of $u-$displacement. 208

Figure 6.21 Piezo-strip in bending: Computed and exact $w-$displacements: (a) Distribution of w on the edge $z = -h$; (b) Comparison of the error of $w-$displacement. 209

Figure 6.22 Piezo-strip in bending: Computed and exact electric potential ϕ: (a) Distribution of ϕ on the edge $x = L$; (b) Comparison of the error of electric potential. 210

Figure 6.23 Two-layer parallel bimorph cantilever beam. 211

Figure 6.24 Convergence behaviour of tip deflection. 213

Figure 6.25 Piezoelectric Cook's membrane. 213

Figure 6.26 Typical meshes of a piezoelectric Cook's membrane: (a) triangular mesh (NSPE-T3, FEM-T3 elements); (b) quadrilateral mesh (NSPE-Q4 elements). 214

Figure 6.27 Piezoelectric Cook's membrane: Convergence behaviours: (a) vertical displacement w at point A; (b) electric potential ϕ at point A. 216

Figure 6.28 Piezoelectric Cook's membrane: Convergence behaviours: (a) first principal stress σ_{1B} at point B; (b) electric flux density D_C at point C. 217

Figure 6.29 A bimorph optical micro-scanner MEMS device. 218

Figure 6.30 Behaviour of the mirror tilt angle under applied voltages. . . 220

Figure 6.31 An infinite piezo-plate with a circular hole subjected to the far field stress. 221

Figure 6.32 Typical meshes of a quadrant of a piezo-plate with a central circular hole: (a) triangular mesh (NSPE-T3 elements); (b) quadrilateral mesh (NSPE-Q4 elements). 222

Figure 6.33 Distribution of σ_r along the line $\theta = 0$. 223

Figure 6.34 Distribution of σ_θ along the line $\theta = 0$. 223

Figure 6.35 Distribution of σ_r along the line $\theta = \pi/2$. 224

Figure 6.36 Distribution of σ_t along the line $\theta = \pi/2$. 224

Figure 6.37 Representative sketch of a piezoelectric transducer. 226

Figure 6.38 Domain discretization of a piezoelectric transducer: (a) triangular mesh and (b) quadrilateral mesh. 226

Figure 6.39 Piezoelectric transducer: the first four mode shapes with (a) triangular mesh and (b) quadrilateral mesh. 228

Figure B.1 Variation of the volume fraction V_c versus the normalized thickness. 238

Chapter 1

Introduction

The goal of this chapter is to establish a motivation for the study of composite laminated plate/shell structures and outline the contributions and improvements that can be derived from the new development of the assumed strain smoothing technology. The chapter begins by presenting a survey of some popular methodologies for laminated composite plate/shell from classical to higher-order equivalent single-layer (ESL) theories and the layer-wise (LW) theories. This is an important step in obtaining a reasonable theory, the ESL first-order shear deformation theory (FSDT), before a literature review of plate/shell finite elements based on the FSDT is introduced. The motivation and objective of the present study is then given, followed by the outline of the dissertation. Finally, the contributions of the research to the literature are summarised.

1.1 General aspects

Fibre-reinforced composite materials have been widely used in various engineering applications such as spacecrafts, aircrafts, vehicles, building and smart highways (i.e. civil infrastructure applications) as well as sport equipment and medical prosthetics. Laminated composite structures consist of two or several layers of different fibre-reinforced laminas stacked together to achieve desired structural properties (e.g. stiffness, strength, wear resistance, damping, etc.). Through the variations of the lamina thickness, lamina material properties, fibre orientations

and stacking sequences, manufacturers can produce properties that exactly fit the requirements of a particular structure for a particular purpose (Reddy, 2004b).

Composite materials exhibit high strength-to-weight and stiffness-to-weight ratios, excellent resistance to corrosive substances and potentially high overall durability which make them ideally suited for use in weight-sensitive structures, especially in space applications. The extensive use of laminated composites in various types of plate and shell lead to considerable interests of the scientific and engineering communities in the field of modelling, analysis and design of composite plate and shell structures. Accurate prediction of structural response characteristics and assessments are often challenging problems for the analysis of laminated composites due to the anisotropic structural behaviour and the presence of various types of complicated constituent couplings (Reddy, 2004b). A number of methodologies for the analysis of laminated composite plates and shells have been developed with various degrees of success. These theories can be broadly classified into two main categories: (1) the equivalent single-layer (ESL) theories derived from the 3D elasticity theory in which a heterogeneous laminate is treated as an equivalent single layer with a complex constitutive behaviour and (2) the layer-wise (LW) theories where each lamina is treated individually with its own identity. The two categories are briefly illustrated in Figure 1.1.

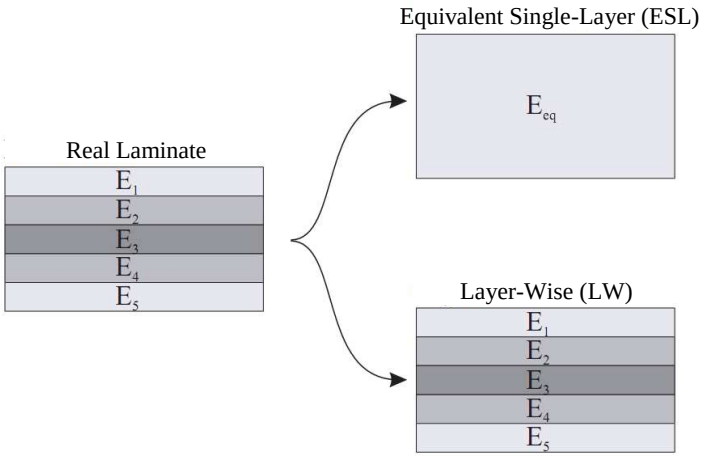

Figure 1.1: Schematic modelling of laminate structures in equivalent single-layer or layer-wise theories.

Among the two approaches mentioned above, the ESL theories have been used ex-

tensively owing to the advantages of simplicity in modelling and formulation, and low computational costs. In addition, the ESL models often provide a sufficiently accurate description of global response for thin to moderately thick laminates. In the context of the ESL theories, there are commonly three classes: the classical laminated plate theory (CLPT), the first-order shear deformation theory (FSDT) and the higher-order shear deformation theories (HSDT). Within each class, several modified versions have been developed to fulfill specific needs, especially for the HSDT. In the following, a representative of each theory is briefly summarized with a focus on the kinematic assumptions and its implementation.

The classical laminated plate theory (CLPT)

The classical laminated plate theory (CLPT) is the simplest one among the ESL theories which neglects the shear deformations. It is based on the Kirchhoff hypothesis that straight lines normal to the undeformed mid-surface remain straight and normal to the deformed mid-surface and do not undergo stretching in thickness direction. These assumptions imply the vanishing of both transverse shear and transverse normal strains. In this theory (see Figure 1.2), the displacement field is:

$$\begin{aligned} u(x,y,z) &= u_0(x,y) - zw_{0,x}, \\ v(x,y,z) &= v_0(x,y) - zw_{0,y}, \\ w(x,y,z) &= w_0(x,y), \end{aligned} \tag{1.1}$$

where $(u_0,\ v_0,\ w_0)$ are the displacements of a point on the mid-surface and z is the distance from the mid-surface to the point considered. From Equation (1.1) it is apparent that the displacement field is C^1-continuous since the strains are functions of the second order derivatives of w. The CPLT only yields satisfactory results for thin isotropic and laminated plates/shells. Conversion of the CLPT to finite element formulation are more numerically inconvenient with the C^1-continuity requirement as they necessitate the use of cubic Hermite interpolation function for the transverse deflection while linear Lagrange polynomials may be used for other displacements.

The first-order shear deformation theory (FSDT)

The first-order shear deformation theory (FSDT), also known as the Reissner-

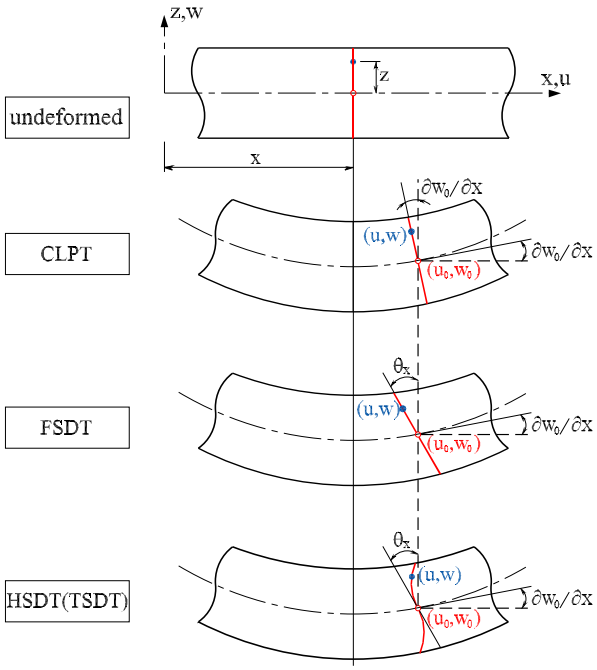

Figure 1.2: Kinematics of deformation in various ESL theories

Mindlin theory, can be considered as an improvement over the CLPT. This is achieved by including the effects of the transverse strains in the kinematic assumptions neglected in the CLPT. Like the CLPT it disregards the effect of transverse normal strains, however, it accounts for transverse shear strain by allowing the normal to rotate. The transverse shear strain is assumed to be constant across the thickness. The displacement field in this theory is:

$$\begin{aligned} u(x,y,z) &= u_0(x,y) + z\theta_x, \\ v(x,y,z) &= v_0(x,y) + z\theta_y, \\ w(x,y,z) &= w_0(x,y). \end{aligned} \tag{1.2}$$

where θ_x, θ_y denote the rotations of the transverse normal about the $y-$ and $x-$axis, respectively (see Figure 1.2).

The FSDT is simpler to implement than the CLPT since displacement field does not contain any derivatives and thereby is C^0-continuous. It also gives better results than those of the CLPT as the transverse shear strains are included. However, the method requires the use of problem-dependent shear correction factors (SCFs).

The higher-order shear deformation theory (HSDT)

To circumvent some of the limitations in the CLPT and the FSDT, several ESL higher-order shear deformation theories (HSDT) have been developed. Such theories account for parabolic or higher powers distribution of the transverse shear strain, correct cross-section warping and do not requires SCFs. One of the more effective methods is the third-order shear deformation theory (TSDT) of Reddy with minimum possible displacement parameters. It is based on the displacement field (see Figure 1.2) as follows.

$$\begin{aligned} u(x,y,z) &= u_0(x,y) + z\theta_x + z^3\left(-\frac{4}{3h^2}\right)(\theta_x + w_{0,x}), \\ v(x,y,z) &= v_0(x,y) + z\theta_y + z^3\left(-\frac{4}{3h^2}\right)(\theta_y + w_{0,y}), \\ w(x,y,z) &= w_0(x,y). \end{aligned} \tag{1.3}$$

The TSDT provides only a slight increase in accuracy relative to the FSDT solution but a drastic increase in computational effort due to additional components in the formula (Reddy, 2004b). In addition, it also requires C^1- continuity in the displacements which complicates the derivation of generalized finite element formulations as seen over the years (Yang et al., 2000). Therefore the HSDT have little practical applications as compared with the FSDT.

A brief review of various ESL theories mentioned above shows how the FSDT with transverse extensibility gives the best compromise between numerical accuracy, simplicity and computational burden for a wide range of plate/shell problems. Firstly, the FSDT models give better results than those based on the CLPT as the transverse shear strains are included in the formulations. Secondly, the FSDT–based element is easier to implement than the CLPT one since only C^0-continuity for all generalized displacement fields is required. This is in contrast with the C^1-continuity of Kirchhoff elements based on the CLPT which are more numerically inconvenient as they involve second partial derivatives of the interpolation functions. Furthermore, C^1-continuity element can neither account for all rigid body modes of a curved element (Cantin and Clough, 1968) nor cope with distorted meshes since the constant curvature criterion could be violated (Zienkiewicz, 1977). As compared with the HSDT, the FSDT is simpler, less expensive and can be implemented in a very straight-forward manner. Last

but not least, experience showed that the HSDT do not contribute considerably to solution accuracy (Jensen et al., 2002) and still require C^1-continuity. A more comprehensive review of the recent literature and comparison of theories can be found in Ghugal and Shimpi (2002) and Reddy and Arciniega (2004), for example.

In conclusion, low-order elements (C^0-element) based on the FSDT are simple to implement for modelling very complex plate/shell structures and underpin the most economical computational approach for nonlinear analysis. However, the primary difficulty of standard low-order elements based on the FSDT is that they are too stiff and suffer from shear locking in analysis of thin plate/shell structures. Many techniques have been proposed over the years to overcome these drawbacks with various degrees of success. A brief review of the relevant literature on the developments of C^0-elements based on the FSDT is discussed in the following section.

1.2 A brief review of recent plate/shell finite elements based on the FSDT

For many years, the development of elements based on the FSDT (Mindlin-Reissner theory) has attracted the attention of many researchers. Various approaches can be found in the literature (Bathe, 1996; Xiang et al., 1996; Zienkiewicz and Taylor, 2000; Xiang and Reddy, 2003; Xiang and Zhang, 2005, etc.). New models are being proposed in very recent works (Cen et al., 2006; Kim et al., 2007; Mai-Duy et al., 2007, etc.). These efforts make the FSDT more convenient and reasonable in practical applications.

During the past 40 years, many researchers have made significant contributions to the development of simple and efficient low-order elements based on the FSDT which is primarily for simplicity in mesh generation and robustness in complex nonlinear problems. The major problem of low-order elements is the appearance of shear-locking as the thickness-to-span ratio of the plate becomes too small (e.g. $h/a < 1/50$). Many techniques have been proposed to overcome this phenomenon with various degrees of success. There is a vast amount of literature on this sub-

ject which is impossible to list altogether and only the most prominent works are cited here. The first significant attempts started with the application of reduced or selective reduced integration techniques proposed by Zienkiewicz et al. (1971) and Hughes *et al.* (Hughes et al., 1977, 1978; Malkus and Hughes, 1978). However, for elements based on these techniques, it was found that in certain cases, extra zero energy modes may exist, which are caused by rank deficiency and hence these elements are not effective for thin-plate situation. Subsequently, remedies were provided by Hughes and Tezduar (1981) with a scheme motivated by the work of MacNeal (1978) where the rank deficiency was corrected by using 2×2 quadrature and the interpolation of the transverse shear was refined. However, these schemes resulted in the loss of the attractiveness of one-point quadrature integration. Another approach with one-point quadrature integration was the stabilization procedure by Belytschko et al. (1981) and Belytschko and Tsay (1983). Working along similar lines, some of the mixed/hybrid elements based on the FSDT, such as the shear-flexible element by Wilt et al. (1990) and the shear-locking-free element by Auricchio and Sacco (1999), seem to be efficient in removing shear-locking. However, their complex formulation and high computational cost render their usage less attractive in practical applications.

MacNeal (1982) developed a new concept called assumed natural strain (ANS) method. In this approach the shear strains are computed via kinematic variables at discrete collocation points of the element other than the nodes. Based on this concept, many successful models were then proposed, including the mixed interpolation tensorial component elements proposed by Bathe's group (Dvorkin and Bathe, 1984; Bathe and Dvorkin, 1985; Brezzi et al., 1989), the linked interpolation elements by Zienkiewicz's group (Zienkiewicz et al., 1993; Taylor and Auricchio, 1993), the discrete shear elements (Batoz and Lardeur, 1989; Lardeur and Batoz, 1989) which, in the limit of thin plates/shells, approach the famous discrete Kirchhoff elements DKT (Batoz et al., 1980) and DKQ (Batoz and Tahar, 1982), the discrete Kirchhoff-Mindlin elements DKMQ (Katili, 1993a) and DKMT proposed by Katili (1993b), etc. More details and reviews on the developmental history of this topic can be found in references (Yang et al., 2000; Ayad and Rigolot, 2002; Gal and Levy, 2006).

In parallel with the above developments, several recent formulations use displace-

ment function of the Timoshenko's beam to develop locking-free plate elements. Ibrahimbegovic (1992, 1993) first used Timoshenko's beam formulas to approximate the kinematic variables and shear strains along element sides and then developed three thin-thick plate elements PQ1, PQ2, PQ3 using the mixed interpolation method. Soh, Cen and Long used another set of Timoshenko's beam formulas to present a 12-DOF quadrilateral element, ARS-Q12 (Soh et al., 2001), and a 9-DOF triangular element, ARS-T9 (Soh et al., 1999) with a scheme similar to those of DKT and DKQ elements. Based on the element ARS-Q12, Cen et al. (2002) added a bilinear in-plane displacement field of the mid-plane to build a 4-node 20-DOF quadrilateral element CTMQ20. Some elements were later developed based on the same Timoshenko's beam function method such as the 9-DOF triangular element RDKTM (Chen and Cheung, 2001), the 20-DOF quadrilateral Mindlin plate element RDKQM (Chen and Cheung, 2000), the refined 15-DOF triangular Mindlin plate element RDTMLC (Ge and Chen, 2002), the 20-DOF and 24-DOF quadrilateral elements RDKQ-L20 and RDKQ-L24 (Zhang and Kim, 2004, 2006). Other surveys about shear deformable plate and shell finite elements can be found in recent detailed reviews of Gal and Levy (2006) and Zhang and Yang (2009), for example.

In addition to the shear-locking problem, existing FSDT-based elements also suffer from other drawbacks, including low accuracy due to mesh coarseness, element distortion, asymmetry of laminates (coupling effect) and high E_1(longitudinal) to E_2(transverse) modulus ratio. Therefore, developments in these specific areas are very desirable.

1.3 Motivation and Objectives

It is well-known that many useful techniques of mesh-free methods have been recently developed to avoid problems related to element distortion encountered in finite element method (FEM). In these methods, mesh generation is not required to discretize the problem domain and the field variables are approximated by a set of scattered nodes within the problem domain as well as on the boundaries. A comprehensive review of the recent literature of mesh-free methods can be found in Belytschko et al. (1996) and Li and Liu (2002).

One of developed mesh-free techniques is the nodal integration proposed by Beissel and Belytschko (1996) and Bonet and Kulasegaram (1999) to remove background meshes for the integration of the Element Free Galerkin (EFG) method. However, direct nodal integration usually leads to numerical instability and low accuracy due to the violation of the integration constraints (IC) in Galerkin approximation. In order to meet the IC, Chen and co-workers (Chen et al., 2001; Wang and Chen, 2004; Wang et al., 2006) introduced a stabilized conforming nodal integration (SCNI) using an assumed strain smoothing (ASS) method for the Galerkin mesh-free approximation which yielded a highly efficient, more accurate and convergent method. The SCNI was then extended to the natural element method (NEM) by Yoo et al. (2004). In mesh-free methods based on the stabilized nodal integration, the entire domain is discretized into cells defined by the field nodes, for example the cells of a Voronoi diagram (Chen et al., 2001; Wang and Chen, 2007). The ASS operation is then applied to compute nodal strains as the spatial average of the original strain field. This technique eliminates spurious modes by evaluating derivatives of mesh-free shape functions at nodes and numerical integration is performed along the boundaries of each cell. Based on the SCNI approach, Liu's group formulated the linearly conforming point interpolation method (LC-PIM) (Liu and Zhang, 2008) and the linearly conforming radial point interpolation method (LC-RPIM) (Zhao et al., 2008).

Although mesh-free methods have good accuracy and high convergence rate, the complex approximation space increases the computational cost for numerical integrations. Recently, the application of the SCNI in the existing FEM for two-dimensional elasticity problems was presented by Liu *et al.* (Liu, Nguyen, Dai and Lam, 2007; Liu, Dai and Nguyen, 2007) as a new smoothed finite element method (SFEM). It is found that the SFEM achieves more accurate results and higher convergence rate as compared with the non-smoothed FEM.

Inspired by the above strengths of the SCNI, this research will result in a further development of the SCNI technique and its incorporation into the conventional FEM will result in a simple, efficient and reliable computational model for analysis of laminated composite structures. Specifically, the objective of this research is to develop a family of novel and robust quadrilateral low-order displacement-based finite elements for numerical analysis of both isotropic and anisotropic plate/shell

structures that meet the following requirements:

- good bending behaviour
- free from membrane/shear locking in the limit of thin plates/shells without any spurious zeros energy modes
- insensitivity to extreme shape distortion
- good accuracy even with coarse mesh
- simple formulation and straightforward implementation of linear/nonlinear constitutive laws
- efficiency and reliability for linear and geometrically nonlinear analysis of thin to moderately thick composite plates/shell structures

The developed elements must handle laminated composite plate/shell structures with a large number of layers efficiently. Performance and accuracy comparisons between existing and the 'novel' element formulations are required in order to reveal advantages and limitations of the new elements. Furthermore, an extension of the applicability of the developed method is sought for coupled electric-structural piezoelectric systems.

To construct elements that fulfill the above requirements, the element formulation is based on the ASS technique of the SCNI mesh-free method which can achieve more accurate results in comparison with the corresponding standard FEM, without increasing the modeling and computational efforts. The significant distinguishing character of the novel elements is that the membrane, the bending and the geometric stiffness matrices are calculated via integration on the boundaries of the smoothing cells. This boundary integration contributes to the preservation of high accuracy of the method even with coarse mesh or when elements are extremely distorted (e.g. when two nodes are collapsed into one so that a quadrilateral becomes a triangle). Domain discretization is therefore more flexible than in the case of the standard FEM. Membrane, bending and geometric field gradients are also computed directly from shape functions themselves using the proposed method. Furthermore, these good features are acquired without increasing the number of field nodes and computational costs. The changes to

existing finite element codes are small and it can be easily implemented into FEM packages.

1.4 Outline of the dissertation

The thesis is divided into seven chapters including the Introduction and it is organized as follows.

- Chapter 2 presents an overview of some formulations of finite elements such as membrane, plate bending and flat shell elements that are to be employed in the developed procedures. This chapter also contains the assumed strain smoothing operation for developing new elements.
- Chapter 3 describes the development of two novel quadrilateral 4-node plate bending elements based on the ASS of the SCNI within the context of the FSDT and their implementations for analysis of laminated composite plates. An exhaustive set of numerical examples is then presented in order to cover, as effectively as possible, all relevant parameters, including geometries, mesh distortion levels and boundary conditions available. The selected examples also serve to show both the convergence and prediction capabilities of the developed elements in linear static, free vibration and buckling analysis of composite plate structures.
- Chapter 4 deals with the development of two quadrilateral flat shell elements based on two developed plate bending elements which are derived in Chapter 3. The verification and investigation of the flat shell models are then carried out in several benchmark problems including bending, dynamic and buckling analysis.
- Chapter 5 is to concentrate on the geometrically nonlinear analysis of plate and shell structures based on two developed elements derived in Chapter 3 and Chapter 4.
- Chapter 6 is to further develop the ASS technique for the analysis of coupling between mechanical and electrical behaviors of piezoelectric systems.

Two techniques for constructing novel elements are reported. The first one, the cell-based element, is based on the subdivision of original quadrilateral finite elements into smoothing cells. The second one, the node-based element, is created by transforming a triangular or quadrilateral mesh into a mesh of new smoothing cells associated with each of the nodes of the original mesh. Numerical studies and comparison between two methods and other numerical/analytic solutions in the literature are also carried out and investigated.

- Chapter 7 gives the closure of the present work. It starts with a summary of the study, followed by concluding remarks and some suggestions for future development of the research.

1.5 Main contributions of the research

According to the best of the author's knowledge, the current research has contributed to the advancement of knowledge in the following aspects.

- Introduce for the first time the assumed strain smoothing technique to displacement-based four-node plate/shell finite element model to mitigate the effect of mesh distortion and to enhance accuracy. This results in two novel simple and effective low-order quadrilateral flat elements for modeling general plate and shell structures which could not only be easily adapted to a particular material type (i.e. composite laminates, isotropic materials) but also improve model accuracy and alleviate the numerical instabilities.

- Demonstrate a wide range of engineering applications of the developed plate/shell elements in structural analysis with various geometric shapes (rectangular, triangular, skew, circular plates; cylindrical, spherical, hyperbolic paraboloid shells, etc.) as well as different type of materials (isotropic, laminated composite and functionally grade material).

- Provide a definitive and better understanding of the effect of modulus ratios (E_1/E_2), fibre orientations, different mixed boundary conditions, span-to-thickness ratios and lay-up sequences (i.e. cross-ply, angle-ply, symmet-

ric/unsymmetric laminates) on the behaviour of laminated composite structures in different regimes, including bending, free vibration and buckling analysis.

- Enhance the capabilities of low-order flat elements to perform efficient geometrically nonlinear analysis of isotropic homogenous material as well as composite laminated plate/shell structures with mesh distortion.

- Develop and extend the use of the assumed strain smoothing method for static and dynamic analysis of electrical-mechanical coupling of piezoelectric structures. This provides two types of new piezoelectric elements, the first one is the cell-based and the other the node-based element.

This research has led to the development of a new finite element model for general laminated composite structures. The simplicity and high performance of this approach would lead to future applications, including limit analysis/plasticity (Vaziri et al., 1992; Corradi and Vena, 2003), impact/damage behaviour (Vaziri et al., 1996), fracture mechanics and delamination growth (Falzon et al., 1999; Wagner et al., 2001) in composite structures.

Chapter 2

Overview of Finite Element Formulations

In this chapter, some basic finite element formulations which are used in the present study, are briefly described. The chapter provides an overview of the finite element formulations for membrane, plate bending and flat shell elements, followed by an outline of the assumed strain smoothing technique.

2.1 Membrane elements

Two membrane finite element formulations are used in this work. The first is the traditional isoparametric quadrilateral membrane element which neglects in-plane rotations. The second is the membrane element with in-plane (drilling) rotations that is investigated by Ibrahimbegovic et al. (1990). A brief review of the two elements is presented in the following sub-sections.

2.1.1 Isoparametric quadrilateral membrane element

In this section, the finite element formulations of the isoparametric quadrilateral membrane element is briefly reviewed for plane stress problems. The four node quadrilateral element has two degrees of freedom per node as shown in Figure 2.1

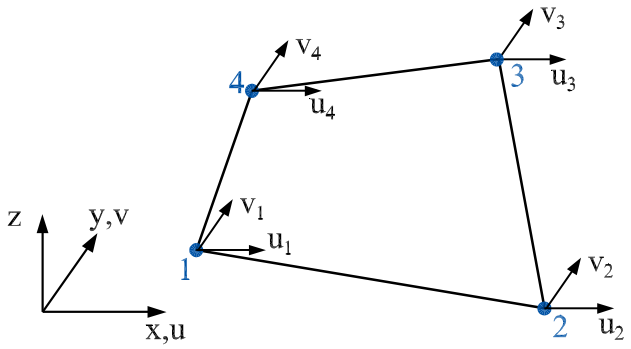

Figure 2.1: A 4-node isoparametric quadrilateral element.

The approximation of in-plane x and y displacements are defined by the following equations.

$$\begin{aligned} u &= \sum_{i=1}^{4} N_i(\xi,\eta)u_i, \\ v &= \sum_{i=1}^{4} N_i(\xi,\eta)v_i, \end{aligned} \tag{2.1}$$

where $N_i = \frac{1}{4}(1+\xi_i\xi)(1+\eta_i\eta)$ denotes the element shape function.

The discrete strain field is obtained by derivatives of the displacement as

$$\boldsymbol{\epsilon}_m = \left\{ \begin{array}{c} \epsilon_x \\ \epsilon_y \\ \gamma_{xy} \end{array} \right\} = \nabla_s \mathbf{u} = \left[\begin{array}{cc} \frac{\partial}{\partial x} & 0 \\ 0 & \frac{\partial}{\partial y} \\ \frac{\partial}{\partial y} & \frac{\partial}{\partial x} \end{array} \right] \mathbf{u} = \mathbf{B}_m \mathbf{q} = \sum_{i=1}^{4} \mathbf{B}_{mi}\mathbf{q}_i, \tag{2.2}$$

where $\mathbf{u} = [u \quad v]^T$, $\mathbf{q}_i = [u_i \quad v_i]^T$ is the nodal displacement vector and $\mathbf{B}_m$ is the gradient matrix

$$\mathbf{B}_{mi} = \left[\begin{array}{cc} N_{i,x} & 0 \\ 0 & N_{i,y} \\ N_{i,y} & N_{i,x} \end{array} \right]. \tag{2.3}$$

By assuming a linear elastic isotropic material, stresses can be obtained as

$$\boldsymbol{\sigma}_m = \left\{ \begin{array}{c} \sigma_x \\ \sigma_y \\ \tau_{xy} \end{array} \right\} = \underbrace{\frac{E}{1-\nu^2} \left[\begin{array}{ccc} 1 & \nu & 0 \\ \nu & 1 & 0 \\ 0 & 0 & \frac{1-\nu}{2} \end{array} \right]}_{\mathbf{D}_m} \boldsymbol{\epsilon}_m = \mathbf{D}_m \boldsymbol{\epsilon}_m. \tag{2.4}$$

The total potential energy Π_m of the element with body force $\mathbf{f}_b$ is given as

$$\Pi_m = \frac{1}{2}\int_\Omega \boldsymbol{\epsilon}_m^T \mathbf{D}_m \boldsymbol{\epsilon}_m d\Omega - \int_\Omega \mathbf{q}^T \mathbf{b} d\Omega. \tag{2.5}$$

Minimization of Equation (2.5) results in the element membrane stiffness matrix as

$$\mathbf{K}_{mem} = \int_\Omega \mathbf{B}_m^T \mathbf{D}_m \mathbf{B}_m d\Omega. \tag{2.6}$$

and the vector of nodal forces as

$$\mathbf{f} = \int_\Omega \mathbf{N}^T \mathbf{f}_b d\Omega. \tag{2.7}$$

2.1.2 Quadrilateral membrane element with drilling degrees of freedom

The 4-node membrane element with drilling DOFs (Figure 2.2) is derived by combining the in-plane displacements using Allman-type interpolation functions (Allman, 1984) and the standard bilinear independent normal (drilling) rotation fields. Details of the formulation can be found in the original reference (Ibrahimbegovic et al., 1990) and only a brief review is presented here.

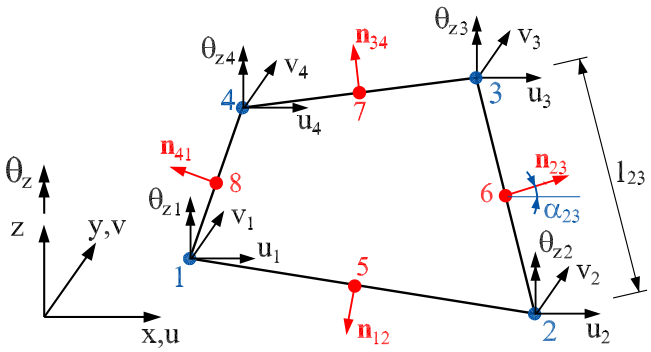

Figure 2.2: A 4-node quadrilateral element with drilling degrees of freedom

The independent rotation field is interpolated as follows.

$$\theta_z = \sum_{i=1}^{4} N_i(\xi,\eta)\theta_{zi}, \tag{2.8}$$

and the in-plane displacement fields are approximated by the Allman-type interpolation

$$\mathbf{u} = \begin{bmatrix} u \\ v \end{bmatrix} = \sum_{i=1}^{4} N_i(\xi,\eta) \begin{bmatrix} u_i \\ v_i \end{bmatrix} + \frac{l_{ij}}{8} \sum_{k=5}^{8} N_k(\xi,\eta)(\theta_{zj} - \theta_{zi})\mathbf{n}_{ij}, \tag{2.9}$$

where l_{ij} and $\mathbf{n}_{ij}$ are the length and the unit outward vector normal to the element side associated with the corner nodes i and j, for example

$$\mathbf{n}_{ij} = \begin{Bmatrix} n_1 \\ n_2 \end{Bmatrix} = \begin{Bmatrix} \cos\alpha_{ij} \\ \sin\alpha_{ij} \end{Bmatrix} = \begin{Bmatrix} \frac{y_{ij}}{l_{ij}} \\ \frac{x_{ij}}{l_{ij}} \end{Bmatrix}, \qquad l_{ij} = (x_{ij}^2 + y_{ij}^2)^{1/2}, \tag{2.10}$$

and the ordered triplets (k,i,j) are given by $(5,1,2)$, $(6,2,3)$, $(7,3,4)$, $(8,4,1)$ and

$$x_{ij} = x_j - x_i, \qquad y_{ij} = y_j - y_i, \tag{2.11}$$

$$N_i(\xi,\eta) = \tfrac{1}{4}(1+\xi_i\xi)(1+\eta_i\eta) \qquad i = 1,2,3,4 \tag{2.12}$$

$$N_k(\xi,\eta) = \tfrac{1}{2}(1-\xi^2)(1+\eta_k\eta) \qquad k = 5,7 \tag{2.13}$$

$$N_k(\xi,\eta) = \tfrac{1}{2}(1+\xi_k\xi)(1-\eta^2) \qquad k = 6,8. \tag{2.14}$$

Substituting Equation (2.10) into Equation (2.9) the approximation of in-plane fields can be rewritten as

$$\mathbf{u} = \begin{bmatrix} u \\ v \end{bmatrix} = \sum_{i=1}^{4} N_i(\xi,\eta) \begin{bmatrix} u_i \\ v_i \end{bmatrix} + \frac{1}{8} \sum_{k=5}^{8} N_k(\xi,\eta)(\theta_{zj} - \theta_{zi}) \begin{bmatrix} y_{ij} \\ x_{ij} \end{bmatrix} \tag{2.15}$$

The linear strain matrix is then given by

$$\boldsymbol{\epsilon}_m = \mathrm{symm}\nabla\mathbf{u} = \sum_{i=1}^{4} \mathbf{B}_{mi}\mathbf{q}_i, \tag{2.16}$$

where $\mathbf{q}_i = [u_i \quad v_i \quad \theta_{zi}]^T$ is the nodal vector and the gradient matrix $\mathbf{B}_{mi}$ has the following form

$$\mathbf{B}_{mi} = \begin{bmatrix} N_{i,x} & 0 & Nx_{i,x} \\ 0 & N_{i,y} & Ny_{i,y} \\ N_{i,y} & N_{i,x} & Nx_{i,y} + Ny_{i,x} \end{bmatrix}. \tag{2.17}$$

in which Nx, Ny are Allman's incompatible shape functions defined as

$$Nx_i = \frac{1}{8}(y_{ij}N_l - y_{ik}N_m), \tag{2.18}$$

$$Ny_i = \frac{1}{8}(x_{ij}N_l - x_{ik}N_m). \tag{2.19}$$

The above indices $i,\ j,\ k,\ l,\ m$ can be expressed in a Matlab-like definition as follows.

$$\begin{aligned} i &= 1,2,3,4;\ m = i+4;\ l = m-1+4*floor(1/i); \\ k &= mod(m,4)+1;\ j = l-4. \end{aligned} \tag{2.20}$$

where $floor(x)$ rounds the elements of x to the nearest integers towards minus infinity and $mod(x,y)$ is the modulus after division of x by y.

Furthermore, the skew-symmetric part of the strain tensor ($\boldsymbol{\epsilon}_{sk}$) can be expressed as

$$\boldsymbol{\epsilon}_{sk} = \text{skew}\nabla\mathbf{u} = \sum_{i=1}^{4} \mathbf{b}_i \mathbf{q}_i + \theta_z, \tag{2.21}$$

where

$$\mathbf{b}_i = \begin{bmatrix} -\frac{1}{2}N_{i,y} \\ \frac{1}{2}N_{i,x} \\ \frac{1}{16}\left(-y_{ij}N_{l,y} + y_{ik}N_{m,y} + x_{ij}N_{l,x} - x_{ik}N_{m,x}\right) - N_i \end{bmatrix}, \tag{2.22}$$

and the indices $i,\ j,\ k,\ l,\ m$ are defined by Equation (2.20).

The variational formulation suggested by Hughes and Brezzi (1989) is described as

$$\Pi_\gamma = \frac{1}{2}\int_\Omega \boldsymbol{\epsilon}_m^T \mathbf{D}_m \boldsymbol{\epsilon}_m d\Omega + \frac{1}{2}\gamma \int_\Omega (\boldsymbol{\epsilon}_{sk} - \theta_z)^2 d\Omega - \int_\Omega \mathbf{q}^T \mathbf{f}_b d\Omega. \tag{2.23}$$

Minimization of Equation (2.23) results in the element membrane stiffness matrix $\mathbf{K}_{mem}$, which is the sum of matrix $\mathbf{K}_m$ and a penalty matrix $\mathbf{P}_\gamma$ as follows.

$$\mathbf{K}_{mem} = \mathbf{K}_m + \mathbf{P}_\gamma = \int_\Omega \mathbf{B}_m^T \mathbf{D}_m \mathbf{B}_m d\Omega + \gamma \int_\Omega \mathbf{b}^T \mathbf{b} d\Omega. \tag{2.24}$$

The positive penalty parameter γ in Equation (2.24) is problem dependent. For isotropic elasticity, the formulation is reported to be insensitive to the value of γ which is taken as the shear modulus value ($\gamma = G$) (Hughes et al., 1989; Ibrahimbegovic et al., 1990). However, many recent numerical studies showed that the smaller value of γ (i.e. value of γ/G between 1/10000 and 1) appeared to give more accurate solutions (Long, Geyer and Groenwold, 2006; Liu et al., 2000; Pimpinelli, 2004). In this study, $\gamma/G = 1/1000$ is used. The vector of nodal forces in this case is the same as in Equation (2.7).

2.2 Shear deformable plate bending element

In this section, a four-node plate bending element based on the Mindlin-Reissner theory is derived. The element is shown in Figure 2.3. Each node of the element possesses three degrees of freedom (DOFs), namely the transverse displacement w in the $z-$direction, and the inplane rotations θ_x, θ_y about the $y-$axis, $x-$axis respectively.

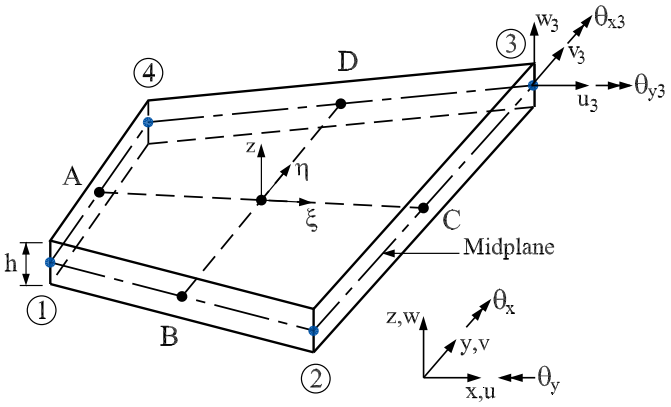

Figure 2.3: A 4-node quadrilateral plate bending element

The displacement field $\mathbf{u}$ of the plate is interpolated as

$$\mathbf{u} = [w \quad \theta_x \quad \theta_y]^T = \sum_{i=1}^{4} \mathbf{N}_i \mathbf{q}_i, \tag{2.25}$$

where $\mathbf{N}_i$ is the bilinear shape function as in Equation (2.12) and $\mathbf{q}_i = [w_i \;\; \theta_{xi} \;\; \theta_{yi}]$ is the nodal displacement vector of the element.

The corresponding approximation of strains is given by

$$\boldsymbol{\epsilon}_b = \left\{ \begin{array}{c} \epsilon_x \\ \epsilon_y \\ \gamma_{xy} \end{array} \right\} = \left[\begin{array}{c} \theta_{x,x} \\ \theta_{y,y} \\ \theta_{x,y} + \theta_{y,x} \end{array} \right] = \mathbf{B}_b \mathbf{q}, \tag{2.26}$$

$$\boldsymbol{\gamma} = \left\{ \begin{array}{c} \gamma_{xz} \\ \gamma_{yz} \end{array} \right\} = \mathbf{B}_s \mathbf{q}, \tag{2.27}$$

where

$$\mathbf{B}_{bi} = \begin{bmatrix} 0 & N_{i,x} & 0 \\ 0 & 0 & N_{i,y} \\ 0 & N_{i,y} & N_{i,x} \end{bmatrix}, \tag{2.28}$$

$$\mathbf{B}_{si} = \begin{bmatrix} N_{i,x} & N_i & 0 \\ N_{i,y} & 0 & N_i \end{bmatrix}. \tag{2.29}$$

The linear elastic stress-strain relations in bending are defined for a homogeneous, isotropic material as

$$\boldsymbol{\sigma}_b = \begin{Bmatrix} \sigma_x \\ \sigma_y \\ \tau_{xy} \end{Bmatrix} = \frac{E}{1-\nu^2} \begin{bmatrix} 1 & \nu & 0 \\ \nu & 1 & 0 \\ 0 & 0 & \frac{1-\nu}{2} \end{bmatrix} \boldsymbol{\epsilon}_b, \tag{2.30}$$

while the linear elastic stress-strain relations in transverse shear are defined as

$$\boldsymbol{\sigma}_s = \begin{Bmatrix} \tau_{xz} \\ \tau_{yz} \end{Bmatrix} = \frac{E}{2(1+\nu)} \begin{bmatrix} 1 & 0 \\ 0 & 1 \end{bmatrix} \boldsymbol{\gamma}. \tag{2.31}$$

The total potential energy Π_p of the plate, with the transverse loading per unit area $\mathbf{p}$, is given as

$$\Pi_p = \frac{1}{2} \int_\Omega \int_{-h/2}^{h/2} \boldsymbol{\sigma}_b^T \boldsymbol{\epsilon}_b dz d\Omega + \frac{k_s}{2} \int_\Omega \int_{-h/2}^{h/2} \boldsymbol{\sigma}_s^T \boldsymbol{\gamma} dz d\Omega - \int_\Omega \mathbf{p} w d\Omega. \tag{2.32}$$

where $k_s = 5/6$ is a shear correction factor.

Substitution of the constitutive relations for both bending and shear components from Equation (2.26) to Equation (2.31) into Equation (2.32) yields

$$\Pi_p = \frac{1}{2} \int_\Omega \boldsymbol{\epsilon}_b^T \mathbf{D}_b \boldsymbol{\epsilon}_b d\Omega + \frac{k_s}{2} \int_\Omega \boldsymbol{\gamma}^T \mathbf{D}_s \boldsymbol{\gamma} d\Omega - \int_\Omega \mathbf{p} w d\Omega, \tag{2.33}$$

where $\mathbf{D}_b$, $\mathbf{D}_s$ are material rigidity matrices for the bending and shear, respectively, which are given as

$$\mathbf{D}_b = \frac{Eh^3}{12(1-\nu^2)} \begin{bmatrix} 1 & \nu & 0 \\ \nu & 1 & 0 \\ 0 & 0 & \frac{1-\nu}{2} \end{bmatrix}, \tag{2.34}$$

$$\mathbf{D}_s = \frac{Eh}{2(1+\nu)} \begin{bmatrix} 1 & 0 \\ 0 & 1 \end{bmatrix}. \tag{2.35}$$

Equilibrium requires that Π_p is stationary, i.e., $\delta\Pi_p = 0$. This results in the element stiffness matrix as follows

$$\mathbf{K}_p = \underbrace{\int_\Omega \mathbf{B}_b^T \mathbf{D}_b \mathbf{B}_b d\Omega}_{\mathbf{K}_b} + \underbrace{k_s \int_\Omega \mathbf{B}_s^T \mathbf{D}_s \mathbf{B}_s}_{\mathbf{K}_s} = \mathbf{K}_b + \mathbf{K}_s, \tag{2.36}$$

and the vector of nodal forces is obtained as

$$\mathbf{f} = \int_\Omega \mathbf{N}^T \ \mathbf{p} d\Omega. \tag{2.37}$$

2.3 Flat shell element

The plate bending and membrane elements presented in the above sections can be combined to form a four-node shell element as shown in Figure 2.4.

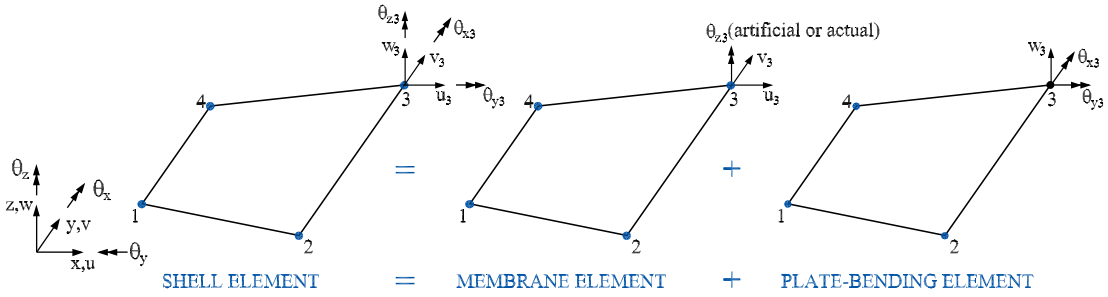

Figure 2.4: A 4-node quadrilateral flat shell element

When all nodes of the flat shell element are placed in the mid-thickness plane of the shell, the stiffness matrix of a shell element can be formed by combining the plate stiffness and membrane stiffness obtained independently as follows.

$$\mathbf{K}_{flat} = \begin{bmatrix} \mathbf{K}_{mem} & 0 \\ 0 & \mathbf{K}_p \end{bmatrix}. \tag{2.38}$$

For some shells with double curvature, it may not be possible to have four nodes of the flat shell element on the same plane (warped geometries) and the flat element stiffness must be modified before transformation to the global reference system by using the rigid link correction suggested by Taylor (1987). For the rigid link correction, the mean plane is formed by connecting central points of each side

and distances between the mean plane and each node are taken to be the same ($|z_i| = h$). Then, the following displacement transformation equation at each node i is employed to transform the nodal variables to the projected flat element variables:

$$\mathbf{q}'_i = \begin{Bmatrix} u'_i \\ v'_i \\ w'_i \\ \theta'_{xi} \\ \theta'_{yi} \\ \theta'_{zi} \end{Bmatrix} = \begin{bmatrix} 1 & 0 & 0 & 0 & 0 & 0 \\ 0 & 1 & 0 & 0 & 0 & 0 \\ 0 & 0 & 1 & 0 & 0 & 0 \\ 0 & z_i & 0 & 1 & 0 & 0 \\ -z_i & 0 & 0 & 0 & 1 & 0 \\ 0 & 0 & 0 & 0 & 0 & 1 \end{bmatrix} \begin{Bmatrix} u_i \\ v_i \\ w_i \\ \theta_{xi} \\ \theta_{yi} \\ \theta_{zi} \end{Bmatrix} = \mathbf{W}_i \mathbf{q}_i, \tag{2.39}$$

where $\mathbf{W}$ is the projection matrix and z_i defines the warpage offset at each node i perpendicular to the flat mean plane as shown in Figure 2.5.

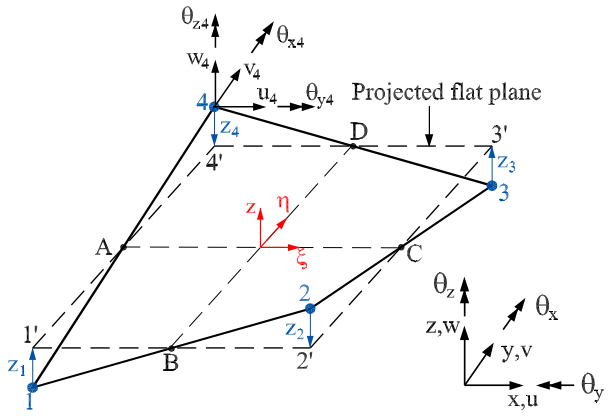

Figure 2.5: The projection of a warped shell element into a flat mean plane

The local element stiffness matrix, considering the warping effects, is obtained as follows.

$$\mathbf{K}_{local} = \mathbf{W}\mathbf{K}_{flat}\mathbf{W}^T. \tag{2.40}$$

Then the element stiffness in the global reference system $\mathbf{K}_{global}$ is obtained via the rotation matrix $\mathbf{R}$

$$\mathbf{K}_{global} = \mathbf{R}^T\mathbf{K}_{local}\mathbf{R}. \tag{2.41}$$

in which

$$\mathbf{R} = \begin{bmatrix} \mathbf{T} & 0 & 0 & 0 \\ 0 & \mathbf{T} & 0 & 0 \\ 0 & 0 & \mathbf{T} & 0 \\ 0 & 0 & 0 & \mathbf{T} \end{bmatrix}, \quad \mathbf{T} = \begin{bmatrix} t_{11} & t_{12} & t_{13} & 0 & 0 & 0 \\ t_{21} & t_{22} & t_{23} & 0 & 0 & 0 \\ t_{31} & t_{32} & t_{33} & 0 & 0 & 0 \\ 0 & 0 & 0 & t_{11} & t_{12} & t_{13} \\ 0 & 0 & 0 & t_{21} & t_{22} & t_{23} \\ 0 & 0 & 0 & t_{31} & t_{32} & t_{33} \end{bmatrix} \tag{2.42}$$

where t_{ij} is the direction cosine between the local axis x_i and the global axis X_j.

It is noted that when an isoparametric membrane element is used as a part of the flat shell element, there is no stiffness associated with the rotation degree of freedom θ_z. This lack of stiffness lead to singularity in the global stiffness matrix when all the elements are coplanar. A simple method for remedying this singularity is to insert a small fictitious stiffness to each drilling degree of freedom (Zienkiewicz and Taylor, 2000). This is done by simply replacing the null values of the stiffness corresponding to the drilling degree of freedom by a value of 1/1000 of the largest diagonal term of the element stiffness matrix. The stiffness matrix at each node of the shell element can thus be represented as follows.

$$\mathbf{K}_i = \begin{bmatrix} [\mathbf{K}_{mem}]_{2\times 2} & \mathbf{0}_{2\times 3} & 0 \\ \mathbf{0}_{3\times 2} & [\mathbf{K}_p]_{3\times 3} & 0 \\ 0 & 0 & 10^{-3}\max(\mathbf{K}_{i,i}) \end{bmatrix} \tag{2.43}$$

2.4 Assumed strain smoothing technique

An assumed strain smoothing method that meets integration constraints was proposed by Chen et al. (2001) as a stabilization of direct nodal integration in Galerkin mesh-free methods. This method avoids evaluating derivatives of mesh-free shape functions at nodes by performing numerical integration along the boundaries of each cell and thus eliminates spurious modes. Consider a domain Ω discretized by a set of nodes, Ω_L denotes the representative domain of a node $\mathbf{x}_L$. The strain smoothing at an arbitrary point $\mathbf{x}_L$ is defined as

$$\tilde{\boldsymbol{\epsilon}}_{ij}(\mathbf{x}_L) = \int_{\Omega_L} \boldsymbol{\epsilon}_{ij}(\mathbf{x})\Phi(\mathbf{x} - \mathbf{x}_L)d\Omega, \tag{2.44}$$

where $\boldsymbol{\epsilon}_{ij}$ is the strain obtained from displacement compatibility condition and Φ is a smoothing function that satisfies the following properties (Chen et al., 2001; Yoo et al., 2004)

$$\Phi \geq 0 \qquad \text{and} \qquad \int_{\Omega_L} \Phi \mathrm{d}\Omega = 1. \tag{2.45}$$

For simplicity, Φ is chosen as a piecewise constant function

$$\Phi(\mathbf{x} - \mathbf{x}_L) = \begin{cases} 1/A_L & \mathbf{x} \in \Omega_L, \\ 0 & \mathbf{x} \notin \Omega_L. \end{cases} \tag{2.46}$$

in which $A_L = \int_{\Omega_L} d\Omega$ is the area of the representative domain of node L

Substituting Φ into Equation (2.44) and applying the divergence theorem, the following equation is obtained

$$\tilde{\boldsymbol{\epsilon}}_{ij}(\mathbf{x}_L) = \frac{1}{2A_L} \int_{\Omega_L} \left(\frac{\partial u_i}{\partial x_j} + \frac{\partial u_j}{\partial x_i} \right) d\Omega = \frac{1}{2A_L} \int_{\Gamma_L} (u_i n_j + u_j n_i) d\Gamma, \tag{2.47}$$

where Γ_L is the boundary of the representative domain of node L and $\mathbf{n}$ is the unit outward vector normal to the boundary Γ_L.

Equation (2.47) forms the basis of strain smoothing stabilization for Galerkin mesh-free method that leads to the fulfilment of integration constraints in nodal integration as demonstrated in Chen et al. (2001); Wang and Chen (2007). This strain smoothing approximation is introduced for the first time into a standard 2D elastic finite element method via an assumed strain technique by Liu, Dai and Nguyen (2007). The strain smoothing technique can be considered as a constraint weakening method to avoid numerical over-stiffening of the elements. One of the advantages of the strain smoothing approach is that the numerical integration to obtain the element stiffness matrix can be performed (partly) on cell boundaries. This method can be advantageous in problems involving softening materials where mesh dependencies are involved only if a suitable number of smoothing cells is chosen for each element. More details on the effect of the number of smoothing cells in an element on accuracy can be found in the original paper of Liu, Dai and Nguyen (2007). Following this idea, the assumed strain smoothing method is further developed and extended to isotropic/anisotropic plate/shell structures and piezoelectric solids in this study. The detailed developments and applications of the assumed strain smoothing finite element method will be presented in the following chapters.

Chapter 3

Assumed Strain Smoothing Plate Finite Elements

This chapter reports the development of two simple but efficient and accurate four-node displacement-based C^0 quadrilateral elements, namely MISQ20 and MISQ24, for modelling of laminated composite plate structures. The developed elements are based on the assumed strain smoothing (ASS) finite element technique within the framework of the FSDT. The most important feature of the present ASS method is the method of evaluation of membrane, bending and geometric stiffness matrices based on integration along the boundary of smoothing elements, which can give more accurate numerical integration even with badly-shaped elements and reduce computational time when compared with domain integration techniques. The performance of the new elements is verified and demonstrated through several benchmark problems and comparative studies with analytic and other numerical solutions in the literature.

3.1 Introduction

In recent years, the use of laminated composite plates has been expanding rapidly in many engineering applications including aerospace, marine and civil infrastructure. Such high level of application has been paralleled by theoretical development

of simpler and more efficient elements for modelling of these structures. It is well-known that the first-order shear deformation plate theory (FSDT) is still the most attractive approach owing to its simplicity, good compromise between numerical accuracy and computational burden. Elements based on FSDT only need C^0-continuity for approximations of displacement fields and are also versatile as they can be applied in the case of thin to moderately thick plates. However, besides shear locking, currently available FSDT-based elements do not perform well when their shapes deviate significantly from a squarish form. There is a need for quadrilateral elements that are able to work well in extremely distorted forms, as problems coming from real life often involve irregular geometries.

Therefore, the objective of this chapter is to describe a contribution to further developments in this field, with the introduction and use of strain smoothing techniques of the SCNI mesh-free method into the conventional 4-node quadrilateral plate finite elements. The main construction steps are as follows: (1) apply the SCNI as strain smoothing technique for membrane and bending strain fields and (2) approximate the shear strain field with an independent interpolation scheme in the natural coordinate system.

Following the above procedure, two new 4-node quadrilateral plate elements denoted as MISQ20 and MISQ24 are formed for modelling and analyzing laminated composite plate structures. The significant distinguishing character of the novel elements is that the membrane, bending and geometric stiffness matrices are calculated via integration on the boundaries of smoothing cells. This boundary integration contributes to the preservation of high accuracy of the method even with coarse mesh or when elements are highly distorted. Domain discretization is therefore more flexible than in the case of the standard FEM.

This chapter is outlined as follows. First, a brief review of the FSDT is introduced in Section 3.2. The description of strain smoothing approaches for membrane strain and curvatures fields together with the assumed natural shear strain of the element are derived in Section 3.3. Several numerical simulations for static, free vibration and buckling analysis are investigated from Section 3.4 to Section 3.6 in order to verify and assess the performances of the proposed elements. Finally, some concluding remarks are presented in Section 3.7

3.2 First-order shear deformation theory of laminated plates

3.2.1 Governing equations

Consider a laminate consisting of n orthotropic layers with a total thickness h. The principal material coordinates $(x_1^k,\ x_2^k,\ x_3^k)$ of the k^{th} lamina is oriented at an angle θ^k to the laminate coordinate as shown in Figure 3.1. The k^{th} layer is located between the point $z = z_{k-1}$ and $z = z_k$ in the thickness direction and the $xy-$plane is taken to be undeformed midsurface of the laminate.

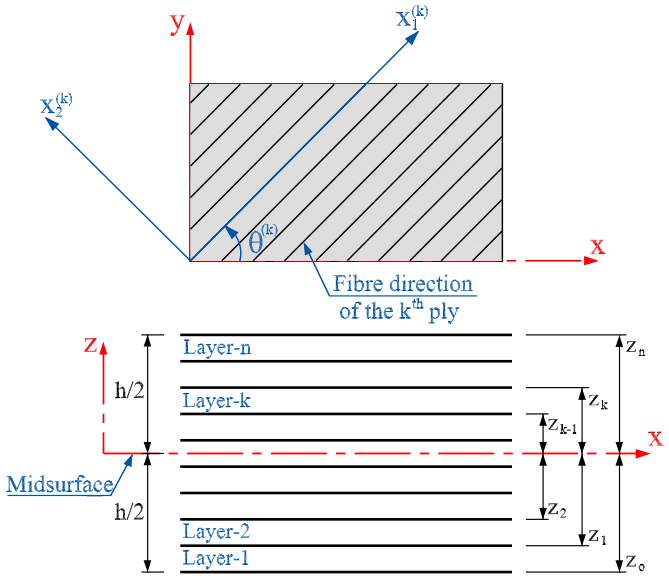

Figure 3.1: Coordinate systems and layer positions defined in a laminate

The first-order shear deformation theory (FSDT) of laminated plates is an extension of the Reissner-Mindlin theory for homogeneous isotropic thick plates. The theory takes into account transverse shear strain in the formulation with the following assumptions (Reddy, 2004b):

- The transverse normals remain straight after deformation but may not be orthogonal to the midsurface of the plate
- The transverse normals do not experience elongation so that the transverse strain $\epsilon_z = 0$

- The out-of-plane normal stress $\sigma_z = 0$
- The layers of the composite plate are perfectly bonded
- The material of each layer is linear elastic and orthotropic

In the FSDT, the plate kinematics is governed by the midplane displacement u_0, v_0, w_0 and the rotation θ_x, θ_y

$$\begin{aligned} u(x,y,z) &= u_0(x,y) + z\theta_x, \\ v(x,y,z) &= v_0(x,y) + z\theta_y, \\ w(x,y,z) &= w_0(x,y). \end{aligned} \tag{3.1}$$

A typical 4-node quadrilateral laminated plate element consisting of n layers with thickness h is shown in Figure 3.2

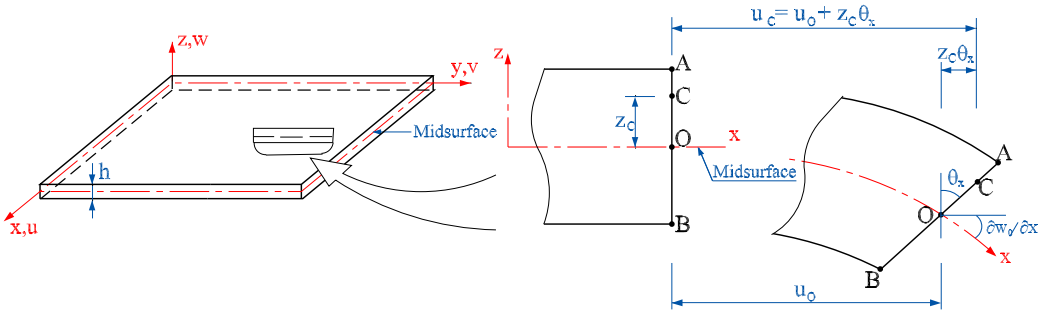

Figure 3.2: Undeformed and deformed geometries of an edge of a plate under the assumptions of the FSDT.

The in-plane strain vector $\boldsymbol{\epsilon} = [\epsilon_x \quad \epsilon_y \quad \gamma_{xy}]^T$ can be rewritten as

$$\boldsymbol{\epsilon} = \boldsymbol{\epsilon}_m + z\boldsymbol{\epsilon}_b, \tag{3.2}$$

where $\boldsymbol{\epsilon}_m$ is the membrane strain and $\boldsymbol{\epsilon}_b$ is the bending strain (curvatures), which are given as follows.

$$\boldsymbol{\epsilon}_m = \left\{ \begin{array}{c} \epsilon_x^m \\ \epsilon_y^m \\ \gamma_{xy}^m \end{array} \right\} = \left\{ \begin{array}{c} u_{0,x} \\ v_{0,y} \\ u_{0,y} + v_{0,x} \end{array} \right\}, \tag{3.3}$$

$$\boldsymbol{\epsilon}_b = \left\{ \begin{array}{c} \epsilon_x^b \\ \epsilon_y^b \\ \gamma_{xy}^b \end{array} \right\} = \left\{ \begin{array}{c} \theta_{x,x} \\ \theta_{y,y} \\ \theta_{x,y} + \theta_{y,x} \end{array} \right\}. \tag{3.4}$$

The transverse shear strain vector $\boldsymbol{\gamma} = [\gamma_{xz} \quad \gamma_{yz}]^T$ is given as

$$\boldsymbol{\gamma} = \left\{ \begin{array}{c} \theta_x - w_{,x} \\ \theta_y - w_{,y} \end{array} \right\}. \tag{3.5}$$

The stress-strain relation with respect to global $x-$ and $y-$axis for the $k^{th}(k = 1..n)$ lamina is expressed as

$$\boldsymbol{\sigma}^{(k)} = \left\{ \begin{array}{c} \sigma_x \\ \sigma_y \\ \tau_{xy} \end{array} \right\}^{(k)} = \left[\begin{array}{ccc} \bar{Q}_{11} & \bar{Q}_{12} & \bar{Q}_{16} \\ \bar{Q}_{12} & \bar{Q}_{22} & \bar{Q}_{26} \\ \bar{Q}_{16} & \bar{Q}_{26} & \bar{Q}_{66} \end{array} \right]^{(k)} \left\{ \begin{array}{c} \epsilon_x \\ \epsilon_y \\ \gamma_{xy} \end{array} \right\}^{(k)} = \bar{\mathbf{Q}}^{(k)} \boldsymbol{\epsilon}^{(k)}, \tag{3.6}$$

$$\boldsymbol{\tau}^{(k)} = \left\{ \begin{array}{c} \tau_{xz} \\ \tau_{yz} \end{array} \right\}^{(k)} = \left[\begin{array}{cc} k_1^2 \bar{Q}_{55}^* & k_1 k_2 \bar{Q}_{45}^* \\ k_1 k_2 \bar{Q}_{45}^* & k_2^2 \bar{Q}_{44}^* \end{array} \right]^{(k)} \left\{ \begin{array}{c} \gamma_{xz} \\ \gamma_{yz} \end{array} \right\}^{(k)} = \bar{\mathbf{C}}_s^{(k)} \boldsymbol{\gamma}^{(k)}, \tag{3.7}$$

where k_1^2, k_2^2 are SCFs and can be estimated by using special methods (Valchoutsis, 1992; Whitney, 1973) for anisotropic plates; $\bar{Q}_{ij}^k$, $\bar{Q}_{ij}^{*k}$ are the elastic constants of the k^{th} lamina (see Figure 3.1), which are given as

$$\bar{\mathbf{Q}}^{(k)} = \mathbf{T}_\epsilon \mathbf{Q}^{(k)} \mathbf{T}_\epsilon^T, \tag{3.8}$$

$$\bar{\mathbf{Q}}^{*(k)} = \mathbf{T}_\gamma \mathbf{Q}^{*(k)} \mathbf{T}_\gamma^T, \tag{3.9}$$

where

$$\mathbf{Q}^{(k)} = \left[\begin{array}{ccc} \frac{E_1}{1-\nu_{12}\nu_{21}} & \frac{\nu_{12}E_2}{1-\nu_{12}\nu_{21}} & 0 \\ \frac{\nu_{21}E_1}{1-\nu_{12}\nu_{21}} & \frac{E_2}{1-\nu_{12}\nu_{21}} & 0 \\ 0 & 0 & G_{12} \end{array} \right]^{(k)}, \tag{3.10}$$

$$\mathbf{Q}^{*(k)} = \left[\begin{array}{cc} G_{13} & 0 \\ 0 & G_{23} \end{array} \right]^{(k)}, \tag{3.11}$$

and $\mathbf{T}_\epsilon$, $\mathbf{T}_\gamma$ are transformation matrices

$$\mathbf{T}_\epsilon = \begin{bmatrix} c^2 & s^2 & -2cs \\ s^2 & c^2 & 2cs \\ cs & -cs & c^2 - s^2 \end{bmatrix}, \tag{3.12}$$

$$\mathbf{T}_\gamma = \begin{bmatrix} c & -s \\ s & c \end{bmatrix}, \tag{3.13}$$

in which $c = \cos\theta^{(k)}$, $s = \sin\theta^{(k)}$.

The equilibrium equations are developed in stress resultant form by considering the balance of forces and moments on an infinitesimal area of the laminate. Neglecting body moments and surface shearing forces, the equilibrium equations in the presence of applied transverse force $\mathbf{p}$ are given by:

$$\begin{aligned} N_{x,x} + N_{xy,y} &= 0, \\ N_{xy,x} + N_{y,y} &= 0, \\ Q_{x,x} + Q_{y,y} + p(x,y) &= 0, \\ M_{x,x} + M_{xy,y} - Q_x &= 0, \\ M_{xy,x} + M_{y,y} - Q_y &= 0. \end{aligned} \tag{3.14}$$

or more compactly as in the following variational form:

$$\int_\Omega [\delta\boldsymbol{\epsilon}_m^T\mathbf{N} + \delta\boldsymbol{\epsilon}_b^T\mathbf{M} + \delta\boldsymbol{\gamma}^T\mathbf{Q} - \mathbf{p}\delta\mathbf{w}]d\Omega = 0, \tag{3.15}$$

where $\mathbf{N} = \{N_x \;\; N_y \;\; N_{xy}\}$ is the in-plane force resultant, $\mathbf{Q} = \{Q_x \;\; Q_y\}$ is the out-of-plane force resultant and $\mathbf{M} = \{M_x \;\; M_y \;\; M_{xy}\}$ is the out-of-plane moment resultant (see Figure 3.3). These resultants are defined as acting per unit length as follows:

$$\begin{aligned} \begin{Bmatrix} N_x \\ N_y \\ N_{xy} \end{Bmatrix} &= \int_{-h/2}^{h/2} \begin{Bmatrix} \sigma_x \\ \sigma_y \\ \sigma_{xy} \end{Bmatrix} dz, \\ \begin{Bmatrix} M_x \\ M_y \\ M_{xy} \end{Bmatrix} &= \int_{-h/2}^{h/2} \begin{Bmatrix} \sigma_x \\ \sigma_y \\ \sigma_{xy} \end{Bmatrix} z dz, \\ \begin{Bmatrix} Q_x \\ Q_y \end{Bmatrix} &= \int_{-h/2}^{h/2} \begin{Bmatrix} \tau_{xz} \\ \tau_{yz} \end{Bmatrix} dz. \end{aligned} \tag{3.16}$$

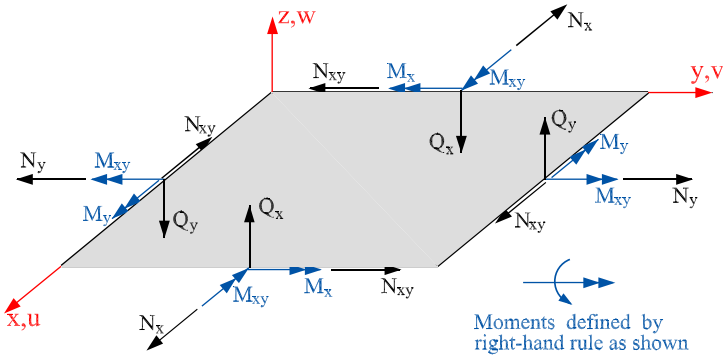

Figure 3.3: Orientation and positive direction of force and moment resultants on a flat plate element

Substituting Equation (3.2)–(3.7) into Equation (3.16), the following relationship between the stress resultants and the strains of the laminate is obtained:

$$\begin{Bmatrix} N_x \\ N_y \\ N_{xy} \end{Bmatrix} = \begin{bmatrix} A_{11} & A_{12} & A_{16} \\ A_{12} & A_{22} & A_{26} \\ A_{16} & A_{26} & A_{66} \end{bmatrix} \begin{Bmatrix} \epsilon_x^m \\ \epsilon_y^m \\ \gamma_{xy}^m \end{Bmatrix} + \begin{bmatrix} B_{11} & B_{12} & B_{16} \\ B_{12} & B_{22} & B_{26} \\ B_{16} & B_{26} & B_{66} \end{bmatrix} \begin{Bmatrix} \epsilon_x^b \\ \epsilon_y^b \\ \gamma_{xy}^b \end{Bmatrix}, \tag{3.17}$$

$$\begin{Bmatrix} M_x \\ M_y \\ M_{xy} \end{Bmatrix} = \begin{bmatrix} B_{11} & B_{12} & B_{16} \\ B_{12} & B_{22} & B_{26} \\ B_{16} & B_{26} & B_{66} \end{bmatrix} \begin{Bmatrix} \epsilon_x^m \\ \epsilon_y^m \\ \gamma_{xy}^m \end{Bmatrix} + \begin{bmatrix} D_{11} & D_{12} & D_{16} \\ D_{12} & D_{22} & D_{26} \\ D_{16} & D_{26} & D_{66} \end{bmatrix} \begin{Bmatrix} \epsilon_x^b \\ \epsilon_y^b \\ \gamma_{xy}^b \end{Bmatrix}, \tag{3.18}$$

$$\begin{Bmatrix} Q_x \\ Q_y \end{Bmatrix} = \begin{bmatrix} k_1^2 \bar{C}_{55}^0 & k_1 k_2 \bar{C}_{45}^0 \\ k_1 k_2 \bar{C}_{45}^0 & k_2^2 \bar{C}_{44}^0 \end{bmatrix} \begin{Bmatrix} \gamma_{xz} \\ \gamma_{yz} \end{Bmatrix}. \tag{3.19}$$

or more compactly in matrix notation as

$$\boldsymbol{\sigma}_p = \begin{Bmatrix} \mathbf{N} \\ \mathbf{M} \end{Bmatrix} = \begin{bmatrix} \mathbf{A} & \mathbf{B} \\ \mathbf{B} & \mathbf{D} \end{bmatrix} \begin{Bmatrix} \boldsymbol{\epsilon}_m \\ \boldsymbol{\epsilon}_b \end{Bmatrix} = \mathbf{C}_p \boldsymbol{\epsilon}_p, \tag{3.20}$$

$$\mathbf{T} = \begin{Bmatrix} Q_x \\ Q_y \end{Bmatrix} = \mathbf{C}_s \boldsymbol{\gamma}. \tag{3.21}$$

where A_{ij} is the extensional stiffness, D_{ij} is the bending stiffness, B_{ij} is the bending-extension coupling stiffness, which are defined in terms of the lamina stiffness $\bar{Q}_{ij}^{(k)}$ as

$$\begin{aligned} A_{ij} &= \sum_{k=1}^{n}(z_k - z_{k-1})\bar{Q}_{ij}^{k}, & i,j = 1,2,6 \\ B_{ij} &= \frac{1}{2}\sum_{k=1}^{n}(z_k^2 - z_{k-1}^2)\bar{Q}_{ij}^{k}, & i,j = 1,2,6 \\ D_{ij} &= \frac{1}{3}\sum_{k=1}^{n}(z_k^3 - z_{k-1}^3)\bar{Q}_{ij}^{k}, & i,j = 1,2,6 \\ C_{ij}^{0} &= \sum_{k=1}^{n}(z_k - z_{k-1})\bar{Q}_{ij}^{*k}, & i,j = 4,5 \end{aligned} \tag{3.22}$$

3.2.2 Finite element formulations

For the static analysis, the total potential energy functional of a laminated plate under a transverse load $\mathbf{p}$ is given as

$$\Pi_{static} = \frac{1}{2}\int_{\Omega}(\boldsymbol{\epsilon}_m^T\mathbf{A}\boldsymbol{\epsilon}+\boldsymbol{\epsilon}_m^T\mathbf{B}\boldsymbol{\epsilon}_b+\boldsymbol{\epsilon}_b^T\mathbf{B}\boldsymbol{\epsilon}_m+\boldsymbol{\epsilon}_b^T\mathbf{D}\boldsymbol{\epsilon}_b+\boldsymbol{\gamma}^T\mathbf{C}_s\boldsymbol{\gamma})d\Omega - \int_{\Omega}\mathbf{p}wd\Omega. \tag{3.23}$$

For free vibration analysis, the total potential energy functional of a laminated plate in the context of the FSDT can be expressed as follows.

$$\Pi_{vibration} = \frac{1}{2}\int_{\Omega}(\boldsymbol{\epsilon}_m^T\mathbf{A}\boldsymbol{\epsilon}+\boldsymbol{\epsilon}_m^T\mathbf{B}\boldsymbol{\epsilon}_b+\boldsymbol{\epsilon}_b^T\mathbf{B}\boldsymbol{\epsilon}_m+\boldsymbol{\epsilon}_b^T\mathbf{D}\boldsymbol{\epsilon}_b+\boldsymbol{\gamma}^T\mathbf{C}_s\boldsymbol{\gamma})d\Omega + \frac{1}{2}\int_{\Omega}\mathbf{u}^T m\ddot{\mathbf{u}}d\Omega. \tag{3.24}$$

For the buckling analysis when the plate is subjected to in-plane pre-buckling stress $\boldsymbol{\sigma}_0$ and in the absence of external forces, the potential energy is given by

$$\Pi_{buckling} = \frac{1}{2}\int_{\Omega}(\boldsymbol{\epsilon}_m^T\mathbf{A}\boldsymbol{\epsilon}+\boldsymbol{\epsilon}_m^T\mathbf{B}\boldsymbol{\epsilon}_b+\boldsymbol{\epsilon}_b^T\mathbf{B}\boldsymbol{\epsilon}_m+\boldsymbol{\epsilon}_b^T\mathbf{D}\boldsymbol{\epsilon}_b+\boldsymbol{\gamma}^T\mathbf{C}_s\boldsymbol{\gamma})d\Omega + \frac{1}{2}\int_{\Omega}\boldsymbol{\epsilon}_g^T\hat{\boldsymbol{\sigma}}_0\boldsymbol{\epsilon}_g d\Omega, \tag{3.25}$$

where

$$\boldsymbol{\sigma}_0 = \begin{bmatrix} \sigma_x^0 & \sigma_{xy}^0 \\ \sigma_{xy}^0 & \sigma_y^0 \end{bmatrix}, \quad \hat{\boldsymbol{\sigma}}_0 = \begin{bmatrix} h\boldsymbol{\sigma}_0 & 0 & 0 \\ 0 & \frac{h^3}{12}\boldsymbol{\sigma}_0 & 0 \\ 0 & 0 & \frac{h^3}{12}\boldsymbol{\sigma}_0 \end{bmatrix}, \quad \boldsymbol{\epsilon}_g = \begin{bmatrix} w_{,x} & 0 & 0 \\ w_{,y} & 0 & 0 \\ 0 & \theta_{x,x} & 0 \\ 0 & \theta_{x,y} & 0 \\ 0 & 0 & \theta_{y,x} \\ 0 & 0 & \theta_{y,y} \end{bmatrix}. \tag{3.26}$$

Consider a bounded domain $\Omega = \sum_{i=1}^{n_e} \Omega^e$ of a composite plate which is discretized into n_e finite elements. The finite element solution $\mathbf{u}$ of a displacement-based 4-node quadrilateral model is approximated as

$$\mathbf{u} = \begin{Bmatrix} u \\ v \\ w \\ \theta_x \\ \theta_y \end{Bmatrix} = \sum_{i=1}^{4} \mathbf{N}_i \mathbf{q}_i, \tag{3.27}$$

where $\mathbf{N}_i$ is the bilinear shape function, $\mathbf{q}_{mi} = [u_i \;\; v_i]^T$, $\mathbf{q}_{bi} = [w_i \;\; \theta_{xi} \;\; \theta_{yi}]^T$ and $\mathbf{q}_i = [\mathbf{q}_{mi} \;\; \mathbf{q}_{bi}]^T$ are the displacement vectors of the element.

The corresponding approximation of membrane, bending, shear and geometric strains can be expressed in the following form

$$\boldsymbol{\epsilon}_m = \mathbf{B}_m \mathbf{q}_m, \quad \boldsymbol{\epsilon}_b = \mathbf{B}_b \mathbf{q}_b, \quad \boldsymbol{\gamma} = \mathbf{B}_s \mathbf{q}_b, \quad \boldsymbol{\epsilon}_g = \mathbf{B}_g \mathbf{q}_b, \tag{3.28}$$

where

$$\mathbf{B}_{mi} = \begin{bmatrix} N_{i,x} & 0 \\ 0 & N_{i,y} \\ N_{i,y} & N_{i,x} \end{bmatrix}, \quad \mathbf{B}_{bi} = \begin{bmatrix} 0 & N_{i,x} & 0 \\ 0 & 0 & N_{i,y} \\ 0 & N_{i,y} & N_{i,x} \end{bmatrix}, \quad \mathbf{B}_{si} = \begin{bmatrix} N_{i,x} & N_i & 0 \\ N_{i,y} & 0 & N_i \end{bmatrix}, \tag{3.29}$$

$$\mathbf{B}_{gi} = \begin{bmatrix} N_{i,x} & 0 & 0 \\ N_{i,y} & 0 & 0 \\ 0 & N_{i,x} & 0 \\ 0 & N_{i,y} & 0 \\ 0 & 0 & N_{i,x} \\ 0 & 0 & N_{i,y} \end{bmatrix}. \tag{3.30}$$

By minimizing Equation (3.23)–(3.25), the finite element formulations of laminated plates can be obtained as follows.

For static analysis:

$$\mathbf{K}\mathbf{q} = \mathbf{F}, \tag{3.31}$$

where $\mathbf{K}$ is the global stiffness matrix and $\mathbf{F}$ is the load vector, which are given as follows.

$$\begin{aligned}\mathbf{K} &= \underbrace{\int_\Omega \mathbf{B}_m^T \mathbf{A} \mathbf{B}_m d\Omega}_{\mathbf{K}_m} + \underbrace{\int_\Omega (\mathbf{B}_m^T \mathbf{B} \mathbf{B}_b + \mathbf{B}_b^T \mathbf{B} \mathbf{B}_m) d\Omega}_{\mathbf{K}_{mb}+\mathbf{K}_{mb}^T} + \\ &\quad + \underbrace{\int_\Omega \mathbf{B}_b^T \mathbf{D} \mathbf{B}_b d\Omega}_{\mathbf{K}_b} + \underbrace{\int_\Omega \mathbf{B}_s^T \mathbf{C}_s \mathbf{B}_s \, d\Omega}_{\mathbf{K}_s} \\ &= \mathbf{K}_m + \mathbf{K}_{mb} + \mathbf{K}_{mb}^T + \mathbf{K}_b + \mathbf{K}_s, \qquad (3.32) \\ \mathbf{F} &= \int_\Omega \mathbf{N}^T \mathbf{p} d\Omega. \qquad (3.33)\end{aligned}$$

For free vibration analysis:

$$(\mathbf{K} - \omega^2 \mathbf{M})\mathbf{q} = 0, \qquad (3.34)$$

where ω is the natural frequency and $\mathbf{M}$ is the global mass matrix which is defined by

$$\mathbf{M} = \int_\Omega \mathbf{N}^T \mathbf{m} \mathbf{N} d\Omega, \quad \mathbf{m} = \rho h \begin{bmatrix} 1 & 0 & 0 & 0 & 0 \\ 0 & 1 & 0 & 0 & 0 \\ 0 & 0 & 1 & 0 & 0 \\ 0 & 0 & 0 & \frac{h^2}{12} & 0 \\ 0 & 0 & 0 & 0 & \frac{h^2}{12} \end{bmatrix}. \qquad (3.35)$$

For buckling analysis:

$$(\mathbf{K} - \lambda \mathbf{K}_g)\mathbf{q} = 0, \qquad (3.36)$$

where λ is the critical buckling load and $\mathbf{K}_g$ is the geometric stiffness matrix which is defined by

$$\mathbf{K}_g = \int_\Omega \mathbf{B}_g^T \hat{\boldsymbol{\sigma}}_0 \mathbf{B}_g d\Omega. \qquad (3.37)$$

3.3 Strain smoothing approach for laminated plate

3.3.1 Smoothed membrane strains

The membrane strains at an arbitrary point $\mathbf{x}_C$ are obtained by using the following strain smoothing operation

$$\tilde{\boldsymbol{\epsilon}}_m(\mathbf{x}_C) = \int_{\Omega_C} \boldsymbol{\epsilon}_m(\mathbf{x}) \Phi(\mathbf{x} - \mathbf{x}_C) d\Omega, \qquad (3.38)$$

where $\boldsymbol{\epsilon}_m$ is the membrane strain obtained from displacement compatibility condition as given in Equation (2.2). Ω_C is the smoothing cell domain on which the smoothing operation is performed. Depending on the stability analysis (Liu, Dai and Nguyen, 2007; Liu, Nguyen, Dai and Lam, 2007), Ω_C may be an entire element or part of an element as shown in Figure 3.4. Φ is a given smoothing function that satisfies at least unity property $\int_{\Omega_C} \Phi d\Omega = 1$ and, in the present work, is defined as

$$\Phi(\mathbf{x} - \mathbf{x}_C) = \begin{cases} 1/A_C & \mathbf{x} \in \Omega_C, \\ 0 & \mathbf{x} \notin \Omega_C. \end{cases} \tag{3.39}$$

where $A_C = \int_{\Omega_C} d\Omega$ is the area of the smoothing cell (subcell).

Substituting Φ into Equation (3.38) and applying the divergence theorem, one can get the smoothed membrane strain

$$\tilde{\boldsymbol{\epsilon}}_m(\mathbf{x}_C) = \frac{1}{2A_C} \int_{\Omega_C} \left(\frac{\partial u_i}{\partial x_j} + \frac{\partial u_j}{\partial x_i} \right) d\Omega = \frac{1}{2A_C} \int_{\Gamma_C} (u_i n_j + u_j n_i) d\Gamma, \tag{3.40}$$

where Γ_C is the boundary segment of the smoothing cell,

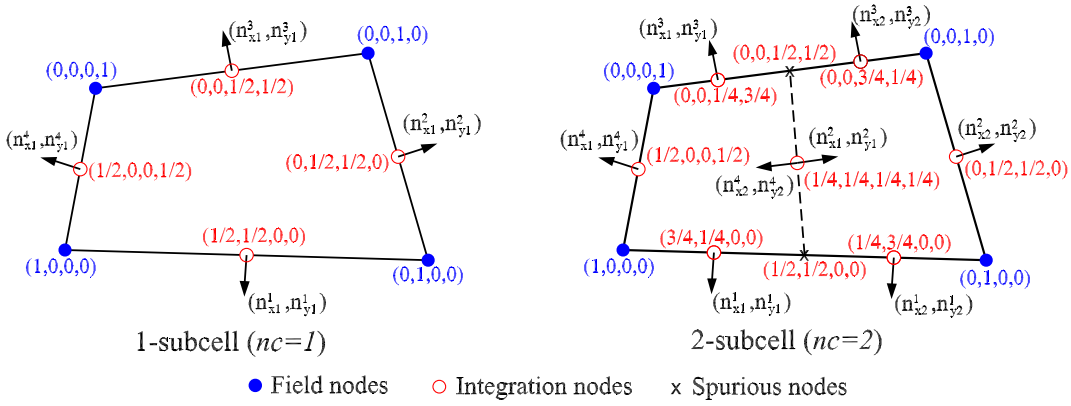

Figure 3.4: Subdivision of elements into nc smoothing cells and the values of shape functions at nodes in the format (N_1, N_2, N_3, N_4).

3.3.1.1 Smoothed isoparametric membrane element

Introducing the finite element approximation of $\mathbf{q}_m = [u \;\; v]^T$ from Equation (2.1) into Equation (3.40) gives

$$\tilde{\boldsymbol{\epsilon}}_m(\mathbf{x}_C) = \tilde{\mathbf{B}}_m(\mathbf{x}_C)\mathbf{q}_m, \tag{3.41}$$

where

$$\tilde{\mathbf{B}}_{mi}(\mathbf{x}_C) = \frac{1}{A_C}\int_{\Gamma_C}\begin{pmatrix} N_i n_x & 0 \\ 0 & N_i n_y \\ N_i n_y & N_i n_x \end{pmatrix} d\Gamma. \tag{3.42}$$

If one Gauss point is used to evaluate Equation (3.42) along each line segment of the boundary Γ_i^C of Ω_C, Equation (3.42) can be transformed as follows.

$$\tilde{\mathbf{B}}_{mi}(\mathbf{x}_C) = \frac{1}{A_C}\sum_{m=1}^{nb}\begin{pmatrix} N_i(\mathbf{x}_m^G) n_x & 0 \\ 0 & N_i(\mathbf{x}_m^G) n_y \\ N_i(\mathbf{x}_m^G) n_y & N_i(\mathbf{x}_m^G) n_x \end{pmatrix} l_m^C, \tag{3.43}$$

where $\mathbf{x}_m^G$ and l_m^C are the midpoint (Gauss point) and the length of Γ_m^C, respectively; nb is the total number of edges of each smoothing cell ($nb = 4$ in this case).

Finally, the smoothed element membrane stiffness matrix can be obtained as

$$\tilde{\mathbf{K}}_{mem} = \tilde{\mathbf{K}}_m = \int_\Omega \tilde{\mathbf{B}}_m^T \mathbf{A} \tilde{\mathbf{B}}_m d\Omega = \sum_{C=1}^{nc} \tilde{\mathbf{B}}_{mC}^T \mathbf{A} \tilde{\mathbf{B}}_{mC} A_C, \tag{3.44}$$

where nc is the number of smoothing cells chosen to be 2 in this case (Nguyen-Van et al., 2007a, 2008d).

3.3.1.2 Smoothed membrane element with drilling degrees of freedom

Introducing the finite element approximation of $\mathbf{q}_m = [u \quad v \quad \theta_z]^T$ into Equation (3.40) gives

$$\tilde{\boldsymbol{\epsilon}}_m(\mathbf{x}_C) = \tilde{\mathbf{B}}_m(\mathbf{x}_C)\mathbf{q}_m, \tag{3.45}$$

where

$$\mathbf{q}_{mi} = [u_i \quad v_i \quad \theta_{zi}]^T, \tag{3.46}$$

$$\tilde{\mathbf{B}}_{mi}(\mathbf{x}_C) = \frac{1}{A_C}\int_{\Gamma_C}\begin{pmatrix} N_i n_x & 0 & Nx_i n_x \\ 0 & N_i n_y & Ny_i n_y \\ N_i n_y & N_i n_x & Nx_i n_y + Ny_i n_x \end{pmatrix} d\Gamma. \tag{3.47}$$

Applying Gauss integration along each segment of the boundary Γ_C of the smoothing domain Ω_C, the above equation can be rewritten in algebraic form as

$$\begin{aligned}\tilde{\mathbf{B}}_{mi}(\mathbf{x}_C) = \frac{1}{A_C}\sum_{m=1}^{ns}\begin{pmatrix} \sum_{n=1}^{nG} w_n N_i(\mathbf{x}_{mn}) n_x & 0 & 0 \\ 0 & \sum_{n=1}^{nG} w_n N_i(\mathbf{x}_{mn}) n_y & 0 \\ \sum_{n=1}^{nG} w_n N_i(\mathbf{x}_{mn}) n_y & \sum_{n=1}^{nG} w_n N_i(\mathbf{x}_{mn}) n_x & 0 \end{pmatrix} \\ + \frac{1}{A_C}\sum_{m=1}^{ns}\begin{pmatrix} 0 & 0 & \sum_{n=1}^{nG} w_n N x_i(\mathbf{x}_{mn}) n_x \\ 0 & 0 & \sum_{n=1}^{nG} w_n N y_i(\mathbf{x}_{mn}) n_y \\ 0 & 0 & \sum_{n=1}^{nG} w_n N x_i(\mathbf{x}_{mn}) n_y + \sum_{n=1}^{nG} w_n N y_i(\mathbf{x}_{mn}) n_x \end{pmatrix}\end{aligned} \tag{3.48}$$

where ns is the number of segments of the boundary Γ_C ($ns = 4$ in this case), nG the number of Gauss integration points, $\mathbf{x}_{mn}$ the Gauss points and w_n the corresponding weighting coefficients. The first term in Equation (3.48), which relates to the in-plane translations is approximated by bilinear shape functions, and therefore is evaluated by one Gauss point ($nG = 1$). The second term, associated with the in-plane rotations, is approximated by quadratic shape functions, and therefore is computed using two Gauss points ($nG = 2$).

The smoothed membrane element stiffness matrix can be obtained as

$$\begin{aligned}\tilde{\mathbf{K}}_{mem} = \tilde{\mathbf{K}}_m + \mathbf{P}_\gamma = & \int_\Omega \tilde{\mathbf{B}}_m^T \mathbf{A} \tilde{\mathbf{B}}_m d\Omega + \gamma \int_\Omega \mathbf{b}^T \mathbf{b} d\Omega \\ = & \sum_{C=1}^{nc} \tilde{\mathbf{B}}_{mC}^T \mathbf{A} \tilde{\mathbf{B}}_{mC} A_C + \gamma \int_\Omega \mathbf{b}^T \mathbf{b} d\Omega,\end{aligned} \tag{3.49}$$

in which nc is the number of smoothing cells. To avoid numerically over-stiffening the membrane, one smoothing cell ($nc = 1$) is used in the present formulation. Higher numbers of smoothing cells will lead to stiffer solutions and the accuracy may not be enhanced considerably. The penalty matrix $\mathbf{P}_\gamma$ is integrated using a 1–point Gauss quadrature to suppress a spurious, zero-energy mode associated with the drilling DOFs. The positive penalty parameter γ is chosen as $\gamma/G_{12} = 1/1000$ in the study.

3.3.2 Smoothed bending strains of the element

Similarly, by using the same constant smoothing function Φ for membrane strain, the smoothed bending strain can be obtained as follows

$$\tilde{\boldsymbol{\epsilon}}_b(\mathbf{x}_C) = \int_{\Omega_C} \boldsymbol{\epsilon}_b(\mathbf{x})\Phi(\mathbf{x}-\mathbf{x}_C)d\Omega = \frac{1}{2A_C}\int_{\Gamma_C}(\theta_i n_j + \theta_j n_i)d\Gamma. \tag{3.50}$$

Then the relationship between the smoothed bending strain field and the nodal displacement is rewritten as

$$\tilde{\boldsymbol{\epsilon}}_b(\mathbf{x}_C) = \tilde{\mathbf{B}}_b(\mathbf{x}_C)\mathbf{q}_b, \tag{3.51}$$

where

$$\mathbf{q}_{bi} = [w_i \quad \theta_{xi} \quad \theta_{yi}], \tag{3.52}$$

$$\tilde{\mathbf{B}}_{bi}(\mathbf{x}_C) = \frac{1}{A_C}\int_{\Gamma_C}\begin{pmatrix} 0 & N_i n_x & 0 \\ 0 & 0 & N_i n_y \\ 0 & N_i n_y & N_i n_x \end{pmatrix} d\Gamma. \tag{3.53}$$

Using integration with one-point Gauss quadrature to evaluate the above equation over each line segment the smoothed gradient matrix is rewritten as

$$\tilde{\mathbf{B}}_{bi}(\mathbf{x}_C) = \frac{1}{A_C}\sum_{b=1}^{4}\begin{pmatrix} 0 & N_i(\mathbf{x}_b^G)n_x & 0 \\ 0 & 0 & N_i(\mathbf{x}_b^G)n_y \\ 0 & N_i(\mathbf{x}_b^G)n_y & N_i(\mathbf{x}_b^G)n_x \end{pmatrix} l_b^C. \tag{3.54}$$

Finally, the smoothed element bending stiffness matrix can be obtained as

$$\tilde{\mathbf{K}}_b = \int_\Omega \tilde{\mathbf{B}}_b^T \mathbf{D}\tilde{\mathbf{B}}_b d\Omega = \sum_{C=1}^{nc}\tilde{\mathbf{B}}_{bC}^T\mathbf{D}\tilde{\mathbf{B}}_{bC}A_C, \tag{3.55}$$

where nc is the number of smoothing cells, chosen to be 2 in this case in order to ensure the rank sufficiency (Nguyen-Van et al., 2007a; Nguyen-Xuan et al., 2008).

3.3.3 Transverse shear strains of the element

The shear strains are approximated with independent interpolation fields in the natural coordinate system (Bathe and Dvorkin, 1985)

$$\begin{bmatrix} \gamma_x \\ \gamma_y \end{bmatrix} = \mathbf{J}^{-1} \begin{bmatrix} \gamma_\xi \\ \gamma_\eta \end{bmatrix} = \mathbf{J}^{-1} \hat{\mathbf{N}} \begin{bmatrix} \gamma_\eta^A \\ \gamma_\xi^B \\ \gamma_\eta^C \\ \gamma_\xi^D \end{bmatrix}, \tag{3.56}$$

in which

$$\mathbf{J} = \begin{bmatrix} x_{,\xi} & y_{,\xi} \\ x_{,\eta} & y_{,\eta} \end{bmatrix}, \tag{3.57}$$

$$\hat{\mathbf{N}} = \frac{1}{2} \begin{bmatrix} (1-\xi) & 0 & (1+\xi) & 0 \\ 0 & (1-\eta) & 0 & (1+\eta) \end{bmatrix}, \tag{3.58}$$

$\mathbf{J}$ is the Jacobian matrix and the midside nodes A, B, C, D are shown in Figure 3.5. Expressing γ_η^A, γ_η^C and γ_ξ^B,γ_ξ^D in terms of the discretized fields $\mathbf{q}$, we obtain the shear matrix

$$\bar{\mathbf{B}}_{si} = \mathbf{J}^{-1} \begin{bmatrix} N_{i,\xi} & b_i^{11} N_{i,\xi} & b_i^{12} N_{i,\xi} \\ N_{i,\eta} & b_i^{21} N_{i,\eta} & b_i^{22} N_{i,\eta} \end{bmatrix}, \tag{3.59}$$

where

$$b_i^{11} = \xi_i x_{,\xi}^M, \; b_i^{12} = \xi_i y_{,\xi}^M, \quad b_i^{21} = \eta_i x_{,\eta}^L, \quad b_i^{22} = \eta_i y_{,\eta}^L \tag{3.60}$$

in which $\xi_i \in \{-1, 1, 1, -1\}$, $\eta_i \in \{-1, -1, 1, 1\}$,
and $(i, M, L) \in \{(1, B, A); (2, B, C); (3, D, C); (4, D, A)\}$.

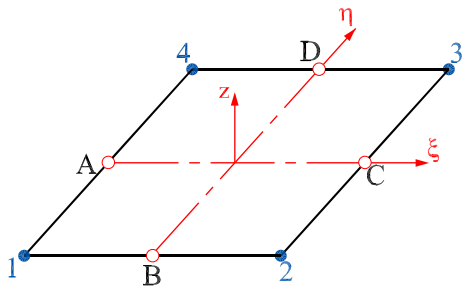

Figure 3.5: Mid-side points used to interpolate the transverse shear deformation.

3.3.4 Smoothed element stiffness matrix

The total potential energy functional of a laminated plate is given by

$$\Pi = \frac{1}{2}\int_{\Omega}(\tilde{\boldsymbol{\epsilon}}_m^T\mathbf{A}\tilde{\boldsymbol{\epsilon}}_m+\tilde{\boldsymbol{\epsilon}}_m^T\mathbf{B}\tilde{\boldsymbol{\epsilon}}_b+\tilde{\boldsymbol{\epsilon}}_b^T\mathbf{B}\tilde{\boldsymbol{\epsilon}}_m+\tilde{\boldsymbol{\epsilon}}_b^T\mathbf{D}\tilde{\boldsymbol{\epsilon}}_b+\boldsymbol{\gamma}^T\mathbf{C}_s\boldsymbol{\gamma})d\Omega-\int_{\Omega}\mathbf{p}wd\Omega \quad (3.61)$$

By minimizing Equation (3.61), the element stiffness matrix can be obtained as follows:

$$\tilde{\mathbf{K}} = \tilde{\mathbf{K}}_m + \tilde{\mathbf{K}}_{mb} + \tilde{\mathbf{K}}_{mb}^T + \tilde{\mathbf{K}}_b + \bar{\mathbf{K}}_s, \quad (3.62)$$

where

$$\tilde{\mathbf{K}}_m = \sum_{C=1}^{2}\tilde{\mathbf{B}}_{mC}^T\mathbf{A}\tilde{\mathbf{B}}_{mC}A_C \text{ (without drilling DOFs)}, \quad (3.63)$$

$$\tilde{\mathbf{K}}_m = \sum_{C=1}^{1}\tilde{\mathbf{B}}_{mC}^T\mathbf{A}\tilde{\mathbf{B}}_{mC}A_C+\gamma\int_{\Omega}\mathbf{b}^T\mathbf{b}d\Omega \text{ (with drilling DOFs)}, \quad (3.64)$$

$$\tilde{\mathbf{K}}_{mb} = \int_{\Omega}\tilde{\mathbf{B}}_m^T\mathbf{B}\tilde{\mathbf{B}}_b d\Omega = \sum_{C=1}^{2}\tilde{\mathbf{B}}_{mC}^T\mathbf{B}\tilde{\mathbf{B}}_{bC}A_C \text{ (without drilling DOFs)}, \quad (3.65)$$

$$\tilde{\mathbf{K}}_{mb} = \int_{\Omega}\tilde{\mathbf{B}}_m^T\mathbf{B}\tilde{\mathbf{B}}_b d\Omega = \sum_{C=1}^{1}\tilde{\mathbf{B}}_{mC}^T\mathbf{B}\tilde{\mathbf{B}}_{bC}A_C \text{ (with drilling DOFs)}, \quad (3.66)$$

$$\tilde{\mathbf{K}}_b = \int_{\Omega}\tilde{\mathbf{B}}_b^T\mathbf{D}\tilde{\mathbf{B}}_b d\Omega = \sum_{C=1}^{2}\tilde{\mathbf{B}}_{bC}^T\mathbf{D}\tilde{\mathbf{B}}_{bC}A_C, \quad (3.67)$$

$$\tilde{\mathbf{K}}_s = \int_{\Omega}\bar{\mathbf{B}}_s^T\mathbf{C}_s\bar{\mathbf{B}}_s d\Omega = \sum_{i=1}^{2}\sum_{j=1}^{2}w_i w_j\bar{\mathbf{B}}_s^T\mathbf{C}_s\bar{\mathbf{B}}_s\left|\mathbf{J}\right|d\xi d\eta. \quad (3.68)$$

Once the displacement variables are known, the in-plane stresses $\boldsymbol{\sigma}_p^k$ for the k^{th} layer are obtained by

$$\tilde{\boldsymbol{\sigma}}_p^k = \bar{\mathbf{Q}}^k(\tilde{\boldsymbol{\epsilon}}_m^0 + z\tilde{\boldsymbol{\epsilon}}_b^0), \quad (3.69)$$

and the transverse shear stresses are calculated by a simple approach of Rolfes and Rohwer (1997) with the details given in Appendix A.

The analysis described above forms the basis of two new four-node quadrilateral flat laminated plate elements, one without drilling DOFs and one with drilling DOFs. The first element with 5 DOFs per node is referred as MISQ20 (Mixed Interpolation Smoothing Quadrilateral element with 20 DOFs), which is defined

by Equation (3.63), Equation (3.65) and Equations (3.67)–(3.68). The second element with 6 DOFs per node is named as MISQ24 (Mixed Interpolation Smoothing Quadrilateral element with 24 DOFs), which is defined by Equation (3.64) and Equations (3.66)–(3.68).

3.3.5 Smoothed element geometric stiffness matrix

In a similar way, by using the same constant smoothing function Φ as in Equation (3.39), the smoothed geometric strain can be obtained as follows

$$\tilde{\boldsymbol{\epsilon}}_g(\mathbf{x}_C) = \tilde{\mathbf{B}}_g(\mathbf{x}_C)\mathbf{q}_b \tag{3.70}$$

where

$$\mathbf{q}_{bi} = [w_i \quad \theta_{xi} \quad \theta_{yi}], \tag{3.71}$$

$$\tilde{\mathbf{B}}_{gi}(\mathbf{x}_C) = \frac{1}{A_C}\int_{\Gamma_C} \begin{pmatrix} N_i n_x & 0 & 0 \\ N_i n_y & 0 & 0 \\ 0 & N_i n_x & 0 \\ 0 & N_i n_y & 0 \\ 0 & 0 & N_i n_x \\ 0 & 0 & N_i n_y \end{pmatrix} d\Gamma \tag{3.72}$$

Equation (3.72) can be evaluated with one-point Gauss quadrature integration as follows

$$\tilde{\mathbf{B}}_{gi}(\mathbf{x}_C) = \frac{1}{A_C}\sum_{g=1}^{nb} \begin{pmatrix} N_i(\mathbf{x}_g^G) n_x & 0 & 0 \\ N_i(\mathbf{x}_g^G) n_y & 0 & 0 \\ 0 & N_i(\mathbf{x}_g^G) n_x & 0 \\ 0 & N_i(\mathbf{x}_g^G) n_y & 0 \\ 0 & 0 & N_i(\mathbf{x}_g^G) n_x \\ 0 & 0 & N_i(\mathbf{x}_g^G) n_y \end{pmatrix} l_g^C, \tag{3.73}$$

in which $nb = 4$ is the number of edges of a smoothing cell.

Finally, the smoothed element geometric stiffness matrix can be obtained as

$$\tilde{\mathbf{K}}_g = \int_\Omega \tilde{\mathbf{B}}_g^T \hat{\boldsymbol{\sigma}}_0 \tilde{\mathbf{B}}_g d\Omega = \sum_{C=1}^{nc} \tilde{\mathbf{B}}_{gC}^T \hat{\boldsymbol{\sigma}}_0 \tilde{\mathbf{B}}_{gC} A_C, \tag{3.74}$$

where nc is the number of smoothing cells, chosen to be 1 in this case.

3.4 Numerical examples: Static analysis

In this section, we will test and assess the MISQ20 and MISQ24 elements through several application studies. Particular plates having different shapes, boundary conditions, thickness ratios, number of layers, fibre orientations are analyzed with these elements and the obtained results are discussed and compared with those obtained from other analytical and/or numerical solutions if available. In all examples, the material properties are assumed to be the same in all the layers and the fibre orientations may be different among the layers. The ply angle of each layer is measured from the global $x-$axis to the fibre direction. The thickness of each layer is identified. The material properties considered in the numerical examples here are given in Table 3.1.

Table 3.1: Material properties.

Moduli	HM graphite epoxy			
	M1	M2	M3	M4
$E_{11} \times 10^6$	25.0	40.0	40.0	5.6
$E_{22} \times 10^6$	1.0	1.0	1.0	1.2
$G_{12} \times 10^6$	0.5	0.6	0.5	0.6
$G_{13} \times 10^6$	0.5	0.6	0.5	0.6
$G_{23} \times 10^6$	0.2	0.5	0.5	0.6
$\nu_{12} = \nu_{23} = \nu_{13}$	0.25	0.25	0.25	0.26

Before substantial examples are presented, the elements will be shown to have passed the patch tests as described in the next section.

3.4.1 Patch tests

A patch test is a sufficient requirement in assessing the convergence of a finite element method. It is an essential check in order to verify whether given elements are able to exhibit states of constant strain and stress in distorted meshes. This property is important to ensure well-behaved convergence characteristics since elements should exhibit constant strain in the limit of infinitely small elements.

A choice of material, mesh and boundary conditions was adopted, following the approach of MacNeal and Harder (1985) as shown in Figure 3.6. In the patch tests, the prescribed displacements are applied at the edges corresponding to the nodes: 1, 2, 3 and 4. Two sets of tests are conducted including in-plane membrane patch test and out-of-plane bending test.

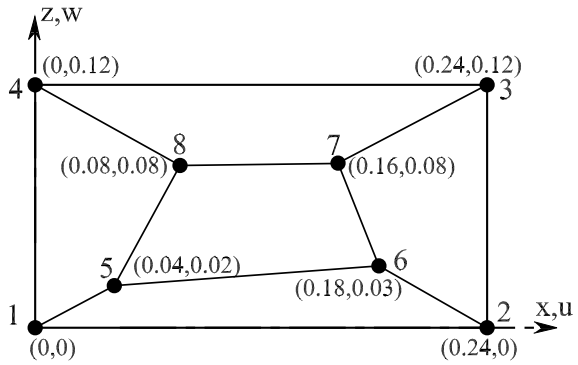

Figure 3.6: Patch test geometry and mesh. Isotropic material properties: $E = 10^6,\ \nu = 0.25,\ h = 0.001$.

The following boundary conditions are used in the patch test:

- Membrane test: $u = 10^{-3}(x + \frac{y}{2}),\ v = 10^{-3}(y + \frac{x}{2}),\ w = 0.$
- Bending test: $w = 10^{-3}(x^2+xy+y^2)/2,\ \theta_x = 10^{-3}(y+\frac{x}{2}),\ \theta_y = 10^{-3}(x+\frac{y}{2}).$

Table 3.2: Results of patch test

Test case	Stress	MISQ20	MISQ24	Exact
Membrane	σ_x	1.33300000E3	1.33300000E3	1333
	σ_y	1.33300000E3	1.33300000E3	1333
	σ_{xy}	0.40000000E3	0.39999999E3	400
Bending	M_x	1.11111111E-7	1.11111111E-7	1.11111111E-7
	M_y	1.11111111E-7	1.11111111E-7	1.11111111E-7
	M_{xy}	0.33333333E-7	0.33333333E-7	0.33333333E-7

As expected, the MISQ20 and MISQ24 give exact results (up to 8 digit machine precision) as shown in Table 3.2 for both test cases and hence both of MISQ20 and MISQ24 elements successfully pass the patch test.

3.4.2 Cross-ply 3-layer symmetric $[0^0/90^0/0^0]$ and 2-layer unsymmetric $[0^0/90^0]$ laminates under uniformly distributed load

The symmetric $[0^0/90^0/0^0]$ and unsymmetric $[0^0/90^0]$ cross-ply laminate square plates of material M1 with length a and thickness h, subjected to simply supported boundary SS1 (Reddy, 2004b) under a uniform transverse load $q_o = 1$ are studied. The shear correction factors are constant and equal to 5/6. Owing to symmetry, only a quarter of the plate is discretized using 3×3, 6×6, 12×12 meshes with regular as well as highly distorted elements as shown in Figure 3.7.

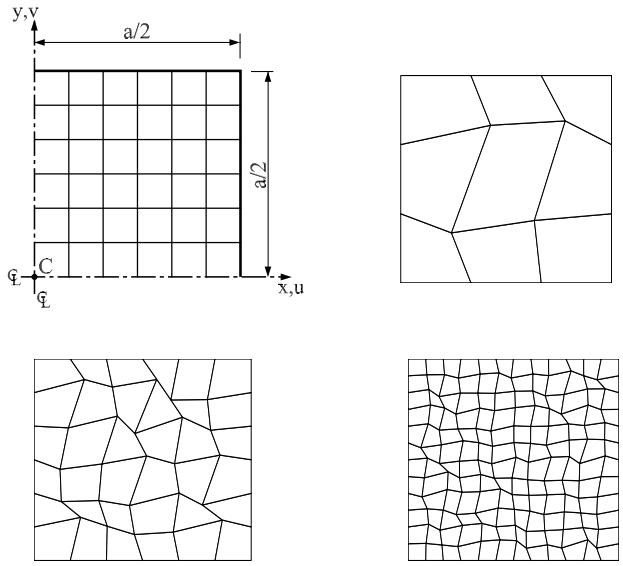

Figure 3.7: Meshes of a quarter of simply supported plate: (a) regular mesh 6×6; (b) irregular mesh 3×3; (c) irregular mesh 6×6; (d) irregular mesh 12×12.

Table 3.3 shows the prediction accuracies and convergence rate for the dimensionless plate center deflections $w^* = 100E_2wh^3/(q_oa^4)$ with the two types of mesh.

It is found that the accuracy of the present element MISQ20 is better than EML4 (Enhance Mixed Linked 4 node) element (Auricchio and Sacco, 1999), HASL (Hybrid Assumed-Strain Laminate) element (Cazzani et al., 2005) in the case of regular meshes 12×12. The performance of MISQ24 element is only better than that of HASL element for this particular problem. Numerical results in Table 3.3 also indicate that the performance of MISQ20 and MISQ24 element, in terms of

rate of convergence and accuracy, with respect to exact solution is excellent.

It is interesting to note that the proposed MISQ20 and MISQ24 elements yield not only accurate results in a wide range of thick to thin plates but also rapid convergence, especially when plates are thin for both regular and extremely distorted meshes. For symmetric cross-ply $[0^0/90^0/0^0]$ laminates, the calculated results with MISQ20 and MISQ24 elements are quite the same while for the unsymmetric cross-ply $[0^0/90^0]$ laminates, the MISQ24 element yields slightly smaller values than those of the MISQ20 element. The effect of distorted mesh and span-to-thickness ratio a/h on the convergence behaviour are depicted in Figure 3.8. It is found that the convergence rate for unsymmetric cross-ply $[0^0/90^0]$ with $a/h = 10$ is faster than $a/h = 100$ in both types of mesh. For symmetric cross-ply $[0^0/90^0/0^0]$, the convergence rate for w^* with $a/h = 10$ is slower than with $a/h = 100$.

Table 3.3: Simply supported cross-ply $[0^0/90^0]$ and $[0^0/90^0/0^0]$ square plate under uniform load: Convergence of normalized central deflection $w^* = 100E_2wh^3/(q_oa^4)$ and comparison with available literature.

a/h	Lay-up	Mesh	EML4	HASL	MISQ20			MISQ24			Exact
			12×12	12×12	3×3	6×6	12×12	3×3	6×6	12×12	
1000		Regular	–	–	1.6897	1.6943	1.6952	1.6691	1.6892	1.6939	–
		Irregular	–	–	1.6813	1.6918	1.6947	1.6568	1.6852	1.6931	
100	$[0^0/90^0]$	Regular	–	–	1.6923	1.6967	1.6979	1.6716	1.6917	1.6964	1.6980
		Irregular	–	–	1.6862	1.6928	1.6973	1.6598	1.6883	1.6958	
10		Regular	1.9470	–	1.9465	1.9469	1.9469	1.9260	1.9418	1.9456	1.9468
		Irregular	–	–	1.9516	1.9478	1.9466	1.9278	1.9422	1.9454	
1000		Regular	–	–	0.6736	0.6676	0.6664	0.6736	0.6676	0.6664	–
		Irregular	–	–	0.6728	0.6676	0.6667	0.6965	0.6696	0.6664	
100	$[0^0/90^0/0^0]$	Regular	–	0.6700	0.6773	0.6713	0.6700	0.6773	0.6713	0.6700	0.6697
		Irregular	–	–	0.7006	0.6736	0.6702	0.7006	0.6737	0.6702	
10		Regular	1.0220	1.0262	1.0367	1.0254	1.0227	1.0367	1.0254	1.0227	1.0219
		Irregular	–	–	1.0735	1.0312	1.0232	1.0735	1.0313	1.0233	

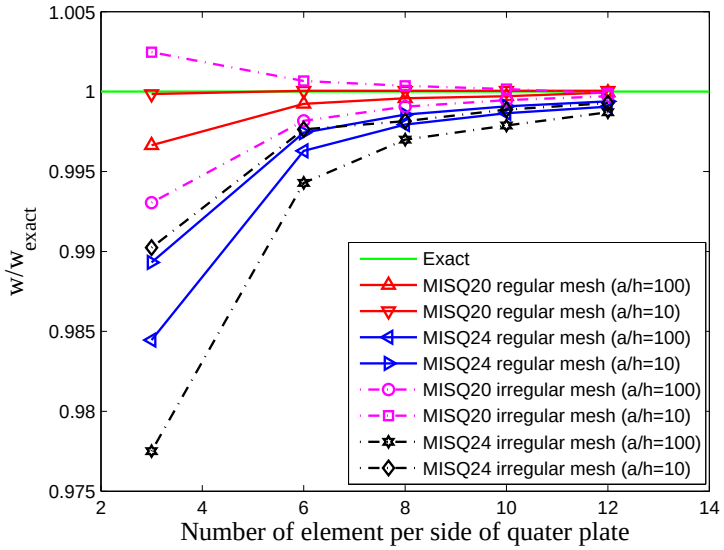

(a)

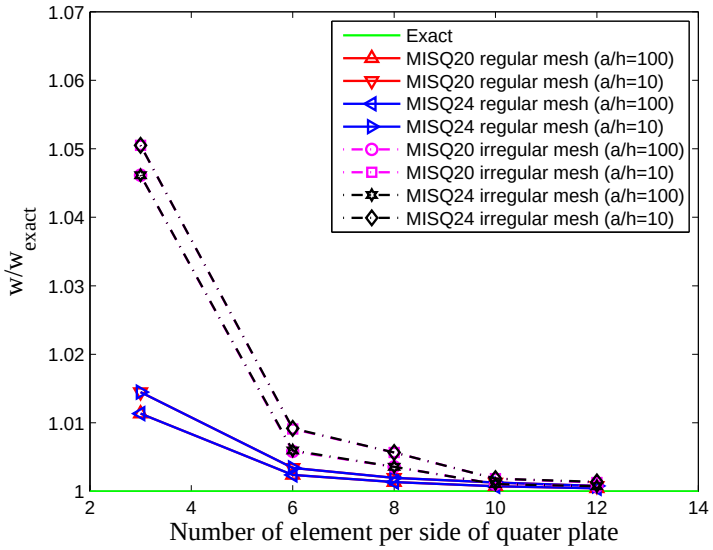

(b)

Figure 3.8: Convergence behaviour of the normalized central deflection w^*: (a) antisymmetric cross-ply $[0^0/90^0]$ and (b) symmetric cross-ply $[0^0/90^0/0^0]$.

3.4.3 Angle-ply $[\theta^0/-\theta^0]$ square plate under uniformly distributed load

A simply supported and clamped two-layer angle-ply $[\theta^0/-\theta^0]$ square plate of material M3 with length $a = 10$ and thickness $h = 0.02$, subjected to a uniformly distributed transverse load $q_o = 1$ is analyzed. Shear correction factors are: $k_1^2 = k_2^2 = 5/6$. The total thicknesses of θ^0 and $-\theta^0$ layers are equal. Due to asymmetry, the entire plate is modelled using 4×4, 6×6, 8×8, 10×10 meshes. A representative sketch of the 6×6 mesh used in this analysis is shown in Figure 3.9.

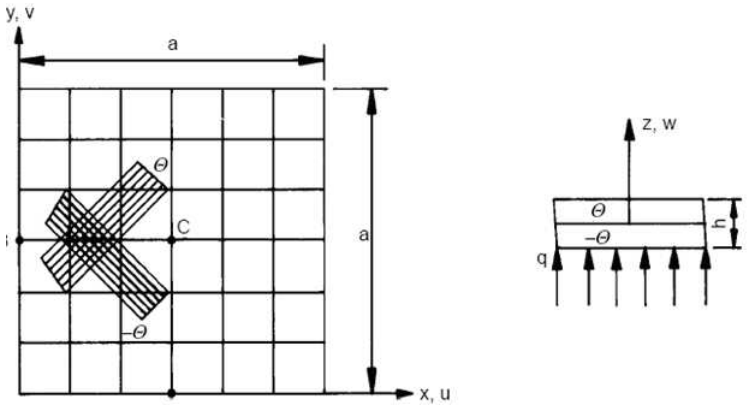

Figure 3.9: Finite element and geometry data for an unsymmetric angle-ply plate.

Table 3.4 presents a convergence study of the normalized central deflection $w^* = 100E_2wh^3/(q_oa^4)$ for the simply supported two-layer square plate with different fibre orientation angles. The normalized central deflection w^* is compared with the numerical solutions obtained using MQH3T (Spilker et al., 1985) (hybrid laminated element), SQUAD4 (Wilt et al., 1990) (mixed laminated element), RDTMLC (Ge and Chen, 2002) (refined discrete triangular laminated element), RDKQ-L20, RDKQ-L24 (Zhang and Kim, 2004) (refined discrete quadrilateral laminate element) and the exact solution given by Whitney (1969, 1970). Similar results are presented in Table 3.5 for the clamped two-layer angle-ply square plate. The effect of fibre orientation on the accuracy of the present methods is also shown in Figure 3.10.

From Table 3.4 and Figure 3.10a, it can be seen that the accuracy of the present

elements compares very favorably with other elements and the method is convergent with mesh refinement as shown in Table 3.4. The accuracy obtained with the present MISQ20 and MISQ24 elements is quite insensitive to fibre angles while other methods behave badly in some cases as shown in Figure 3.10a and Table 3.4.

From Table 3.5 for the case of clamped edges, it is evident that with an 8×8 mesh for the whole plate, the present element gives more accurate results than the SQUAD4 element with a 10×10 mesh and the RDKQ-L20, RDKQ-L24 element with a 10×10 mesh. The MISQ20 results with a 10×10 mesh are comparable to those of MQH3T with a 6×6 mesh and RDTMLC with an 8×8 mesh but the degrees of freedom associated with MQH3T elements are much larger (665 DOF compared with 605 DOF). In this case, the performance of RDTMLC with respect to fibre angles can be considered as the best one, but in the case of simply supported plate, it is the worst behaviour (see Figure 3.10a).

It is clear from these numerical results of simply supported and clamped plates that the MISQ20 and MISQ24 elements exhibit very favorable performance with respect to fibre angle variation. It is also observed that the effect of strong boundary layers together with the asymmetry of angle-ply lamination made the predictions of displacements for the case of the CCCC boundary less accurate than that of the SSSS boundary.

Table 3.4: Simply supported 2-layer angle-ply $[\theta/-\theta]$ square plate under uniform load: Convergence of the normalized central deflection $w^* = 100E_2wh^3/(q_o a^4)$ with different fibre angles and comparison with available literature.

Fibre angle	Exact	MQH3T	SQUAD4	RDTMLC	RDKQ-L20	RDKQ-L24	MISQ20			MISQ24		
		6×6 (665DOF)	10×10 (605DOF)	10×10 (605DOF)	10×10 (605DOF)	10×10 (726DOF)	6×6	8×8	10×10 (605DOF)	6×6	8×8	10×10 (726DOF)
$\pm 5^0$	0.4736	0.4764	0.4776	0.4760	0.4739	0.4749	0.4793	0.4758	0.4748	0.4793	0.4751	0.4739
$\pm 15^0$	0.7142	0.7160	–	0.7064	0.7141	0.7164	0.7191	0.7164	0.7155	0.7199	0.7167	0.7156
$\pm 25^0$	0.7870	0.7870	0.8030	0.7720	0.7860	0.7875	0.7901	0.7886	0.7880	0.7878	0.7870	0.7869
$\pm 35^0$	0.7561	0.7555	0.7745	0.7480	0.7546	0.7550	0.7581	0.7571	0.7567	0.7540	0.7547	0.7551
$\pm 45^0$	0.7322	0.7315	0.7506	0.7184	0.7309	0.7312	0.7340	0.7331	0.7327	0.7275	0.7295	0.7305

Table 3.5: Clamped 2-layer angle-ply $[\theta/-\theta]$ square plate under uniform load: Convergence of normalized central deflection $w^* = 100E_2wh^3/(q_oa^4)$ with different fibre angles and comparison with available literature.

Fibre angle	Exact	MQH3T 6×6 (665DOF)	SQUAD4 10×10 (605DOF)	RDTMLC 10×10 (605DOF)	RDKQ-L20 10×10 (605DOF)	RDKQ-L24 10×10 (726DOF)	MISQ20 6×6	MISQ20 8×8	MISQ20 10×10 (605DOF)	MISQ24 6×6	MISQ24 8×8	MISQ24 10×10 (726DOF)
$\pm5^0$	0.0946	0.1083	0.1040	0.1074	0.1046	0.1049	0.1010	0.1013	0.1023	0.1022	0.1018	0.1025
$\pm15^0$	0.1691	0.2009	–	0.1959	0.1990	0.1993	0.1961	0.1964	0.1971	0.1980	0.1976	0.1977
$\pm25^0$	0.2355	0.2572	0.2602	0.2508	0.2600	0.2599	0.2578	0.2579	0.2580	0.2582	0.2583	0.2584
$\pm35^0$	0.2763	0.2844	0.2914	0.2782	0.2908	0.2907	0.2909	0.2895	0.2889	0.2881	0.2882	0.2882
$\pm45^0$	0.2890	0.2929	0.3013	0.2868	0.3004	0.3004	0.3013	0.2993	0.2986	0.2947	0.2956	0.2962

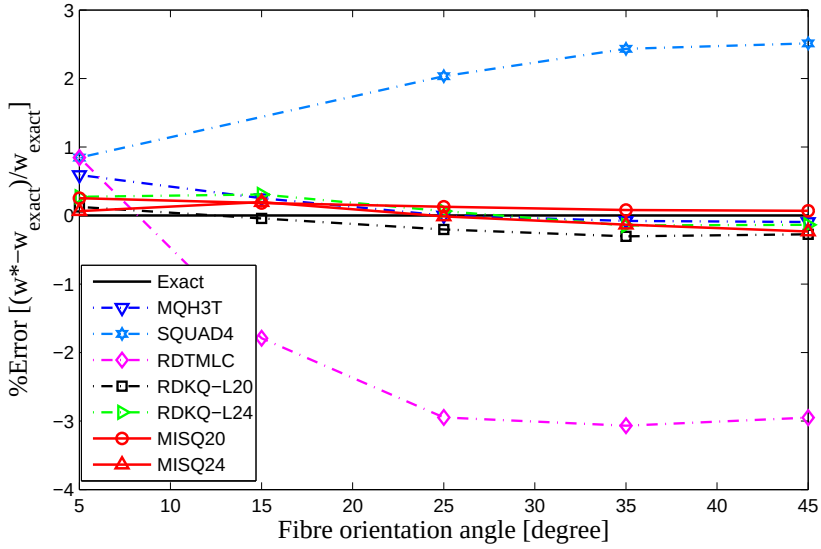

(a)

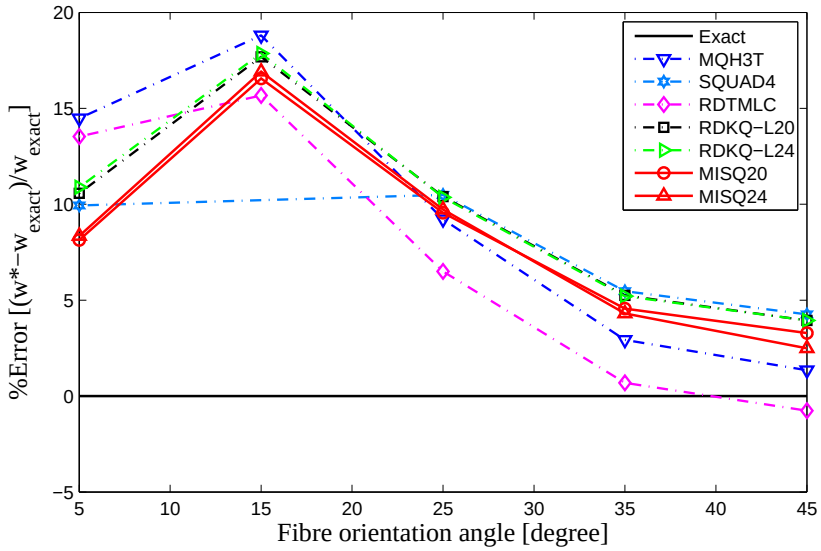

(b)

Figure 3.10: Angle-ply $[\theta^0/-\theta^0]$ square plates: The effect of θ on the accuracy of w^*: (a) simply supported edges and (b) clamped edges.

3.4.4 Antisymmetric angle-ply $[-45^0/45^0]$ and $[-45^0/45^0]_4$ square plate under a double sinusoidal load

To study the combined effect of bending-inplane shear, extension twist coupling caused by B_{16} and B_{26} in Equation (3.18) and transverse shear flexibility on the performance of the proposed element, we analyse simply-supported 2-layer $[-45^0/45^0]$ and 8-layer $[-45^0/45^0]_4$ angle-ply square plates, with length a and thickness h subjected to doubly sinusoidal loading $q = q_0 sin(x/a) sin(y/a)$ as shown in Figure 3.11. The SCFs for the plate made of material M3 are assumed to be 5/6.

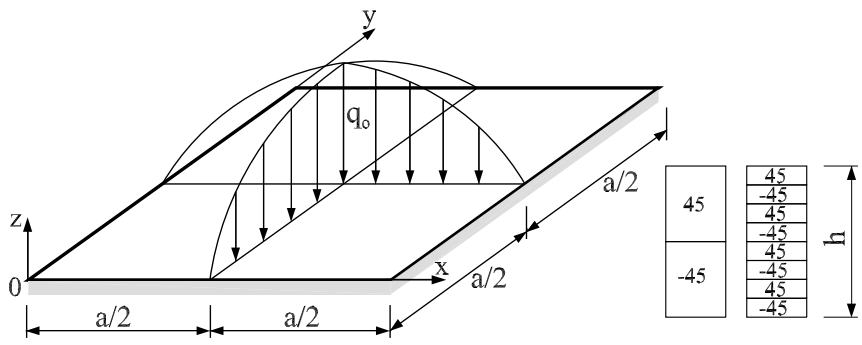

Figure 3.11: Geometry data for unsymmetric angle-ply square plate.

Due to anti-symmetry, the whole plate is modelled with 10×10 meshes. The present numerical results are shown in Table 3.6 and Table 3.7 together with some other solutions in the literature. Calculations are performed for the normalized central deflection $w^* = 1000E_2wh^3/(q_oa^4)$; the normalized stress $\sigma_x^* = \sigma_x h^2/(q_oa^2)$ at point $(a/2, a/2, h/2)$; the shear stress $\tau_{xy}^* = \tau_{xy}h^2/(q_oa^2)$ at point $(0, 0, -h/2)$ and the normalized transverse shear stress $\tau_{xz}^* = \tau_{xz}h/(q_oa)$ at point $(0, a/2, h/4)$.

It can be seen that the results obtained by the MISQ20 and MISQ24 element, with regards to the central deflections, normal and shear stresses, are in excellent agreement with the exact FSDT solutions for all span-to-thickness ratios a/h. The present elements also yield better solutions than those obtained by other elements cited here as shown in Table 3.6-3.7

Table 3.6: Simply supported 2-layer angle-ply $[-45^0/45^0]$ square plate under doubly sinusoidal loading: Comparison of normalized central deflection and normalized stresses.

a/h	Model	$w^*(\frac{a}{2},\frac{a}{2})$	$\sigma_x^*(\frac{a}{2},\frac{a}{2},\frac{h}{2})$	$\tau_{xy}^*(0,0,-\frac{h}{2})$	$\tau_{xz}^*(0,\frac{a}{2},\frac{h}{4})$
100	CTMQ20 (8×8)	0.6519	0.2474	0.2295	0.1194
	RDKQ-L20 (10×10)	0.6533	0.2488	0.2302	0.1245
	RDKQ-L24 (10×10)	0.6546	0.2500	0.2316	0.1597
	MFE (8×8)	0.6558	–	–	–
	MISQ20 (10×10)	0.6553	0.2459	0.2304	0.1884
	MISQ24 (10×10)	0.6535	0.2452	0.2298	0.1884
	Exact (FSDT)	0.6564	0.2498	0.2336	0.2143
20	CTMQ20 (8×8)	0.6906	0.2523	0.2333	0.1773
	RDKQ-L20 (10×10)	0.6931	0.2513	0.2311	0.1882
	RDKQ-L24 (10×10)	0.6960	0.2516	0.2316	0.2020
	MFE (8×8)	–	–	–	–
	MISQ20 (10×10)	0.6973	0.2456	0.2304	0.1884
	MISQ24 (10×10)	0.6956	0.2452	0.2298	0.1884
	Exact (FSDT)	0.6981	0.2498	0.2336	0.2143
10	CTMQ20 (8×8)	0.8218	0.2543	0.2349	0.2005
	RDKQ-L20 (10×10)	0.8241	0.2517	0.2316	0.2053
	MFE (8×8)	0.8257	–	–	–
	MISQ20 (10×10)	0.8286	0.2459	0.2304	0.1884
	MISQ24 (10×10)	0.8269	0.2452	0.2298	0.1884
	Exact (FSDT)	0.8284	0.2498	0.2336	0.2143

Table 3.7: Simply supported 8-layer angle-ply $[-45^0/45^0]_4$ square plate under doubly sinusoidal loading: Comparison of normalized central deflection and normalized stresses.

a/h	Model	$w^*(\frac{a}{2},\frac{a}{2})$	$\sigma_x^*(\frac{a}{2},\frac{a}{2},\frac{h}{2})$	$\tau_{xy}^*(0,0,-\frac{h}{2})$	$\tau_{xz}^*(0,\frac{a}{2},\frac{h}{4})$
100	CTMQ20 (8×8)	0.2463	0.1459	0.1356	0.1791
	RDKQ-L20 (10×10)	0.2466	0.1464	0.1359	0.1813
	RDKQ-L24 (10×10)	0.2467	0.1465	0.1361	0.1840
	MFE (8×8)	0.2472	–	–	–
	MISQ20 (10×10)	0.2475	0.1427	0.1368	0.2358
	MISQ24 (10×10)	0.2475	0.1427	0.1368	0.2358
	Exact (FSDT)	0.2479	0.1445	0.1384	0.2487
20	CTMQ20 (8×8)	0.2846	0.1496	0.1353	0.2225
	RDKQ-L20 (10×10)	0.2861	0.1506	0.1366	0.2305
	RDKQ-L24 (10×10)	0.2863	0.1506	0.1367	0.2315
	MFE (8×8)	–	–	–	–
	MISQ20 (10×10)	0.2895	0.1427	0.1368	0.2358
	MISQ24 (10×10)	0.2895	0.1427	0.1368	0.2358
	Exact (FSDT)	0.2896	0.1445	0.1384	0.2487
10	CTMQ20 (8×8)	0.4157	0.1507	0.1361	0.2384
	RDKQ-L20 (10×10)	0.4171	0.1512	0.1370	0.2420
	RDKQ-L24 (10×10)	0.4173	0.1513	0.1371	0.2423
	MFE (8×8)	0.4189	–	–	–
	MISQ20 (10×10)	0.4208	0.1427	0.1368	0.2358
	MISQ24 (10×10)	0.4208	0.1427	0.1368	0.2358
	Exact (FSDT)	0.4198	0.1445	0.1384	0.2487

3.4.5 Cross-ply 9-layer $[(0^0/90^0)_2/0]_s$ square plates under uniformly distributed load

A clamped 9-layer symmetrically cross-ply $[(0^0/90^0)_2/0]_s$ square plate of length a and thickness h under uniform load q_o is considered. The SCFs are: $k_1^2 = 1.054$ and $k_2^2 = 0.917$ (Zhang and Kim, 2004). The total thicknesses of 0^0 and 90^0 layers of material M1 are the same. This particular lay-up is known as especially orthotropic as it does not exhibit any normal-shear coupling in the plane of the laminate. Making use of this feature, only one quarter of the plate is discretized.

The normalized central deflection $w^* = 1000E_2wh^3/(q_oa^4)$ of the clamped square plate with various aspect ratios h/a is calculated with a 5×5 mesh. To the author's knowledge, there is no analytic solution for this problem. The present results are compared in Table 3.8 with those from other elements such as QUAD4 (Somashekar et al., 1987) with an 8×8 mesh, TRIPLT (Pagano, 1970) with a 4×4 mesh MFE (Singh et al., 2000) with an 8×8 mesh, RDTMLC (Ge and Chen, 2002) with a 10×10 mesh, RDKQ-L20, RDKQ-24 (Zhang and Kim, 2004) with a 5×5 mesh and Hermitian SQH element (Noor and Mathers, 1975). The normalized central moment resultants $M_x^* = 100E_2M_x/(q_oa^2)$ for various span-to-thickness ratios are also reported and compared in Table 3.9. It is observed that there is a close agreement between the present results and the MFE ones in predictions of deflections and moment resultants.

To assess the effect of boundary conditions on MISQ20 and MISQ24 element, the plate is re-analyzed with simply supported boundaries. The results are listed in Table 3.10 and Table 3.11 for central deflections and moment resultants, respectively, which show that the present results are accurate and comparable with those obtained with other elements and exact FSDT solution (Reddy, 2004b). The present MISQ20, MISQ24 elements can provide accurate prediction of the solution with much reduced degrees of freedom in some cases.

Table 3.8: Clamped 9-layer cross-ply $[(0^0/90^0)_2/0]_s$ square plate under uniform load: Comparison of normalized central deflection $w^* = 1000E_2wh^3/(q_oa^4)$.

a/h	QUAD4 8×8 (405DOF)	TRIPLT 4×4 (375DOF)	MFE 8×8 (486DOF)	RDTML 10×10 (605DOF)	RDKQ-L20 5×5 (180DOF)	RDKQ-L24 5×5 (216DOF)	MISQ20 5×5 (180DOF)	MISQ24 5×5 (216DOF)	SQH
10000	0.944	–	–	0.957	0.969	0.969	0.940	0.940	–
1000	0.944	0.934	0.949	0.957	0.969	0.969	0.940	0.940	0.949
100	0.957	0.964	0.963	0.969	0.983	0.983	0.955	0.955	0.963
10	2.316	2.320	2.331	2.318	2.351	2.351	2.341	2.341	2.319

Table 3.9: Clamped 9-layer cross-ply $[(0^0/90^0)_2/0]_s$ square plate under uniform load: Comparison of normalized central moment resultant $M_x^* = 100E_2M_x/(q_oa^2)$.

a/h	QUAD4	TRIPLT	MFE	MISQ20	MISQ24
100	-6.61	-6.62	-6.58	-6.50	-6.50
10	-5.66	-5.66	-5.59	-5.57	-5.57

Table 3.10: Simply supported 9-layer cross-ply $[(0^0/90^0)_2/0]_s$ square plate under uniform load: Comparison of normalized central deflection $w^* = 1000E_2wh^3/(q_oa^4)$.

a/h	QUAD4 8×8 (405DOF)	TRIPLT 4×4 (375DOF)	MFE 8×8 (486DOF)	RDTML 10×10 (605DOF)	RDKQ-L20 5×5 (180DOF)	RDKQ-L24 5×5 (216DOF)	MISQ20 5×5 (180DOF)	MISQ24 5×5 (216DOF)	Exact
10000	4.46	–	–	4.470	4.475	4.475	4.467	4.467	4.47
1000	4.46	4.45	4.47	4.471	4.475	4.475	4.467	4.467	4.47
100	4.47	4.48	4.49	4.483	4.488	4.488	4.481	4.481	4.49
10	5.84	5.85	5.86	5.858	5.851	5.851	5.864	5.864	5.85

Table 3.11: Simply supported 9-layer cross-ply $[(0^0/90^0)_2/0]_s$ square plate under uniform load: Comparison of normalized central moment resultant $M_x^* = 1000E_2M_x/(q_oa^2)$.

a/h	QUAD4	TRIPLT	MFE	MISQ20	MISQ24	Exact
1000	8.88	8.42	8.90	9.02	9.02	8.89
100	8.88	8.81	8.90	9.02	9.02	8.88
10	8.84	8.42	8.44	8.80	8.80	8.42

Note that the RDKQ-L20(24) denotes both RDKQ-L20 (20 DOFs per node) and RDKQ-L24 (24 DOFs per node) elements while the MISQ20(24) denotes MISQ20 (20 DOFs per node) and MISQ24 (24 DOFs per node) elements. The RDKQ-L20(24) formulations are based in the Timoshenko's beam function method while the MISQ20(24) elements are based on the assumed strain smoothing method. The MISQ20(24) formulations are quite different from the RDKQ-L20(24) and hence they have different accuracies.

3.4.6 Cross-ply $[0^0/90^0/0^0]$ and angle-ply $[45^0/-45^0/45^0]$ skew laminated plates under uniformly distributed load

This section deals with symmetric cross-ply $[0^0/90^0/0^0]$ and angle-ply $[45^0/-45^0/45^0]$ skew laminated plates of material M1 with length $a = 10$ and thickness $h = 0.1$, subjected to simply supported boundary under a uniform load as shown in Figure 3.12. The SCFs are equal to 5/6. The skew angle α is varied from 0^0 to 45^0. The entire plate is modelled using 8×8, 10×10 and 12×12 meshes. A representative example of the 10×10 mesh used in this analysis is shown in Figure 3.12.

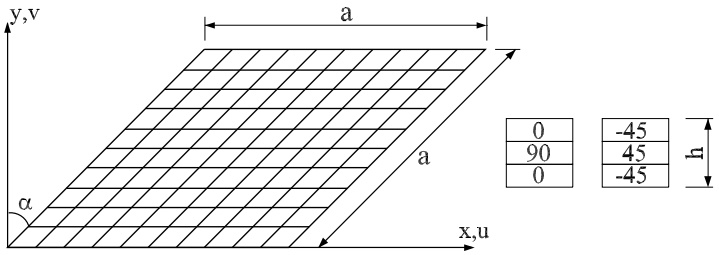

Figure 3.12: Finite element and geometry data of skew plate.

Since very few results are available for static analysis of skew composite plates, the present results are only compared with some results of Chakrabarti et al. (2004) based on FSDT and higher order shear deformation theory (HSDT) as given in the Table 3.12. It can be seen that both of MISQ20 and MISQ24 yield the same solutions and the obtained results in general indicate a good agreement. However, it is observed that the deflection and stress are closer to those of FSDT than HSDT.

Table 3.12: Simply supported $[0^0/90^0/0^0]$ and $[45^0/-45^0/45^0]$ skew plate: Comparison of normalized central deflection and stress ($a/h = 100$).

α	Model		$[0^0/90^0/0^0]$		$[45^0/-45^0/45^0]$	
			$w^*(\frac{a}{2},\frac{a}{2},0)$	$\sigma_x^*(\frac{a}{2},\frac{a}{2},\frac{h}{2})$	$w^*(\frac{a}{2},\frac{a}{2},0)$	$\sigma_x^*(\frac{a}{2},\frac{a}{2},\frac{h}{2})$
0^0	MISQ20	8×8	6.7365	0.7846	5.9825	0.2770
		10×10	6.7219	0.7930	6.0128	0.2766
		12×12	6.7146	0.7975	6.0397	0.2771
	MISQ24	8×8	6.7365	0.7846	5.9825	0.2770
		10×10	6.7219	0.7930	6.0128	0.2766
		12×12	6.7146	0.7975	6.0397	0.2771
	HSDT (16×16)		6.7222	0.8211	5.9502	0.2739
	FSDT (16×16)		6.7090	0.8159	5.9515	0.2743
15^0	MISQ20	8×8	6.4526	0.7493	6.4700	0.2559
		10×10	6.4417	0.7587	6.4873	0.2622
		12×12	6.4367	0.7634	6.5027	0.2656
	MISQ24	8×8	6.4526	0.7493	6.4700	0.2559
		10×10	6.4417	0.7587	6.4873	0.2622
		12×12	6.4367	0.7634	6.5027	0.2656
	HSDT (16×16)		6.4437	0.7858	6.4391	0.2692
	FSDT (16×16)		6.4321	0.7812	6.4332	0.2693
30^0	MISQ20	8×8	5.4708	0.6321	5.8039	0.2511
		10×10	5.4681	0.6424	5.8150	0.2563
		12×12	5.4687	0.6476	5.8234	0.2593
	MISQ24	8×8	5.4708	0.6321	5.8039	0.2511
		10×10	5.4681	0.6424	5.8150	0.2563
		12×12	5.4687	0.6476	5.8234	0.2593
	HSDT (16×16)		5.4732	0.6664	5.7955	0.2658
	FSDT (16×16)		5.4654	0.6634	5.7904	0.2651
45^0	MISQ20	8×8	3.6305	0.4208	3.5984	0.2210
		10×10	3.6333	0.4326	3.6149	0.2251
		12×12	3.6396	0.4387	3.6275	0.2270
	MISQ24	8×8	3.6305	0.4208	3.5984	0.2210
		10×10	3.6333	0.4326	3.6149	0.2251
		12×12	3.6396	0.4387	3.6275	0.2270
	HSDT (16×16)		3.6323	0.4516	3.6324	0.2329
	FSDT (16×16)		3.6300	0.4505	3.6301	0.2323

3.4.7 Circular plate subjected to uniform pressure

A clamped circular plate of material M4 with radius R and various aspect ratios of R/h subjected to uniformly distributed load is considered. The laminate is unidirectional with fibers oriented at $\theta = 0^o$ with respect to the global coordinates. The SCFs are 5/6. Owing to symmetry, only a quarter of the circular plate is modelled with 12 and 48 elements as shown in Figure 3.13.

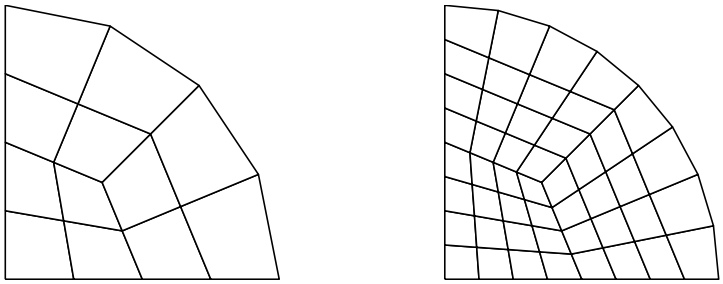

(a) (b)

Figure 3.13: Typical meshes of a circular laminated plate: (a) a mesh of 12 elements and (b) a mesh of 48 elements.

The results are compared with numerical results of the SQUAD4 element (Wilt et al., 1990), the RDKQ-L20, RDKQ-L24 element (Zhang and Kim, 2004), RDTMLC element (Ge and Chen, 2002) and the exact solution (Reddy, 2004b) in Table 3.13. Note that the normalized central deflection of the circular plate in Table 3.13 is $w^* = wD/(qR^4)$ with $D = 3(D_{11} + D_{22}) + 2(D_{12} + 2D_{66})$, where $D_{11}, D_{22}, D_{12}, D_{66}$ are bending rigidity coefficients of the laminate found by laminate theory.

From the data of Table 3.13, it can be seen that the present elements MISQ20 and MISQ24 yield the same results and give more accurate solution for both thick and thin plate than those of cited elements.

3.4.8 Triangular plate subjected to uniform pressure

The last problem considered in this section is that of a triangular plate, clamped on all sides subjected to a uniform load q_o. The unidirectional laminate of material

Table 3.13: Clamped circular plate under uniform loading: Comparison of normalized central deflection $w^* = wD/(qR^4)$.

R/h	RDTMLC	SQUAD4	RDKQ-L20(24)		MISQ20(24)		Exact
	96	48	12	48	12	48	
1000	0.1265	0.1231	0.1269	0.1259	0.1271	0.1258	0.1250
100	0.1266	0.1242	0.1245	0.1251	0.1273	0.1259	–
50	0.1268	0.1247	0.1244	0.1251	0.1277	0.1264	–
25	0.1276	0.1264	0.1244	0.1251	0.1293	0.1280	–
16.67	0.1291	0.1291	0.1244	0.1251	0.1320	0.1308	–
10	0.1344	0.1378	0.1244	0.1251	0.1407	0.1394	–

M4 is investigated with the fibres oriented at an angle $\theta = 0^0$ with respect to global $x-$axis. The reference solution is taken from Wilt et al. (1990) and a typical mesh of 48 elements as shown in Figure 3.14 was chosen on the basis of results from SQUAD4 element (Wilt et al., 1990).

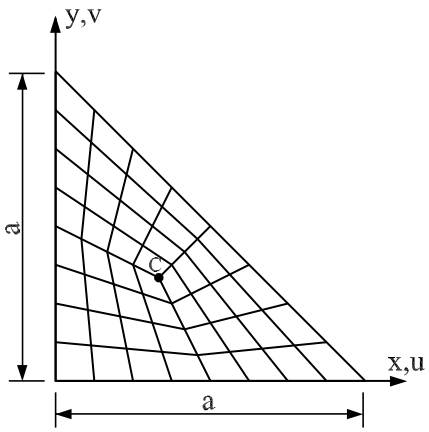

Figure 3.14: Finite element and geometry data for triangular plate.

The deflections $w^* = 1000E_2wh^3/(q_oa^4)$ for various plate aspect ratios are given in Table 3.14. As shown, the discrepancy between the present MISQ20 (MISQ24) and SQUAD4 results decreases when the a/h ratio increases, except for the case $a/h = 1000$. However, in all cases of the span-to-thickness a/h ratio, the difference between the two results is always less than 4%.

Table 3.14: Clamped triangular plate under uniform load: Comparison of normalized centroidal deflection $w_C^* = 1000E_2w_Ch^3/(q_oa^4)$.

Model	a/h					
	10	16.667	25	50	100	1000
SQUAD4	1.9200	1.3517	1.1641	1.0406	0.9975	0.9452
MISQ20(24)	1.8515	1.3085	1.1289	1.0174	0.9890	0.9795
%Error	-3.568%	-3.196%	-3.024%	-2.229%	-0.852%	3.629%

3.4.9 Thermo-mechanical analysis of functionally graded material (FGM) plates

This section deals with the static behaviour of FGM plates. The developed MISQ20 element is modified to adapt to the classical Reissner-Mindlin model for FGM plates. The unknowns of the Reissner-Mindlin model are the normal displacement w and the rotations $\theta_x,\ \theta_y$ of the normal about the $y-$ and $x-$axis, respectively. Therefore, the DOFs of MISQ20 is reduced to 12 DOFs per element and there is no membrane part in the formulations. The reduced MISQ20 element is termed as MISQ20R and its detailed formulation for FGM plates is presented in Appendix B.

In this section, the bending analysis of FGM plates made of a ceramic-metal bi-material, is performed under mechanical and thermal loads. The plate consists of a Zirconia layer (ceramic material) at the top and an aluminum layer (metal material) at the bottom. Through-thickness material properties vary with the following power-law distribution:

$$V(z) = (V_t - V_b)V_c + V_b, \tag{3.75}$$

$$V_c = \left(\frac{1}{2} + \frac{z}{h}\right)^n, \quad (n \geq 0,\ -\frac{h}{2} \leq z \leq \frac{h}{2}). \tag{3.76}$$

where V denotes generic material properties including the Young's modulus, thermal expansion and thermal conductivity; $V_t,\ V_b$ represent the material properties at the top (ceramic) and bottom (metal) faces of the plate, respectively, z is the thickness coordinate; V_c is the volume fraction and n is the volume fraction ex-

ponent ranging from $n = 0$ to 5. Physical material properties are summarized in Table 3.15. For any case of plates exposed in a temperature field, the temperature is assumed to be constant at the ceramic and metal surfaces. The Poisson's ratio is assumed to be constant. The temperature distribution $T(z)$ across the thickness of the FGM plate is obtained from the solution of the one-dimensional steady-state heat conduction as

$$T(z) = T_t - \frac{T_t - T_b}{\int_{-h/2}^{h/2}(dz/\lambda(z))} \int_z^{h/2} \frac{d\xi}{\lambda(\xi)} \tag{3.77}$$

where the thermal conductivity $\lambda(z)$ varies according to the power-law distribution of Equation (3.75). A constant temperature of $T_t = 300^0$C is imposed on the top surface while the bottom surface is held at $T_b = 20^0$C. A uniform load $q_0 = -1 \times 10^6$ Pa and regular meshes are used in all examples. The geometry data and material distribution of a representative FGM plate is shown in Figure 3.15.

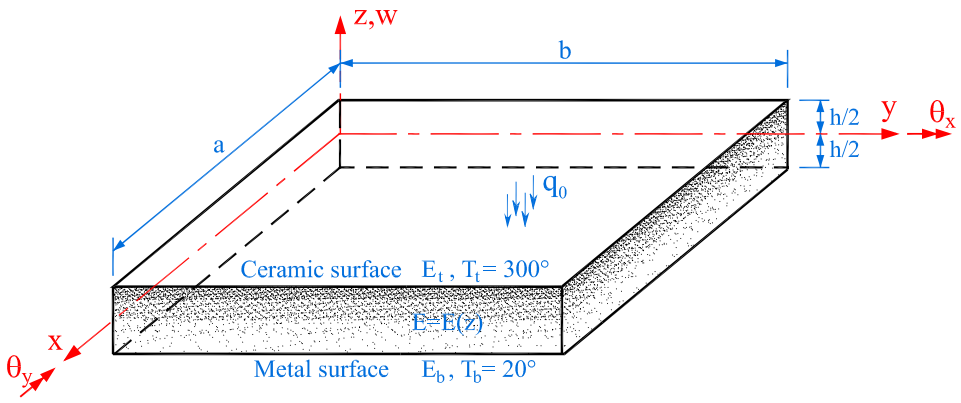

Figure 3.15: Geometry and material distribution of the functionally graded plate.

Table 3.15: Material properties of the FGM components

Properties	Aluminum (Al)	Zirconia (ZrO_2-1)	Zirconia (ZrO_2-2)
Young's modulus	70 GPa	200 GPa	151 GPa
Poisson's ratio	0.3	0.3	0.3
Thermal conductivity	204 W/mK	2.09 W/mK	2.09 W/mK
Thermal expansion	23×10^{-6}/C	10×10^{-6}/C	10×10^{-6}/C

3.4.9.1 Convergence study

This section deals with the convergence of the non-dimensional central deflections of the Al/ZrO_2-1 square plates subjected to a uniform transverse load q_0. Two boundary conditions, namely simply supported (SSSS) and fully clamped (CCCC), are considered. The span-to-thickness ratio a/h is chosen to be 10.

Table 3.16 shows the values of non-dimensional central deflection with mesh refinement together with the solutions reported by Zienkiewicz and Taylor (2000). It can be seen that the solutions converge with mesh refinement. The results with $n = 0$ and a mesh of 12×12, agree well with those given in the literature. It is also observed that the values of volume fraction exponent n do not affect the convergence rate of the solutions.

Table 3.16: Square FGM Al/ZrO_2-1 plates: Convergence study of non-dimensional central deflections ($a/h = 10$, $D_0 = E_{Zr}h^3/(12(1-\nu_{Zr}^2))$, $w^* = 100wD_0/(q_0a^4)$).

B.C	Model	Mesh	n				
			0	0.2	0.5	1	2
SSSS	MISQ20R	4×4	0.4280	0.4929	0.5633	0.6340	0.7043
		8×8	0.4277	0.4926	0.5629	0.6336	0.7038
		12×12	0.4276	0.4925	0.5628	0.6335	0.7037
		16×16	0.4276	0.4925	0.5628	0.6335	0.7037
	Zienkiewicz and Taylor (2000)]		0.4280				
CCCC	MISQ20R	4×4	0.1503	0.1726	0.1972	0.2227	0.2493
		8×8	0.1506	0.1730	0.1976	0.2232	0.2499
		12×12	0.1507	0.1731	0.1977	0.2233	0.2500
		16×16	0.1507	0.1731	0.1977	0.2233	0.2500
	Zienkiewicz and Taylor (2000)]		0.1480				

Figure 3.16 shows the effect of the volume fraction exponent and span-to-thickness ratio on the non-dimensional central deflections of simply supported and clamped square FGM Al/ZrO_2-1 plates under a mechanical uniform load. It can be seen

that the deflection of the plates with a certain volume fraction, decreases as the span-to-thickness ratio increases up to approximately 40. This can be explained from a physical point of view that the effect of shear deformation in the Reissner-Mindlin formulation (thick plate formulation) is to increase the deflection. However, the deflection remain unchanged when the value of span-to-thickness ratio is greater than 40. It is concluded that the effect of the span-to-thickness ratio on the displacement is independent with the variation of volume fraction and has no influence for thin plates ($a/h > 40$).

Figure 3.17a depicts the effect of the volume fraction exponent and span-to-thickness ratio on the non-dimensional normal stress $\sigma_x^* = \sigma_x h^2/q_0 a^2$ at the top surface of the center of simply supported FGM Al/ZrO_2-1 square plate under a uniform load. It can be seen that the span-to-thickness ratio has no effect on the normal stress σ_x. For the plates under clamped edges, the effect of the span-to-thickness ratio also has a minor effect on the normal stress σ_x when $a/h < 40$ and no influence with $a/h > 40$, as shown in Figure 3.17b.

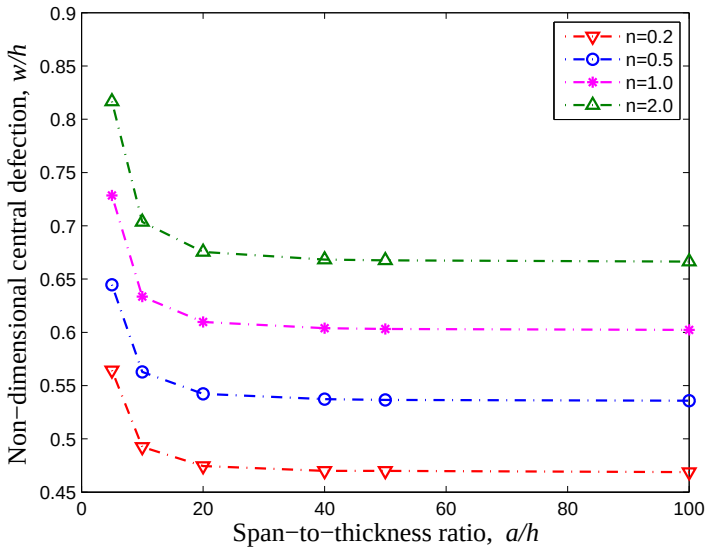

(a)

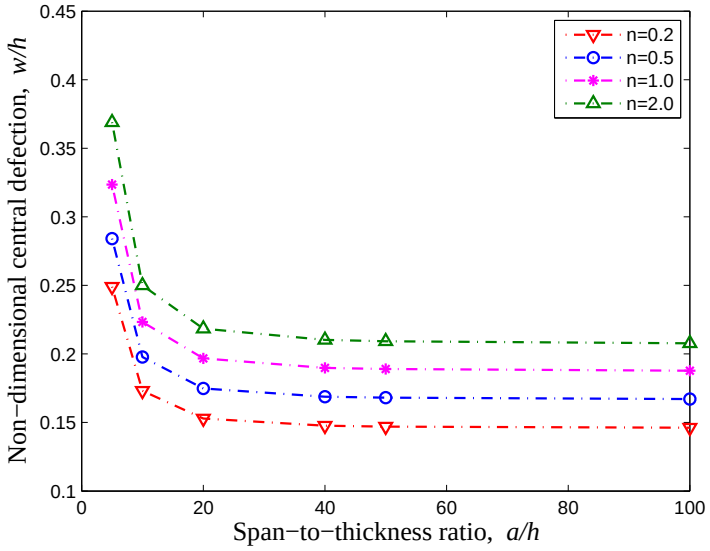

(b)

Figure 3.16: Square FGM Al/ZrO_2–1 plates under uniform load: non-dimensional central deflections versus the span-to-thickness ratios for (a) simply supported edges and (b) fully clamped edges.

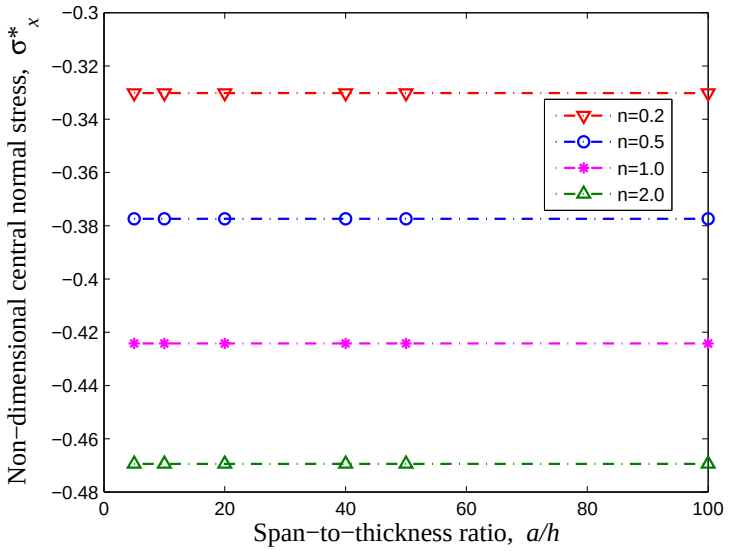

(a)

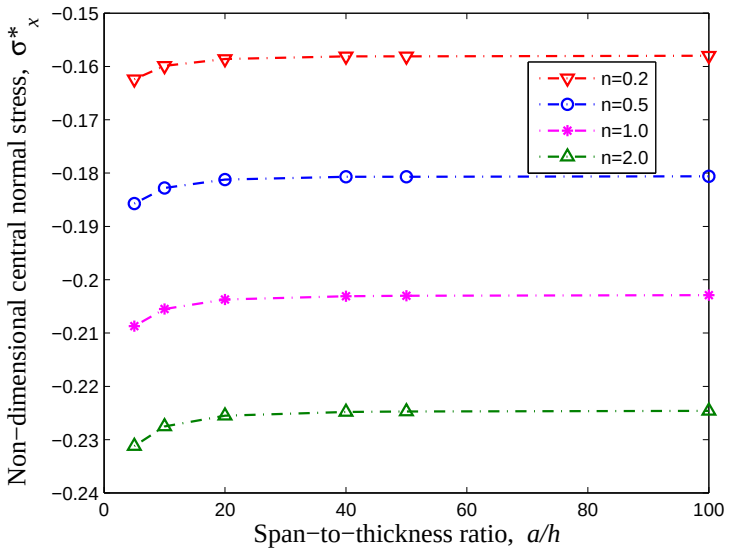

(b)

Figure 3.17: Square FGM Al/ZrO_2–1 plates under uniform load: non-dimensional central normal stress σ_x^* at the top surface versus the span-to-thickness ratios for (a) simply supported edges and (b) fully clamped edges.

3.4.9.2 Thermal-mechanical analysis

This section deals with the behaviour of the simply supported FGM Al/ZrO_2-2 square plate of side $a = 0.2m$ and thickness $h = 0.01m$ subjected to increasing mechanical uniform load with or without the presence of temperature field. A uniform load $q_0 = -1 \times 10^6 Nm^{-2}$ and a regular mesh of 12×12 elements are used in the analysis.

Figure 3.18 demonstrates the non-dimensional central deflection with respect to mechanical load $P = q_0 a^4/(E_b h^4)$ for various values of exponent n. From Figure 3.18a, it can be seen that the deflection of the metallic and ceramic plates have the largest and smallest magnitude, respectively while the deflection of the graded plates belongs to the intermediate range. In the case of the presence of the temperature field, it is observed from Figure 3.18b that the deflections of graded plates are not intermediate to those of the metal and ceramic plates. With the effect of temperature, the deflections of all plates are initially positive and tend towards negative values with increasing loads similar to the case of pure mechanical load. It is also noted that the present results are in good agreement with those reported in Reddy (2000); Croce and Venini (2004)

Figure 3.19a shows the behaviour of the non-dimensional normal stress $\sigma_x^* = \sigma_x h^2/(q_0 a^2)$ evaluated at the center of the plates through the thickness when subjected only to mechanical load P while Figure 3.19b display normal stress when a temperature field and mechanical load are applied. It is observed that the non-dimensional normal stresses σ_x are compressive both at the top and bottom surfaces. All normal stresses of graded plates are close to each other and their values are less than those of homogeneous plates. All the results are also in good agreement with those reported in Reddy (2000); Croce and Venini (2004)

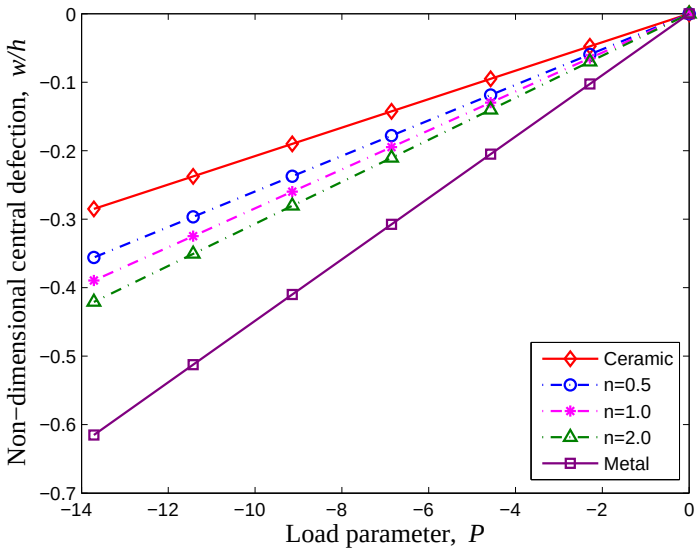

(a)

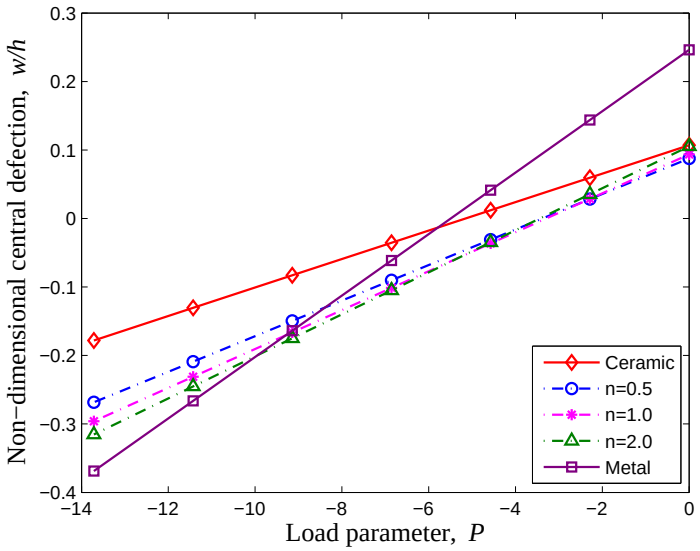

(b)

Figure 3.18: Square FGM Al/ZrO_2–2 plates: non-dimensional central deflections versus load parameter P under (a) mechanical load and (b) thermo-mechanical load.

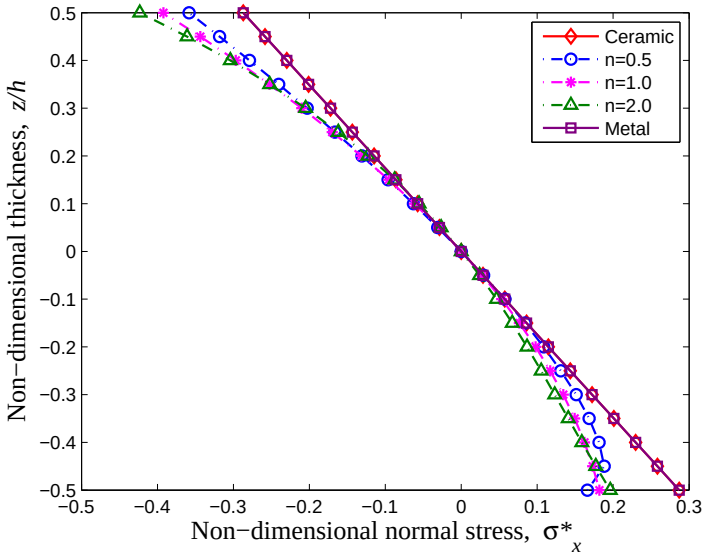

(a)

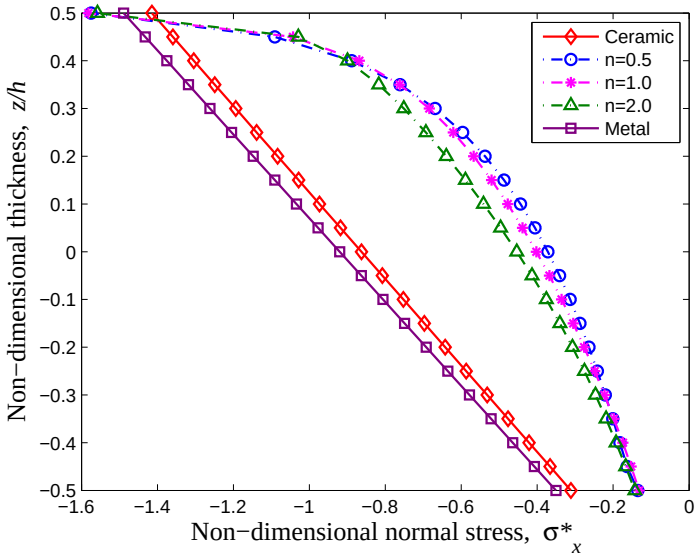

(b)

Figure 3.19: Square FGM Al/ZrO_2–2 plates: non-dimensional central normal stress profile through the thickness under (a) mechanical load and (b) thermo-mechanical load.

3.5 Numerical examples: Free vibration analysis

In this section, a number of numerical examples are presented to demonstrate the performance of the MISQ20 and MISQ24 elements in the analysis of free vibration of laminated plates. Particular plate structures with various boundary conditions, span-to-thickness ratios and modulus ratios (the degree of orthotropy) are analyzed. In all examples, the material properties are assumed to be the same in all the layers and the fibre orientations may be different among the layers. The ply angle of each layer is measured from the global $x-$axis to the fibre direction. The thickness of each layer is identified and the mass density ρ is taken to be uniform in the thickness direction. Unless otherwise specified, shear correction factors $k_1^2 = k_2^2 = \frac{\pi^2}{12}$ are used for all computations. The following material parameters of a layer are used in all plate examples unless otherwise stated:

$E_1/E_2 = 10,\ 20,\ 30$ or $40;\ G_{12} = G_{13} = 0.6E_2;\ G_{23} = 0.5E_2;\ \nu_{12} = \nu_{13} = \nu_{23} = 0.25;\ \rho = 1.$

3.5.1 Square laminated plates

This section deals with cross-ply laminated square plates with various span-to-thickness ratios, number of layers, boundary conditions and lay-up stacking sequences. A typical representative sketch of a mesh of 14×14 used in these analyses is shown in Figure 3.20.

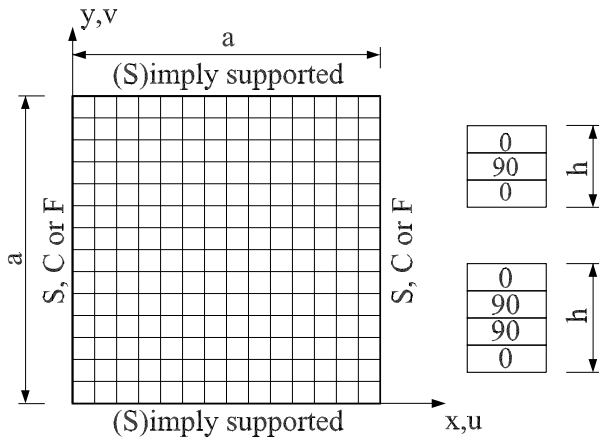

Figure 3.20: Geometry and discretization of square laminated plates

3.5.1.1 Convergence study and effect of modulus ratios

A simply supported four-layer cross-ply [0/90/90/0] square laminated plate is chosen to study the convergence of the present method using MISQ20 and MISQ24 elements. The span-to-thickness ratio of the plate a/h is taken to be 5 in the computation. Table 3.17 shows the convergence and comparison of the normalized fundamental frequencies of the present method with other solutions for various degrees of orthotropy of the individual layers (E_1/E_2 ratio). It is found that the MISQ20 and MISQ24 elements yield the same results and the obtained results are not only relatively accurate in a wide range of E_1 to E_2 ratios but also rapidly convergent as shown in Figure 3.21a. The effect of various modulus ratios of E_1/E_2 on the accuracy of the fundamental frequency is also displayed in Figure 3.21b. It can be seen that the present results are in good agreement with exact solutions (Reddy, 2004b; Khdeir and Librescu, 1988) and closer to MLSDQ's solutions by Liew et al. (2003) than RBF's results of Ferreira et al. (2005).

Table 3.17: Simply supported cross-ply $[0^0/90^0/90^0/0^0]$ square plate: Convergence of normalized fundamental frequencies and comparison with other solutions ($\omega^* = (\omega a^2/h)\sqrt{\rho/E_2}, a/h = 5$).

Model	Mesh	E_1/E_2			
		10	20	30	40
MISQ20	6×6	8.4443	9.7149	10.4729	11.0001
	10×10	8.3384	9.6010	10.3548	10.8792
	12×12	8.3203	9.5815	10.3346	10.8585
	14×14	8.3094	9.5698	10.3224	10.8471
MISQ24	6×6	8.4443	9.7149	10.4729	11.0001
	10×10	8.3384	9.6010	10.3548	10.8792
	12×12	8.3203	9.5698	10.3346	10.8585
	14×14	8.3094	9.5698	10.3224	10.8471
MLSDQ		8.2924	9.5613	10.320	10.849
RBF		8.3101	9.5801	10.349	10.864
Exact		8.2982	9.5671	10.326	10.854

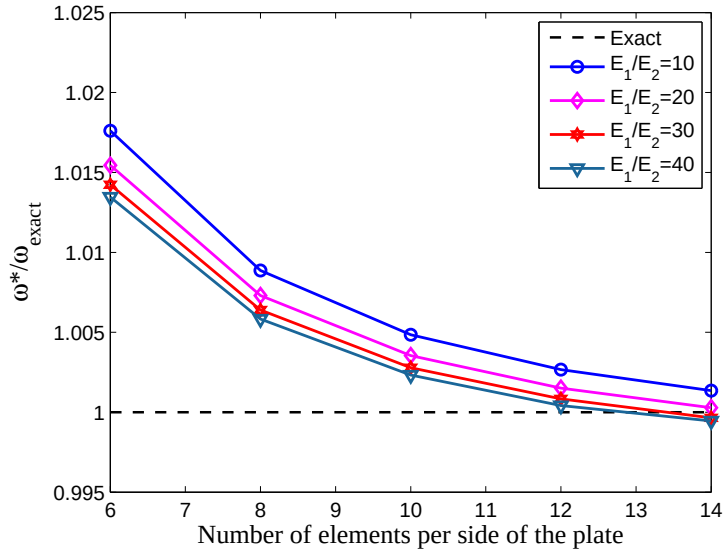

(a)

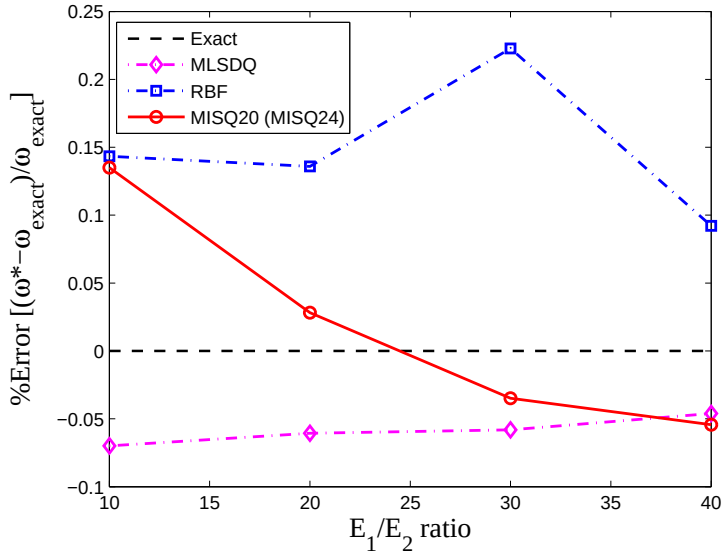

(b)

Figure 3.21: Cross-ply $[0^0/90^0/90^0/0^0]$ square laminated plate: (a) convergence of the present method and (b) effect of modulus ratio on the accuracy of fundamental frequencies.

Note that the present elements are formulated based on assumed strain smoothing method which leads to softer element stiffness matrices than those of the standard FEM. This explains why the present results are slightly lower than the 'exact' frequency in Table 3.17. The MLSDQ is a mesh-free method with higher-order approximants and hence it is possible to obtain more flexible predictions than the 'exact' frequencies for this particular problem.

3.5.1.2 Effect of mesh distortion

The influence of mesh distortion is studied in this section. The plate of the first example (Section 3.5.1.1) is analyzed again using distorted element created by irregular interior nodes. These interior nodes are derived from a set of regular nodes by using a controlling distortion factor s. Thus, the coordinates of an irregular mesh are obtained by the following expressions

$$\begin{aligned} x' &= x + r_c s \Delta x, \\ y' &= y + r_c s \Delta y, \end{aligned} \tag{3.78}$$

where r_c is a computer-generated random number between -1.0 and 1.0, $\Delta x, \Delta y$ are initial regular element sizes in the x–and y–directions, respectively and $s \in [0, 0.4]$ is used to control the shapes of the distorted elements: the bigger value of s, the more irregular the shape of generated elements. Typical irregular meshes of the analysis are shown in Figure 3.22.

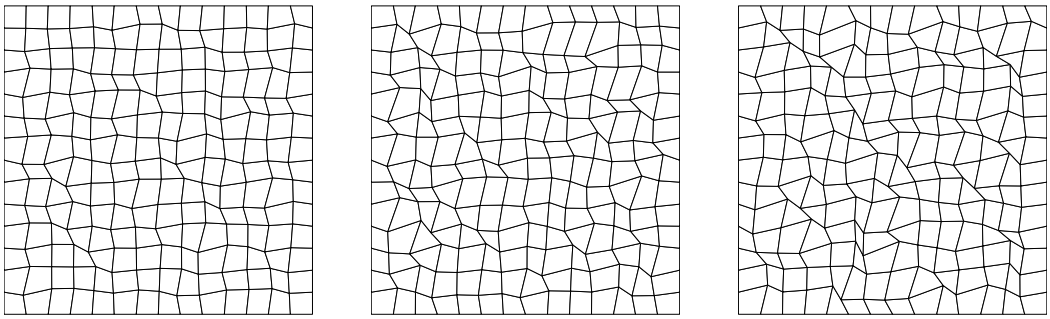

$s = 0.2$ $s = 0.3$ $s = 0.4$

Figure 3.22: Typical irregular meshes of 14×14 with various distortion factor s.

The effect of the mesh distortion on the fundamental frequency of the plate obtained by the present method is shown in Table 3.18 and Figure 3.23. It is found that the accuracy of the fundamental frequencies associated with irregular mesh decreases in comparison with regular meshes. However, the deterioration is very small and the overall performance is insensitive to mesh distortion to the extent that the maximum error of frequency is below 0.3% (in the case of $E_1/E_2 = 10$). For the cases of $E_1/E_2 = 30$ and 40, Figure 3.23 indicates that the error at some s could become even smaller than those at $s = 0$ (regular mesh).

Table 3.18: Simply supported cross-ply $[0^0/90^0/90^0/0^0]$ square plate: Effect of mesh distortion on the normalized fundamental frequencies ($\omega^* = (\omega a^2/h)\sqrt{\rho/E_2},\ a/h = 5$).

s	Model	E_1/E_2			
		10	20	30	40
0	MISQ20 (14×14)	8.3094	9.5698	10.3224	10.8471
	MISQ24 (14×14)	8.3094	9.5698	10.3224	10.8471
0.1	MISQ20 (14×14)	8.3108	9.5712	10.3239	10.8476
	MISQ24 (14×14)	8.3108	9.5712	10.3239	10.8476
0.2	MISQ20 (14×14)	8.3125	9.5728	10.3257	10.8495
	MISQ24 (14×14)	8.3125	9.5728	10.3257	10.8495
0.3	MISQ20 (14×14)	8.3140	9.5749	10.3283	10.8528
	MISQ24 (14×14)	8.3140	9.5749	10.3283	10.8528
0.4	MISQ20 (14×14)	8.3207	9.5820	10.3354	10.8597
	MISQ24 (14×14)	8.3207	9.5820	10.3354	10.8597

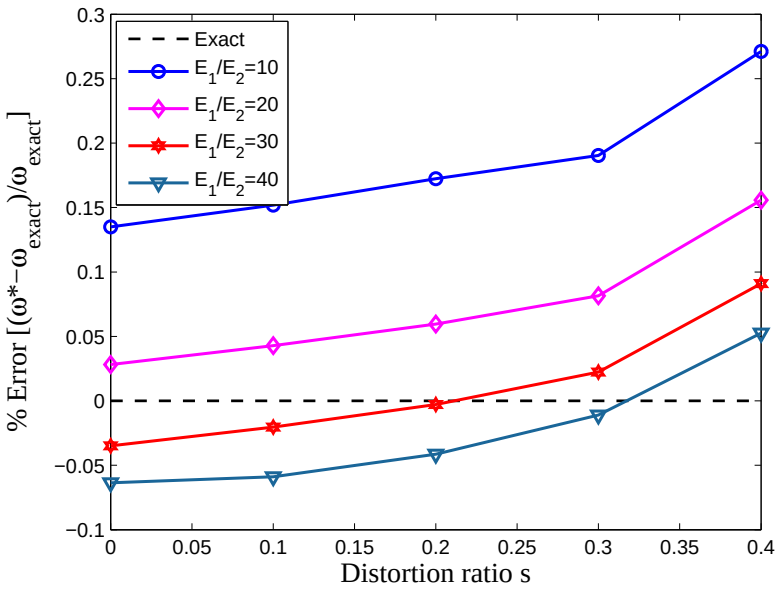

Figure 3.23: Square cross-ply [0/90/90/0] laminated plate: Effect of mesh distortion on the accuracy of the fundamental frequency.

3.5.1.3 Effect of span-to-thickness ratio

This section deals with the effect of the span-to-thickness ratio (a/h) on the fundamental frequency of a simply supported square cross-ply plate made of material having $E_1/E_2 = 40$. Table 3.19 presents a convergence study on the normalized fundamental frequency. The present numerical results are comparable with those of Reddy and Phan (1985) who used higher-order shear deformation theory (HSDT), Liew (1996) who used a p-Ritz solution, Ferreira and Fasshauer (2007) who used RBF-pseudospectral method, Wu and Chen (1994) who used local higher-order theory, Matsunaga (1991) who used global higher-order theory, Striz et al. (1991) who used higher-order individual-layer (HOIL) theory and Zhen and Wanji (2006) who used global-local higher-order theory.

Table 3.19: Simply supported cross-ply $[0^0/90^0/90^0/0^0]$ square plate with various a/h ratios: Convergence of normalized fundamental frequencies and comparison with other solutions ($E_1/E_2 = 40$, $\omega^* = (\omega a^2/h)\sqrt{\rho/E_2}$).

Model		a/h					
		5	10	20	25	50	100
MISQ20	6×6	11.0001	15.4187	18.0504	18.4839	19.1221	19.2939
	10×10	10.8792	15.2201	17.7903	18.2122	18.8325	18.9992
	14×14	10.8461	15.1658	17.7192	18.1380	18.7535	18.9189
MISQ24	6×6	11.0001	15.4187	18.0504	18.4839	19.1221	19.2939
	10×10	10.8792	15.2201	17.7903	18.2122	18.8325	18.9992
	14×14	10.8461	15.1658	17.7192	18.1380	18.7535	18.9189
p-Ritz		10.8550	15.1434	17.6583	18.0718	18.6734	18.8359
RBF-pseudospectral		10.8074	15.1007	17.6338	18.0490	18.6586	18.8223
HSDT		10.9891	15.2689	17.6669	18.0490	18.4624	18.7561
HOIL theory		10.673	15.066	17.535	18.054	18.670	18.835
Local theory		10.682	15.069	17.636	18.055	18.670	18.835
Global theory		10.6876	15.0721	17.6369	18.0557	18.6702	18.8352
Global-local theory		10.7294	15.1658	17.8035	18.2404	18.9022	19.1566

However, it can be seen that the present results are in closer agreement with re-

sults of Liew (1996) than other methods cited here. From Table 3.19, it is also noticed that the span-to-thickness ratio has a considerable effect on the fundamental frequency of plates at lower a/h ratios. At higher a/h ratios ($a/h > 25$), the influence on the fundamental frequency is minor.

3.5.1.4 Effect of lay-up sequence and fibre orientation

To investigate the effect of lay-up sequence and fibre orientation, this section reports the analysis of two composite plates with lamination sequence $[\theta/0/0/\theta]$ and $[0/\theta/\theta/0]$ with simply supported (SSSS) and clamped (CCCC) edges. The span-to-thickness ratio of the plate $a/h = 100$ and modulus ratio $E_1/E_2 = 10$ are used in the computation. Figure 3.24 shows the effects of both fibre orientation and lay-up sequence on the fundamental frequencies. It is found that there is symmetry for the orientation angle of 45 degrees in both cases of simply supported and clamped conditions. Moreover, in the case of SSSS edge conditions, the $[\theta/0/0/\theta]$ lamination results in a higher fundamental frequencies than the corresponding ones for the $[0/\theta/\theta/0]$ sequence. In the case of CCCC edge conditions, the behaviour of the fundamental frequencies is opposite to the above SSSS results. It appears that, in both cases, the fundamental frequencies has an extremum at ply angle $\theta = 45^o$.

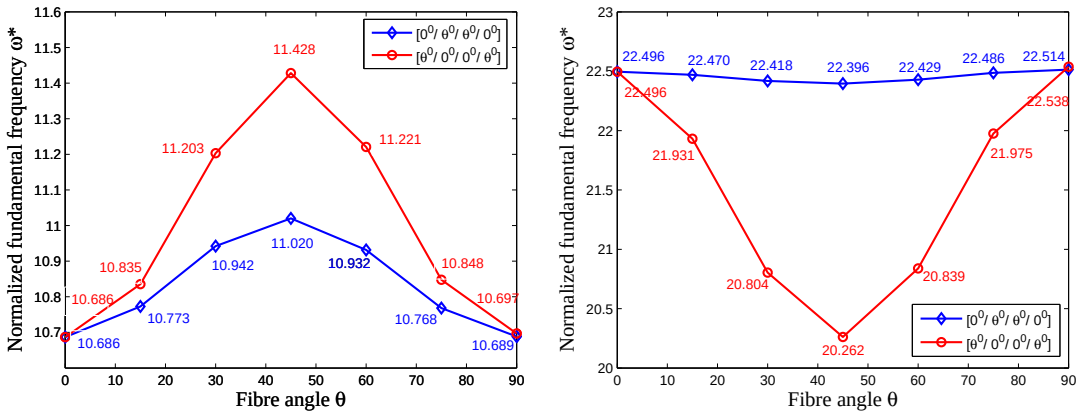

(a) SSSS edge condition.

(b) CCCC edge condition.

Figure 3.24: Effect of fibre orientation and stacking sequence on fundamental frequencies of square laminated plates.

3.5.1.5 Effect of mixed boundaries and span-to-thickness ratio

The influence of the mixed boundary conditions and span-to-thickness ratio are now considered. The plate is simply supported along the edges parallel to the $x-$axis while the other edges have simply supported (S), clamped (C) or free (F) boundary conditions. The notation SS, SC, CC, FF, FS and FC refer to the boundary conditions of two edges parallel to the $y-$axis only. The three layer cross-ply $[0^0/90^0/0^0]$ square plate is analyzed with $E_1 = 40E_2$ and a 14×14 mesh as indicated in Figure 3.20. Table 3.20 contains the normalized fundamental frequencies for various span-to-thickness ratios obtained by the present method and other solutions of Liew et al. (2003) using MLSDQ method, RBF's results by Ferreira et al. (2005) and exact solutions Reddy (2004b); Khdeir and Librescu (1988). It can be seen that the accuracy of the present method compares very well with exact solutions and other numerical results.

Furthermore, the comparison of the first five natural frequencies of a clamped 3-layer cross-ply $[0^0/90^0/0^0]$ square plate with other methods including p-Ritz method (Liew, 1996), global-local theory (Zhen and Wanji, 2006), MLSDQ method (Lanhe et al., 2005) and Jian's solution (Jian et al., 2004) is also presented in Table 3.21. The first six mode shapes obtained by the present method are also depicted on Figure 3.25. It is found that the present results in general indicate good agreement with other cited solutions.

Table 3.20: Cross-ply $[0^0/90^0/0^0]$ square plate with various mixed boundaries and span-to-thickness ratios: Comparison of normalized fundamental frequencies with other solutions ($E_1/E_2 = 40$, $\omega^* = (\omega a^2/h)\sqrt{\rho/E_2}$).

a/h	Model	SS	SC	CC	FF	FS	FC
5	MISQ20	10.2780	10.6280	11.2387	4.0717	4.5613	5.9370
	MISQ24	10.2780	10.6280	11.2387	4.0717	4.5613	5.9370
	RBF	10.307	10.658	11.274	–	–	–
	MLSDQ	10.290	10.647	11.266	4.054	4.545	5.938
	Exact	10.290	10.646	11.266	4.053	4.544	5.937
10	MISQ20	14.7823	17.1806	19.6614	4.3679	4.9401	7.3372
	MISQ24	14.7823	17.1806	19.6614	4.3679	4.9401	7.3372
	RBF	14.804	17.199	19.678	–	–	–
	MLSDQ	14.767	17.176	19.669	4.343	4.917	7.333
	Exact	14.766	17.175	19.669	4.343	4.914	7.331
100	MISQ20	18.9095	28.4750	40.5937	4.4835	5.1007	8.2665
	MISQ24	18.9095	28.4750	40.5937	4.4835	5.1007	8.2665
	RBF	18.355	28.165	40.234	–	–	–
	MLSDQ	18.769	28.164	40.004	4.439	5.301	8.451
	Exact	18.891	28.501	40.743	4.457	5.076	8.269

Table 3.21: Clamped cross-ply $[0^0/90^0/0^0]$ square plate: Comparison of the first five natural frequencies with other solutions ($E_1/E_2 = 40$, $D_0 = E_2h^3/(12(1 - \nu_{12}\nu_{21}))$, $\omega^* = (\omega a^2/\pi^2)\sqrt{\rho h/D_0}$).

a/h	Model	Mode				
		1	2	3	4	5
5	MISQ20	4.4671	6.7365	7.7706	8.7678	9.2988
	MISQ24	4.4671	6.7365	7.7706	8.7678	9.2988
	p-Ritz	4.447	6.642	7.700	9.185	9.738
	Global-local theory	4.540	6.524	8.178	9.473	9.492
10	MISQ20	7.4542	10.5909	14.0808	16.0497	16.0868
	MISQ24	7.4542	10.5909	14.0808	16.0497	16.0868
	p-Ritz	7.411	10.393	13.913	15.429	15.806
	Global-local theory	7.484	10.207	14.340	14.863	16.070
	Jian's solution	7.451	10.451	13.993	15.534	15.896
	MLSDQ	7.432	10.399	13.958	15.467	15.838
20	MISQ20	11.0454	14.2988	21.4609	23.6389	25.4605
	MISQ24	11.0454	14.2988	21.4609	23.6389	25.4605
	p-Ritz	10.953	14.028	20.388	23.196	24.978
	Global-local theory	11.003	14.064	20.321	23.498	25.350
	Jian's solution	11.015	14.152	20.691	23.323	25.142
100	MISQ20	14.6199	17.7013	25.5625	38.2411	39.3269
	MISQ24	14.6199	17.7013	25.5625	38.2411	39.3269
	p-Ritz	14.666	17.614	24.511	35.532	39.157
	Global-local theory	14.601	17.812	25.236	37.168	38.528
	Jian's solution	14.583	17.762	25.004	36.644	38.073
	MLSDQ	14.674	17.668	24.594	35.897	39.625

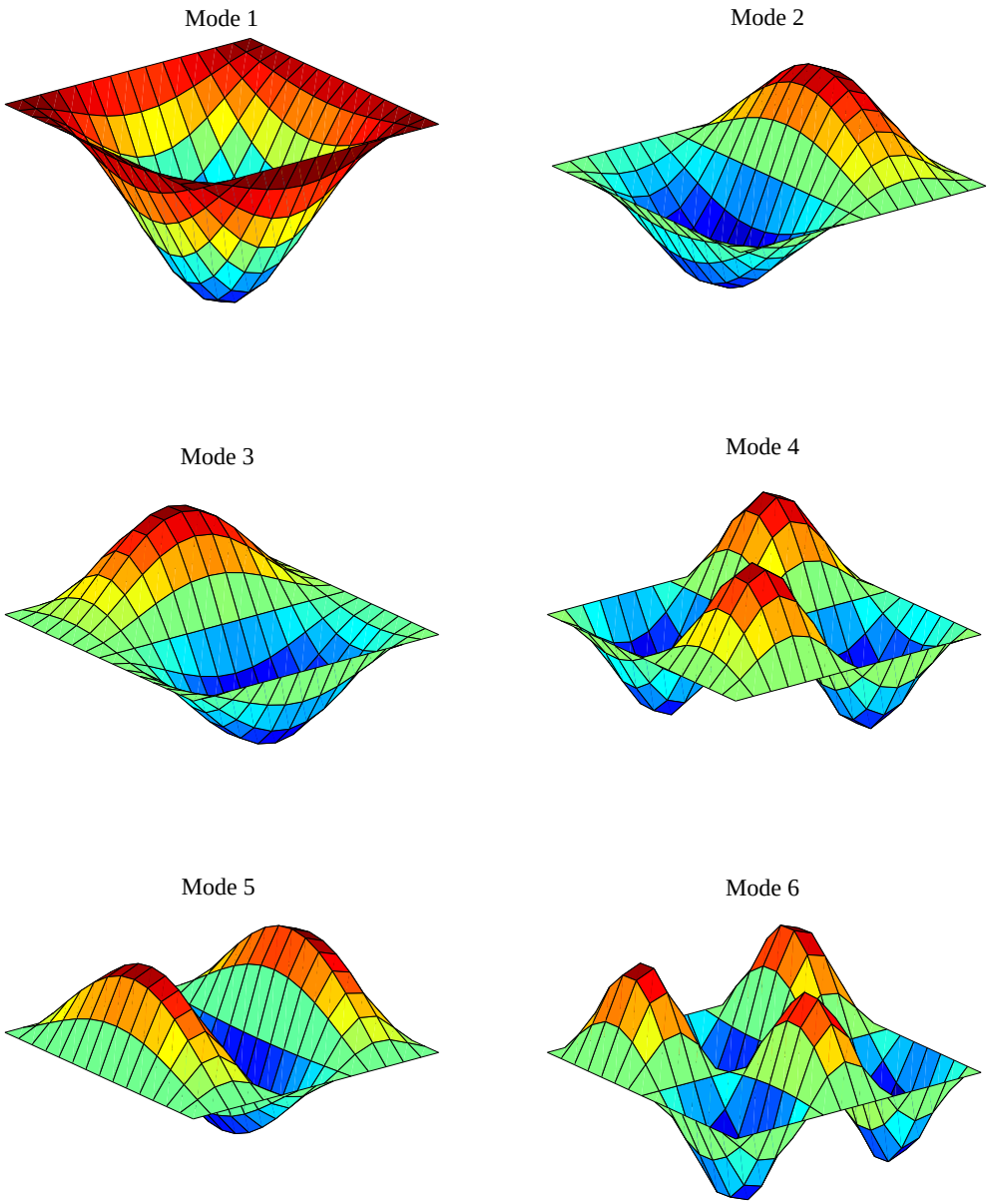

Figure 3.25: Clamped cross-ply $[0^0/90^0/0^0]$ square plate ($E_1/E_2 = 40,\ a/h = 10$): the first six mode shapes.

3.5.2 Skew laminated plates

This section deals with five-layer symmetric cross-ply and angle-ply skew laminated plates. Simply supported and clamped edges are considered with various skew angles α from 0^o to 60^o. The span-to-thickness ratio a/h is taken to be 10 and the entire plate is modelled using $6 \times 6, 10 \times 10$ and 14×14 meshes. A representative sketch of the 10×10 mesh used in the analysis is displayed in Figure 3.26.

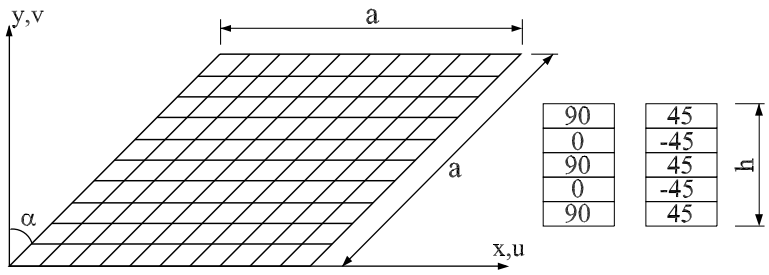

Figure 3.26: Geometry and discretization of skew laminated plates

Table 3.22 and Table 3.23 present the normalized fundamental frequencies of the cross-ply $[90^0/0^0/90^0/0^0/90^0]$ with simply supported and clamped edges, respectively while Table 3.24 and Table 3.25 show the normalized fundamental frequencies of the angle-ply $[45/-45/45/-45/45]$ with simply supported and clamped boundaries. The results calculated using MLSDQ method by Liew et al. (2003), B-spline Rayleigh-Ritz method of Wang (1997) and RBF of Ferreira et al. (2005) are also listed for comparison. It can be seen that there is a good agreement between the present results and other existing solutions for both cases of cross-ply and angle-ply laminates. The numerical results are slightly dependent on the skew angle α (accuracy deteriorates with increasing α) but insensitive to lay-up sequence.

Table 3.22: Simply supported cross-ply $[90^0/0^0/90^0/0^0/90^0]$ skew plate with various skew angles: Convergence of fundamental frequencies and comparison with other solutions ($E_1/E_2 = 40,\ a/h = 10,\ \omega^* = \omega a^2\sqrt{\rho/E_2}/(\pi^2 h)$).

Model	Mesh	α				
		0^0	15^0	30^0	45^0	60^0
MISQ20	6×6	1.6030	1.7267	2.1441	3.0021	4.7710
	10×10	1.5797	1.6977	2.0963	2.9141	4.6033
	14×14	1.5733	1.6896	2.0820	2.8855	4.5412
MISQ24	6×6	1.6030	1.7267	2.1441	3.0021	4.7710
	10×10	1.5797	1.6977	2.0963	2.9141	4.6033
	14×14	1.5733	1.6896	2.0820	2.8855	4.5412
MLSDQ		1.5709	1.6886	2.1026	2.8798	4.4998
RBF		1.5791	1.6917	2.0799	2.8228	4.3761
B-spline		1.5699	–	2.0844	2.8825	–

Table 3.23: Clamped cross-ply $[90^0/0^0/90^0/0^0/90^0]$ skew plate with various skew angles: Convergence of fundamental frequencies and comparison with other solutions ($E_1/E_2 = 40,\ a/h = 10,\ \omega^* = \omega a^2\sqrt{\rho/E_2}/(\pi^2 h)$).

Model	Mesh	α				
		0^0	15^0	30^0	45^0	60^0
MISQ20	6×6	2.4550	2.5528	2.8901	3.6260	5.2538
	10×10	2.4014	2.4958	2.8194	3.5200	5.0610
	14×14	2.3869	2.4803	2.7998	3.4893	4.9989
MISQ24	6×6	2.4550	2.5528	2.8901	3.6260	5.2538
	10×10	2.4014	2.4958	2.8194	3.5200	5.0610
	14×14	2.3869	2.4803	2.7998	3.4893	4.9989
MLSDQ		2.3790	2.4725	2.7927	3.4723	4.9430
RBF		2.4021	2.4932	2.8005	3.4923	4.9541
B-spline		2.3820	–	2.7921	3.4738	–

Table 3.24: Simply supported angle-ply $[45^0/-45^0/45^0/-45^0/45^0]$ skew plate with various skew angles: Convergence of fundamental frequencies and comparison with other solutions ($E_1/E_2 = 40$, $a/h = 10$, $\omega^* = \omega a^2\sqrt{\rho/E_2}/(\pi^2 h)$).

Model	Mesh	α				
		0^0	15^0	30^0	45^0	60^0
MISQ20	6×6	1.8768	1.9255	2.1546	2.7185	4.1758
	10×10	1.8491	1.8969	2.1093	2.6286	4.0249
	14×14	1.8413	1.8889	2.0955	2.5672	3.9718
MISQ24	6×6	1.8768	1.9255	2.1546	2.7185	4.1758
	10×10	1.8491	1.8969	2.1093	2.6286	4.0249
	14×14	1.8413	1.8889	2.0955	2.5672	3.9718
MLSDQ		1.8248	1.8838	2.0074	2.5028	4.0227
RBF		1.8357	1.8586	2.0382	2.4862	3.8619
B-spline		1.8792	–	2.0002	2.4788	–

Table 3.25: Clamped angle-ply $[45^0/-45^0/45^0/-45^0/45^0]$ skew plate with various skew angles: Convergence of fundamental frequencies and comparison with other solutions ($E_1/E_2 = 40,\ a/h = 10$, $\omega^* = \omega a^2\sqrt{\rho/E_2}/(\pi^2 h)$).

Model	Mesh	α				
		0^0	15^0	30^0	45^0	60^0
MISQ20	6×6	2.3551	2.4242	2.7566	3.5013	5.1549
	10×10	2.3045	2.3713	2.6892	3.3977	4.9605
	14×14	2.2908	2.3570	2.6708	3.3683	4.8982
MISQ24	6×6	2.3551	2.4242	2.7566	3.5013	5.1549
	10×10	2.3045	2.3713	2.6892	3.3977	4.9605
	14×14	2.2908	2.3570	2.6708	3.3683	4.8982
MLSDQ		2.2787	2.3504	2.6636	3.3594	4.8566
RBF		2.3324	2.3962	2.6981	3.3747	4.8548
B-spline		2.2857	–	2.6626	3.3523	–

3.5.3 Circular laminated plates

A circular symmetric 4-layer $[\theta/-\theta/-\theta/\theta]$ laminated plate with a diameter D and a thickness h as shown in Figure 3.27 is analysed. The span-to-thickness ratio a/h is taken to be 10 in the computation. Two types of boundary conditions, simply supported (SSSS) and clamped (CCCC) with various fibre orientation angles $\theta = 0^o, 15^o, 30^o, 45^o$ are considered.

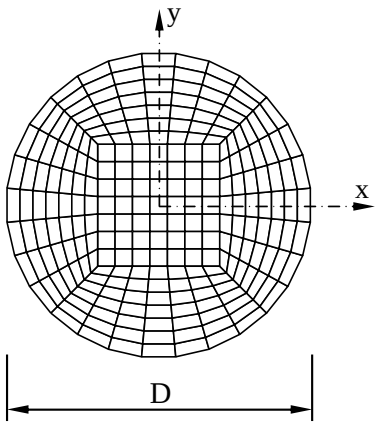

Figure 3.27: Geometry and discretization of a circular laminated plate

The effect of the ply's angle θ on the normalized fundamental frequency of the simply supported and clamped circular laminated plate is presented in Table 3.26. The natural frequencies of the first six modes in the case of clamped edge conditions are also presented in Table 3.27 together with the corresponding mode shapes in Figure 3.28. It is observed that the numerical results obtained by the present methods are comparable with results obtained by MLSDQ method of Liew et al. (2003).

Table 3.26: Circular 4-layer $[\theta/-\theta/-\theta/\theta]$ laminated plates with various boundary conditions and ply angles: Comparison of fundamental frequencies with other solutions ($\omega^* = (\omega a^2/h)\sqrt{\rho/E_2},\ E_1/E_2 = 40,\ a/h = 10$).

Model	B.C	θ			
		0	15	30	45
MISQ20	SSSS	16.168	16.448	16.924	17.162
MISQ24		16.168	16.448	16.924	17.162
MLSDQ		16.167	16.475	16.928	17.119
MISQ20	CCCC	22.123	22.698	24.046	24.766
MISQ24		22.123	22.698	24.046	24.766
MLSDQ		22.211	22.774	24.071	24.752

Table 3.27: Clamped circular 4-layer $[\theta/-\theta/-\theta/\theta]$ laminated plate: Comparison of the normalized natural frequencies of the first six modes ($\omega^* = (\omega a^2/h)\sqrt{\rho/E_2}, E_1/E_2 = 40, a/h = 10$).

θ	Model	Mode					
		1	2	3	4	5	6
0	MISQ20	22.123	29.768	41.726	42.805	50.756	56.950
	MISQ24	22.123	29.768	41.726	42.805	50.756	56.950
	MLSDQ	22.211	29.651	41.101	42.635	50.309	54.553
15	MISQ20	22.698	31.568	43.635	44.318	53.468	60.012
	MISQ24	22.698	31.568	43.635	44.318	53.468	60.012
	MLSDQ	22.774	31.455	43.350	43.469	52.872	57.386
30	MISQ20	24.046	36.399	44.189	52.028	57.478	67.099
	MISQ24	24.046	36.399	44.189	52.028	57.478	67.099
	MLSDQ	24.071	36.153	43.968	51.074	56.315	66.220
45	MISQ20	24.766	39.441	43.817	57.907	57.945	66.297
	MISQ24	24.766	39.441	43.817	57.907	57.945	66.297
	MLSDQ	24.752	39.181	43.607	56.759	56.967	65.571

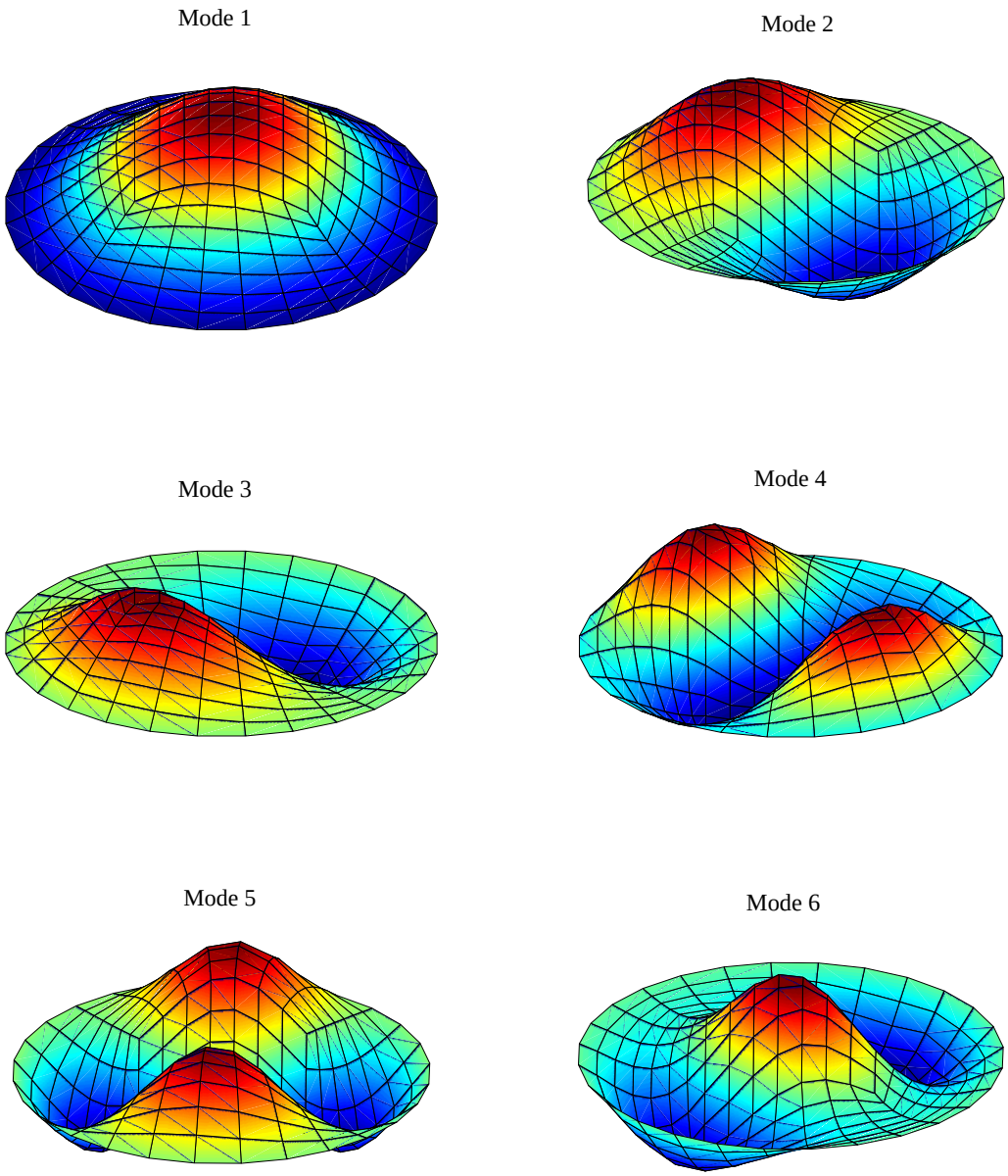

Figure 3.28: Clamped circular angle-ply $[45^0/-45^0/-45^0/45^0]$ laminated plate: the first six mode shapes.

3.5.4 Right-angle triangular laminated plates

This section deal with the free vibration of symmetric/antisymmetric cross-ply and angle-ply right-angle triangular plates as shown in Figure 3.14. The following material properties are used in the analysis:

$$E_1/E_2 = 25;\ G_{12} = G_{13} = 0.5E_2;\ G_{23} = 0.5E_2;\ \nu_{12} = \nu_{13} = \nu_{23} = 0.25;\ \rho = 1.$$

Table 3.28 reports the present normalized natural frequencies of the first six modes with various lay-up of cross-ply and angle-ply sequences, together with the solutions using LS12 higher-order element (Haldar and Sengupta, 2003). It is observed that the present results give a little larger value than those obtained by LS12 element. It may be the use of consistent matrices in the present formula which usually yields results greater than those by LS12 formula using the lumped mass matrices (Cook et al., 2002). The first six mode shapes are also displayed in Figure 3.29.

Table 3.28: Clamped right-angle triangular laminated plate: Comparison of the normalized natural frequencies of the first six modes ($\omega^* = (\omega a^2/h)\sqrt{\rho/E_2}, E_1/E_2 = 25, a/h = 100$).

Lay-up	Model	Mode					
		1	2	3	4	5	6
$[0^0/90^0]$	MISQ20	52.453	91.179	105.284	144.020	156.290	178.941
	MISQ24	52.516	91.357	105.561	144.274	156.950	179.809
	LS12	51.933	89.391	102.88	139.28	149.94	172.06
$[0^0/90^0/0^0]$	MISQ20	70.000	109.088	148.223	160.771	203.320	221.969
	MISQ24	70.000	109.088	148.223	160.771	203.320	221.969
	LS12	69.252	106.73	143.88	155.06	193.84	210.11
$[30^0/-30^0]$	MISQ20	52.222	84.840	113.245	127.063	159.778	178.549
	MISQ24	52.172	84.630	113.019	126.735	159.177	178.205
	LS12	51.735	83.376	110.71	123.05	153.62	169.81
$[45^0/-45^0]$	MISQ20	52.571	86.269	113.882	130.911	160.286	186.491
	MISQ24	52.624	86.392	114.102	131.150	160.734	186.982
	LS12	52.057	84.715	111.25	126.73	153.86	177.31

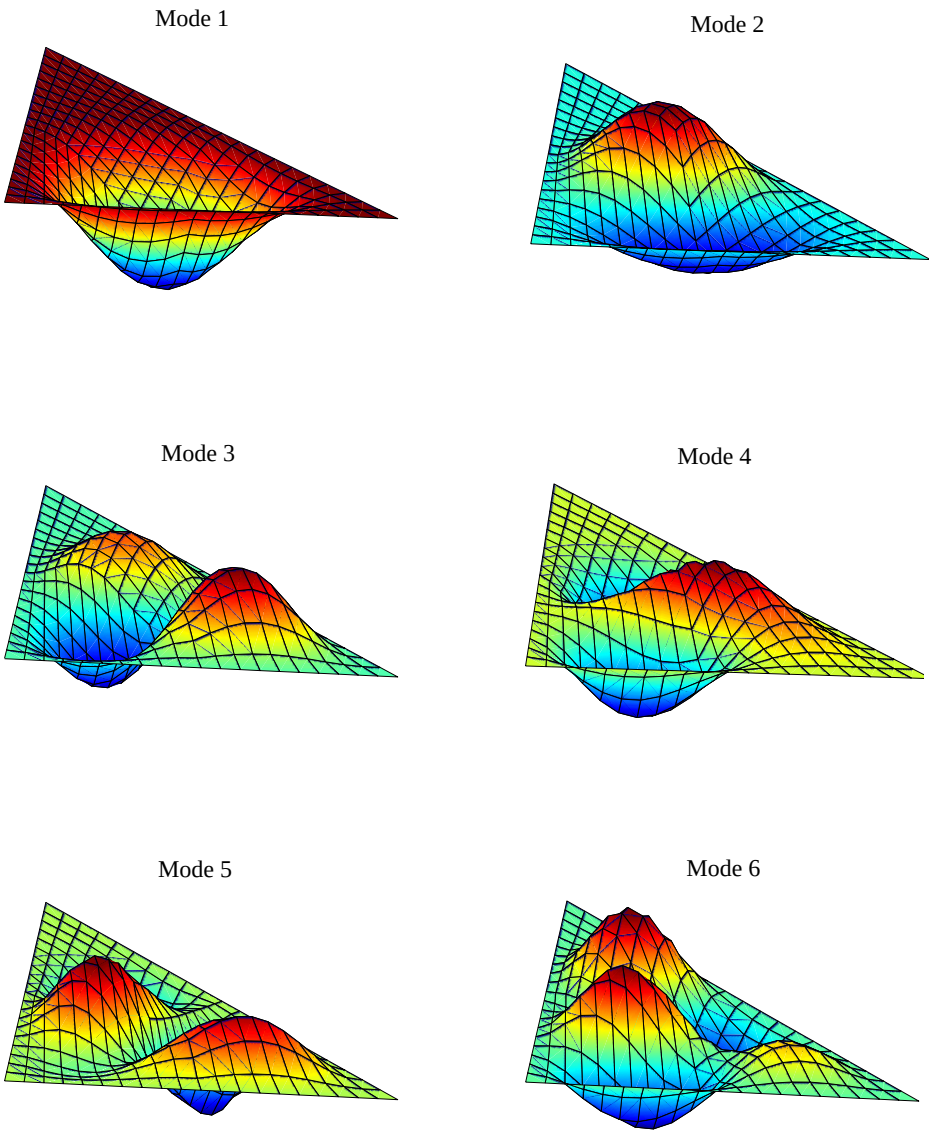

Figure 3.29: Clamped cross-ply $[0^0/90^0/0^0]$ right-angle triangular plates: the first six mode shapes.

3.6 Numerical examples: Buckling analysis

In this section, a number of numerical examples are presented to demonstrate the performance of the MISQ20 and MISQ24 elements in buckling analysis of laminated plates. Particular plate structures with various boundary conditions, span-to-thickness ratios and modulus ratios (the degree of orthotropy) are analyzed. In all examples, the material properties are assumed to be the same in all the layers and the fibre orientations may be different among the layers. The ply angle of each layer is measured from the global $x-$axis to the fibre direction. The thickness of each layer is identified. Unless otherwise specified, shear correction factors $k_1^2 = k_2^2 = \frac{\pi^2}{12}$ are used for all computations. The following two sets of typical graphite-epoxy material properties are used in the analysis unless otherwise stated:

- Material I: $E_1/E_2 = 3,\ 10,\ 20,\ 30$ or $40;\ G_{12} = G_{13} = 0.6E_2;\ G_{23} = 0.5E_2;\ \nu_{12} = \nu_{13} = \nu_{23} = 0.25.$
- Material II: $E_1/E_2 = 25;\ G_{12} = G_{13} = 0.5E_2;\ G_{23} = 0.2E_2;\ \nu_{12} = \nu_{13} = \nu_{23} = 0.25.$

3.6.1 Cross-ply $[0^0/90^0/90^0/0^0]$ square plate under uniaxial compression

3.6.1.1 Convergence study and effect of modulus ratios

A simply supported four-layer cross-ply $[0^0/90^0/90^0/0^0]$ square laminated plate is chosen to study the convergence of the present method using MISQ20 and MISQ24 elements. Figure 3.30 shows the plate geometry and boundary conditions. The span-to-thickness ratio of the plate a/h is taken to be 10 in the computation.

Table 3.29 shows the convergence and comparison of the normalized fundamental frequencies of the present method with other solutions for various degrees of orthotropy of the individual layers (E_1/E_2 ratio). It is found that the MISQ20 and MISQ24 elements yield the same solution with relatively accurate results in a wide range of E_1 to E_2 ratios.

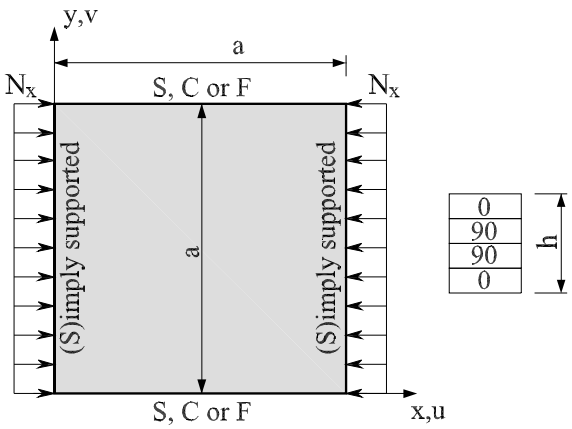

Figure 3.30: Cross-ply square laminated plate subjected to in-plane compression.

The effect of various modulus ratios of E_1/E_2 on the accuracy of the critical buckling load is also displayed in Figure 3.31. It can be seen that the present results are in good agreement with the 3D elasticity solutions of Noor (1975) and slightly better than those of FSDT-based RPIM's solutions of Liu, Chua and Ghista (2007). It is also found that the present MISQ20 and MISQ24 solution is quite insensitive to the variation of modulus ratios as can be seen in Figure 3.31

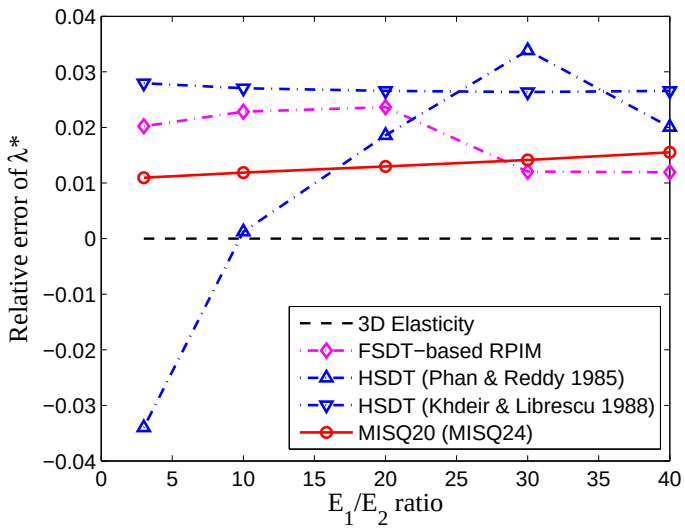

Figure 3.31: Effect of modulus ratios on the accuracy of critical buckling loads.

Table 3.29: Simply supported cross-ply $[0^0/90^0/90^0/0^0]$ square plate: Convergence of normalized critical buckling loads with various E_1/E_2 ratios and comparison with other solutions ($\lambda^* = N_x a^2/(E_2 h^3)$, $a/h = 10$).

Model	Mesh	E_1/E_2				
		3	10	20	30	40
MISQ20	6×6	5.583	10.279	15.803	20.308	24.080
	10×10	5.409	9.978	15.360	19.759	23.446
	12×12	5.380	9.927	15.287	19.667	23.340
	16×16	5.352	9.878	15.214	19.577	23.236
		(1.096%)	(1.188%)	(1.298%)	(1.414%)	(1.551%)
MISQ24	6×6	5.583	10.279	15.803	20.308	24.080
	10×10	5.409	9.978	15.360	19.759	23.446
	12×12	5.380	9.927	15.287	19.667	23.340
	16×16	5.352	9.878	15.214	19.577	23.236
		(1.096%)	(1.188%)	(1.298%)	(1.414%)	(1.551%)
Liu, Chua and Ghista (2007)		5.401	9.985	15.374	19.537	23.154
		(2.021%)	(2.284%)	(2.364%)	(1.207%)	(1.193%)
Phan and Reddy (1985)		5.114	9.774	15.298	19.957	23.340
		(-3.400%)	(1.230%)	(1.858%)	(3.383%)	(2.006%)
Khdeir and Librescu (1988)		5.442	10.026	15.418	19.813	23.489
		(2.796%)	(2.704%)	(2.657%)	(2.637%)	(2.657%)
Noor (1975)		5.294	9.762	15.019	19.304	22.881

Values in parentheses correspond to relative error compared to 3D elasticity solution.

3.6.1.2 Effect of mesh distortion

The influence of mesh distortion is studied in this section. The plate of the first example (Section 3.6.1.1) is analyzed again using distorted element created by irregular interior nodes. These interior nodes are derived from a set of regular nodes by using a controlling distortion factor s as in Equation (3.78) of Section 3.5.1.2. Typical irregular meshes of the analysis are shown in Figure 3.32.

The effect of the mesh distortion on the critical buckling loads of the plate obtained

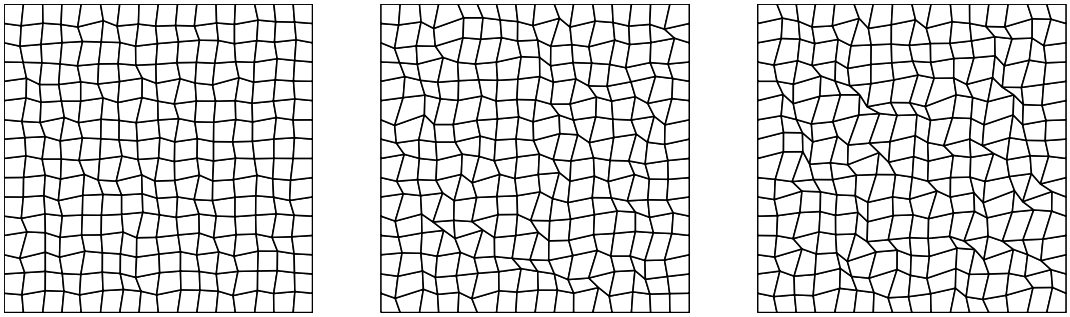

$s = 0.2$ $s = 0.3$ $s = 0.4$

Figure 3.32: Typical irregular meshes of 16×16 with various distortion factor s.

by the present method is shown in Table 3.30 and Figure 3.33. It is found that the accuracy of the fundamental critical buckling loads associated with irregular mesh decreases in comparison with regular meshes. For the cases of $E_1/E_2 = 20,\ 30$ and 40, Figure 3.33 indicates that the error at some s could become even smaller than those at $s = 0$ (regular mesh).

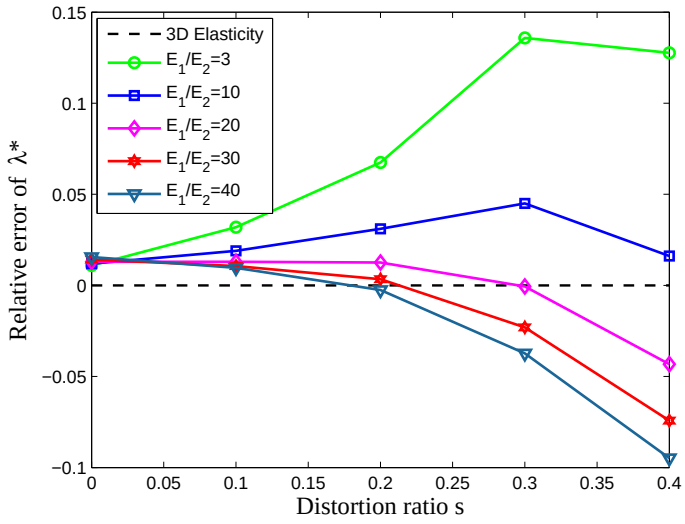

Figure 3.33: Cross-ply $[0^0/90^0/90^0/0^0]$ square plate: Effect of mesh distortion on the accuracy of critical buckling load.

Table 3.30: Simply supported cross-ply $[0^0/90^0/90^0/0^0]$ square plate: Effect of mesh distortion on the normalized critical buckling loads ($\lambda^* = N_x a^2/(E_2 h^3),\ a/h = 10$).

E_1/E_2	Model	s				
		0	0.1	0.2	0.3	0.4
3	MISQ20 (16×16)	5.352	5.463	5.651	6.013	5.970
	MISQ24 (16×16)	5.352	5.463	5.651	6.013	5.970
10	MISQ20 (16×16)	9.878	9.947	10.065	10.201	9.919
	MISQ24 (16×16)	9.878	9.947	10.065	10.201	9.919
20	MISQ20 (16×16)	15.214	15.214	15.208	15.010	14.369
	MISQ24 (16×16)	15.214	15.214	15.208	15.010	14.369
30	MISQ20 (16×16)	19.577	19.509	19.369	18.859	17.871
	MISQ24 (16×16)	19.577	19.509	19.369	18.859	17.871
40	MISQ20 (16×16)	23.236	23.102	22.823	22.026	20.710
	MISQ24 (16×16)	23.236	23.102	22.823	22.026	20.710

3.6.2 Symmetric/anti-symmetric cross-ply and angle-ply square plates under uniaxial compression

This section deals with the effect of the span-to-thickness ratio and various edge support conditions to symmetric/antisymmetric cross-ply and angle-ply square plates. The influence of the number of layers on the critical buckling load is also presented with 2-,4- and 10-layer laminates. A typical representative sketch of the laminated plate is shown in Figure 3.34.

3.6.2.1 Effect of span-to-thickness ratio

The effect of the span-to-thickness ratio (a/h) on the uniaxial critical buckling load is studied for simply supported symmetric/antisymmetric cross-ply and angle-ply square plates made of Material I having $E_1/E_2 = 40$. The results obtained by the

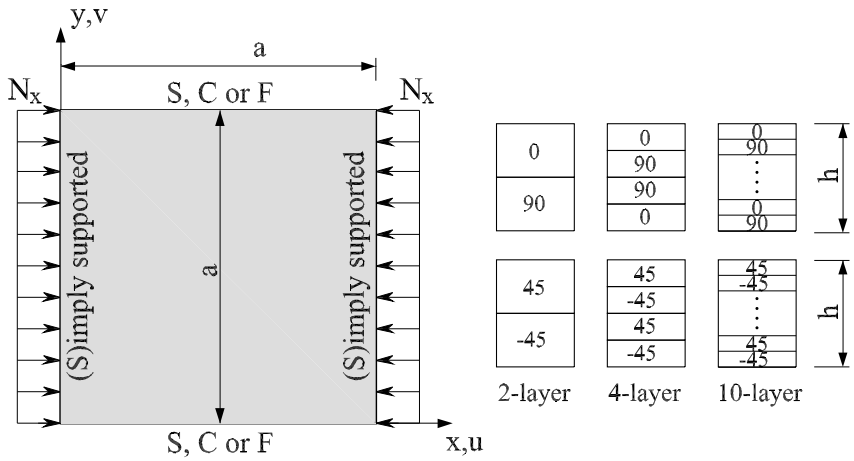

Figure 3.34: Geometry and discretization of square laminated plates.

present MISQ20, MISQ24 elements are shown from Table 3.31 to Table 3.34 in comparison with those obtained by FSDT (Chakrabarti and Sheikh, 2003; Reddy and Phan, 1985) and HSDT (Reddy and Phan, 1985).

The numerical results show that the present solutions converge with mesh refinement for various span-to-thickness ratios $a/h = 10,\ 20,\ 50,\ 100$. It is also observed that the normalized critical buckling loads increase with increasing span-to-thickness ratio and increasing number of layers for both of cross-ply and angle-ply laminates. Both of MISQ20 and MISQ24 elements give the same critical buckling loads for symmetric laminates and almost the same results for all cases of unsymmetric laminates. The obtained numerical results are comparable with other solutions and in closer agreement with HSDT than FSDT.

Table 3.31: Simply supported symmetric cross-ply $[0^0/90^0/90^0/0^0]$ square plate with various a/h ratios: Convergence of normalized critical buckling loads and comparison with other solutions ($E_1/E_2 = 40,\ \lambda^* = N_x a^2/(E_2 h^3)$).

Model		a/h			
		10	20	50	100
MISQ20	6×6	24.080	33.037	37.081	37.750
	10×10	23.446	32.067	35.939	36.578
	16×16	23.236	31.747	35.561	36.190
MISQ24	6×6	24.080	33.037	37.081	37.750
	10×10	23.446	32.067	35.939	36.578
	16×16	23.236	31.747	35.561	36.190
FSDT (Chakrabarti and Sheikh, 2003)		23.409	31.625	35.254	35.851
FSDT (Reddy and Phan, 1985)		23.471	31.707	35.356	35.955
HSDT (Reddy and Phan, 1985)		23.349	31.637	35.419	35.971

Table 3.32: Simply supported unsymmetric cross-ply $[0^0/90^0]$ square plate with various a/h ratios: Convergence of normalized critical buckling loads and comparison with other solutions ($E_1/E_2 = 40,\ \lambda^* = N_x a^2/(E_2 h^3)$).

Model		a/h			
		10	20	50	100
MISQ20	6×6	11.663	13.113	13.595	13.667
	10×10	11.291	12.668	13.123	13.190
	16×16	11.169	12.520	12.967	13.033
MISQ24	6×6	12.083	13.373	13.819	13.911
	10×10	11.604	12.798	13.210	13.296
	16×16	11.446	12.609	13.011	13.095
FSDT (Chakrabarti and Sheikh, 2003)		11.349	12.510	12.879	12.934
FSDT (Reddy and Phan, 1985)		11.353	12.515	12.884	12.939
HSDT (Reddy and Phan, 1985)		11.563	12.577	12.895	12.942

Table 3.33: Simply supported angle-ply $[45^0/-45^0]$ square plate with various a/h ratios: Convergence of normalized critical buckling loads and comparison with other solutions ($E_1/E_2 = 25,\ \lambda^* = N_x a^2/(E_2 h^3)$).

Model		a/h			
		10	20	50	100
MISQ20	6×6	12.539	15.149	16.101	16.247
	10×10	12.180	14.672	15.577	15.716
	16×16	12.062	14.515	15.404	15.540
MISQ24	6×6	12.615	15.256	16.222	16.370
	10×10	12.206	14.709	15.618	15.758
	16×16	12.072	14.528	15.419	15.557
HSDT (Chakrabarti and Sheikh, 2003)		12.600	14.629	15.329	15.435
HSDT (Phan and Reddy, 1985)		12.622	14.644	15.336	15.441

Table 3.34: Simply supported angle-ply $[45^0/-45^0/45^0/-45^0]$ square plate with various a/h ratios: Convergence of normalized critical buckling loads and comparison with other solutions ($E_1/E_2 = 25,\ \lambda^* = N_x a^2/(E_2 h^3)$).

Model		a/h			
		10	20	50	100
MISQ20	6×6	20.833	32.539	36.937	37.666
	10×10	20.018	31.564	35.756	36.450
	16×16	19.764	31.241	35.366	36.048
MISQ24	6×6	20.955	32.562	36.966	37.697
	10×10	20.111	31.572	35.766	36.460
	16×16	19.848	31.244	35.370	36.052
HSDT (Chakrabarti and Sheikh, 2003)		19.593	30.949	35.084	35.769
HSDT (Phan and Reddy, 1985)		21.962	31.032	35.120	35.795

3.6.2.2 Effect of mixed boundaries

The influence of the mixed boundary conditions and span-to-thickness ratio are now considered. The plate is always simply supported (S) along the edges parallel to the $y-$axis while the other edges have simply supported (S), clamped (C) or free (F) boundary conditions. The notation SSFC, for example, refers to the simply supported of two edges parallel to the $y-$axis and the free and fully clamped for the two edges parallel to the $x-$axis as shown in Figure 3.34. The 2-layer $[0^0/90^0]$, $[45^0/-45^0]$ and 10-layer $[0^0/90^0]_5$, $[45^0/-45^0]_5$ square plates are analyzed with $E_1 = 40E_2$ (Material I) and a 10×10 mesh .

Table 3.35–3.36 contain the normalized critical buckling loads of cross-ply lay-ups for various mixed boundaries obtained by the present method and other solutions of Huang and Li (2004) using FSDT-based MLSDQ method, RKPM's results by Wang et al. (2002) and FSDT, HSDT solutions of Reddy and Khdeir (1989). It can be seen that the accuracy of the present method compares very well with FSDT solutions and other numerical results cited here. The buckling modes of the 10-layer $[0^0/90^0]_5$ plate under various edge conditions are also shown in Figure 3.35.

Table 3.37–3.38 show the effect of mixed boundary conditions on the normalized critical buckling load of 2-layer $[45^0/-45^0]$ and 10-layer $[45^0/-45^0]_5$ angle-ply plates together with other solutions in the literature. Again, the present results are in close agreements with the FSDT solutions cited here.

Table 3.35: Cross-ply $[0^0/90^0]$ square plate with various mixed boundaries: Comparison of normalized critical buckling loads with other solutions ($E_1/E_2 = 40,\ a/h = 10,\ \lambda^* = N_x a^2/(E_2 h^3)$).

Model	SSSS	SSFF	SSCC	SSSC	SSFC	SSFS
MISQ20	11.291	4.860	20.082	16.470	6.140	5.342
MISQ24	11.604	4.860	20.330	16.814	6.244	5.395
MLSDQ (Huang and Li, 2004)	11.301	4.823	19.871	–	–	–
RKPM (Wang et al., 2002)	11.582	4.996	20.624	16.872	6.333	5.502
FSDT (Reddy and Khdeir, 1989)	11.353	4.851	20.067	16.437	6.166	5.351
HSDT (Reddy and Khdeir, 1989)	11.562	4.940	21.464	17.133	6.274	5.442

Table 3.36: Cross-ply 10-layer $[0^0/90^0]_5$ square plate with various mixed boundaries: Comparison of normalized critical buckling loads with other solutions ($E_1/E_2 = 40,\ a/h = 10,\ \lambda^* = N_x a^2/(E_2 h^3)$).

Model	SSSS	SSFF	SSCC	SSSC	SSFC	SSFS
MISQ20	25.525	12.131	35.105	32.870	14.352	12.541
MISQ24	25.534	12.131	34.531	32.874	14.356	12.543
MLSDQ (Huang and Li, 2004)	25.338	12.030	34.604	–	–	–
RKPM (Wang et al., 2002)	25.703	12.224	35.162	32.950	14.495	12.658
FSDT (Reddy and Khdeir, 1989)	25.450	12.092	34.837	32.614	14.358	12.524
HSDT (Reddy and Khdeir, 1989)	25.423	12.077	35.376	32.885	14.351	12.506

Table 3.37: Angle-ply $[45^0/-45^0]$ square plate with various mixed boundaries: Comparison of normalized critical buckling loads with other solutions ($E_1/E_2 = 40,\ a/h = 10,\ \lambda^* = N_x a^2/(E_2 h^3)$).

Model	SSSS	SSFF	SSCC
MISQ20	17.510	2.362	19.849
MISQ24	17.512	2.455	21.191
FSDT-based MLSDQ (Huang and Li, 2004)	17.527	2.450	19.858
FSDT (Khdeir, 1989)	17.552	2.327	19.957

Table 3.38: Angle-ply $[45^0/-45^0]_5$ square plate with various mixed boundaries: Comparison of normalized critical buckling loads with other solutions ($E_1/E_2 = 40,\ a/h = 10,\ \lambda^* = N_x a^2/(E_2 h^3)$).

Model	SSSS	SSFF	SSCC
MISQ20	33.487	4.531	33.653
MISQ24	31.288	4.206	31.555
FSDT-based MLSDQ (Huang and Li, 2004)	33.027	4.741	33.205
FSDT (Khdeir, 1989)	33.173	4.401	33.356

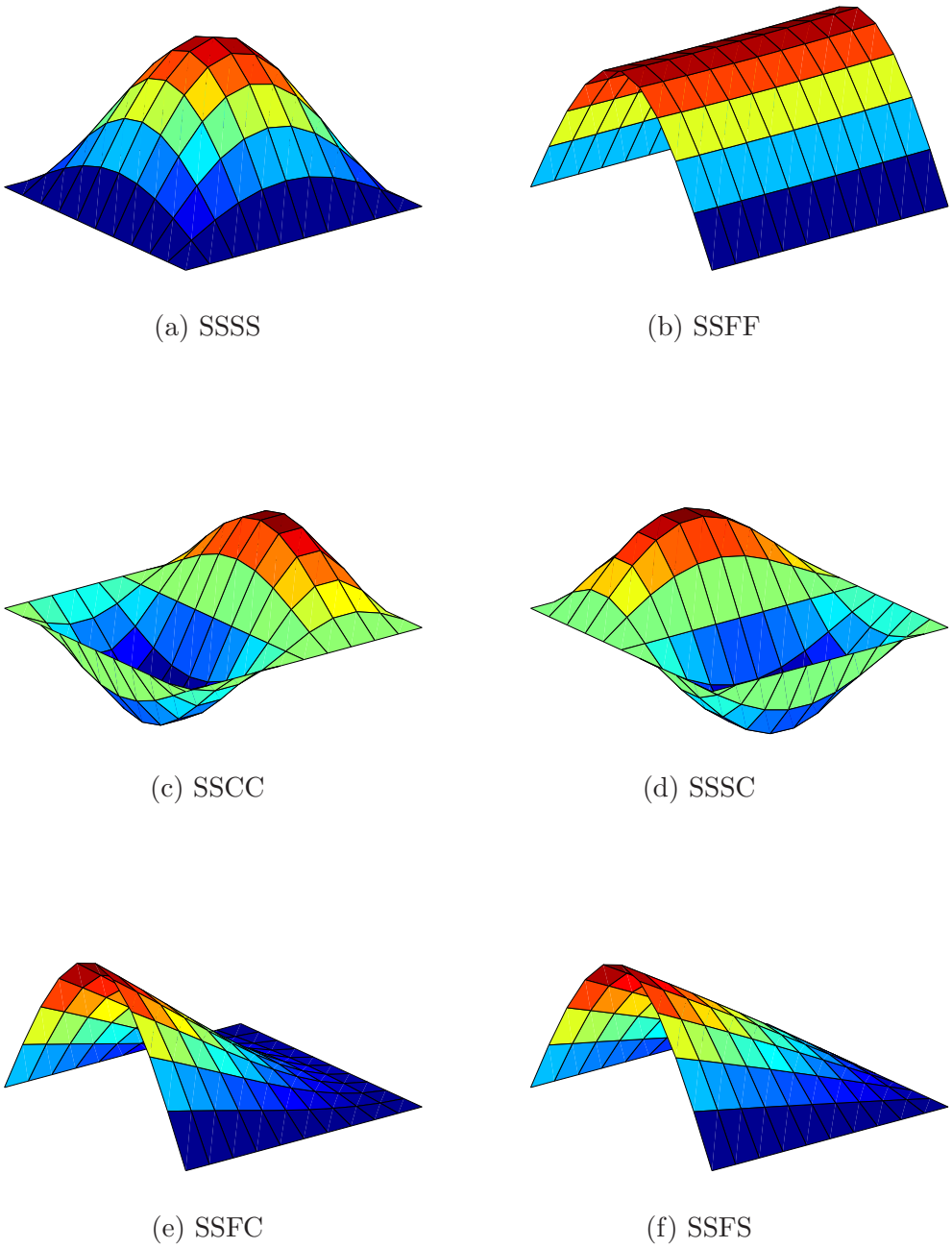

(a) SSSS (b) SSFF

(c) SSCC (d) SSSC

(e) SSFC (f) SSFS

Figure 3.35: Fundamental buckling modes of cross-ply 10-layer $[0^0/90^0]_5$ square plate with various mixed boundaries: (a) SSSS; (b) SSFF; (c) SSCC; (d) SSSC; (e) SSFC and (f) SSFS.

3.6.3 Cross-ply skew plates with various skew angles and span-to-thickness ratios under uniaxial compression

This section deals with 4-layer symmetric cross-ply skew laminated plates under uniaxial compression as shown in Figure 3.36. Simply supported plates at the four edges are considered with various skew angle from 0 to 30^0. The span-to-thickness ratio a/h is taken to be 10, 20, 50 and 100 and the entire plate is modelled using 10×10 mesh. In this problem, the material properties used for each individual layer are: $E_1 = 128$ GPa, $E_2 = 11$ GPa, $G_{12} = G_{13} = 4.48$ GPa, $G_{23} = 1.53$ GPa and $\nu_{12} = \nu_{13} = \nu_{23} = 0.25$.

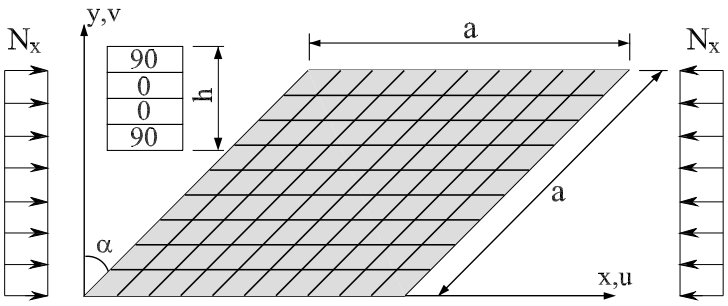

Figure 3.36: Geometry and discretization of cross-ply skew plates.

Table 3.39 presents the normalized critical buckling load obtained by the present MISQ20 and MISQ24 elements together with those of Chakrabarti and Sheikh (2003) and Hu and Tzeng (2000).

It can be seen that there is a good agreement between the present results and other existing solutions. Numerical results also show that the critical buckling load increases as the skew angle or as the span-to-thickness ratio increases.

Table 3.39: Simply supported cross-ply $[90^0/0^0/0^0/90^0]$ skew plate with various skew angles and span-to-thickness ratios: Comparison of the critical buckling loads with other solutions ($\lambda^* = N_x a^2/(E_2 h^3)$).

Skew Angle	Model	a/h			
		10	20	50	100
0	MISQ20	8.623	10.976	11.939	12.094
	MISQ24	8.623	10.976	11.939	12.094
	Chakrabarti and Sheikh (2003)	9.392	11.324	12.029	12.138
	Hu and Tzeng (2000)	–	–	–	12.045
10	MISQ20	8.979	11.600	12.757	12.960
	MISQ24	8.978	11.599	12.757	12.960
	Chakrabarti and Sheikh (2003)	9.871	12.057	12.888	13.020
	Hu and Tzeng (2000)	–	–	–	13.000
20	MISQ20	10.104	13.577	15.369	15.753
	MISQ24	10.104	13.576	15.369	15.753
	Chakrabarti and Sheikh (2003)	11.367	14.441	16.701	15.915
	Hu and Tzeng (2000)	–	–	–	15.636
30	MISQ20	12.185	17.314	20.294	21.050
	MISQ24	12.185	17.314	20.294	21.050
	Chakrabarti and Sheikh (2003)	13.753	18.920	20.188	21.605
	Hu and Tzeng (2000)	–	–	–	21.500

3.6.4 Cross-ply square plates under biaxial compression

In this section, 3-layer symmetric cross-ply $[0^0/90^0/0^0]$ square plate is chosen to compute the bi-axial buckling load under various edge support conditions (see Figure 3.37). The plate is of width a and thickness h and the span-to-thickness ratio a/h is taken to be 10. Material I is used in this computation.

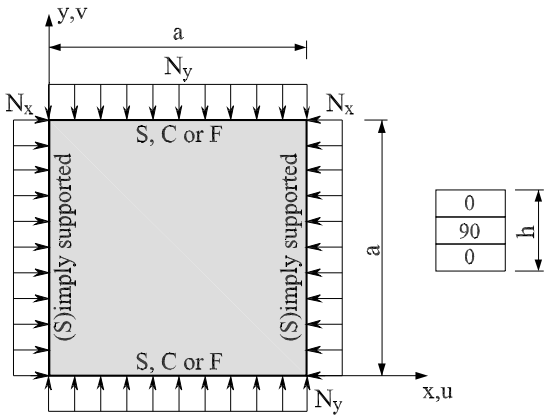

Figure 3.37: Geometry and discretization of cross-ply square plates.

3.6.4.1 Effect of material anisotropy

The effect of modulus ratio E_1/E_2 on the critical bi-axial buckling load is studied in this section. Table 3.40 reports the normalized critical buckling loads obtained by the present elements together with the FSDT solution of Fares and Zenkour (1999)and HSDT solution of Khdeir and Librescu (1988). The present results in general indicate a good agreement with other referenced results and closer to those of HSDT than FSDT. It is also observed than the critical bi-axial buckling load increases with the degree of orthotropy (E_1/E_2 ratio).

3.6.4.2 Effect of mixed boundary conditions

The effect of mixed edge support conditions on the critical biaxial buckling load is now investigated. Table 3.41 reports the present critical biaxial buckling loads together with the FSDT solutions of (Khdeir and Librescu, 1988; Liew and Huang, 2003) and HSDT solutions of (Liu, Chua and Ghista, 2007; Khdeir and Librescu,

1988). Once again, the MISQ20 and MISQ24 yield the same results and they are in good agreement with other numerical results cited here.

Table 3.40: Simply supported cross-ply $[0^0/90^0/0^0]$ square plate with various modulus ratio: Comparison of the critical bi-axial buckling loads with other solutions ($\lambda^* = N_x a^2/(E_2 h^3)$).

Model	E_1/E_2			
	10	20	30	40
MISQ20 (10×10)	4.939	7.488	9.016	10.252
MISQ24 (10×10)	4.939	7.488	9.016	10.252
FSDT (Fares and Zenkour, 1999)	4.963	7.588	8.575	10.202
HSDT (Khdeir and Librescu, 1988)	4.963	5.516	9.056	10.259

Table 3.41: Cross-ply $[0^0/90^0/0^0]$ square plate with various mixed boundaries under biaxial compression: Comparison of normalized critical buckling loads with other solutions ($E_1/E_2 = 40,\ a/h = 10,\ \lambda^* = N_x a^2/(E_2 h^3)$).

Model	SSSS	SSFF	SSCC	SSSC	SSFC
MISQ20 (10×10)	10.252	1.858	13.249	11.613	5.964
MISQ24 (10×10)	10.252	1.858	13.249	11.613	5.964
MLSDQ (Liew and Huang, 2003)	10.120	1.926	13.225	11.523	5.517
RPIM (Liu, Chua and Ghista, 2007)	10.091	1.928	12.952	–	–
FSDT (Khdeir and Librescu, 1988)	10.202	1.937	13.290	11.602	5.551
HSDT (Khdeir and Librescu, 1988)]	10.259	1.937	13.288	–	–

3.7 Concluding remarks

In this chapter, the development of two novel, simple, robust and efficient low-order displacement-based elements has been reported and described for linear-elastic analysis of thin to moderately thick laminated composite plates of various shapes. The two developed four-node 20-DOF and four-node 24-DOF elements, namely MISQ20 and MISQ24, are based on mixed interpolation with strain

smoothing technique used in Galerkin mesh-free method within the framework of the FSDT. With this combination, the elements maintain a sufficient rank and free from shear locking and any spurious modes.

Several numerical examples of laminated composite plates of various shapes from single layer to multi-layer, from cross-ply to angle-ply stacking sequences, from symmetric to anti-symmetric laminations are investigated in detail to verify and assess the performance of the two proposed elements. The applicability of the present approaches is demonstrated over a wide range of static bending, free vibration, buckling test problems associated with different parameters such as boundary conditions, types of laminates, mesh distortion, fibre orientation, span-to-thickness ratio, mixed boundaries and modulus ratios. Comparison of the numerical results computed using the MISQ20 and MISQ24 elements together with analytic solution and other FSDT-based, HSDT-based elements also form a major part of the present investigation.

Based on the results obtained from the numerical evaluations, the presently developed elements have been shown to pass the patch tests, to possess satisfactory rate of convergence and excellent accuracy within reasonable mesh refinement for multi-layer laminated plates of both homogeneous isotropic and laminated anisotropic materials. No evidence of shear locking or spurious modes has been found in any of the examples carried out to date. The MISQ20 and MISQ24 elements also appear to be insensitive to shape distortion and to be able to yield accurate results even with coarse discretization irrespective of the span-to-thickness ratio and stacking sequence as shown in many examples.

It is observed that the performance of MISQ20 and MISQ24 elements is the same for analysis of symmetric laminates. For anti-symmetric laminates (or highly anisotropic), the behaviour of MISQ20 and MISQ24 is slightly different due to the coupling between membrane and bending parts. As the MISQ24 element has more DOFs (additional drilling) than MISQ20 element while both elements behave very similarly, MISQ20 should be more economical and preferred to MISQ24 even though there is a small difference in dealing with anti-symmetric laminates. A reduced four-node 12-DOF element, termed as MISQ20R, has also been successfully developed for thermo-mechanical static analysis of functionally graded material plates. This element is also found to be free of shear locking and exhibits

excellent accuracy characteristics.

The simplicity, robustness and efficiency of the developed elements may be attributable to the fact that the merits of the strain smoothing improvement of the SCNI mesh-free method are merged in a complementary manner in the formulations of the developed elements through the assumed strain finite element method. In the next chapter, the MISQ20 and MISQ24 elements will be further extended for geometrically linear analysis of shell structures.

Chapter 4

Assumed Strain Smoothing Flat Shell Finite Elements

The two proposed MISQ20 and MISQ24 elements, which were described and verified in the previous chapter for plate bending problems, are further developed for shell problems in this chapter. The performance of the elements is validated and demonstrated through several numerical benchmark problems. Convergence studies and comparison with other existing solutions in the literature suggest that the present elements are free of lockings and efficient for linear analysis of thin to moderately thick shell structures.

4.1 Introduction

The wide application of shell structures in engineering practice has caught the interests of many researchers in the fields of analysis and design of such structures. A great body of research work has been proposed over several decades towards the development of simple and efficient shell finite elements through three major approaches: (1) the curved shell elements based on classical shell theory with curvilinear coordinates; (2) the degenerated shell elements derived from three-dimensional solid elements and (3) the flat shell elements obtained by the combination of the membrane and bending behaviour of plate elements.

In general, it is difficult to identify which shell element is the most advantageous. Among these approaches, the flat shell elements are regarded to be the most attractive as they can be readily built by combining existing plate and membrane elements. They have been used extensively because of the simplicity in their formulation, the effectiveness in performing computation and the flexibility in applications to both shell and folder plate structures. In addition, the inclusion of transverse shear effect with the aid of Reissner-Mindlin kinematics and the incorporation of drilling degrees of freedom, also significantly improved the performance of the flat elements for thick to thin shell structures (Darilmaz and Kumbasar, 2006).

Although triangular flat elements are most efficient for discretizing arbitrary shell geometries, quadrilateral elements are usually used owing to their better performance with respect to convergence rates than that of triangular elements (Lee and Bathe, 2004). The difficulty in the development of the four-node shell element is that such elements are too stiff and suffer from locking phenomenon. This phenomenon originates from the shortcoming in the interpolation of the displacement. Two well-known locking types that may occur in four-node flat elements in analysis of shell structures are: (1) the transverse shears locking which arises as the ratio of the thickness-to-characteristic length of a shell becomes small (e.g. $t/L \leq 1/100$), and (2) the membrane locking which occurs when coarse or distorted meshes are used, especially in bending dominated problems.

With the development of shell elements, many methods have been proposed to circumvent these disadvantages. For a summary, the readers are referred to Yang et al. (2000). More works on the problems related to the membrane locking of flat shell elements can be found in the references by Cook (1994), Taylor (1987), Groenwold and Slander (1995), and Choi and Lee (1999, 2003), etc.

A large number of four-node shell element formulations have been presented to date and showed good performance, however, there is still room to improve the behaviour of flat shell elements, in order to enhance the efficiency, accuracy and stability even when meshes are coarse or elements are badly-shaped. The objective of this chapter is to extend the improved formulations of locking-free quadrilateral flat shell elements that is able to reduce the mesh distortion sensitivity and enhance the coarse mesh accuracy. Moreover, the incorporation of the ASS

technique also facilitates relatively simple implementation procedure which makes coding easier (Nguyen-Van et al., 2007b, 2008d, 2009).

In the following sections, a brief review of the strain smoothing approach for two four-node flat shell finite elements is first introduced. This is followed by numerical benchmark tests in static, free vibration and buckling analysis to investigate and assess the performance of the two proposed four-node flat shell elements before some concluding remarks are presented.

4.2 Assumed strain smoothing flat shell finite element formulations

Based on the previous chapters, the smoothed membrane, bending and geometric strain fields of flat shell elements, MISQ20 and MISQ24, can be rewritten as

$$\tilde{\boldsymbol{\epsilon}}_m(\mathbf{x}_C) = \tilde{\mathbf{B}}_m^C(\mathbf{x}_C)\mathbf{q}, \tag{4.1}$$

$$\tilde{\boldsymbol{\epsilon}}_b(\mathbf{x}_C) = \tilde{\mathbf{B}}_b^C(\mathbf{x}_C)\mathbf{q}, \tag{4.2}$$

$$\tilde{\boldsymbol{\epsilon}}_g(\mathbf{x}_C) = \tilde{\mathbf{B}}_g^C(\mathbf{x}_C)\mathbf{q}, \tag{4.3}$$

where $\mathbf{q}_i = [u_i \;\; v_i \;\; w_i \;\; \theta_{xi} \;\; \theta_{yi} \;\; \theta_{zi}]^T$ is the nodal displacement vector; $\tilde{\mathbf{B}}_m^C$, $\tilde{\mathbf{B}}_b^C$, $\tilde{\mathbf{B}}_g^C$ the smoothed membrane gradient matrix, the smoothed bending gradient matrix and the smoothed geometric gradient matrix, respectively.

The smoothed membrane gradient matrix $\tilde{\mathbf{B}}_{mi}^C$ of the MISQ24 element is given as

$$\tilde{\mathbf{B}}_{mi}^C(\mathbf{x}_C) = \frac{1}{A_C}\sum_{m=1}^{4}\begin{pmatrix} \sum_{n=1}^{nG} w_n N_i(\mathbf{x}_{mn})n_x & 0 & 0 & 0 & 0 & 0 \\ 0 & \sum_{n=1}^{nG} w_n N_i(\mathbf{x}_{mn})n_y & 0 & 0 & 0 & 0 \\ \sum_{n=1}^{nG} w_n N_i(\mathbf{x}_{mn})n_y & \sum_{n=1}^{nG} w_n N_i(\mathbf{x}_{mn})n_x & 0 & 0 & 0 & 0 \end{pmatrix} + \frac{1}{A_C}\sum_{m=1}^{4}\begin{pmatrix} 0 & 0 & 0 & 0 & 0 & \sum_{n=1}^{nG} w_n Nx_i(\mathbf{x}_{mn})n_x \\ 0 & 0 & 0 & 0 & 0 & \sum_{n=1}^{nG} w_n Ny_i(\mathbf{x}_{mn})n_y \\ 0 & 0 & 0 & 0 & 0 & \sum_{n=1}^{nG} w_n Nx_i(\mathbf{x}_{mn})n_y + \sum_{n=1}^{nG} w_n Ny_i(\mathbf{x}_{mn})n_x \end{pmatrix} \tag{4.4}$$

while the smoothed membrane gradient matrix $\tilde{\mathbf{B}}^C_{mi}$ of the MISQ20 element is

$$\tilde{\mathbf{B}}^C_{mi}(\mathbf{x}_C) = \frac{1}{A_C}\sum_{m=1}^{4}\begin{pmatrix} N_i(\mathbf{x}^G_m)n_x & 0 & 0 & 0 & 0 & 0 \\ 0 & N_i(\mathbf{x}^G_m)n_y & 0 & 0 & 0 & 0 \\ N_i(\mathbf{x}^G_m)n_y & N_i(\mathbf{x}^G_m)n_x & 0 & 0 & 0 & 0 \end{pmatrix} l^C_m \tag{4.5}$$

The smoothed bending gradient matrix and the smoothed geometric gradient matrix of the MISQ20 and MISQ24 are the same and they are given as follows.

$$\tilde{\mathbf{B}}^C_{bi}(\mathbf{x}_C) = \frac{1}{A_C}\sum_{b=1}^{4}\begin{pmatrix} 0 & 0 & 0 & N_i(\mathbf{x}^G_b)n_x & 0 & 0 \\ 0 & 0 & 0 & 0 & N_i(\mathbf{x}^G_b)n_y & 0 \\ 0 & 0 & 0 & N_i(\mathbf{x}^G_b)n_y & N_i(\mathbf{x}^G_b)n_x & 0 \end{pmatrix} l^C_b, \tag{4.6}$$

$$\tilde{\mathbf{B}}^C_{gi}(\mathbf{x}_C) = \frac{1}{A_C}\sum_{g=1}^{4}\begin{pmatrix} \mathbf{0}_{4\times 6} & 0 & 0 & 0 & 0 \\ 0 & N_i(\mathbf{x}^G_g)n_x & 0 & 0 & 0 \\ 0 & N_i(\mathbf{x}^G_g)n_y & 0 & 0 & 0 \\ 0 & 0 & N_i(\mathbf{x}^G_g)n_x & 0 & 0 \\ 0 & 0 & N_i(\mathbf{x}^G_g)n_y & 0 & 0 \\ 0 & 0 & 0 & N_i(\mathbf{x}^G_g)n_x & 0 \\ 0 & 0 & 0 & N_i(\mathbf{x}^G_g)n_y & 0 \\ 0 & 0 & 0 & 0 & \mathbf{0}_{2\times 6} \end{pmatrix} l^C_g, \tag{4.7}$$

The shear strains of MISQ20 and MISQ24 elements are approximated with independent interpolation schemes in the natural coordinate system and given as follows.

$$\boldsymbol{\gamma} = \bar{\mathbf{B}}_s\mathbf{q}, \tag{4.8}$$

where

$$\bar{\mathbf{B}}_{si} = \mathbf{J}^{-1}\begin{pmatrix} 0 & 0 & N_{i,\xi} & b^{11}_i N_{i,\xi} & b^{12}_i N_{i,\xi} & 0 \\ 0 & 0 & N_{i,\eta} & b^{21}_i N_{i,\eta} & b^{22}_i N_{i,\eta} & 0 \end{pmatrix}, \tag{4.9}$$

and $\mathbf{J}$ is the Jacobian operator relating the natural coordinate derivatives to the local coordinate derivatives which is defined as

$$\mathbf{J} = \begin{bmatrix} x_{,\xi} & y_{,\xi} \\ x_{,\eta} & y_{,\eta} \end{bmatrix}. \tag{4.10}$$

Finally the smoothed element stiffness matrix of a flat shell laminated element in the local coordinate is obtained as

$$\tilde{\mathbf{k}} = \tilde{\mathbf{k}}_m + \tilde{\mathbf{k}}_{mb} + \tilde{\mathbf{k}}_{mb}^T + \tilde{\mathbf{k}}_b + \bar{\mathbf{k}}_s, \tag{4.11}$$

where

$$\begin{aligned}
\tilde{\mathbf{k}}_m^{MISQ20} &= \int_\Omega \tilde{\mathbf{B}}_m^T \mathbf{A} \tilde{\mathbf{B}}_m d\Omega = \sum_{C=1}^{2} \tilde{\mathbf{B}}_{mC}^T \mathbf{A} \tilde{\mathbf{B}}_{mC} A_C, && (4.12)\\
\tilde{\mathbf{k}}_m^{MISQ24} &= \int_\Omega \tilde{\mathbf{B}}_m^T \mathbf{A} \tilde{\mathbf{B}}_m d\Omega + \gamma \int_\Omega \mathbf{b}^T \mathbf{b} d\Omega \\
&= \sum_{C=1}^{1} \tilde{\mathbf{B}}_{mC}^T \mathbf{A} \tilde{\mathbf{B}}_{mC} A_C + \gamma \sum_{i=1}^{1}\sum_{j=1}^{1} w_i w_j \mathbf{b}^T \mathbf{b} \left|\mathbf{J}\right| d\xi d\eta, && (4.13)\\
\tilde{\mathbf{k}}_{mb}^{MISQ20} &= \int_\Omega \tilde{\mathbf{B}}_m^T \mathbf{B} \tilde{\mathbf{B}}_b d\Omega = \sum_{C=1}^{2} \tilde{\mathbf{B}}_{mC}^T \mathbf{B} \tilde{\mathbf{B}}_{bC} A_C, && (4.14)\\
\tilde{\mathbf{k}}_{mb}^{MISQ24} &= \int_\Omega \tilde{\mathbf{B}}_m^T \mathbf{B} \tilde{\mathbf{B}}_b d\Omega = \sum_{C=1}^{1} \tilde{\mathbf{B}}_{mC}^T \mathbf{B} \tilde{\mathbf{B}}_{bC} A_C, && (4.15)\\
\tilde{\mathbf{k}}_b &= \int_\Omega \tilde{\mathbf{B}}_b^T \mathbf{D} \tilde{\mathbf{B}}_b d\Omega = \sum_{C=1}^{2} \bar{\mathbf{B}}_{bC}^T \mathbf{D} \bar{\mathbf{B}}_{bC} A_C, && (4.16)\\
\bar{\mathbf{k}}_s &= \int_\Omega \bar{\mathbf{B}}_s^T \mathbf{C}_s \bar{\mathbf{B}}_s d\Omega = \sum_{i=1}^{2}\sum_{j=1}^{2} w_i w_j \bar{\mathbf{B}}_s^T \mathbf{C}_s \bar{\mathbf{B}}_s \left|\mathbf{J}\right| d\xi d\eta, && (4.17)
\end{aligned}$$

The smoothed element geometric stiffness matrix is obtained in a similar way in the local coordinate system as

$$\tilde{\mathbf{k}}_g = \sum_{C=1}^{1} \tilde{\mathbf{B}}_{gC}^T \hat{\boldsymbol{\sigma}}_0 \tilde{\mathbf{B}}_{gC} A_C, \tag{4.18}$$

where $\hat{\boldsymbol{\sigma}}_0$ is defined in Equation (3.26)

To deal with the effect of out-of-plane warp, the so-called rigid link correction of Taylor (1987) is employed to transformed the nodal variable into the projected flat element variable as in Equation (2.39) of Chapter 2 as follows.

$$\begin{aligned}
\tilde{\mathbf{k}}_{proj}^{MISQ20(24)} &= \mathbf{W} \tilde{\mathbf{k}}^{MISQ20(24)} \mathbf{W}^T, && (4.19)\\
\tilde{\mathbf{k}}_{g_{proj}} &= \mathbf{W} \tilde{\mathbf{k}}_g \mathbf{W}^T. && (4.20)
\end{aligned}$$

The local corrected warping element stiffness matrices are then transformed to the global coordinate system as

$$\tilde{\mathbf{K}}^{MISQ20(24)}_{global} = \mathbf{R}^T \tilde{\mathbf{k}}^{MISQ20(24)}_{proj} \mathbf{R}, \tag{4.21}$$

$$\tilde{\mathbf{K}}_{g_{global}} = \mathbf{R}^T \tilde{\mathbf{k}}_{g_{proj}} \mathbf{R}, \tag{4.22}$$

where $\mathbf{W}$, $\mathbf{R}$ are defined in Equation (2.39) and Equation (2.42), respectively.

4.3 Numerical examples: Static analysis

In this section, several benchmark problems are presented to validate and demonstrate the performance of the MISQ20 and MISQ24 flat elements in linear-elastic static, free vibration and buckling analysis of shell structures. The performance of the developed elements is compared with that of a fairly complete set of other four-node shell elements in the literature. The list of shell elements used for comparison with the proposed elements is outlined in Table 4.1.

Table 4.1: List of shell elements used for comparison in the present study.

Name	Brief description
DKQ-4	4-node discrete Kirchoff quadrilateral element of Taylor (1987)
SRI-4	bilinear degenerated shell element, with selective reduced integration of Hughes and Liu (1981)
RSDS-4	bilinear resultant-stress degenerated-shell element, with uniform reduced integration and stability (Liu et al., 1986)
URI-4	4-node uniformly reduced integrated element (Belytschko et al., 1989)
QPH	quadrilateral shell element with physical hourglass control of Belytschko and Leviathan (1994)
IBRA-4	4-node shell element with drilling DOF developed by Ibrahimbegovic and Frey (1994)
MITC4	4-node fully integrated shell element based on assumed shear strain field of Dvorkin and Bathe (1984)
Mixed	bilinear element with mixed formulation for membrane and bending stress and full 2x2 quadrature of Simo et al. (1989)
MIN4T	4-node flat shell with drilling DOF via explicit Kirchhoff constrains (Liu et al., 2000)
NMS-4F	defect-free 4-node flat shell element with drilling DOF (Choi and Lee, 1999)
XSHELL41/42	4-node quasi-conforming flat shell element with DDOF (Kim et al., 2003)
QC5D-SA	4-node flat shell with drilling DOF and 5-point quadrature by Groenwold and Slander (1995)
SHELL63	4-node thin shell element with drilling DOF in ANSYS (1998)
T029	4-node Mindlin shell element in Samtech (2003)
HBQ8	8-node quadrilateral assumed-stress hybrid shell element (Darilmaz and Kumbasar, 2006)
KUMBA	8-node curved shell element with reduced integration (Kumbasar and Aksu, 1995)

4.3.1 Scordelis-lo (Barrel vault) roof

The Scordelis-Lo roof provides one of the standard tests to assess the performance of shell elements in a combined bending-membrane problem with the membrane action being dominant. The roof is modelled as a short cylinder shell, loaded by self-weight and supported by rigid diaphragms at the curved edges while the straight edges are free. Geometry, material data and boundary conditions of the problem are shown in the Figure 4.1.

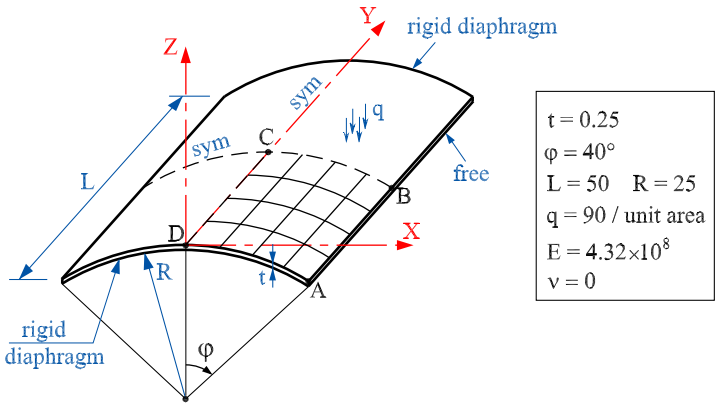

Figure 4.1: The Scordelis-Lo roof: Geometry and material data.

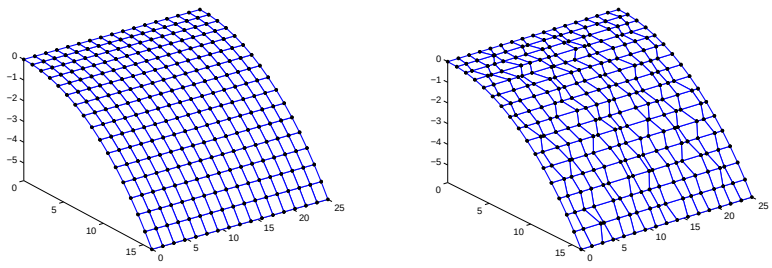

(a) (b)

Figure 4.2: The Scordelis-Lo roof: (a) typical regular mesh and (b) irregular mesh.

According to MacNeal and Harder (1985), the theoretical value for the vertical deflection at the center of the free edge is 0.3086, but a slightly lower value 0.3024 seems to have become the reference solution for many publications. In this study the latter value is used to normalize numerical results. Taking advantage of symmetry, only a quadrant of the roof is discretized and analyzed. Two typical types

of mesh, namely $N \times N$ uniform elements and $N \times N$ distorted elements are shown in Figure 4.2.

Table 4.2: The Scordelis-Lo roof: displacements at point B, normalized by 0.3024.

Model	Mesh			
	4×4	8×8	12×12	16×16
MISQ20 (regular mesh)	1.0776	1.0180	1.0137	1.0105
MISQ20 (irregular mesh)	1.0657	1.0193	1.0171	1.0097
MISQ24 (regular mesh)	1.1912	1.0420	1.0154	1.0063
MISQ24 (irregular mesh)	1.1925	1.0422	1.0155	1.0066
SRI-4	0.964	0.984	–	0.999
RSDS-4	1.201	1.046	–	1.010
T029 (SAMCEF)	0.976	0.986	–	0.993
NMS-4F	1.047	1.005	–	0.997
QPH	0.940	0.980	–	1.010
DKQ-4	1.048	1.005	–	0.996
IBRA-4	1.047	1.005	–	0.997
URI-4	1.219	1.054	–	1.017

Table 4.2 shows the normalized deflections at the midpoint of the free edge (point B) obtained by the present elements with different meshes, together with those of other 4-node shell elements available in the literature. The results show that the present elements, MISQ20 and MISQ24, perform quite well in both types of mesh in comparison with the reference solution and other shell elements.

The numerical convergence is also plotted in Figure 4.3. As can be seen, the convergence rate of the present elements for both types of mesh is nearly equivalent. It is also observed that the MISQ24's rate of convergence is slightly slower than that of the MISQ20 element, the SRI-4 element, the MITC4 element and the Mixed element. However, it is interesting to note that the MISQ24 element appears to converge monotonically to the reference solution even with a highly distorted mesh. Convergence rates of the present elements in this problem indeed

appear satisfactory.

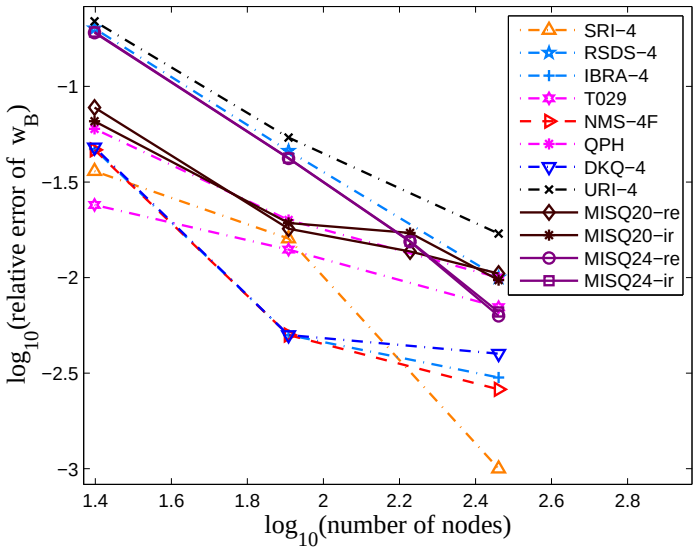

Figure 4.3: The Scordelis-Lo roof: Convergence behaviour of normalized displacements at point B.

4.3.2 Pinched cylinder with end diaphragms

In this section, a pinched cylinder with end diaphragms is considered. This problem is regarded as one of the most severe tests for the performance of the element to present both in-extensional bending and complex membrane states of stress. The cylinder is supported by rigid diaphragms at both ends and pinched with two opposite radial concentrated loads at the middle of the length as shown in Figure 4.4 where the geometrical and material properties of the cylinder are also depicted.

Owing to symmetry, only one octant of cylinder is modelled with a mesh of uniform elements as well as distorted elements. Two typical meshes used in the analysis are shown in Figure 4.5.

The theoretical solution of the radial deflection at the loading point (point C) given by Belytschko and Leviathan (1994) is 1.8248×10^{-5} for isotropic material. The present numerical results with meshes of 4×4, 8×8, 12×12 and 16×16 elements are compared versus other solutions from the literature using 4–node

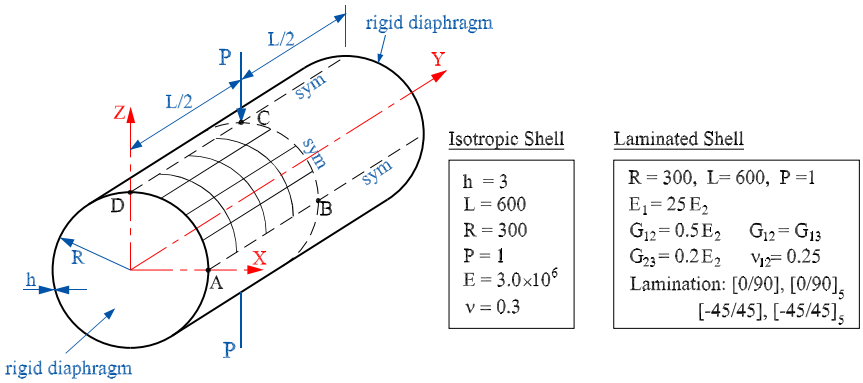

Figure 4.4: A pinched cylinder with end diaphragms: Geometry and material data.

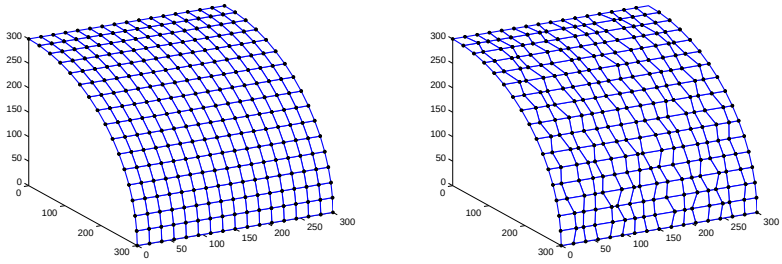

(a) (b)

Figure 4.5: A pinched cylinder with end diaphragms: (a) typical regular mesh and (b) irregular mesh.

quadrilateral elements. All the numerical results, normalized with respect to the analytical value, are given in the Table 4.3. It is observed that the performance of the present elements, MISQ20 and MISQ24, are in good agreement with the analytic solution for both types of mesh and the MISQ24 performance is better than other shell elements considered in this study.

The convergence behaviours of all cited elements are also plotted together in Figure 4.6. As can be seen, the MISQ24 elements yield the most rapidly converging solutions to theoretical value. In the case of highly distorted elements, it is particularly interesting to point out that the MISQ24 elements faces no difficulties converging at the same rate as some of the most efficient contemporary four-node shell elements using uniform elements. The MISQ24's convergence rate is slightly

Table 4.3: An isotropic pinched cylinder with end diaphragms: normalized displacements at point C. Normalized by: 1.8248×10^{-5}

Model	Mesh			
	4×4	8×8	12×12	16×16
MISQ20 (regular)	0.4418	0.7878	0.9022	0.9482
MISQ20 (irregular)	0.4148	0.7679	0.9115	0.9541
MISQ24 (regular)	0.6416	0.9411	0.9921	1.0018
MISQ24 (irregular)	0.6477	0.9375	0.9915	1.0010
MIN4T	0.5040	0.8374	–	0.9619
XSHELL41	0.625	0.926	–	0.995
XSHELL42	0.625	0.918	–	0.992
SRI-4	0.373	0.747	–	0.935
RSDS-4	0.469	0.791	–	0.946
SHELL63(ANSYS)	0.6302	0.9371	–	1.0029
QC5D-SA	0.3759	0.7464	–	0.9300
QPH	0.370	0.740	–	0.930
IBRA-4	0.3704	0.7367	–	0.9343
DKQ-4	0.6357	0.9459	–	1.0160
MICT4	0.3699	0.7398	–	0.9300
Mixed	0.3989	0.7628	–	0.9349

better than the SHELL63 element used in the commercial finite element software ANSYS for this problem.

The pinched circular cylinder problem is also analyzed when the shell is made of laminated composite material with cross-ply and angle-ply lay-ups as shown in Figure 4.4. Table 4.4 reports the normalized deflections for 2-layer and 10-layer antisymmetric cross-ply $[0^0/90^0/0^0/...]$ and angle-ply $[-45^0/45^0/-45^0/...]$ laminated shell for different radius-to-thickness ratio, $S = R/h$. The present

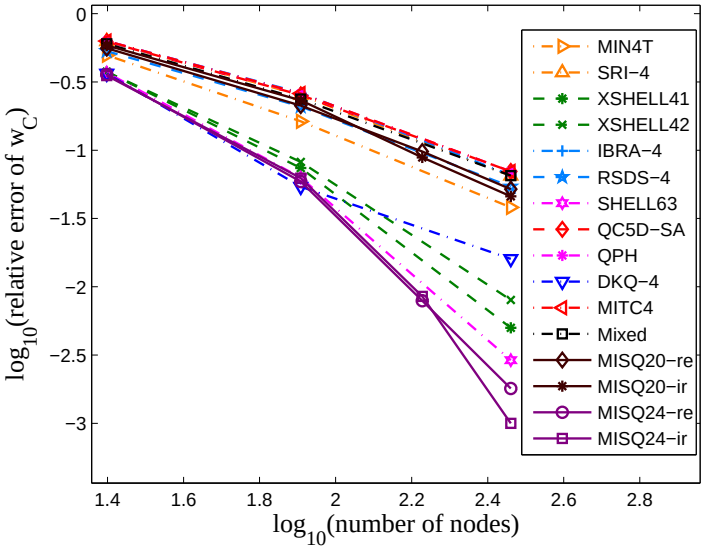

Figure 4.6: An isotropic pinched cylinder with end diaphragms: Convergence behaviour.

results are obtained using 32×32 uniform mesh. It can be seen that the MISQ24 solutions are in good agreement with the FSDT solutions of Reddy (2004b) while the MISQ20 solutions are not in as good agreement as the MISQ24 is.

Table 4.4: A laminated composite pinched cylinder problem: normalized displacements at point C, $w_c^* = 10w_c(\frac{a}{2}, \frac{a}{2})E_1h^3/(PR^2)$

$S = R/h$	Model	Lay-up			
		$[0^0/90^0]$	$[-45^0/45^0]$	$[0^0/90^0]_5$	$[-45^0/45^0]_5$
20	MISQ20 (32×32)	4.4678	5.4868	3.7960	4.0132
	MISQ24 (32×32)	6.0162	5.7883	4.2020	3.5418
	Reddy (2004b)	6.0742	5.2275	4.2118	3.6457
50	MISQ20 (32×32)	1.7988	2.1124	1.6559	1.3496
	MISQ24 (32×32)	2.3604	2.2222	1.4773	1.1363
	Reddy (2004b)	2.3756	2.2283	1.4527	1.2986
100	MISQ20 (32×32)	0.8162	1.0500	0.4895	0.7084
	MISQ24 (32×32)	1.2536	1.3153	0.7566	0.6238
	Reddy (2004b)	1.2450	1.3065	0.7405	0.7373

4.3.3 Pinched hemispherical shell with an 18^0 hole

Figure 4.7 shows the hemispherical shell with an 18^0 hole subjected to concentrated diametrical loads of opposite signs every 90^0 in the equatorial plane. This problem is a very useful example to check the ability of the element to handle rigid body rotation about the normal to the shell surface and the inextensible bending modes. Shell elements with membrane locking cannot solve correctly this problem. Taking advantage of symmetry, a quadrant of the shell is modelled with uniform elements.

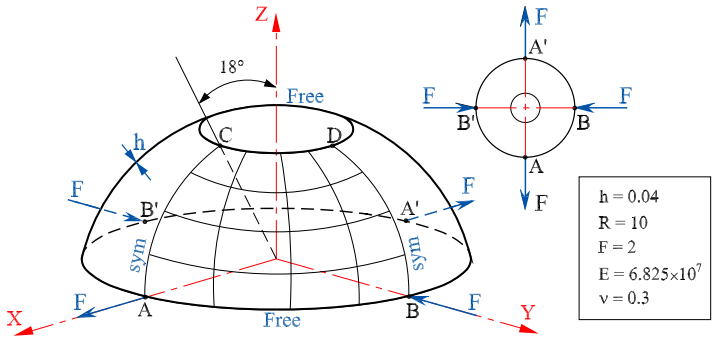

Figure 4.7: A pinched hemispherical shell with 18^0 hole: Geometry and material data.

Table 4.5 shows numerical results for the radial displacement at the loading point (u_A) for different elements. The values are normalized with the theorical value of 0.094 reported by MacNeal and Harder (1985). All normalized radial displacements are also plotted in Figure 4.8 to assess the convergence behaviour of each element. It can be seen that the present elements yield the most monotonic convergence towards the reference solution while some other elements do not. The plot also shows that the present elements, MISQ20 and MISQ24, exhibit an excellent accuracy with a 16×16 mesh. No membrane locking is detected and the performance of the present elements in this problem is remarkable.

Table 4.5: A hemispherical shell with an 18^0 hole: displacements at point A, normalized by 0.0940

Model	Mesh			
	4×4	8×8	12×12	16×16
MISQ20 (regular)	0.8765	0.9778	0.9889	0.9918
MISQ24 (regular)	0.7670	0.9798	0.9954	0.9960
MIN4T	0.136	0.651	0.897	–
IBRA-4	0.999	0.991	–	0.990
XSHELL41	1.027	1.001	–	0.990
XSHELL42	0.266	0.652	–	0.960
QC5D-SA	0.386	0.951	–	0.991
DKQ-4	0.897	0.999	–	0.995
NMS-4F	0.935	0.989	–	0.991
Mixed	0.993	0.987	–	0.988

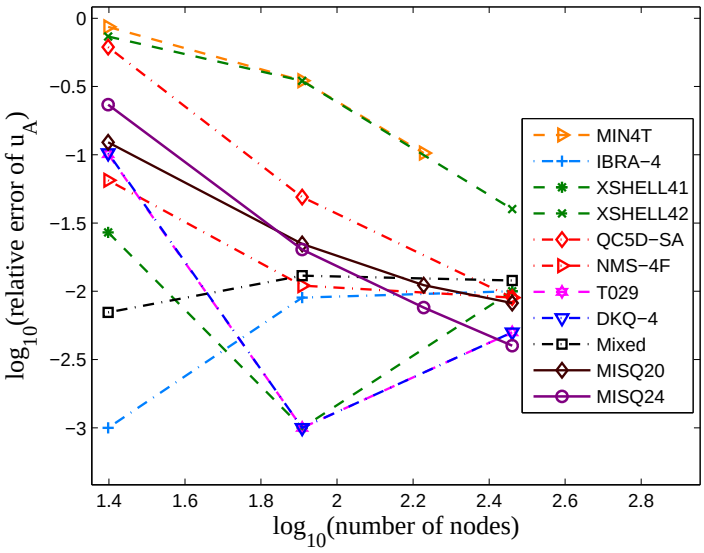

Figure 4.8: A pinched hemispherical shell with an 18^0 hole: Convergence behaviour of radial displacements at point A.

4.3.4 Shallow spherical shells

A shallow spherical shell is considered in this section. The shell is simply supported on four sides and subjected to uniform loading. The geometric and material parameters are shown in Figure 4.9. By making use of symmetry of geometry and boundary conditions, only one quadrant of the shell is analysed with 8×8, 12×12 and 16×16 elements.

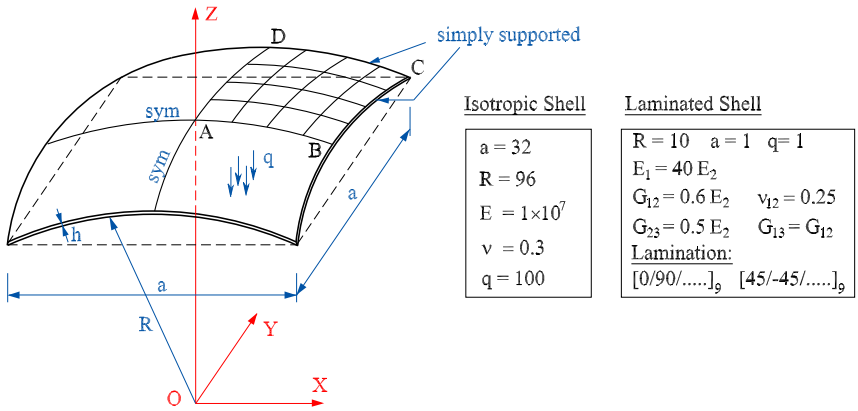

Figure 4.9: A shallow spherical shell: Geometry and material data.

The comparison of vertical deflection w_A at the center point A of an isotropic shell with various thickness h is given in Table 4.6 together with the plot in Figure 4.10. It can be seen that the accuracy of the present method compares very favorably with other high-order elements and it is slightly insensitive to thickness variations.

A laminated composite shallow spherical shell is also studied. Nine-layer cross-ply $[(0^0/90^0)_4/0^0]$ and angle-ply $[(45^0/-45^0)_4/45^0]$ laminates are considered with span-to-thickness ratio $a/h = 100$ and 1000. Similar to the isotropic case, the present elements converge quickly with mesh refinement and compare favorable with analytic solutions. The computed results are reported in Table 4.7 together with other numerical results and analytic solutions.

Table 4.6: Isotropic shallow spherical shell: vertical deflection $w_A \times 10^3$ at the center point A with various thickness h.

Model	Thickness h			
	0.32	1.6	3.2	6.4
MISQ20 (8×8)	309.291	51.708	12.012	2.127
(12×12)	311.776	51.032	11.742	2.068
(16×16)	312.644	50.706	11.619	2.042
MISQ24 (8×8)	308.881	51.698	12.000	2.123
(12×12)	311.931	51.021	11.734	2.066
(16×16)	312.437	50.698	11.616	2.042
HBQ8	310.382	48.671	10.903	1.917
KUMBA	330.469	51.583	11.482	1.929
Analytic (Reddy, 1984b)	313.860	49.695	11.265	1.976

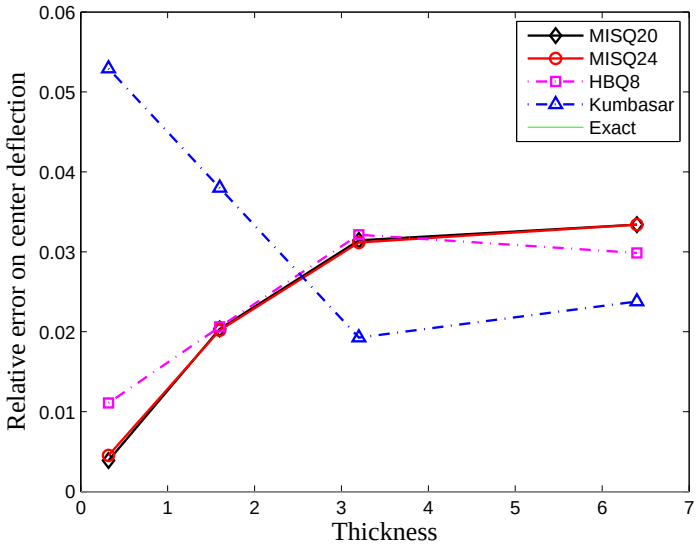

Figure 4.10: Isotropic shallow spherical shell: effect of thickness on the accuracy of central deflection.

Table 4.7: Laminated composite shallow spherical shells: Convergence of central deflection $w_A \times 10^{-3}$ at the center point A with various span-to-thickness a/h.

a/h	Model	Mesh	Lay-up	
			$[(0^0/90^0)_4/0^0]$	$[(45^0/-45^0)_4/45^0]$
100	MISQ20	8×8	2.9311	0.5436
		12×12	2.8407	0.5395
		16×16	2.8005	0.5369
	MISQ24	8×8	2.7117	0.5163
		12×12	2.6914	0.5122
		16×16	2.6808	0.5098
	To and Wang (1998)		2.717	0.5259
	Park et al. (2006)]		2.701	0.5337
	Somashekar et al. (1987)		2.727	0.5270
	Analytic (Reddy, 1984a)		2.717	0.5170
1000	MISQ20	8×8	0.0595	0.0116
		12×12	0.0593	0.0117
		16×16	0.0592	0.0116
	MISQ24	8×8	0.0586	0.0063
		12×12	0.0587	0.0063
		16×16	0.0588	0.0063
	To and Wang (1998)		0.0588	0.0101
	Park et al. (2006)]		0.0591	0.0105
	Somashekar et al. (1987)		0.0599	0.0088
	Analytic (Reddy, 1984a)		0.0592	0.0105

4.3.5 A hypar shell

A hyperbolic paraboloid shell or hypar shell (Figure 4.11) as proposed in Gruttmann and Wagner (2005) is studied. This problem is used to assess the performance of elements in dealing with warped geometry and the effect of membrane locking. The geometry of the hypar shell is defined by the expression $z = \frac{xy}{8L}$. The shell is subjected to a uniform load p_z in the vertical direction with the following boundary conditions:

$w(-L/2, y) = w(L/2, y) = w(x, -L/2) = w(x, L/2) = 0;$

$u_A = u_B = 0;\ v_C = v_D = 0.$

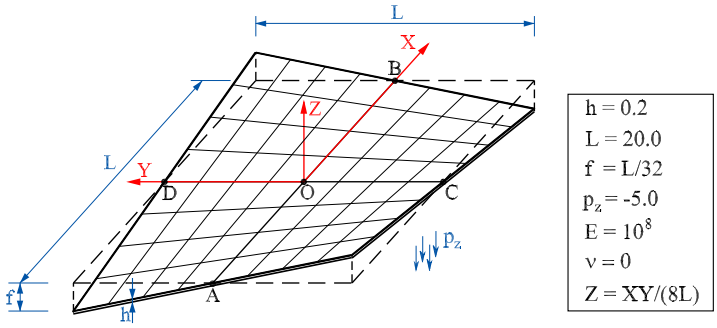

Figure 4.11: A hypar shell: Geometry and material data.

The entire hypar shell is modelled and analyzed with meshes of uniform elements. Table 4.8 presents the computed vertical displacement at the center point with different models. Numerical results indicate that the behaviour of the present elements is in a close agreement with other reference solutions. It is observed that the present elements does not show any sign of membrane locking. The MISQ24 element demonstrates an excellent performance where the displacement prediction error for the coarse mesh of 8×8 elements is about 0.609%.

The displacements presented in Table 4.8 are also shown graphically in Figure 4.12 to assess the convergence with mesh refinement. As can be seen from the plot, the present elements converge quickly with mesh refinement. The performance of MISQ24 element is superior to that of the MISQ20 element and slightly better than those of other elements cited here for this problem.

Table 4.8: A hypar shell: central deflection w_0 for different elements

Model	Mesh				
	4×4	8×8	16×16	32×32	64×64
MISQ20	3.320	4.190	4.447	4.509	4.536
MISQ24	4.500	4.572	4.589	4.594	4.601
DKQ-4	4.51	4.55	4.56	–	4.57
Sauer (1998)	4.51	4.56	4.58	–	4.60
Gruttmann and Wagner (2005)	4.52	4.56	4.58	–	4.60
Analytic (Duddeck, 1962)					4.6

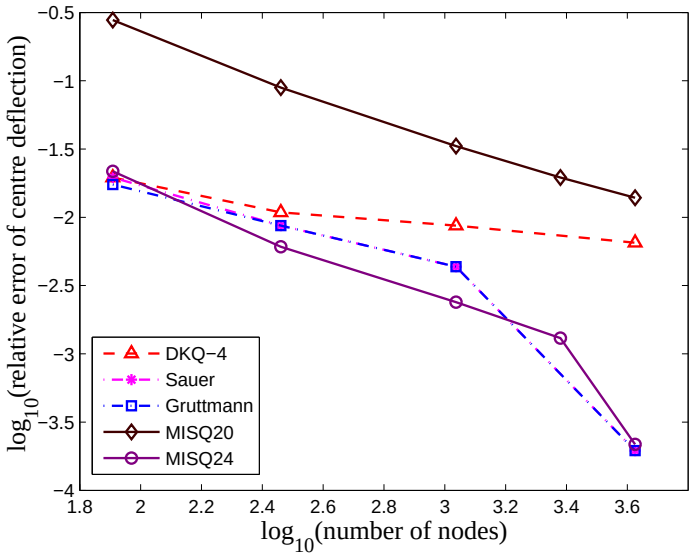

Figure 4.12: A hypar shell: normalized central deflections with mesh refinement.

4.3.6 Partly clamped hyperbolic paraboloid shells

The problem considered in this section is that of a hyperbolic paraboloid shell, clamped along one side and free on three edges and loaded by self-weight. This is a pure bending dominated problem and known to be a very hard test for locking behaviour as suggested in Chapelle and Bathe (1998); Bathe et al. (2000). The

shell geometry is describe by the following equation:

$$z = x^2 - y^2; (x, y) \in \left[-\frac{L}{2}; \frac{L}{2}\right] \tag{4.23}$$

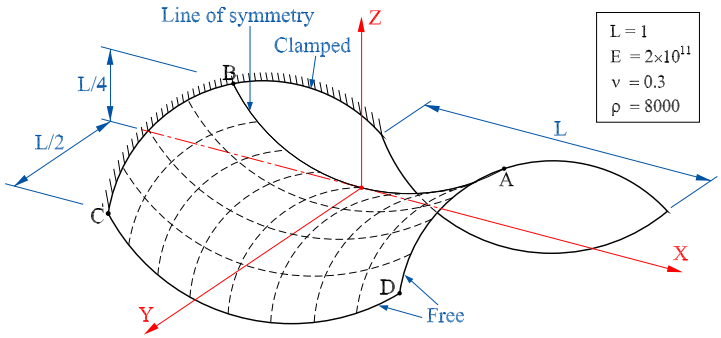

Figure 4.13: A partly clamped hypar shell: Geometry and material data.

One symmetric half of the shell, with uniform mesh patterns of $N \times N/2$ elements, is analyzed in the present work. Two typical meshes of 16×8 and 32×16 uniform elements are shown in Figure 4.14. To the author's knowledge, there is no analytic solution for this problem and the reference solution for displacement and strain energy obtained by Bathe et al. (2000) with a refined mesh of high-order element MITC16, are used for comparison. Two thickness-to-length (t/L) ratios of 1/100, 1/1000 are adapted from the proposal of Bathe et al. (2000) to check locking behaviour of the present elements MISQ20 and MISQ24.

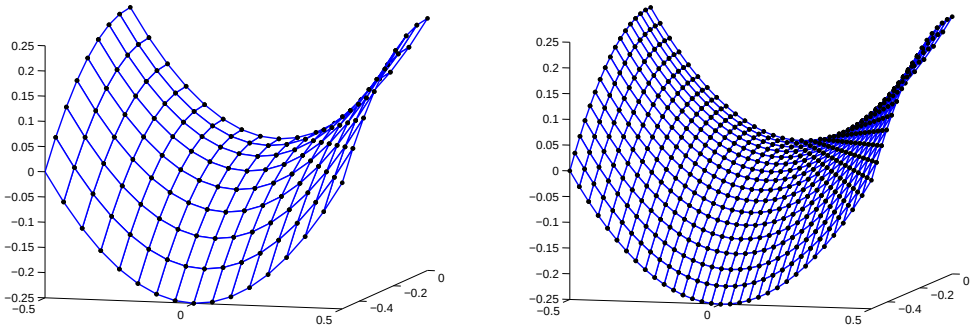

(a) (b)

Figure 4.14: A partly clamped hypar shell: Typical meshes (a) a mesh of 16×8 uniform elements and (b) a mesh of 32×16 uniform elements.

Figure 4.15 and Figure 4.16 demonstrate the convergence of displacement and strain energy. It can be seen that the proposed element perform well and are insensitive to the decrease in thickness. It is observed that the convergence in the case of $t/L = 1/1000$ is slower than that for $h/L = 1/100$.

Table 4.9: A partly clamped hyperbolic paraboloid shell: deflection at point A with mesh refinement.

Mesh	$h/L = 1/100$			$h/L = 1/1000$		
	MISQ20	MISQ24	MICT16	MISQ20	MISQ24	MITC16
8×4	8.2866E-5	9.9088E-5	–	6.5826E-3	7.1209E-3	–
16×8	9.0138E-5	9.4681E-5	–	6.3349E-3	6.7129E-3	–
32×16	9.3317E-5	9.3665E-5	–	6.3467E-3	6.4677E-3	–
48×24	9.4160E-5	9.3501E-5	9.3355E-5	6.3691E-3	6.4264E-3	6.3941E-3

Table 4.10: A partly clamped hyperbolic paraboloid shell: strain energy with mesh refinement

Mesh	$h/L = 1/100$			$h/L = 1/1000$		
	MISQ20	MISQ24	MICT16	MISQ20	MISQ24	MITC16
8×4	1.4742E-3	1.8028 E-3	–	1.1380E-2	1.2512E-2	–
16×8	1.6113E-3	1.7073E-3	–	1.0903E-2	1.1633E-2	–
32×16	1.6744E-3	1.6858E-3	–	1.0925E-2	1.1155E-2	–
48×24	1.6917E-3	1.6822E-3	1.6790E-3	1.0963E-2	1.1077E-2	1.1013E-2

4.3.7 Pre-twisted cantilever beams

A pre-twisted cantilever beam shown in Figure 4.17 is considered in this section. The cantilevered beam undergoes 90^0 of twist over its length. Two load cases are studied: a unit shear force P in the width direction and a unit shear force Q in the thickness direction. This example, proposed by MacNeal and Harder (1985),

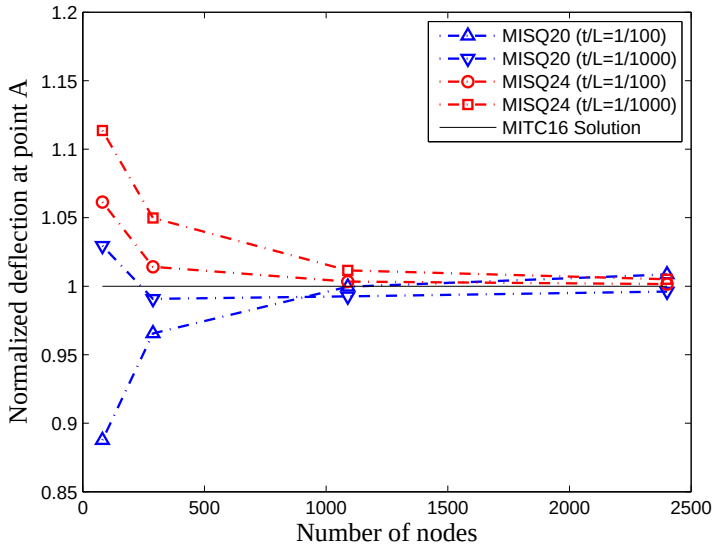

Figure 4.15: A partly clamped hypar shell: Convergence of the displacement at point A.

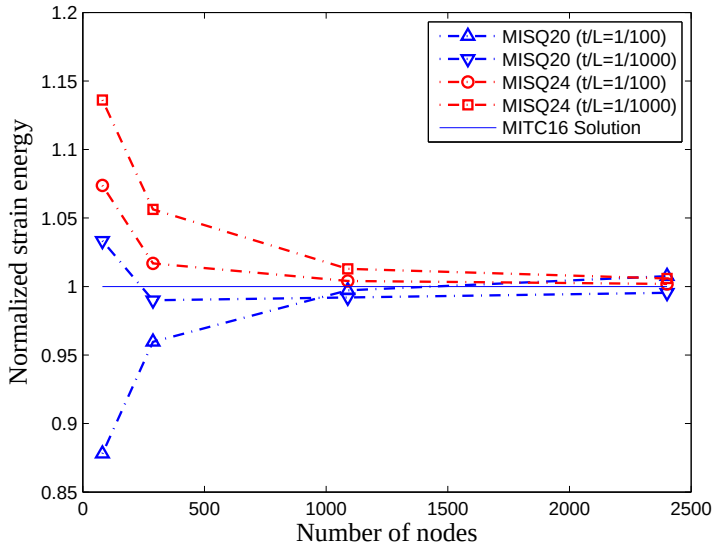

Figure 4.16: A partly clamped hypar shell: Convergence of the strain energy.

is an excellent test for assessing the element performance when the geometry configuration is warped. In the case of isotropic material, the theoretical deflections at the beam's tip are 0.00542 (in-plane shear P) and 0.001754 (out-of-plane shear Q), respectively, for the two load cases.

Typical meshes used in the present calculation are shown in Figure 4.18. Ta-

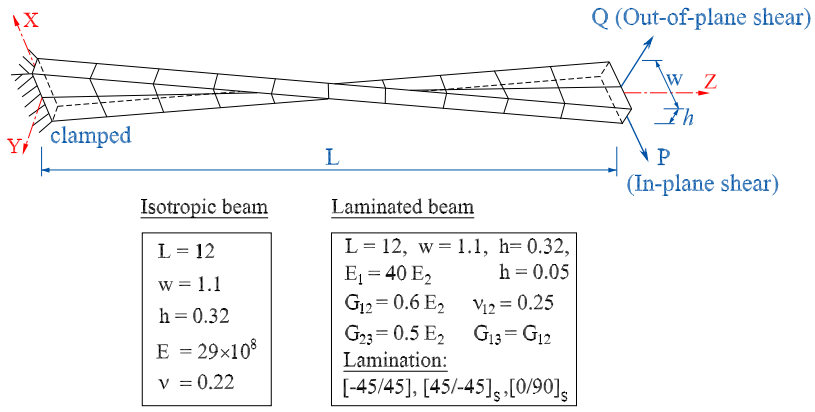

Figure 4.17: Pre-twisted cantilever beams: geometry and material data.

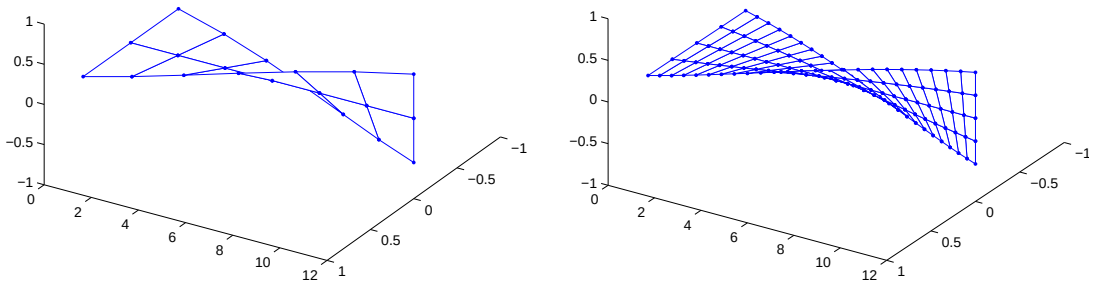

(a) (b)

Figure 4.18: The pre-twisted cantilever beam: (a) typical regular mesh of 2×6 elements and (b) 4×24 elements.

ble 4.11 presents the obtained results with mesh refinement together with other numerical solutions in the literature. It is observed that the MISQ20 converges very slowly and does not appear to work well in a warped configuration. However, it still yield a better results than the RSDS-4 element for both load cases. In contrast to MISQ20 performance, the MISQ24 element has no difficulties in dealing with warped geometries. Its performance is found to be superior to that of MISQ20 and better than that of some other elements cited here such as XSHELL42, RSDS-4 and MITC4 elements. It is also observed that both MISQ20 and MISQ24 have a slow convergence for the out of plane case but they still give reasonable and better results with 4x24 elements than those of XSHELL42 and RSDS-4 elements.

A laminated composite pre-twisted beam is also analyzed with cross-ply and angle-

ply lay-ups. The numerical results are tabulated in Table 4.12 and Table 4.13 for a thick ($h = 0.32$) and a thin beam ($h = 0.05$) respectively. Once again, it is found that the results obtained with MISQ24 elements are in closer agreement with QC5D-SA results than those of MISQ20 elements for both thin and thick beam except for the case of the $[45^0/-45^0]$ layup under in-plane loading.

Table 4.11: Isotropic pre-twisted cantilever beam: tip displacements, normalized by 5.424×10^{-2} for in-plane displacements and by 1.754×10^{-2} for out-of-plane displacements.

Load case	Model	Mesh		
		2×6	4×12	4×24
In-plane	MISQ20	0.418	1.357	1.358
	MISQ24	0.979	1.006	1.008
	DKQ-4	–	–	0.996
	XSHELL41	–	–	0.997
	XSHELL42	–	–	1.228
	RSDS-4	–	–	1.411
	MITC4	–	–	0.996
Out-of plane	MISQ20	0.462	1.215	1.261
	MISQ24	0.811	0.928	1.015
	DKQ-4	–	–	0.998
	XSHELL41	–	–	0.999
	XSHELL42	–	–	1.473
	RSDS-4	–	–	1.361
	MITC4	–	–	0.974

Table 4.12: Thick laminated pre-twisted beam: Convergence of tip displacements and comparison with other solutions.

Load case	Model	Lay-up		
		$[-45^0/45^0]$	$[45^0/-45^0]_s$	$[0^0/90^0]_s$
In-plane	MISQ20 (2×6)	0.0271	0.0265	0.0121
	(4×12)	0.0771	0.0763	0.0448
	(4×24)	0.0757	0.0747	0.0448
	MISQ24 (2×6)	0.0955	0.0864	0.0351
	(4×12)	0.0983	0.0885	0.0356
	(4×24)	0.0983	0.0886	0.0356
	QC5D-SA (4×24)	0.0802	0.0850	0.0354
Out-of plane	MISQ20 (2×6)	0.0126	0.0117	0.0033
	(4×12)	0.0253	0.0241	0.0107
	(4×24)	0.0260	0.0247	0.0111
	MISQ24 (2×6)	0.0267	0.0244	0.0068
	(4×12)	0.0307	0.0281	0.0083
	(4×24)	0.0339	0.0310	0.0091
	QC5D-SA (4×24)	0.0286	0.0298	0.0095

Table 4.13: Thin laminated pre-twisted beam: Convergence of tip displacements and comparison with other solutions.

Load case	Model	Lay-up		
		$[-45^0/45^0]$	$[45^0/-45^0]_s$	$[0^0/90^0]_s$
In-plane	MISQ20 (2×6)	12.349	10.512	4.349
	(4×12)	18.020	17.478	7.985
	(4×24)	17.832	17.212	7.964
	MISQ24 (2×6)	17.976	15.576	8.399
	(4×12)	23.448	19.982	9.191
	(4×24)	23.787	20.359	9.224
	QC5D-SA (4×24)	17.54	19.80	9.170
Out-of plane	MISQ20 (2×6)	3.716	3.063	1.619
	(4×12)	6.559	6.325	3.458
	(4×24)	6.282	6.078	3.389
	MISQ24 (2×6)	3.337	3.051	1.377
	(4×12)	5.247	4.844	1.841
	(4×24)	5.896	5.446	2.048
	QC5D-SA (4×24)	5.474	5.909	2.243

4.4 Numerical examples: Free vibration and Buckling analysis

4.4.1 Free vibration of cross-ply laminated cylindrical shells

The cross-ply laminated cylindrical panel with a radius $R = 100$, a side length $L = 20$ and an angle $\varphi = 0.1$ radian, subjected to simply supported boundaries is studied. The total thickness of the panel is $h = 0.2$. All layers have equal thickness and are made of the same material: $E_1/E_2 = 25$, $G_{12} = G_{13} = 0.5E_2$, $G_{23} = 0.2E_2$, $\nu_{12} = \nu_{13} = \nu_{23} = 0.25$, $\rho = 1$. The SCFs are assumed to be 5/6. Three kinds of lay-up sequence, namely $[0^0/90^0]$, $[0^0/90^0/0^0]$ and $[0^0/90^0/90^0/0^0]$, are considered. Considering only doubly symmetric modes, a quadrant designated as ABCD as shown in Figure 4.19 is modelled. The $4 \times 4, 6 \times 6$ and 8×8 meshes are used in computing the fundamental frequencies associated with the doubly symmetric modes.

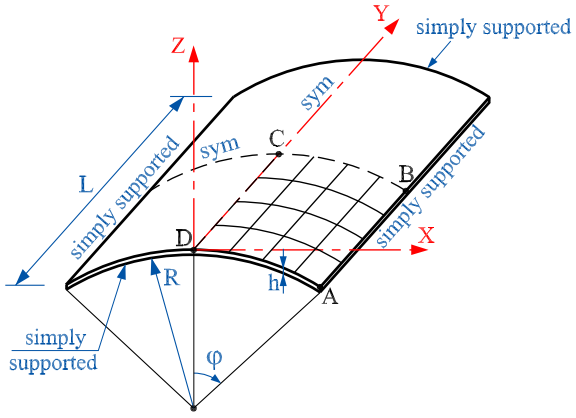

Figure 4.19: Geometry and discretization of laminated cylindrical shells.

The convergence study of the normalized fundamental frequency is presented in Table 4.14. The present results are also compared with other numerical solutions such as results of Liu and To (2003) using layer-wise shell element, of Jayasankar et al. (2007) using 9-node degenerated shell element and the analytical solution by Reddy (1984a).

It can be seen that the accuracy of the present elements, MISQ20 and MISQ24, are

compared very favourably with other elements and the method is also convergent with mesh refinement. The present elements can provide accurate prediction of the solution with much reduced degrees of freedom and their performances with respect to analytical solution are excellent as measured by relative errors shown in Table 4.14.

Table 4.14: Simply supported cross-ply cylindrical shells: Convergence of normalized fundamental frequencies $\omega^* = (\omega L^2/h)\sqrt{\rho/E_2}$ for doubly symmetric modes and comparison with other solutions.

Model	Mesh	Lay-up		
		$[0^0/90^0]$	$[0^0/90^0/0^0]$	$[0^0/90^0/90^0/0^0]$
MISQ20	4×4	17.061	20.575	20.694
	6×6	16.833	20.340	20.461
	8×8	16.736	20.240	20.367
		(0.408%)	(-0.452%)	(0.029%)
MISQ24	4×4	17.099	20.585	20.703
	6×6	16.873	20.367	20.481
	8×8	16.794	20.292	20.404
		(0.756%)	(-0.197%)	(0.211%)
LW theory (Liu and To, 2003)	8×8	17.390	20.960	20.960
		(4.332%)	(3.089%)	(2.942%)
Jayasankar et al. (2007)	5×5	17.7	–	–
		(6.192%)	–	–
Analytic (Reddy, 1984a)		16.668	20.332	20.361

4.4.2 Free vibration of angle-ply laminated cylindrical shells

To assess the effect of fibre orientation on fundamental frequencies, the cylindrical shell of the previous example is reanalyzed with 2-layer $[\theta^0/-\theta^0]$ angle-ply lamination. The fibre angle θ is varied from 0^0 to 60^0. The span-to-thickness ratio of the shell is $L/h = 20$ and the shallowness angle $\varphi = 22.5^0$. All layers have equal thickness and are made of the same material: $E_1/E_2 = 40, G_{12} = G_{13} =$

$0.6E_2, G_{23} = 0.5E_2, \nu_{12} = \nu_{13} = \nu_{23} = 0.25, \rho = 1.$

Table 4.15 reports the normalized fundamental frequencies for doubly symmetric modes obtained by the present elements together with other solutions such as the parabolic shear deformation theory (PSDT) of Soldatos (1987), the generalized differential quadrature (GDQ) of Loy et al. (1999) and the 18-node solid element of Rattanawangcharoen et al. (2005). The present results in general indicate a good agreement with other solution cited here for different fibre angle θ. It is also observed that the fundamental frequency increases with increasing fibre angle.

Table 4.15: Simply supported angle-ply cylindrical shells: Convergence of normalized fundamental frequencies $\omega^* = (\omega L^2/h)\sqrt{\rho/E_2}$ for doubly symmetric modes and comparison with other solutions.

Model	Mesh	θ				
		0	15	30	45	60
MISQ20	4×4	23.559	22.748	33.827	51.181	67.108
	6×6	23.409	22.968	34.478	51.049	65.165
	8×8	23.355	23.007	34.337	49.866	62.657
MISQ24	4×4	23.549	22.318	32.497	50.080	60.769
	6×6	23.379	22.759	33.742	50.376	62.995
	8×8	23.321	22.611	33.214	49.387	58.523
Rattanawangcharoen et al. (2005)		23.23	27.93	30.06	48.38	51.29
GDQ (Loy et al., 1999)		24.281	21.861	31.829	52.392	74.625
PSDT (Soldatos, 1987)		22.85	–	31.42	51.73	54.16

4.4.3 Free vibration of cross-ply laminated spherical shells

A clamped nine-layered cross-ply $[0^0/90^0/0^0/90^0/0^0/90^0/0^0/90^0/0^0]$ laminated spherical panel as shown in Figure 4.20 is considered. The panel has a radius $R = 10$ and a side length $a = 1$. The total thickness of the panel is $h = 0.01$. All layers are of equal thickness and same material properties: $E_1 = 2.0685 \times 10^{11}$, $E_2 = E_1/40$, $G_{12} = G_{13} = 0.5E_2$, $G_{23} = 0.6E_2$, $\nu_{12} = 0.25$ and $\rho = 1605$. The SCFs

are $k_1^2 = k_2^2 = 5/6$. Three different finite element meshes are used $6 \times 6, 10 \times 10$, and 14×14 for modelling the full shell.

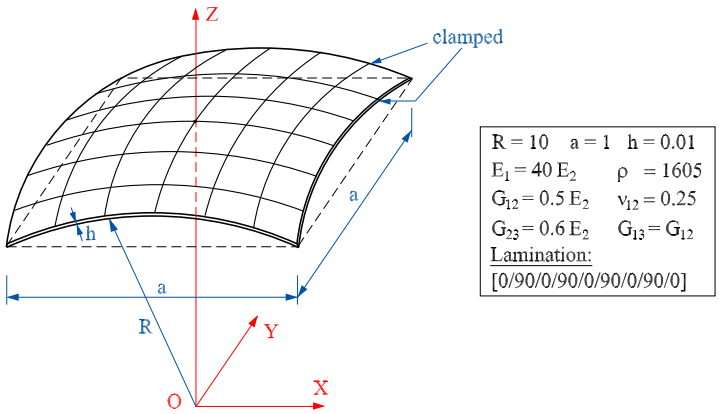

Figure 4.20: Geometry and discretization of a laminated spherical shell.

Table 4.16 gives the first four normalized natural frequencies obtained by the present method in comparison with the solution of Jayasankar et al. (2007) using nine-node degenerated shell element. It can be seen that the present results obtained by using MISQ20 and MISQ24 elements agree well with the solutions given by Jayasankar. The first six mode shapes are also displayed in Figure 4.21.

Table 4.16: Clamped 9-layer $[(0^0/90^0)_4/0^0]$ cross-ply spherical shell: Comparison of the normalized frequencies $\omega^* = (\omega a^2/h)\sqrt{\rho/E_2}$ with other solutions.

Model	Mesh	Mode 1	Mode 2	Mode 3	Mode 4
MISQ20	6×6	69.61	98.25	118.15	136.05
	10×10	67.94	88.24	104.45	119.73
	14×14	67.51	86.00	101.27	115.88
MISQ24	6×6	69.61	98.25	118.15	136.05
	10×10	67.94	88.24	104.45	119.73
	14×14	67.51	86.00	101.27	115.88
Jayasankar et al. (2007)	15×15	67.43	84.16	99.71	113.70

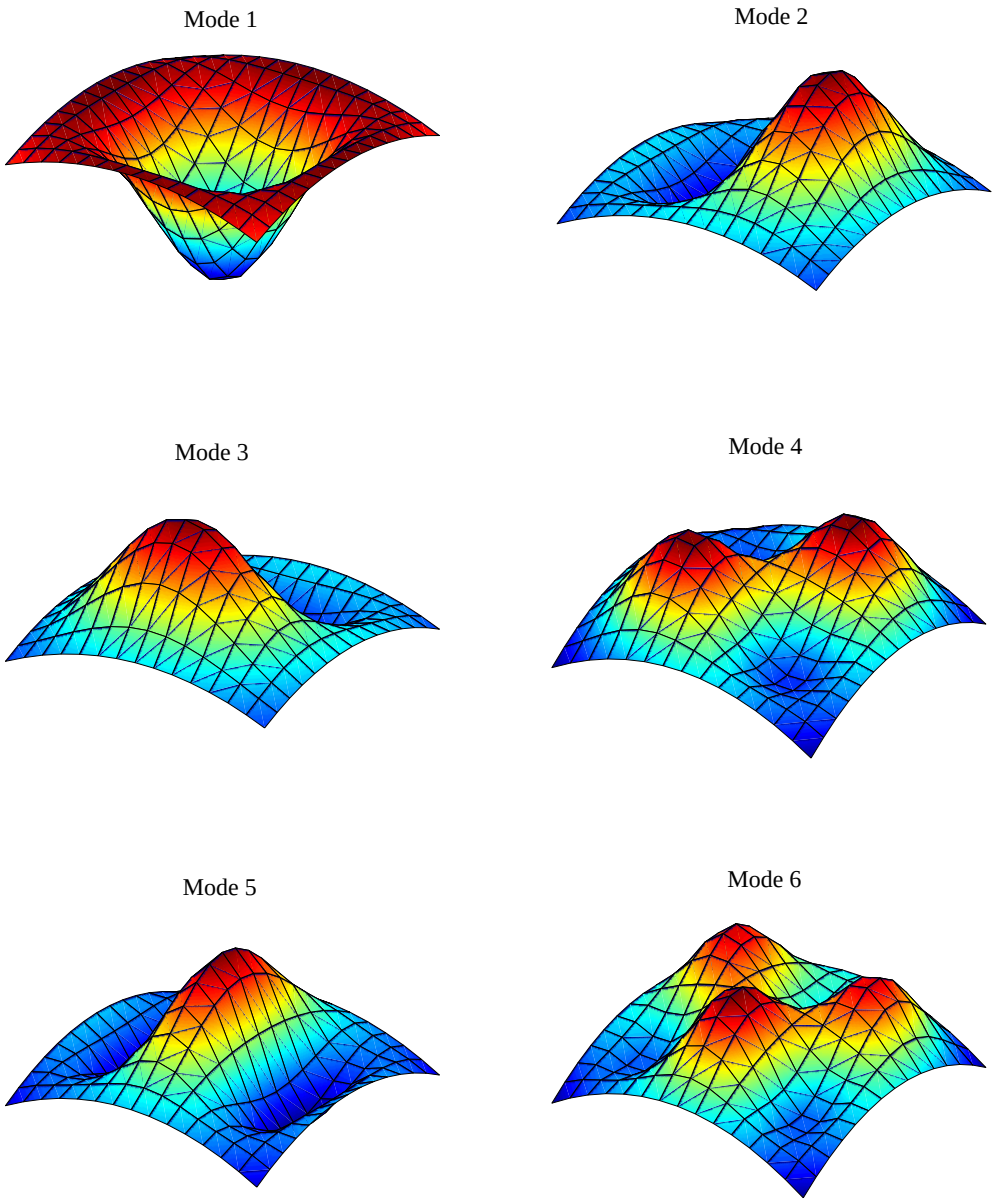

Figure 4.21: Clamped 9-layer cross-ply $[(0^0/90^0)_4/0^0]$ spherical shell: the first six mode shapes.

4.4.4 Uniaxial buckling of multi-layer cylindrical shallow shell panels

This section deal with the uniaxial buckling analysis of simply supported cross-ply laminated cylindrical shell panels (see Figure 4.22). The thickness of each layer is identified and shear correction factors $k_1^2 = k_2^2 = \frac{\pi^2}{12}$ are used for all computations, unless otherwise specified. The following two sets of typical graphite-epoxy material properties are used in the analysis:

- Material I: $E_1/E_2 = 40$; $G_{12} = G_{13} = 0.5E_2$; $G_{23} = 0.6E_2$; $\nu_{12} = \nu_{13} = \nu_{23} = 0.25$.
- Material II: $E_1/E_2 = 25$; $G_{12} = G_{13} = 0.5E_2$; $G_{23} = 0.2E_2$; $\nu_{12} = \nu_{13} = \nu_{23} = 0.25$.

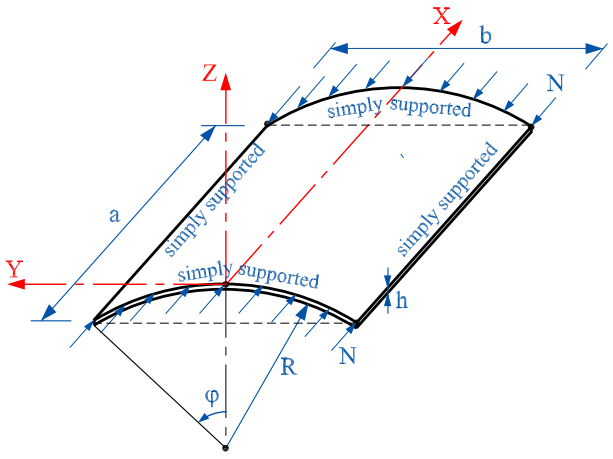

Figure 4.22: Geometry data of a cylindrical shallow shell subjected to uniaxial compression.

4.4.4.1 Effect of span-to-thickness ratio

A symmetric cross-ply 5-layer $[0^0/90^0/0^0/90^0/0^0]$ shell panel of Material I is chosen to study the effect of span-to-thickness ratios on the critical buckling load. The panel is simply supported at all the edges, with aspect ratio $a/b = 1$ and $R/a = 20$. Table 4.17 reports the normalized critical buckling loads obtained by MISQ20 and

MISQ24 elements for various span-to-thickness ratios a/h together with FSDT-based higher order element solutions (Kumar et al., 2003; Prusty and Satsangi, 2001) and an analytic FSDT solution of Sciuva and Carrera (1990).

As can be seen that both MISQ20 and MISQ24 yield the same results and show a slightly better performance than those of Kumar et al. (2003); Prusty and Satsangi (2001) for ratios $a/h < 50$. It is also observed that increasing ratio a/h leads to the higher critical buckling loads but this effect will have a minor influence with $a/h > 50$.

Table 4.17: Simply supported cross-ply $[0^0/90^0/0^0/90^0//0^0]$ cylindrical shell panel: Comparison of the normalized critical buckling loads with other solutions ($\lambda^* = N_x a^2/(E_2 h^3)$).

Model	a/h				
	10	20	30	50	100
MISQ20 (8×8)	24.412	32.557	34.796	36.081	36.656
(12×12)	24.088	32.077	34.268	35.525	36.087
(16×16)	23.976	31.911	34.086	35.334	35.891
MISQ24 (8×8)	24.412	32.557	34.796	36.081	36.656
(12×12)	24.088	32.077	34.268	35.525	36.087
(16×16)	23.976	31.911	34.086	35.334	35.891
Kumar et al. (2003)	23.97	31.79	–	35.40	36.85
Prusty and Satsangi (2001)	23.96	31.89	33.98	35.39	36.84
FSDT (Sciuva and Carrera, 1990)	24.19	31.91	34.04	35.42	36.86

4.4.4.2 Effect of the number of layers

The effect of the number of layers on the critical buckling load is now studied with two span-to-thickness ratios $a/h = 5$ and 10. A simply supported cross-ply $k-$layer $[0^0/90^0/...]_k$ cylindrical shallow shell of Material II, with aspect ratio $R/a = 2$ and $a/b = 1$ is considered.

Table 4.18 reports the normalized critical buckling loads obtained by the present

elements together with the analytic solution of Matsunaga (2007) with various value of k. The numerical results show that the present solutions of MISQ20 and MISQ20 are in good agreement with the analytic solution. The effect of the number of layers is also found to be a weak influence on the critical buckling loads.

Table 4.18: Simply supported cross-ply $k-$layer $[0^0/90^0/...]_k$ cylindrical shallow shell: Comparison of normalized critical buckling loads ($\lambda^* = N_x/(E_2 h)$, $R/a = 2$, $a/b = 1$).

k	$a/h = 5$			$a/h = 10$		
	MISQ20	MISQ24	Matsunaga (2007)	MISQ20	MISQ24	Matsunaga (2007)
2	0.2204	0.2344	0.2227	0.0810	0.0956	0.0879
3	0.2964	0.2964	0.2660	0.1498	0.1498	0.1424
4	0.2820	0.2828	0.2763	0.1477	0.1506	0.1400
5	0.3093	0.3093	0.2973	0.1601	0.1601	0.1561
10	0.2858	0.2858	0.3487	0.1635	0.1639	0.1686

4.5 Concluding remarks

This chapter has demonstrated a successful adaption of flat shell element approach for two developed MISQ20 and MISQ24 elements in geometrically linear analysis of shell structures within the context of the FSDT. Two novel four-node quadrilateral elements, one with fictional drilling DOFs (MISQ20) and one with actual drilling DOFs (MISQ24), are examined for their capacity to accurately simulate the behavior of moderately thick to thin shell structures including isotropic and laminated composite materials. As opposed to general trend to use curved higher order finite elements for the analysis of shells, it is shown that the flat element formulations herein is adequately accurate in all test cases.

Despite the fact that the developed elements are based on flat shell configuration, the results obtained herein with MISQ20 and MISQ24 elements exhibit the same high accuracy as the other geometrically-exact hybrid shell element of Simo et al. (1989) over the wide range of standard benchmark problems from shallow to deep, from thin to moderately thick shell structures. In all tests carried out to date with

the same mesh, it is observed that the MISQ24 element achieves better accuracy than the MISQ20 element for static bending, free vibration and buckling problems. The MISQ24 element has also shown its robust performance in highly distorted configurations, i.e. warping geometries. As a results, the MISQ24 element can be considered as a very suitable candidate for an adaptive finite element refinement strategy.

In conclusion, the two novel flat shell elements provide excellent results to most of problems when compared with analytic solutions and many high-performance four-node shell elements in the literature. The reported numerical results also highlight that both developed elements are free of membrane and shear locking and could be good candidates for general shell structural analysis in engineering practice in which the range of thickness-to-length (t/L) is usually from 1/10 to 1/1000. Further development of MISQ20 and MISQ24 for geometrically nonlinear plate and shell structures will be reported in the subsequent chapter.

Chapter 5

Geometrically Nonlinear Analysis of Plate/Shell Structures

This chapter reports the extension of the formulation of MISQ20 and MISQ24 elements, reported in previous chapters, for the present purpose of geometrically nonlinear analysis of plate and shell structures. The von Karman's large deflection theory and the Total Lagrangian (TL) approach are employed in the formulation of the elements to describe small strain geometric nonlinearity with large deformations. The predictive capability of the present models is demonstrated by comparing the present results with analytical/experimental and other numerical solutions available in the literature.

5.1 Introduction

Plate/shell structures have been widely used in practical engineering applications where geometrically nonlinear analysis of these structures becomes important for a full investigation of their behaviour in the large deformation regime.

Geometrically nonlinear analysis usually refers to a nonlinear equilibrium path with linear elastic material behaviour. In the geometrically nonlinear analysis, the equilibrium is achieved in the deformed configuration and not in the initial configuration as with linear analysis. Therefore, geometrically nonlinear analy-

sis is considered as a complex issue that requires efficient and reliable advanced numerical methods. Numerical methods such as FEM have been developed and widely used for nonlinear analysis of these structures with complex geometry and loading history. There is a vast amount of literature on geometrically nonlinear analysis of plates/shells which is impossible to list altogether here. An excellent review of the development of plate/shell finite elements during the past 20 years was presented by Yang et al (2000). Further extensive references on plates/shells can be found in a detailed review by Gal and Levy (2006) and Zhang and Yang (2009), for example.

As discussed in Chapter 4, flat elements have been often and widely used owing to the ease to mix with other types of element, the simplicity in their formulation and the effectiveness of computation. Consequently, flat elements are advantageous in solving the geometrically nonlinear problems in which the response of the structure at each increment/iteration needs to be computed and stored with a large number of history variables. The goal of this chapter is to further develop the flat elements MISQ20 and MISQ24, whose performances in linear analysis have already been verified and demonstrated in Chapter 3 and Chapter 4, for geometrically nonlinear analysis of general plate and shell structures. The von Karman's large deflection theory and the Total Lagrangian approach are utilized in the small strain-large deformation formulation and then the solution of the nonlinear equilibrium equations is obtained by the full Newton-Raphson method. Numerical examples show that the present method exhibits good accuracy and stability in capturing geometric nonlinearity in plate/shell structures.

This chapter is outlined as follows. First, a brief review of the FSDT finite element formulations for geometrically nonlinear analysis is introduced in Section 5.2. The description of strain smoothing approaches for the nonlinear membrane strain and the tangent stiffness matrix of the element are derived in Section 5.3. Several numerical examples are presented in Section 5.4 in order to verify and assess the performance of the proposed elements. Finally, some concluding remarks are reported in Section 5.5.

5.2 Finite element formulation for geometrically nonlinear analysis

5.2.1 Kinematic equations

Based on the FSDT, the laminated composite plate kinematics is governed by the midplane displacement u_0, v_0, w_0 and the rotation θ_x, θ_y of the mid-surface normal about $y-$ and $x-$axis, respectively

$$\begin{aligned} u(x,y,z) &= u_0(x,y) + z\theta_x, \\ v(x,y,z) &= v_0(x,y) + z\theta_y, \\ w(x,y,z) &= w_0(x,y). \end{aligned} \tag{5.1}$$

For large deformation analysis, the in-plane vector of Green-Lagrangian strain at any point in a plate element is:

$$\boldsymbol{\epsilon} = \left\{ \begin{array}{c} \epsilon_x \\ \epsilon_y \\ \epsilon_{xy} \end{array} \right\} = \left\{ \begin{array}{c} u_{,x} + \frac{1}{2}(u_{,x}^2 + v_{,x}^2 + w_{,x}^2) \\ v_{,y} + \frac{1}{2}(u_{,y}^2 + v_{,y}^2 + w_{,y}^2) \\ u_{,y} + v_{,x} + (u_{,x}u_{,y} + v_{,x}v_{,y} + w_{,x}w_{,y}) \end{array} \right\} \tag{5.2}$$

Substituting Equation (5.2) into Equation (5.1) and considering the von Karman's large deflection assumption, the in-plane strain vector can be rewritten as

$$\boldsymbol{\epsilon} = \boldsymbol{\epsilon}_m + z\boldsymbol{\epsilon}_b, \tag{5.3}$$

in which

$$\boldsymbol{\epsilon}_b = \left\{ \begin{array}{c} \theta_{x,x} \\ \theta_{y,y} \\ \theta_{x,y} + \theta_{y,x} \end{array} \right\}, \tag{5.4}$$

$$\boldsymbol{\epsilon}_m = \left\{ \begin{array}{c} u_{0,x} + \frac{1}{2}w_{,x}^2 \\ v_{0,y} + \frac{1}{2}w_{,y}^2 \\ u_{0,y} + v_{0,x} + w_{,x}w_{,y} \end{array} \right\} = \underbrace{\left\{ \begin{array}{c} u_{0,x} \\ v_{0,y} \\ u_{0,y} + v_{0,x} \end{array} \right\}}_{linear\ part} + \underbrace{\left\{ \begin{array}{c} \frac{1}{2}w_{,x}^2 \\ \frac{1}{2}w_{,y}^2 \\ w_{,x}w_{,y} \end{array} \right\}}_{nonlinear\ part} \tag{5.5}$$

$$= \boldsymbol{\epsilon}_m^L + \boldsymbol{\epsilon}_m^{NL}. \tag{5.6}$$

The nonlinear term of the membrane strain-displacement vector can be rewritten as follows

$$\boldsymbol{\epsilon}_m^{NL} = \frac{1}{2}\underbrace{\begin{bmatrix} w_{,x} & 0 \\ 0 & w_{,y} \\ w_{,y} & w_{,x} \end{bmatrix}}_{\mathbf{H}}\underbrace{\begin{Bmatrix} w_{,x} \\ w_{,y} \end{Bmatrix}}_{\boldsymbol{\theta}} = \frac{1}{2}\mathbf{H}\boldsymbol{\theta}, \tag{5.7}$$

in which $\boldsymbol{\theta}$ is termed the slope vector.

The transverse shear strain vector is given as

$$\boldsymbol{\gamma} = \begin{Bmatrix} \gamma_{xz} \\ \gamma_{yz} \end{Bmatrix} = \begin{Bmatrix} \theta_x - w_{,x} \\ \theta_y - w_{,y} \end{Bmatrix}. \tag{5.8}$$

The constitutive relationship of laminated plates can be expressed as

$$\boldsymbol{\sigma}^* = \mathbf{D}^*\boldsymbol{\epsilon}^* \tag{5.9}$$

where

$$\boldsymbol{\sigma}^* = \begin{bmatrix} \mathbf{N} \\ \mathbf{M} \\ \mathbf{T} \end{bmatrix}, \quad \boldsymbol{\epsilon}^* = \begin{bmatrix} \boldsymbol{\epsilon}_m \\ \boldsymbol{\epsilon}_b \\ \boldsymbol{\gamma} \end{bmatrix}, \quad \mathbf{D}^* = \begin{bmatrix} \mathbf{A} & \mathbf{B} & 0 \\ \mathbf{B} & \mathbf{D} & 0 \\ 0 & 0 & \mathbf{C}_s \end{bmatrix}, \tag{5.10}$$

where $\mathbf{N} = \{N_x \;\; N_y \;\; N_{xy}\}$ is the in-plane traction, $\mathbf{T} = \{Q_x \;\; Q_y\}$ is the out-of-plane traction and $\mathbf{M} = \{M_x \;\; M_y \;\; M_{xy}\}$ is the out-of-plane moment resultant. $\mathbf{A}$ is the extensional stiffness, $\mathbf{D}$ is the bending stiffness, $\mathbf{B}$ is the bending-extension coupling stiffness and $\mathbf{C}_s$ is the transverse shear stiffness, which are given in detail in Chapter 3.

5.2.2 Total Lagrangian finite element formulation

The Total Lagrangian (TL) approach, in which the original configuration is taken as the reference, is usually used for geometrically nonlinear analysis. The finite element equation in the TL approach can be expressed in the following form:

$${}^t\mathbf{K}_T\boldsymbol{\Delta}\mathbf{q} = {}^{t+\Delta t}\mathbf{P} - {}^t\mathbf{F} \tag{5.11}$$

where ${}^t\mathbf{F}$ is the element internal force at time t, ${}^{t+\Delta t}\mathbf{P}$ is the element external force at time $t+\Delta t$, ${}^t\mathbf{K}_T$ is the element tangent stiffness matrix at time t and $\mathbf{\Delta q}$ is the element displacement increment.

The element tangent stiffness matrix $\mathbf{K}_T$ is defined as

$$\mathbf{K}_T = \mathbf{K}_L + \mathbf{K}_{NL} + \mathbf{K}_g, \tag{5.12}$$

where $\mathbf{K}_L$ represent the linear stiffness matrix, $\mathbf{K}_{NL}$ denotes the nonlinear stiffness matrix and $\mathbf{K}_g$ is the geometric stiffness matrix.

The linear stiffness matrix $\mathbf{K}_L$ is known from the linear analysis as

$$\mathbf{K}_L = \int_\Omega \mathbf{B}_L^T \mathbf{D}^* \mathbf{B}_L d\Omega \tag{5.13}$$

where $\mathbf{B}_L$ is the linear gradient matrix given as

$$\mathbf{B}_L = \begin{bmatrix} \mathbf{B}_m^L \\ \mathbf{B}_b \\ \mathbf{B}_s \end{bmatrix} \tag{5.14}$$

The linear membrane, bending and transverse shear gradient matrix, $\mathbf{B}_m,\ \mathbf{B}_b,\ \mathbf{B}_s$, respectively, can be obtained from the following strain-displacement equations:

$$\mathbf{\Delta\epsilon}_m^L = \mathbf{B}_m^L \mathbf{\Delta q}_m, \quad \mathbf{\Delta\epsilon}_b = \mathbf{B}_b \mathbf{\Delta q}_b, \quad \mathbf{\Delta\gamma} = \mathbf{B}_s \mathbf{\Delta q}_b. \tag{5.15}$$

in which
$\mathbf{\Delta q}_{mi} = [\Delta u_i \ \ \Delta v_i]^T$ for MISQ20 and $\mathbf{\Delta q}_{mi} = [\Delta u_i \ \ \Delta v_i \ \ \Delta\theta_{zi}]^T$ for MISQ24,
$\mathbf{\Delta q}_{bi} = [\Delta w_i \ \ \Delta\theta_{xi} \ \ \Delta\theta_{yi}]^T$,
$\mathbf{B}_{mi}^L,\ \mathbf{B}_{bi},\ \mathbf{B}_{si}$ are defined in Equation (3.29) of Chapter 3.

The nonlinear stiffness matrix $\mathbf{K}_{NL}$ is defined as

$$\mathbf{K}_{NL} = \int_\Omega (\mathbf{B}_L^T \mathbf{D}^* \mathbf{B}_{NL} + \mathbf{B}_{NL}^T \mathbf{D}^* \mathbf{B}_L + \mathbf{B}_{NL}^T \mathbf{D}^* \mathbf{B}_{NL}) d\Omega \tag{5.16}$$

where $\mathbf{B}_{NL}$ is the nonlinear gradient matrix given by

$$\mathbf{B}_{NL} = \begin{bmatrix} \mathbf{B}_m^{NL} \\ 0 \\ 0 \end{bmatrix} \tag{5.17}$$

and $\mathbf{B}_m^{NL}$ can be obtained as follows.

Taking the variation of Equation (5.7) yields

$$d\boldsymbol{\epsilon}_m^{NL} = \frac{1}{2} d\mathbf{H}\boldsymbol{\theta} + \frac{1}{2}\mathbf{H}d\boldsymbol{\theta}. \tag{5.18}$$

It is easily proven that

$$d\mathbf{H}\boldsymbol{\theta} = \begin{bmatrix} w_{,x}dw_{,x} \\ w_{,y}dw_{,y} \\ w_{,x}dw_{,y} + w_{,y}dw_{,x} \end{bmatrix} = \begin{bmatrix} w_{,x} & 0 \\ 0 & w_{,y} \\ w_{,y} & w_{,x} \end{bmatrix} \begin{Bmatrix} dw_{,x} \\ dw_{,y} \end{Bmatrix} = \mathbf{H}d\boldsymbol{\theta} \tag{5.19}$$

Then

$$d\boldsymbol{\epsilon}_m^{NL} = \mathbf{H}d\boldsymbol{\theta}. \tag{5.20}$$

The interpolation of θ can be written as

$$\boldsymbol{\theta} = \begin{Bmatrix} w_{,x} \\ w_{,y} \end{Bmatrix} = \underbrace{\begin{bmatrix} N_{i,x} & 0 & 0 \\ N_{i,y} & 0 & 0 \end{bmatrix}}_{\mathbf{G}} \begin{Bmatrix} w \\ \theta_x \\ \theta_y \end{Bmatrix} = \mathbf{G}\mathbf{q}_b, \tag{5.21}$$

$$d\boldsymbol{\theta} = \mathbf{G}d\mathbf{q}_b.$$

Substituting Equation (5.21) into Equation (5.20) we obtain

$$d\boldsymbol{\epsilon}_m^{NL} = \underbrace{\mathbf{H}\mathbf{G}}_{\mathbf{B}_m^{NL}} d\mathbf{q}_b = \mathbf{B}_m^{NL} d\mathbf{q}_b. \tag{5.22}$$

From Equation (5.22) a general expression for the nonlinear gradient matrix $\mathbf{B}_m^{NL} = \mathbf{H}\mathbf{G}$ is derived and hence the nonlinear stiffness matrix $\mathbf{K}_{NL}$ can be computed from Equation (5.16).

Finally, the strain components $\boldsymbol{\epsilon}^*$ from Equation (5.10) can be separated into linear part $\boldsymbol{\epsilon}_L$ and nonlinear part $\boldsymbol{\epsilon}_{NL}$ as follows.

$$\boldsymbol{\epsilon}^* = \boldsymbol{\epsilon}_L + \boldsymbol{\epsilon}_{NL} = (\mathbf{B}_L + \frac{1}{2}\mathbf{B}_{NL})\mathbf{q}. \tag{5.23}$$

The element geometric stiffness matrix is described as

$$\mathbf{K}_g = \int_\Omega \mathbf{G}^T \hat{\mathbf{N}} \mathbf{G} d\Omega \tag{5.24}$$

where $\mathbf{G}$ is given in Equation (5.21) and the traction matrix $\hat{\mathbf{N}}$ is defined as

$$\hat{\mathbf{N}} = \begin{bmatrix} N_x & N_{xy} \\ N_{xy} & N_y \end{bmatrix}. \tag{5.25}$$

5.3 Strain smoothing formulation for geometrically nonlinear analysis

As in the case of linear strains, the nonlinear strain field is smoothed by a weighted average of the original nonlinear strain using the same constant smoothing function Φ as follows.

$$\begin{aligned}\tilde{\boldsymbol{\epsilon}}^*(\mathbf{x}_C) &= \int_{\Omega_C} \boldsymbol{\epsilon}^*(\mathbf{x})\Phi(\mathbf{x}-\mathbf{x}_C)d\Omega \\ &= \underbrace{\int_{\Omega_C} \boldsymbol{\epsilon}_L(\mathbf{x})\Phi(\mathbf{x}-\mathbf{x}_C)d\Omega}_{\tilde{\boldsymbol{\epsilon}}_L(\mathbf{x}_C)} + \underbrace{\int_{\Omega_C} \boldsymbol{\epsilon}_{NL}(\mathbf{x})\Phi(\mathbf{x}-\mathbf{x}_C)d\Omega}_{\tilde{\boldsymbol{\epsilon}}_{NL}(\mathbf{x}_C)}. \end{aligned} \tag{5.26}$$

Introducing the approximation of the linear strain and nonlinear strain in Equation (5.23) to the above equation yields

$$\tilde{\boldsymbol{\epsilon}}_L(\mathbf{x}_C) = \tilde{\mathbf{B}}_L\mathbf{q}, \tag{5.27}$$

$$\tilde{\boldsymbol{\epsilon}}_{NL}(\mathbf{x}_C) = \frac{1}{2}\tilde{\mathbf{B}}_{NL}\mathbf{q}, \tag{5.28}$$

where $\tilde{\mathbf{B}}_L,\ \tilde{\mathbf{B}}_{NL}$ are the smoothed linear and nonlinear gradient matrix, respectively, which are given as

$$\tilde{\mathbf{B}}_L = \begin{bmatrix} \tilde{\mathbf{B}}_m^L \\ \tilde{\mathbf{B}}_b \\ \bar{\mathbf{B}}_s \end{bmatrix}, \qquad \tilde{\mathbf{B}}_{NL} = \begin{bmatrix} \tilde{\mathbf{B}}_m^{NL} \\ 0 \\ 0 \end{bmatrix} \tag{5.29}$$

in which $\tilde{\mathbf{B}}_m^L,\ \tilde{\mathbf{B}}_b,\ \bar{\mathbf{B}}_s$ are defined in the linear analysis part of Chapter 3.

$\tilde{\mathbf{B}}_m^{NL}$ is the smoothed nonlinear strain matrix in the smoothing cell given as

$$\tilde{\mathbf{B}}_{mi}^{NL} = \tilde{\mathbf{H}}\tilde{\mathbf{G}}_i, \tag{5.30}$$

in which

$$\tilde{\mathbf{G}}_i = \frac{1}{A_C}\sum_{g=1}^{4} \begin{pmatrix} 0 & 0 & N_i(\mathbf{x}_g^G)n_x & 0 & 0 & 0 \\ 0 & 0 & N_i(\mathbf{x}_g^G)n_y & 0 & 0 & 0 \end{pmatrix} l_g^C, \tag{5.31}$$

$$\tilde{\mathbf{H}} = \sum_{i=1}^{4} \begin{pmatrix} \frac{1}{A_C}\sum\limits_{j=1}^{4} N_i(\mathbf{x}_j^G)n_x l_j^C w_i & 0 \\ 0 & \frac{1}{A_C}\sum\limits_{j=1}^{4} N_i(\mathbf{x}_j^G)n_y l_j^C w_i \\ \frac{1}{A_C}\sum\limits_{j=1}^{4} N_i(\mathbf{x}_j^G)n_y l_j^C w_i & \frac{1}{A_C}\sum\limits_{j=1}^{4} N_i(\mathbf{x}_j^G)n_x l_j^C w_i \end{pmatrix}, \tag{5.32}$$

where w_i is the deflection at the node i of the element.

The element tangent stiffness matrix $\mathbf{K}_T$ is modified as

$$\tilde{\mathbf{K}}_T = \tilde{\mathbf{K}}_L + \tilde{\mathbf{K}}_{NL} + \tilde{\mathbf{K}}_g, \tag{5.33}$$

where

$$\tilde{\mathbf{K}}_L = \sum_{i=1}^{nc} \tilde{\mathbf{B}}_{Li}^T \mathbf{D}^* \tilde{\mathbf{B}}_{Li} A_i, \tag{5.34}$$

$$\tilde{\mathbf{K}}_{NL} = \sum_{i=1}^{nc} (\tilde{\mathbf{B}}_{Li}^T \mathbf{D}^* \tilde{\mathbf{B}}_{NLi} + \tilde{\mathbf{B}}_{NLi}^T \mathbf{D}^* \tilde{\mathbf{B}}_{Li} + \tilde{\mathbf{B}}_{NLi}^T \mathbf{D}^* \tilde{\mathbf{B}}_{NLi}) A_i, \tag{5.35}$$

$$\tilde{\mathbf{K}}_g = \sum_{i=1}^{nc} \tilde{\mathbf{G}}_i^T \hat{\mathbf{N}} \tilde{\mathbf{G}}_i A_i, \tag{5.36}$$

and the number of smoothing cells $nc = 2$ is chosen in this study.

The internal forces at the time t, computed from the stress state in the structures, can be rewritten as

$${}^t\tilde{\mathbf{F}} = \int_\Omega (\tilde{\mathbf{B}}_L + \tilde{\mathbf{B}}_{NL})^t \boldsymbol{\sigma}^* d\Omega \tag{5.37}$$

in which the stress resultant after the i^{th} iteration is

$${}^t\boldsymbol{\sigma}_{i+1}^* = {}^t\boldsymbol{\sigma}_i^* + {}^t\Delta\boldsymbol{\sigma}^*, \tag{5.38}$$

and the incremental stress is expressed as

$${}^t\Delta\boldsymbol{\sigma}^* = \mathbf{D}^* \Delta\boldsymbol{\epsilon}^* = \mathbf{D}^* (\tilde{\mathbf{B}}_L + \tilde{\mathbf{B}}_{NL}) \Delta\mathbf{q}. \tag{5.39}$$

Finally, the nonlinear equations can be rewritten as

$${}^t\tilde{\mathbf{K}}_T \boldsymbol{\Delta}\mathbf{q} = {}^{t+\Delta t}\mathbf{P} - {}^t\tilde{\mathbf{F}}. \tag{5.40}$$

By transforming Equation (5.40) to the global coordinates via the standard rotation matrix $\mathbf{R}$ defined in Equation (2.42), the resultant nonlinear equations can be used to analyse the geometrically nonlinear problem of shells. In this study, such nonlinear system of equations are solved by a full Newton-Raphson procedure with the following incremental/iterative algorithm:

- Input geometry, material properties and solution parameters

- Initialize $\mathbf{P}^0 = 0$, $\mathbf{F}^0_{(0)} = 0$, $\mathbf{u}^0_{(0)} = 0$, $\epsilon_D = 0.001$(convergence tolerance)
- LOOP over load increments, $n = 1..maxinc$
  - Calculate load factor $\lambda = 1/maxinc$
  - Compute incremental force $\Delta\mathbf{P} = \lambda\mathbf{P}$
  - Set $Error = 1,\ i = 0$
  - Set $\mathbf{P}^n = \mathbf{P}^{n-1} + \Delta\mathbf{P},\ \mathbf{u}^n_{(0)} = \mathbf{u}^{n-1}$, $\mathbf{K}^n_{T(0)} = \mathbf{K}^{n-1}_T$
  - DO WHILE $(i < maxinc)$ & $(Error > \epsilon_D)$
    - $i = i + 1$
    - Solve the equations of equilibrium: $\mathbf{K}^n_{T(i-1)}\Delta\mathbf{u}_{(i)} = \mathbf{P}^n - \mathbf{F}^n_{(i-1)}$
    - Update nodal displacements: $\mathbf{u}^n_{(i)} = \mathbf{u}^n_{(i-1)} + \Delta\mathbf{u}_{(i)}$
    - Find $Error = \left\| \Delta\mathbf{u}_{(i)} \right\| / \left\| \mathbf{u}^n_{(i)} \right\|$
  - END DO
  - Update nodal coordinates
- END LOOP

5.4 Numerical examples

In this section, we will test and assess the MISQ20 and MISQ24 element through several geometrically nonlinear applications. Composite plates/shells having different shapes, boundary conditions, thickness ratios, stacking sequences are analyzed and the obtained results are discussed and compared with those obtained from other analytical/experimental and numerical solutions if available. In all the examples, the full Newton-Raphson method is used to solve the nonlinear finite element equations and the convergence tolerance ϵ_D is taken to be 0.001. For simplicity, the external load is considered to be conservative and it does not change with the deformation of geometry. Unless otherwise specified, the SCFs are $k_1^2 = k_2^2 = 5/6$. Note that in some examples, non-SI units are used so that comparison with published results can be made.

5.4.1 Clamped cross-ply 4-layer symmetric $[0^0/90^0/90^0/0^0]$ square plate under uniform pressure

A clamped cross-ply 4-layer symmetric $[0^0/90^0/90^0/0^0]$ square plate subjected to uniformly distributed load is considered. The plate has a thickness $h = 0.096$ in and a side length $L = 12$ in with the material properties: $E_1 = 1.8282 \times 10^6$ psi, $E_2 = 1.8315 \times 10^6$ psi, $G_{12} = G_{13} = G_{23} = 3.125 \times 10^5$ psi, $\nu_{12} = 0.23949$. Owing to symmetry, only a quarter of the plate is discretized using 3×3, 4×4, 5×5 meshes with regular as well as highly distorted elements as shown in Figure 5.1.

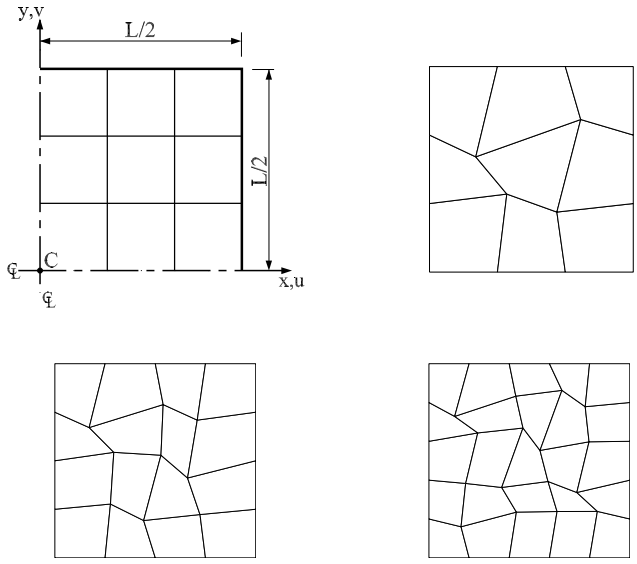

Figure 5.1: Meshes of a quarter of a simply supported plate: (a) typical regular mesh 3×3; (b) irregular mesh 3×3; (c) irregular mesh 4×4; (d) irregular mesh 5×5.

Table 5.1 shows the calculated central deflections obtained by present elements with uniform mesh and distorted mesh refinement and those from experiment (Putcha and Reddy, 1986), the mixed element by Putcha and Reddy (1986) and the RDKQ-NL20(24) elements of Zhang and Kim (2006). The load-deflection curves are also plotted in Figure 5.2 for comparison.

It can be seen that both MISQ20 and MISQ24 elements yield almost the same solution and the present results are in good agreement with other solutions. It is interesting to note that the present solutions are closer to the experimental results

than those of other numerical results cited here.

The effect of distorted mesh on central deflection under the variation of load intensity is plotted in Figure 5.3. It can be seen that the present elements, MISQ20 and MISQ24, are relatively insensitive to mesh distortion.

Table 5.1: A clamped cross-ply $[0^0/90^0/90^0/0^0]$ square plate: Central deflections under a uniformly distributed load q_0.

Model		q_0				
		0.4	0.8	1.2	1.6	2.0
MISQ20	3×3 (regular)	0.059	0.102	0.130	0.150	0.167
	3×3 (irregular)	0.059	0.103	0.129	0.147	0.165
	4×4 (regular)	0.058	0.099	0.125	0.146	0.162
	4×4 (irregular)	0.059	0.100	0.123	0.145	0.162
	5×5 (regular)	0.058	0.097	0.123	0.143	0.159
	5×5 (irregular)	0.058	0.094	0.121	0.142	0.158
MISQ24	3×3 (regular)	0.055	0.096	0.126	0.148	0.166
	3×3 (irregular)	0.059	0.104	0.134	0.155	0.173
	4×4 (regular)	0.059	0.099	0.126	0.147	0.163
	4×4 (irregular)	0.060	0.097	0.127	0.148	0.166
	5×5 (regular)	0.058	0.098	0.124	0.144	0.160
	5×5 (irregular)	0.059	0.100	0.128	0.147	0.164
RDKQ-NL20(24)		0.061	0.096	0.120	0.139	0.155
Mixed element		0.062	0.096	0.119	0.140	0.150
Experiment		0.078	0.122	0.148	0.174	0.187

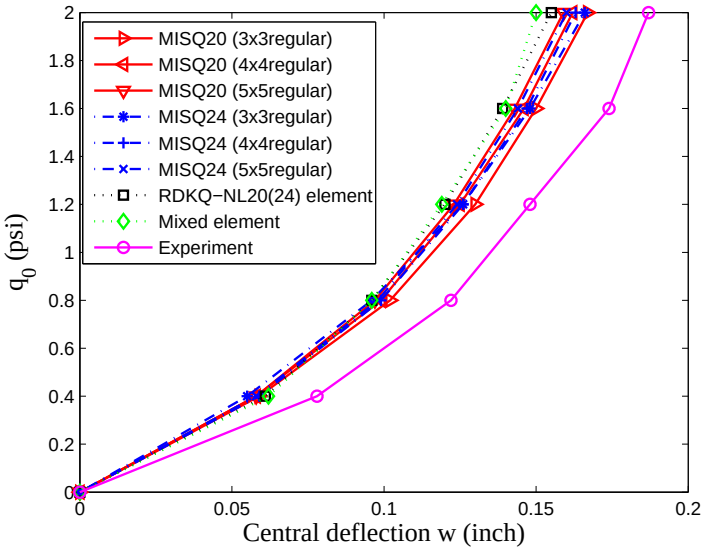

Figure 5.2: Clamped cross-ply 4-layer [0/90/90/0] square plate: Load-deflection relationship curves.

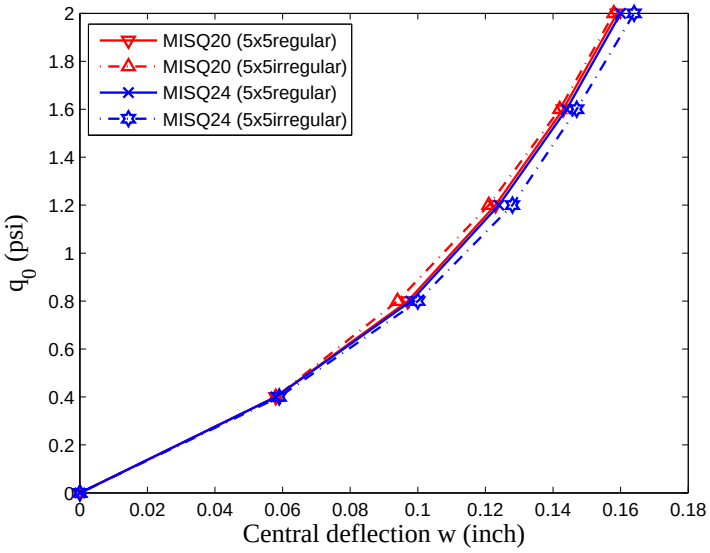

Figure 5.3: Clamped cross-ply 4-layer [0/90/90/0] square plate: Effect of mesh distortion.

5.4.2 Simply supported unidirectional 8-layer $[0^0]_8$ square plate under uniform pressure

This section deals with a simply supported unidirectional 8-layer $[0^0]_8$ square plate with a length $L = 12$ in and a thickness $h = 0.138$ in, under uniform pressure load. The material properties are $E_1 = 3.0 \times 10^6$ psi, $E_2 = 1.28 \times 10^6$ psi, $G_{12} = G_{13} = G_{23} = 3.7 \times 10^5$ psi, $\nu_{12} = 0.32$.

The following simply supported boundary conditions are used:
At edges parallel to $x-$axis: $u = w = \theta_x = 0$,
At edges parallel to $y-$axis: $v = w = \theta_y = 0$.

The full plate is discretized with 10×10 uniform elements as well as distorted elements as shown in Figure 5.4

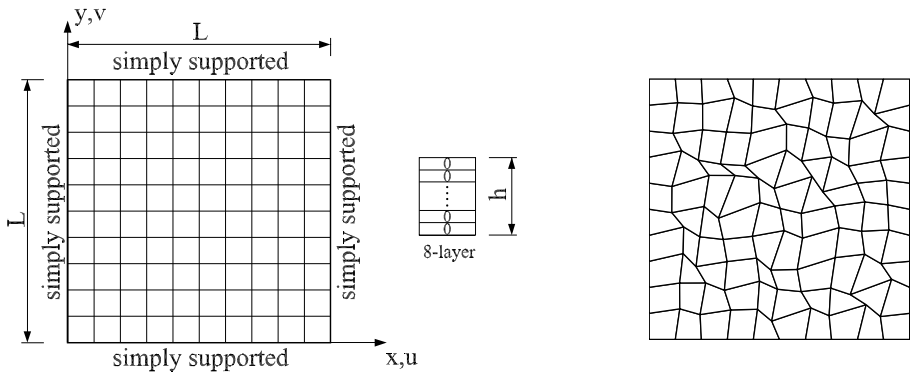

(a) (b)

Figure 5.4: Simply supported unidirectional 8-layer $[0^0]_8$ square plate: (a) regular mesh and (b) irregular mesh.

The nonlinear solutions of the central deflection obtained with the present elements, RDKQ-NL20(24) elements of Zhang and Kim (2006), the 3-node multi-layered facet element of Argyris and Tenek (1994) and by experiment of Zaghloul and Kennedy (1975), are reported in Table 5.2. The load-deflection relationship curves are plotted in Figure 5.5. It is obvious that the present results are in reasonable agreement with the experimental results and the present elements show better performance than that of RDKQ-NL20(24) elements with the same mesh and DOFs. The effect of mesh distortion on the MISQ20 and MISQ24's performance displayed in Figure 5.6 does show that the present elements are relatively

insensitive to badly-shaped elements.

Table 5.2: A simply supported unidirectional $[0^0]_8$ square plate: Central deflections under a uniformly distributed load q_0.

Model		q_0				
		0.4	0.8	1.2	1.6	2.0
MISQ20	10×10 (regular)	0.080	0.142	0.174	0.211	0.236
	10×10 (irregular)	0.079	0.148	0.174	0.204	0.231
MISQ24	10×10 (regular)	0.079	0.137	0.184	0.211	0.238
	10×10 (irregular)	0.079	0.138	0.184	0.212	0.244
RDKQ-NL20	10×10	0.071	0.121	0.157	0.187	0.212
RDKQ-NL24	10×10	0.078	0.131	0.171	0.202	0.229
Argyris and Tenek (1994)		0.084	0.141	0.177	0.215	0.236
Experiment (Zaghloul and Kennedy, 1975)		0.081	0.140	0.177	0.215	0.230

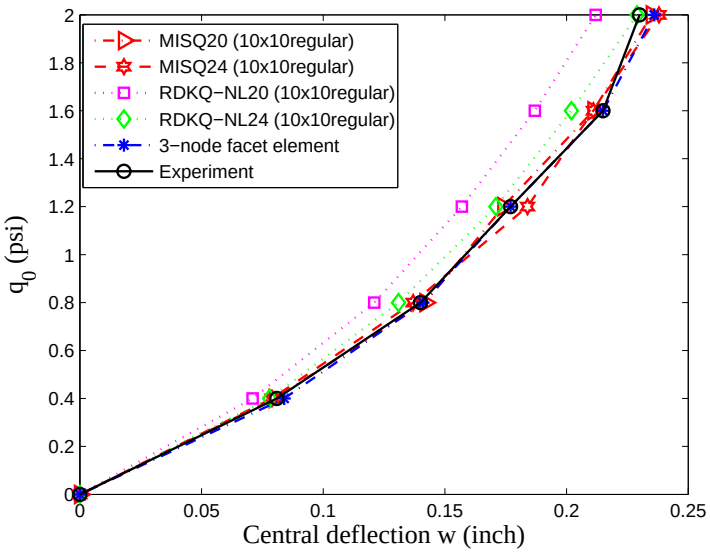

Figure 5.5: Simply supported unidirectional 8-layer $[0^0]_8$ square plate: Load-deflection relationship curves.

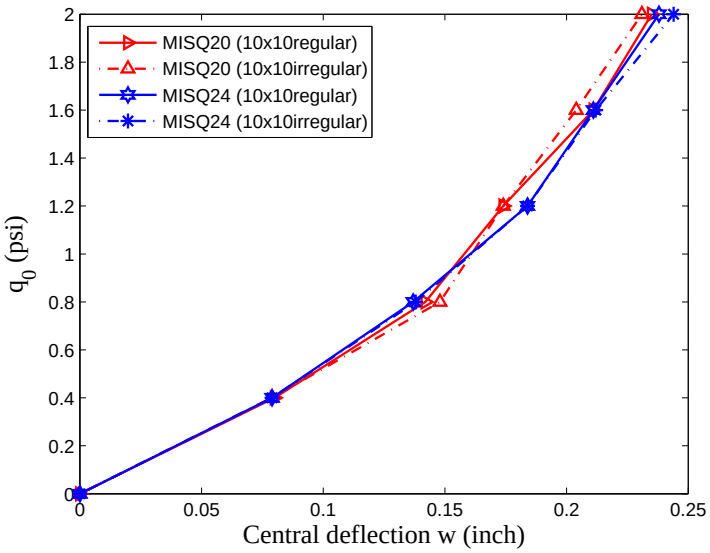

Figure 5.6: Simply supported unidirectional 8-layer $[0^0]_8$ square plate: Effect of mesh distortion.

5.4.3 Simply supported cross-ply 4-layer $[0^0/90^0/90^0/0^0]$ square plate under uniform pressure

A simply supported 4-layer $[0^0/90^0/90^0/0^0]$ square plate under uniform pressure is analysed with various span-to-thickness ratios $L/h = 40$, 20 and 10. The material properties are $E_1/E_2 = 25,\ G_{12} = G_{13} = 0.5E_2,\ G_{23} = 0.2E_2,\ \nu_{12} = 0.25$. Owing to symmetry, a 4×4 uniform mesh is used to model a quarter of the plate. The simply supported boundary conditions are the same as in Section 5.4.2.

The present results together with other numerical and analytic solutions are listed in Table 5.3 and plotted in Figure 5.7 to Figure 5.8 for various span-to-thickness ratios $L/h = 10,\ 20,\ 40$. The present results apparently agree well with the analytical solutions (Kant and Kommineni, 1992) and other numerical results such as RDKQ-20(24) solutions (Zhang and Kim, 2006) and HSDT solution (Kant and Kommineni, 1992). For the present method, the effect of span-to-thickness ratios on the central deflections is also plotted and compared in Figure 5.8b. It is observed that the deflections in thick plates is more pronounced than those in the cases of thin plates due to the effect of shear deformation.

Table 5.3: Simply supported cross-ply $[0^0/90^0/90^0/0^0]$ square plate with various span-to-thickness ratios L/h: Comparison of normalized central deflections $w^* = w/h$ with other solutions under uniformly distributed load.

$\frac{L}{h}$	$\frac{q_0 L^4}{(E_2 h^4)}$	MISQ20	MISQ24	RDKQ-NL20	RDKQ-NL24	HSDT	Analytic
40	50	0.290	0.292	0.291	0.294	0.293	0.293
	100	0.464	0.469	0.461	0.467	0.464	0.464
	150	0.585	0.590	0.577	0.587	0.582	0.582
	200	0.679	0.683	0.667	0.679	0.664	0.664
	250	0.755	0.758	0.740	0.754	0.738	0.738
20	50	0.311	0.326	0.323	0.327	0.320	0.320
	100	0.480	0.484	0.487	0.494	0.493	0.486
	150	0.598	0.601	0.597	0.608	0.592	0.592
	200	0.689	0.692	0.682	0.695	0.680	0.680
	250	0.762	0.766	0.751	0.766	0.752	0.752
10	50	0.356	0.365	0.363	0.370	0.360	0.356
	100	0.518	0.519	0.514	0.525	0.520	0.510
	150	0.628	0.634	0.616	0.629	0.624	0.610
	200	0.716	0.721	0.695	0.710	0.696	0.689
	250	0.786	0.789	0.761	0.777	0.760	0.747

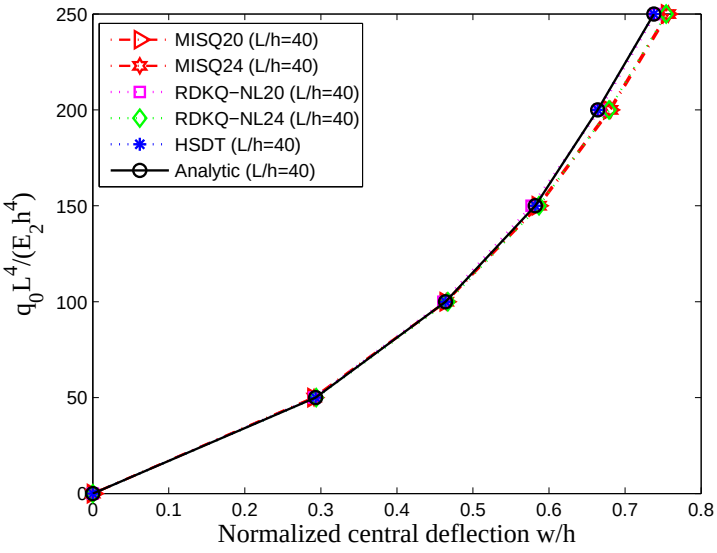

(a)

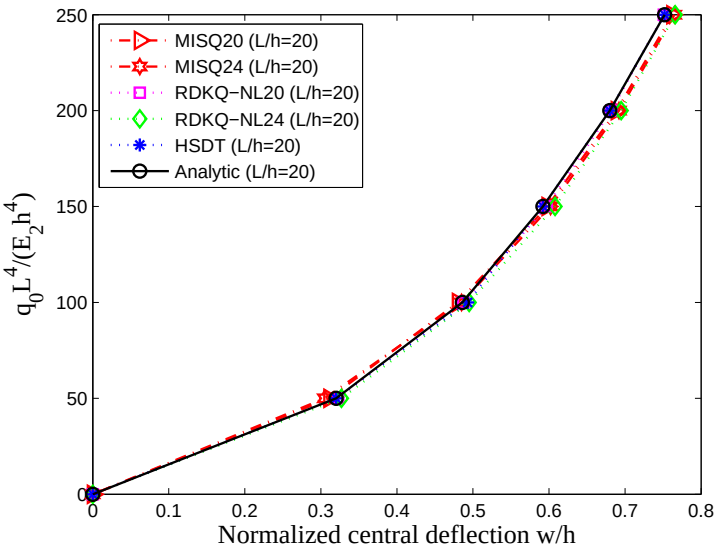

(b)

Figure 5.7: Simply supported cross-ply $[0^0/90^0/90^0/0^0]$ square plate: Load-deflection curves with (a) $L/h = 40$ and (b) $L/h = 20$.

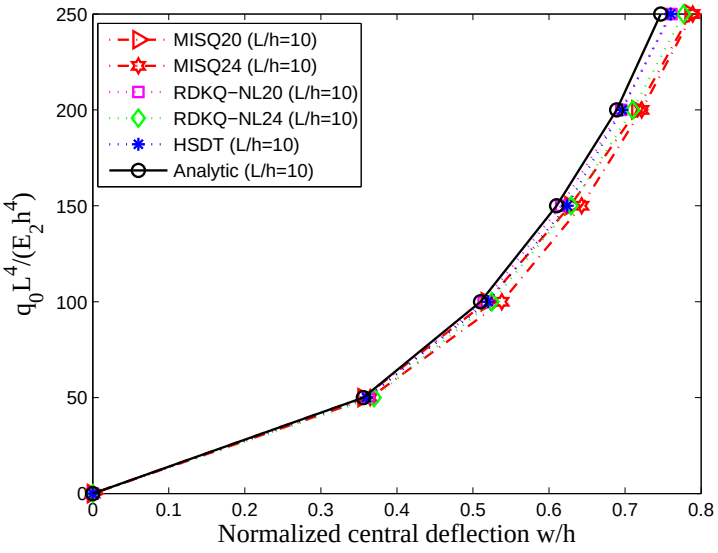

(a)

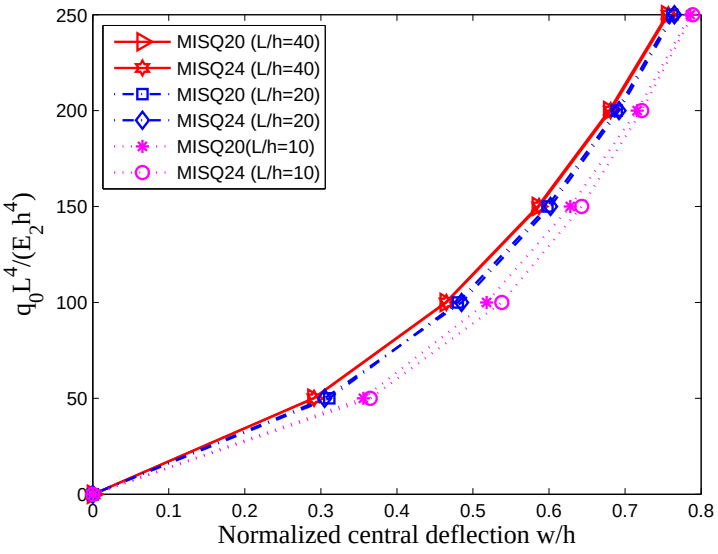

(b)

Figure 5.8: Simply supported cross-ply $[0^0/90^0/90^0/0^0]$ square plate: Load-deflection curves with (a) $L/h = 10$ and (b) the effect of span-to-thickness ratios.

5.4.4 Clamped antisymmetric cross-ply and angle-ply square plates under uniform pressure

This section is concerned with the nonlinear bending response of clamped antisymmetric cross-ply $[0^0/90^0]$ and angle-ply $[45^0/-45^0]$ square plates under uniform pressure. All layers are of equal thickness and same material properties: $E_1/E_2 = 40,\ G_{12} = G_{13} = 0.6E_2,\ G_{23} = 0.5E_2,\ \nu_{12} = 0.25$.

A quadrant of the plate is modelled with a uniform mesh of 4×4 elements in the simulation. Table 5.4 reports the computed values of the central deflection obtained by the present method under increasing load parameter $\frac{q_0 L^4}{E_2 h^4}$ with various span-to-thickness L/h ratios.

Figures 5.9a–b show load-deflection curves of clamped antisymmetric cross-ply $[0^0/90^0]$ and angle-ply $[45^0/-45^0]$ laminates for various span-to-thickness ratio, respectively. It is observed that the degree of nonlinearity in thick plates is more pronounced than in thin plates owing to the effect of shear deformation for both two-layer angle-ply and cross-ply plates.

The effect of span-to-thickness ratios and lamination schemes on the central deflections of two-layer cross-ply and angle-ply laminates are shown in Figure 5.10. It can be seen that for the same span-to-thickness ratio, the angle-ply lamination is stiffer than cross-ply lamination and exhibits a lesser degree of nonlinearity compared to the cross-ply laminates.

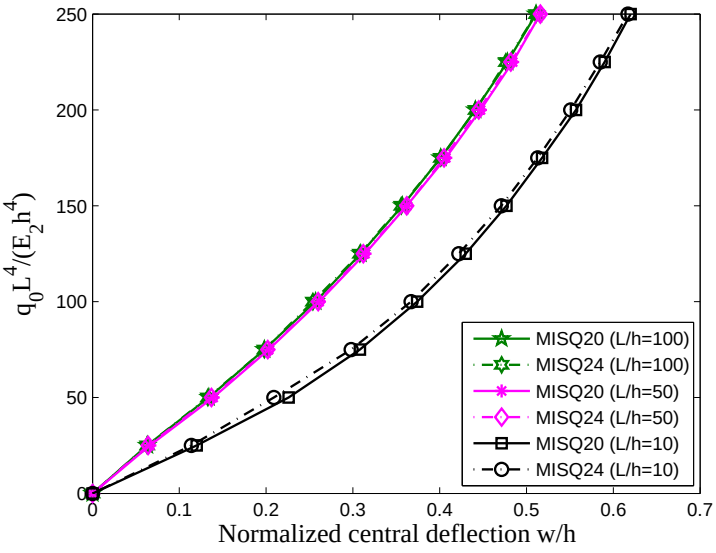

(a)

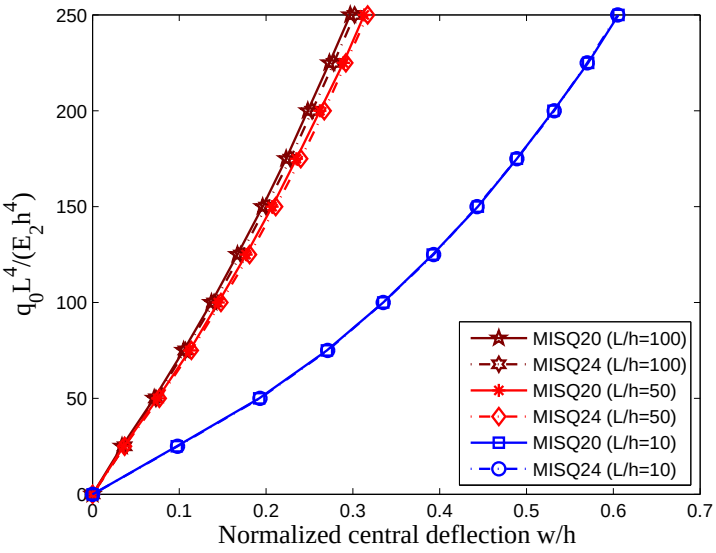

(b)

Figure 5.9: Effect of span-to-thickness ratio L/h on the central deflection of clamped two-layer square plates: (a) cross-ply lamination (b) angle-ply lamination.

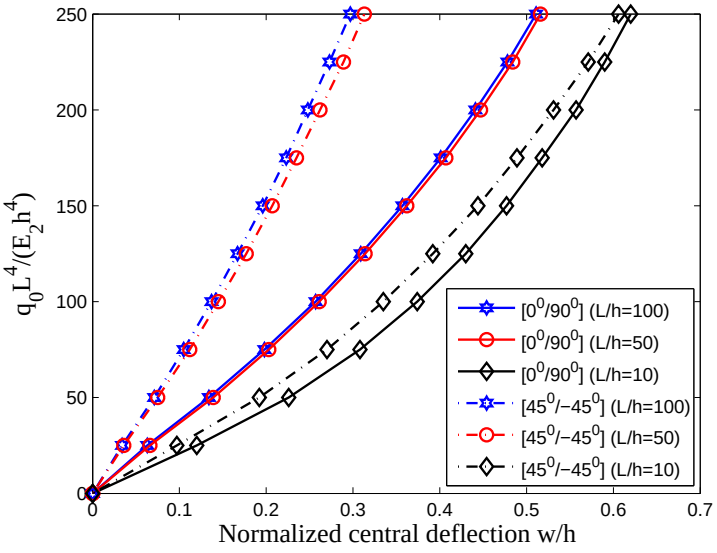

Figure 5.10: Effect of span-to-thickness ratio L/h and lamination scheme on the central deflection of clamped antisymmetric cross-ply and angle-ply square plates.

5.4.5 Clamped isotropic circular plate under uniform pressure

The large deformation analysis of a clamped isotropic circular plate under uniform pressure q_0 is considered in this section. The geometry data and material properties are: radius $R = 100$, thickness $h = 2$, Young's modulus $E = 10^7$, Poisson's ratio $\nu = 0.3$. Owing to symmetry, a quadrant of the plate is modelled with a 27-element mesh as shown in Figure 5.11.

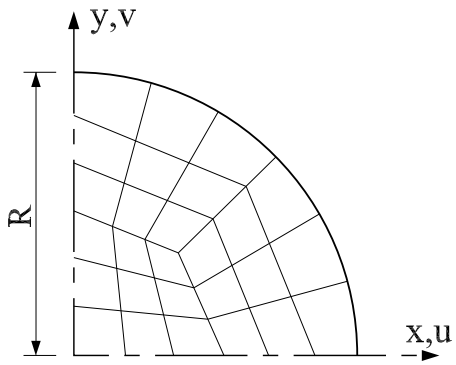

Figure 5.11: A quadrant of a clamped isotropic circular plate under uniform pressure with a mesh of 27 elements.

Table 5.4: Clamped cross-ply $[0^0/90^0]$ and angle-ply $[45^0/-45^0]$ square plates: Effect of the span-to-thickness ratios on normalized central deflections.

L/h	$\frac{q_0 L^4}{E_2 h^4}$	$[0^0/90^0]$		$[45^0/-45^0]$	
		MISQ20	MISQ24	MISQ20	MISQ24
10	25	0.120	0.114	0.097	0.098
	50	0.226	0.209	0.192	0.193
	75	0.308	0.298	0.270	0.271
	100	0.374	0.367	0.335	0.335
	125	0.430	0.422	0.392	0.393
	150	0.477	0.471	0.444	0.443
	175	0.518	0.513	0.489	0.489
	200	0.557	0.551	0.531	0.532
	225	0.590	0.585	0.571	0.570
	250	0.620	0.617	0.606	0.605
50	25	0.066	0.064	0.036	0.037
	50	0.139	0.137	0.075	0.077
	75	0.203	0.202	0.112	0.114
	100	0.261	0.260	0.145	0.148
	125	0.314	0.312	0.177	0.181
	150	0.362	0.362	0.207	0.211
	175	0.407	0.405	0.235	0.240
	200	0.447	0.445	0.262	0.267
	225	0.484	0.482	0.289	0.292
	250	0.516	0.516	0.313	0.317
100	25	0.063	0.063	0.034	0.037
	50	0.134	0.133	0.071	0.073
	75	0.198	0.198	0.105	0.107
	100	0.257	0.254	0.137	0.140
	125	0.309	0.308	0.167	0.171
	150	0.357	0.356	0.196	0.200
	175	0.401	0.401	0.223	0.228
	200	0.441	0.441	0.248	0.253
	225	0.478	0.476	0.273	0.278
	250	0.511	0.511	0.297	0.302

The computed normalized central deflection w/h of the present method, together with the analytic solution of Schoop (1989), and those obtained with Kirchhoff-based elements such as QS element (Pica et al., 1980), DKT element (Stricklin et al., 1969) and RNEM element (Zhang and Kim, 2005) in Table 5.5. The load-deflection curves are also plotted in Figure 5.12 for comparison. It is interesting to note that, the present elements, MISQ20 and MISQ24, show better performance than that of the DKT and RNEM elements for this thin plate problem even through the present elements are based on the thick plate theory.

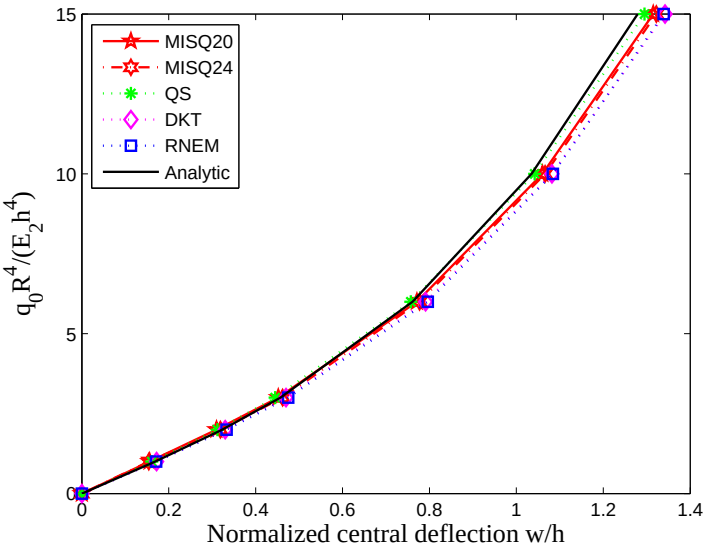

Figure 5.12: Clamped isotropic circular plate under uniformly distributed load: Load-deflection relationship curve.

Table 5.5: Clamped isotropic circular plate under uniformly distributed load: Comparison of normalized central deflections $w^* = w/h$ with other solutions.

$\frac{q_0L^4}{(E_2h^4)}$	MISQ20	MISQ24	QS	DKT	RNEM	Analytic
1	0.156	0.154	0.161	0.172	0.171	0.169
2	0.310	0.319	0.312	0.330	0.333	0.323
3	0.452	0.462	0.445	0.470	0.475	0.457
6	0.771	0.777	0.757	0.791	0.796	0.761
10	1.060	1.066	1.042	1.082	1.084	1.035
15	1.315	1.322	1.295	1.342	1.339	1.279

5.4.6 Clamped isotropic cylindrical shell

A clamped shallow cylindrical shell subjected to a uniformly distributed pressure p is examined (Figure 5.13). The geometry parameters of the shell are: $L = 20,\ R = 100,\ h = 0.125,\ \varphi = 0.1$ and the material properties are: $E = 4.5 \times 10^5,\ \nu = 0.3$.

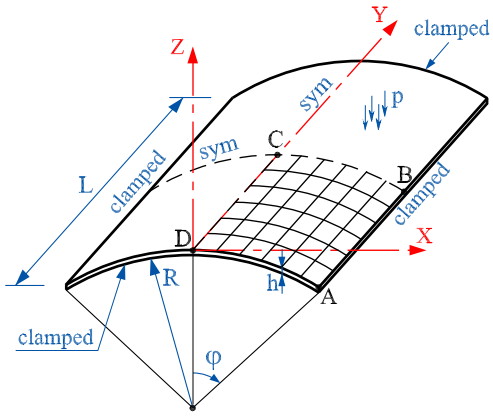

Figure 5.13: Clamped isotropic cylindrical shell under uniform pressure.

Owing to symmetry, only a quadrant of the shell is modelled by 6×6 uniform elements. Figure 5.14 shows the deflection w_c at the center of the shell versus the applied pressure p obtained by the present models together with other solutions of Reddy (2004a) and Palazotto and Dennis (1992). It is observed that the deflection response of this cylindrical shell change from softening to hardening and the trends of these solutions agree well with each others with only small disparities. The present MISQ20 and MISQ24 solutions are closer to those obtained by Reddy with slightly higher values.

5.4.7 Hinged antisymmetrical angle-ply cylindrical shell

This section deals with a two layer angle-ply $[-45^0/45^0]$ cylindrical shell under uniformly distributed transversal pressure p as shown in Figure 5.15. The length of the shell panel is $L = 0.508$ m with a shell radius $R = 2.54$ m, an open angle $2\varphi = 0.2$ rad and a total thickness $h = 0.0124$ m. All layers are of same material properties: $E_1 = 3.2993 \times 10^9$ Pa, $E_2 = 1.0998 \times 10^9$ Pa, $G_{12} = G_{13} = 6.5985 \times 10^8$ Pa, $G_{23} = 4.4128 \times 10^8$ Pa, $\nu_{12} = 0.25$.

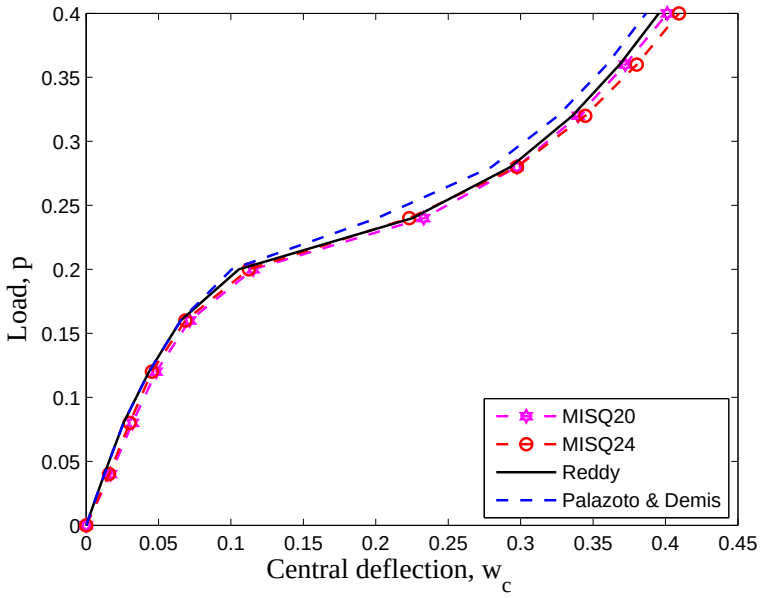

Figure 5.14: Clamped isotropic circular plate under uniformly distributed load: Load-deflection relationship curve.

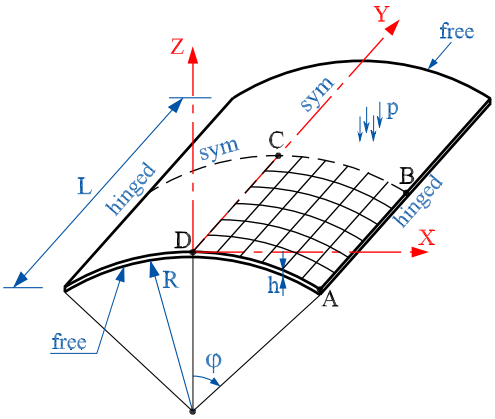

Figure 5.15: A free-hinged angle-ply cylindrical shell under a uniform pressure.

Owing to symmetry, only a quadrant of the shell is modelled by 6×6 uniform elements. The present MISQ20 and MISQ24 results for the central deflection are compared with those obtained by the hybrid strain-based triangular element (HLCTS) of To and Wang (1999). They are plotted together in Figure 5.16. As can be seen, the trends of these results are in good agreement with only slight disparities and they have a limit point at about the same load level. The present elements are also found to be softer than that of the HLCTS element for this problem.

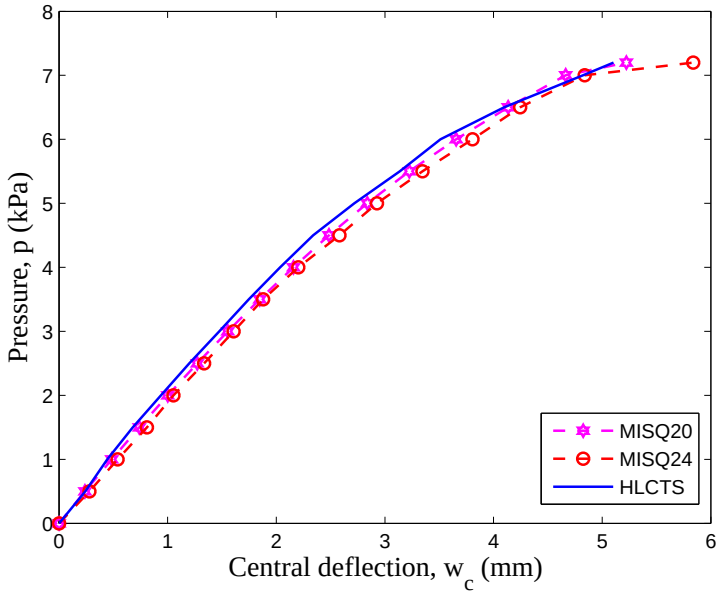

Figure 5.16: A free-hinged angle-ply cylindrical shell under a uniform pressure.

5.4.8 Simply supported cross-ply spherical shell

A simply supported cross-ply 9-layer $[0^0/90^0...]_9$ doubly curved spherical shell under uniform pressure p are analysed in this section. The total thickness of the shell is $h = 0.01$m. The thickness of 0^0 layers is $h/2$ and 90^0 layers is $h/8$. The radius of the shell is $R = 10$m and the projected side length is $a = 1$m. All layers are of same material properties: $E_1 = 2.0685 \times 10^{11}$ Pa, $E_2 = E_1/40$, $G_{12} = 0.6E_2$, $G_{23} = G_{13} = 0.5E_2$, $\nu_{12} = 0.25$.

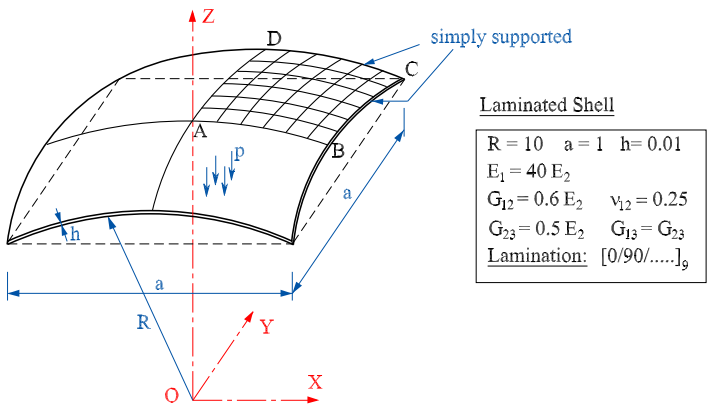

Figure 5.17: A cross-ply spherical shell: Geometry and material data.

By making use of symmetry of geometry and boundary conditions, only one quadrant of the shell is analysed with a 6×6 mesh as shown in Figure 5.17. The present MISQ20 and MISQ24 results for the central deflection are compared with those obtained by the FSDT-based HLCTS element of To and Wang (1999) and the layerwised-based HLCTS element of To and Liu (2001). They are presented together as load-central deflection curves in Figure 5.18. As can be seen, generally the results are in good agreement. The differences may be due to the different shell formulations and solution strategies.

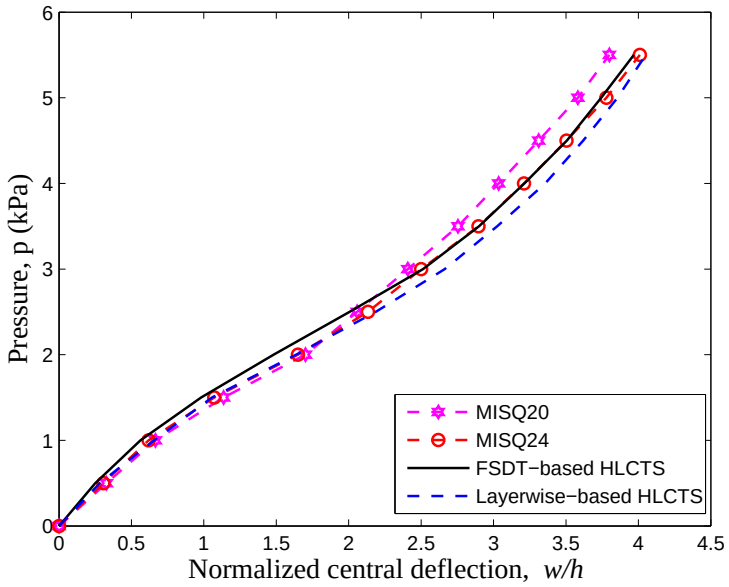

Figure 5.18: A free-hinged angle-ply cylindrical shell under a uniform pressure.

5.4.9 Pinched semi-cylindrical cross-ply laminated shells

The last problem considered in this section is that of a pinched semi-cylindrical cross-ply $[0^0/90^0/0^0]$ shell, subjected to a point load at the middle of the free-hanging circumferential segment while the other circumferential edge is fully clamped. The shell is also hinged along its longitudinal edges. Geometry data and material properties of the shell are shown in Figure 5.19.

Taking advantage of symmetry, a half of the shell is modelled and analysed with 16×16 elements. The present computed results for the downward normalized

deflection of point A are plotted together with those reported by Andrade et al. (2007), using the 8-node hexahedral element, in Figure 5.20, where good agreement is observed for both MISQ20 and MISQ24 elements.

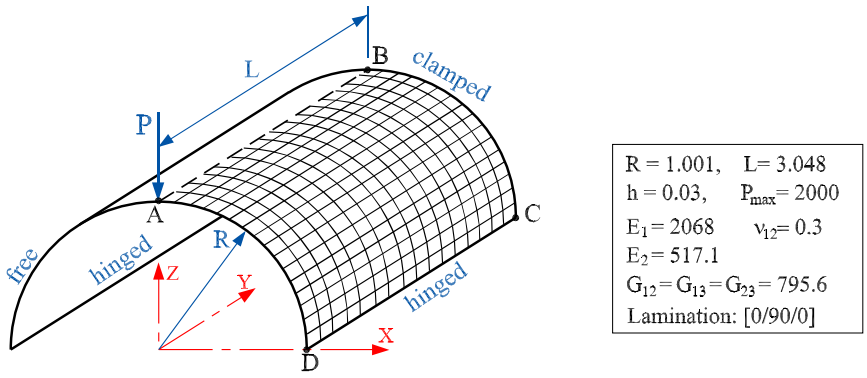

Figure 5.19: Semi-cylindrical shell under an end pinching force: Geometry and material data.

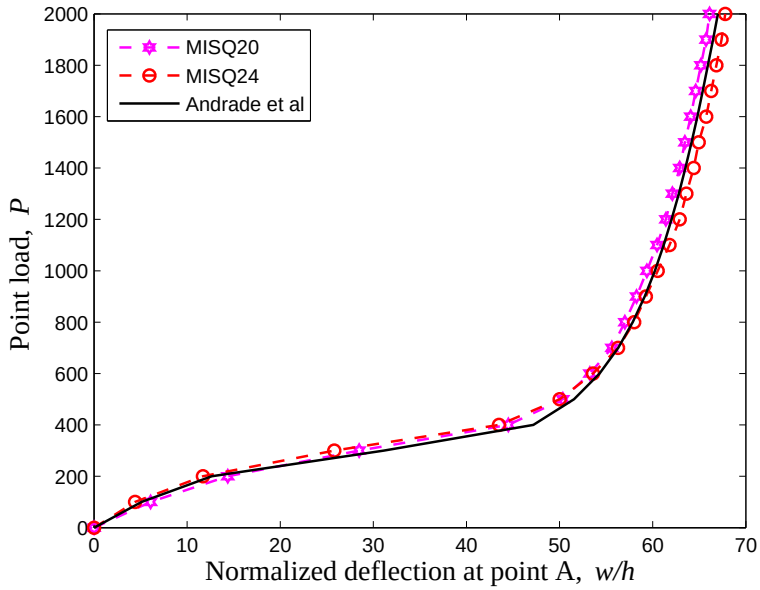

Figure 5.20: Semi-cylindrical shell under an end pinching force: Load-deflection curves at point load.

5.5 Concluding remarks

In this chapter, the present MISQ20 and MISQ24 elements have been extended successfully to geometrically nonlinear analysis of plate and shell structures in the framework of the FSDT. The von Karman's large deflection theory and the Total Lagrangian approach are employed in the formulation of the elements to describe small strain geometric nonlinearity with large displacements. Several numerical examples have been carried out and the present elements are found to yield satisfactory results in comparison with other available finite element solutions as well as theorical/experimental results. Both MISQ20 and MISQ24 elements are able to offer good prediction in geometrically nonlinear analysis of thin to moderately thick plates/shells. No shear-locking is found in the numerical investigations and the elements provide good accuracy even with coarse meshes or distorted elements. In addition, the present elements have the advantage of being simple in formulation and ready for use in both plate and shell structures with a minimal amount of effort to implement. The success of the present flat/shell elements provide a further demonstration of efficient flat quadrilateral elements for nonlinear analysis.

Chapter 6

Assumed Strain Smoothing Methods for Piezoelectric Materials

In this chapter, two types of the novel piezoelectric elements based on the assumed strain smoothing technique (Nguyen-Van et al., 2008a,b,c) are presented for static and dynamic analysis of the electromechanical coupling behaviour of piezoelectric solids. Two approaches are proposed to transform original finite elements into smoothing elements in which the strain smoothing operation of the SCNI is performed. The first scheme forms the so-called cell-based element approach and the second the node-based element approach. In both approaches, the approximations of mechanical strains and electric potential fields are normalized by the smoothing constant function of the SCNI technique over each smoothing cell. This method allows field gradients to be directly computed from interpolating shape functions using boundary integrations along the boundary of the smoothing element. The boundary integration will contribute to the preservation of high accuracy of the method even when elements are extremely distorted, for example, a concave quadrilateral. No mapping or coordinate transformation and derivatives of shape functions are necessary so that the original meshes with badly shaped elements, can be used. Furthermore, the present elements do not introduce any additional degrees of freedom and are easy to implement into an existing FEM.

Numerical examples and comparative studies with analytic solutions are presented to demonstrate the simplicity, efficiency and accuracy of the developed elements.

6.1 Introduction

Piezoelectric materials are perhaps the most widely used of the smart materials. They are usually integrated with structural systems to form a class of smart/intelligent or adaptive structures. Piezoelectric materials have a great range of engineering applications owing to its inexpensive cost, light weight, high stiffness and the ease with which these materials can be shaped and bonded to surfaces or embedded into structures. The material generates an electric charge under a mechanical load or imposed deformation, which is called the direct piezoelectric effect and conversely, mechanical stress or strain occurs when the material is subjected to an applied electric potential, which is termed as the converse piezoelectric effect. Therefore, piezoelectric materials can be used as sensor (passive) or actuator (active) or both at different times to monitor and actively control vibration, noise and shape of a structural system. They can be also used as a medium to transform electrical and acoustic waves in telecommunication or in an accelerometer.

Significant progress has been made over past decades in analyzing such materials and structures with various approaches, including analytic methods and experimental/numerical models, by many researchers. For example, analytical methods were initially proposed for analysis of beam with piezoelectric patches (Crawley and Luis, 1987; Im and Atluri, 1989; Shen, 1995) and later for piezoelectric flat panels and plates (Tzou and Tiersten, 1994; Bisegna and Maceri, 1996; Ray et al., 1998; Han et al., 2006), etc. However, due to the complexity of governing equations in piezoelectricity, so far only a few simple problems have been solved analytically.

The first significant numerical attempt using finite element implementation for piezoelectric phenomenon was a piezoelectric vibration analysis proposed by Allik and Hughes (1970). Since then, the FEM has been considered as a powerful tool for the numerical analysis and design of piezoelectric devices and smart/adaptive

structural systems. Most of the finite element models, following the work of Allik and Hughes, are based on the interpolation of displacement and electric potential as kinematic field variables that satisfy compatibility equations. These elements are often too stiff, inaccurate and sensitive to mesh distortion. To overcome these shortcomings, hybrid and mixed finite element have been developed, with notable contributions from Cannarozzi and Ubertini (2001) and Sze's group (Sze and Pan, 1999; Sze and Yao, 2000; Wu et al., 2001; Sze et al., 2004). Other relevant works include piezoelectric elements with drilling degrees of freedom of Long, Loveday and Groenwold (2006) and Zemcik et al. (2007). More details and reviews on the development of the finite element methods applied to the modeling and analysis of piezoelectric material and smart structures can be found in Mackerle (2003). So far, many researchers are still actively involved in the development of new special elements as can be seen from recent works of Benjeddou (2000) and Carrera and Boscolo (2007).

Although the FEM is considered to be a versatile and effective numerical method, there often exist difficulties and deteriorations in performance when mesh distortion occurs. On the other hand, several mesh-free methods have become an alternative approach for analysis of piezoelectric material, including the Radial Point Interpolation Meshfree (RIPM) method (Liu et al., 2003), the Point Interpolation Meshfree (PIM) method (Liu et al., 2002), the Point Collocation Meshfree (PCM) method (Ohs and Aluru, 2001), the Element Free Galerkin (EFG) method (Liew et al., 2002), the Meshless Local Petrov-Galerkin (MLPG) method (Sladek et al., 2006, 2007), etc. However, the complex approximation space of mesh-free methods increases the computational cost for numerical integrations.

In this chapter, new formulations for piezoelectric solids based on the ASS technique of the SCNI are further developed in order to remedy the shortcomings mentioned above. In these new element formulations, the approximation of mechanical and dielectric displacements are similar to the conventional finite element method while mechanical strains and electric potential fields are normalized by a constant smoothing function on smoothing cells (smoothing elements). Two different schemes are developed to transform an original finite element or a group of original finite elements into smoothing elements. The first scheme forms the so-called cell-based element approach and the second one the node-based element

approach. The cell-based element is constructed by the subdivision of original quadrilateral elements into smoothing-cells while the node-based element is created by transforming a given more general mesh (triangular or quadrilateral elements) into a mesh of new smoothing cells and each of these new elements is associated with a single node of the original mesh. Problem domains, therefore, can be discretized with more flexibility in terms of element shapes. Several numerical examples and comparison with other numerical or analytic solutions in the literature are carried out here to demonstrate the capability, efficiency and reliability of the present novel element. Numerical experiment does show that the proposed elements are robust and uniformly accurate in modelling static behavior of planar electro-mechanical problems even in the case of extremely distorted meshes or coarse discretization.

This chapter is outlined as follows. First, a brief review of the constitutive relations of linear piezoelectricity is introduced in Section 6.2. Finite element formulations for modelling piezoelectric solids are then summarized in Section 6.3. The description of strain smoothing method for piezoelectric material is derived in Section 6.4. Several numerical applications are investigated in Section 6.5 to assess the performances of the proposed elements. Finally, some concluding remarks are drawn in Section 6.6.

6.2 Linear piezoelectric constitutive relations

An important characteristic of piezoelectric materials compared to other smart materials is its linear behaviour within a certain range. In this section, only the piezoelectric coupling is considered and the thermoelectric terms are neglected. The following constitutive relations are referred to as the $e-$forms and given in more detail in references (Lines and Glass, 1977; Ikeda, 1996). The related energy expression is defined as Gibb's free energy G

$$G = \frac{1}{2}\boldsymbol{\epsilon}^T\mathbf{c}^E\boldsymbol{\epsilon} - \mathbf{E}^T\mathbf{e}\boldsymbol{\epsilon} - \frac{1}{2}\mathbf{E}^T\mathbf{g}\mathbf{E}, \tag{6.1}$$

where $\boldsymbol{\epsilon}$ is the strain vector, $\mathbf{E}$ is the electric field vector, $\mathbf{c}^E$ is the elastic stiffness matrix computed at constant electric field $\mathbf{E}$, $\mathbf{e}$ is the piezoelectric matrix which

couples electrical and mechanical fields and $\mathbf{g}$ is the dielectric constant matrix computed at constant mechanical strain $\boldsymbol{\epsilon}$.

The terms relating to the independent and dependent field variables are defined by the following well-known material constants

$$g_{mn} = -\frac{\partial^2 G}{\partial E_m \partial E_n}, \qquad e_{nij} = -\frac{\partial^2 G}{\partial E_n \partial \epsilon_{ij}}, \qquad c^E_{ijkl} = \frac{\partial^2 G}{\partial \epsilon_{kl} \partial \epsilon_{ij}} \tag{6.2}$$

The stress vector $\boldsymbol{\sigma}$ and the electric displacement vector $\mathbf{D}$ can be obtained by the expressions

$$\boldsymbol{\sigma} = \frac{\partial G}{\partial \boldsymbol{\epsilon}} \tag{6.3}$$

$$\mathbf{D} = -\frac{\partial G}{\partial \mathbf{E}} \tag{6.4}$$

Substituting Equation (6.1) into Equation (6.3)–(6.4), the constitutive equations can be expressed in the $e-$form as follows:

$$\boldsymbol{\sigma} = \mathbf{c}^E \boldsymbol{\epsilon} - \mathbf{e}^T \mathbf{E}, \text{ (converse effect)} \tag{6.5}$$

$$\mathbf{D} = \mathbf{e}\boldsymbol{\epsilon} + \mathbf{g}\mathbf{E}. \text{ (direct effect)} \tag{6.6}$$

The explicit constitutive forms in the material reference system $1-2-3$ are

$$\begin{bmatrix} \sigma_1 \\ \sigma_2 \\ \sigma_3 \\ \sigma_4 \\ \sigma_5 \\ \sigma_6 \end{bmatrix} = \begin{bmatrix} c_{11} & c_{12} & c_{13} & 0 & 0 & c_{16} \\ c_{12} & c_{22} & c_{23} & 0 & 0 & c_{26} \\ c_{13} & c_{23} & c_{33} & 0 & 0 & c_{36} \\ 0 & 0 & 0 & c_{44} & c_{45} & 0 \\ 0 & 0 & 0 & c_{45} & c_{55} & 0 \\ c_{16} & c_{26} & c_{36} & 0 & 0 & c_{66} \end{bmatrix} \begin{bmatrix} \epsilon_1 \\ \epsilon_2 \\ \epsilon_3 \\ \epsilon_4 \\ \epsilon_5 \\ \epsilon_6 \end{bmatrix} - \begin{bmatrix} 0 & 0 & e_{31} \\ 0 & 0 & e_{32} \\ 0 & 0 & e_{33} \\ e_{14} & e_{24} & 0 \\ e_{15} & e_{25} & 0 \\ 0 & 0 & e_{36} \end{bmatrix} \begin{bmatrix} E_1 \\ E_2 \\ E_3 \end{bmatrix} \tag{6.7}$$

$$\begin{bmatrix} D_1 \\ D_2 \\ D_3 \end{bmatrix} = \begin{bmatrix} 0 & 0 & 0 & e_{14} & e_{15} & 0 \\ 0 & 0 & 0 & e_{24} & e_{25} & 0 \\ e_{31} & e_{32} & e_{33} & 0 & 0 & e_{36} \end{bmatrix} \begin{bmatrix} \epsilon_1 \\ \epsilon_2 \\ \epsilon_3 \\ \epsilon_4 \\ \epsilon_5 \\ \epsilon_6 \end{bmatrix} + \begin{bmatrix} g_{11} & g_{12} & 0 \\ g_{12} & g_{22} & 0 \\ 0 & 0 & g_{33} \end{bmatrix} \begin{bmatrix} E_1 \\ E_2 \\ E_3 \end{bmatrix} \tag{6.8}$$

By incorporating the plane assumptions and taking the $z-$axis as the poling direction, the constitutive relations can be reduced and expressed in the following forms

$$\begin{bmatrix} \sigma_x \\ \sigma_z \\ \tau_{xz} \end{bmatrix} = \begin{bmatrix} c_{11} & c_{13} & 0 \\ c_{13} & c_{33} & 0 \\ 0 & 0 & c_{55} \end{bmatrix} \begin{bmatrix} \epsilon_x \\ \epsilon_z \\ \gamma_{xz} \end{bmatrix} - \begin{bmatrix} 0 & e_{31} \\ 0 & e_{33} \\ e_{15} & 0 \end{bmatrix} \begin{bmatrix} E_x \\ E_z \end{bmatrix}, \tag{6.9}$$

$$\begin{bmatrix} D_x \\ D_z \end{bmatrix} = \begin{bmatrix} 0 & 0 & e_{15} \\ e_{31} & e_{33} & 0 \end{bmatrix} \begin{bmatrix} \epsilon_x \\ \epsilon_z \\ \gamma_{xz} \end{bmatrix} - \begin{bmatrix} g_{11} & 0 \\ 0 & g_{33} \end{bmatrix} \begin{bmatrix} E_x \\ E_z \end{bmatrix}. \tag{6.10}$$

If the piezoelectric stress constants are unavailable in Equation (6.9) or (6.10), they can be obtained by using the following relationship

$$\begin{bmatrix} 0 & 0 & e_{15} \\ e_{31} & e_{33} & 0 \end{bmatrix} = \begin{bmatrix} 0 & 0 & d_{15} \\ d_{31} & d_{33} & 0 \end{bmatrix} \begin{bmatrix} c_{11} & c_{13} & 0 \\ c_{13} & c_{33} & 0 \\ 0 & 0 & c_{55} \end{bmatrix}. \tag{6.11}$$

in which $[d]$ is the piezoelectric strain constant matrix.

6.3 Review of finite element formulations for 2D piezoelectric problems

In this section, the variational form and finite element formulations of piezoelectric solids are briefly reviewed. A two-dimensional piezoelectric problem in domain Ω bounded by Γ is considered. For linear piezoelectric materials, the governing equations and boundary conditions can be described as

$$\sigma_{ij,i} + f_j = \rho \ddot{u}_j, \tag{6.12}$$

$$\epsilon_{ij} = \frac{1}{2}(u_{i,j} + u_{j,i}), \tag{6.13}$$

$$D_{i,i} = 0, \tag{6.14}$$

$$E_i = -\phi_{,i}, \tag{6.15}$$

together with the following boundary conditions

$$\sigma_{ij}n_j = \bar{t}_i \quad \text{on} \quad \Gamma_\sigma, \qquad u_i = \bar{u}_i \quad \text{on} \quad \Gamma_u, \tag{6.16}$$

$$\phi = \bar{\phi} \quad \text{on} \quad \Gamma_\phi, \qquad D_i n_i = -\bar{q} \quad \text{on} \quad \Gamma_q, \tag{6.17}$$

where σ_{ij}, ϵ_{ij} represent stress and strain tensor respectively, f_j is the body force density, u_j is the mechanical displacement vector, ρ is the mass density, D_i is the dielectric displacement vector, E_i is the electric field vector and ϕ is the scalar electric potential field.

The Lagrangian functional L is obtained by summing the kinetic energy, strain energy, dielectric energy and potential energy of external fields as follows.

$$L = \int_\Omega \left[\frac{1}{2}\rho\dot{\mathbf{u}}^T\dot{\mathbf{u}} - \frac{1}{2}\boldsymbol{\epsilon}^T\boldsymbol{\sigma} + \frac{1}{2}\mathbf{D}^T\mathbf{E} + \mathbf{u}^T\mathbf{f}\right] d\Omega + \int_\Gamma \left[\mathbf{u}^T\bar{\mathbf{t}} + \phi^T\bar{\mathbf{q}}\right] d\Gamma. \tag{6.18}$$

Then the variational form of the equations of motion can be derived using Hamilton's principle

$$\int_\Omega [\delta\boldsymbol{\epsilon}^T\boldsymbol{\sigma} + \delta\mathbf{u}^T\rho\ddot{\mathbf{u}} - \delta\mathbf{E}^T\mathbf{D} - \delta\mathbf{u}^T\mathbf{f}]d\Omega - \int_\Gamma [\delta\mathbf{u}^T\bar{\mathbf{t}} + \delta\phi^T\bar{\mathbf{q}}]d\Gamma = 0. \tag{6.19}$$

The finite element approximation solution for 2D piezoelectric problems using the standard 4-node quadrilateral element can be expressed as

$$\mathbf{u} = \sum_{i=1}^{4} \mathbf{N}_u^i \mathbf{q}_i = \mathbf{N}_u\mathbf{q}, \tag{6.20}$$

$$\boldsymbol{\phi} = \sum_{i=1}^{4} \mathbf{N}_\phi^i \boldsymbol{\phi}_i = \mathbf{N}_\phi\boldsymbol{\varphi}, \tag{6.21}$$

where $\mathbf{q}$ and $\boldsymbol{\varphi}$ are the nodal displacement and nodal electric potential vectors, $\mathbf{N}_u$ and $\mathbf{N}_\phi$ are shape function matrices. They are given by

$$\mathbf{q}_i = [u_i \quad v_i], \tag{6.22}$$

$$\boldsymbol{\phi}_i = [\phi_i], \tag{6.23}$$

$$\mathbf{N}_u^i = \begin{bmatrix} N_i & 0 \\ 0 & N_i \end{bmatrix}, \tag{6.24}$$

$$\mathbf{N}_\phi^i = [N_i], \tag{6.25}$$

in which $N_i = \frac{1}{4}(1+\xi_i\xi)(1+\eta_i\eta)$ is the bilinear shape function of the four-node serendipity element.

The corresponding approximation of the linear strain $\boldsymbol{\epsilon}$ and electric field $\mathbf{E}$ are

$$\boldsymbol{\epsilon} = \nabla_s \mathbf{u} = \begin{bmatrix} \frac{\partial}{\partial x} & 0 \\ 0 & \frac{\partial}{\partial z} \\ \frac{\partial}{\partial z} & \frac{\partial}{\partial x} \end{bmatrix} \mathbf{u} = \sum_{i=1}^{4} \mathbf{B}_u^i \mathbf{q}_i, \tag{6.26}$$

$$\mathbf{E} = -\nabla\phi = -\sum_{i=1}^{4} \mathbf{B}_\phi^i \boldsymbol{\phi}_i, \tag{6.27}$$

where

$$\mathbf{B}_u^i = \begin{bmatrix} N_{i,x} & 0 \\ 0 & N_{i,z} \\ N_{i,z} & N_{i,x} \end{bmatrix}, \tag{6.28}$$

$$\mathbf{B}_\phi^i = \begin{bmatrix} N_{i,x} \\ N_{i,z} \end{bmatrix}. \tag{6.29}$$

It should be noted that Equation (6.28)–(6.29) are derived for plane stress/strain problems. For axisymmetric problems, they should be modified into the following expressions

$$\mathbf{B}_u^i = \begin{bmatrix} N_{i,r} & 0 \\ \frac{N_i}{r} & 0 \\ 0 & N_{i,z} \\ N_{i,z} & N_{i,r} \end{bmatrix}, \tag{6.30}$$

$$\mathbf{B}_\phi^i = \begin{bmatrix} N_{i,r} \\ \frac{N_i}{r} \\ N_{i,z} \end{bmatrix}. \tag{6.31}$$

where r is evaluated at the centroid of the element.

Substituting Equations (6.26)–(6.29) into Equation (6.19) leads to the piezoelectric dynamic equations

$$\begin{bmatrix} \mathbf{M}_{uu} & 0 \\ 0 & 0 \end{bmatrix} \begin{Bmatrix} \ddot{\mathbf{q}} \\ \ddot{\boldsymbol{\varphi}} \end{Bmatrix} + \begin{bmatrix} \mathbf{K}_{uu} & \mathbf{K}_{u\phi} \\ \mathbf{K}_{u\phi} & \mathbf{K}_{\phi\phi} \end{bmatrix} \begin{Bmatrix} \mathbf{q} \\ \boldsymbol{\varphi} \end{Bmatrix} = \begin{Bmatrix} \mathbf{F} \\ \mathbf{Q} \end{Bmatrix}, \tag{6.32}$$

in which

$$\mathbf{M}_{uu} = \int_{\Omega} \rho \mathbf{N}_u^T \mathbf{N}_u d\Omega, \tag{6.33}$$

$$\mathbf{K}_{uu} = \int_{\Omega} \mathbf{B}_u^T \mathbf{c}^E \mathbf{B}_u d\Omega, \tag{6.34}$$

$$\mathbf{K}_{u\phi} = \int_{\Omega} \mathbf{B}_u^T \mathbf{e}^T \mathbf{B}_\phi d\Omega, \tag{6.35}$$

$$\mathbf{K}_{\phi\phi} = -\int_{\Omega} \mathbf{B}_\phi^T \mathbf{g} \mathbf{B}_\phi d\Omega, \tag{6.36}$$

$$\mathbf{F} = \int_{\Omega} \mathbf{N}_u^T \mathbf{f} d\Omega + \int_{\Gamma_\sigma} \mathbf{N}_u^T \bar{\mathbf{t}} d\Gamma, \tag{6.37}$$

$$\mathbf{Q} = \int_{\Gamma_q} \mathbf{N}_\phi^T \bar{\mathbf{q}} d\Gamma. \tag{6.38}$$

For free vibration and considering the n^{th} mode, Equation (6.32) can be written as

$$(\mathbf{K}_{uu} - \omega_n^2 \mathbf{M}_{uu})\mathbf{q} + \mathbf{K}_{u\phi}\boldsymbol{\varphi} = 0, \tag{6.39}$$

$$\mathbf{K}_{\phi u}\mathbf{q} + \mathbf{K}_{\phi\phi}\boldsymbol{\varphi} = 0, \tag{6.40}$$

where ω_n is the natural frequency of mode n. By performing the condensation of the electric potential degree of freedom, the eigenvalue equation can be obtained as follows.

$$[(\mathbf{K}_{uu} - \mathbf{K}_{u\phi}\mathbf{K}_{\phi\phi}^{-1}\mathbf{K}_{\phi u}) - \omega_n^2 \mathbf{M}_{uu}]\mathbf{q} = 0. \tag{6.41}$$

6.4 Strain smoothing approach for piezoelectric finite element method

6.4.1 Cell-based strain smoothing approach

The smoothed strain and smoothed electric field at an arbitrary point $\mathbf{x}_C$ are obtained by

$$\tilde{\boldsymbol{\epsilon}}(\mathbf{x}_C) = \int_{\Omega_C} \boldsymbol{\epsilon}(\mathbf{x}) \Phi(\mathbf{x} - \mathbf{x}_C) d\Omega, \tag{6.42}$$

$$\tilde{\mathbf{E}}(\mathbf{x}_C) = \int_{\Omega_C} \mathbf{E}(\mathbf{x}) \Phi(\mathbf{x} - \mathbf{x}_C) d\Omega, \tag{6.43}$$

where $\boldsymbol{\epsilon}$, $\mathbf{E}$ are respectively the mechanical strain and electric field obtained from displacement compatibility condition as given in Equations (6.26)–(6.27). Ω_C is the smoothing cell domain on which the smoothing operation is performed. Depending on the stability analysis (Liu, Dai and Nguyen, 2007; Liu, Nguyen, Dai and Lam, 2007), Ω_C may be an entire element or part of an element as shown in Figure 6.1. Φ is a smoothing function that satisfies the following properties

$$\Phi \geq 0 \qquad \text{and} \qquad \int_\Omega \Phi \mathrm{d}\Omega = 1. \tag{6.44}$$

For simplicity, Φ is chosen as a constant function

$$\Phi(\mathbf{x} - \mathbf{x}_C) = \begin{cases} 1/A_C & \mathbf{x} \in \Omega_C, \\ 0 & \mathbf{x} \notin \Omega_C. \end{cases} \tag{6.45}$$

where $A_C = \int_{\Omega_C} d\Omega$ is the area of the smoothing cell (subcell).

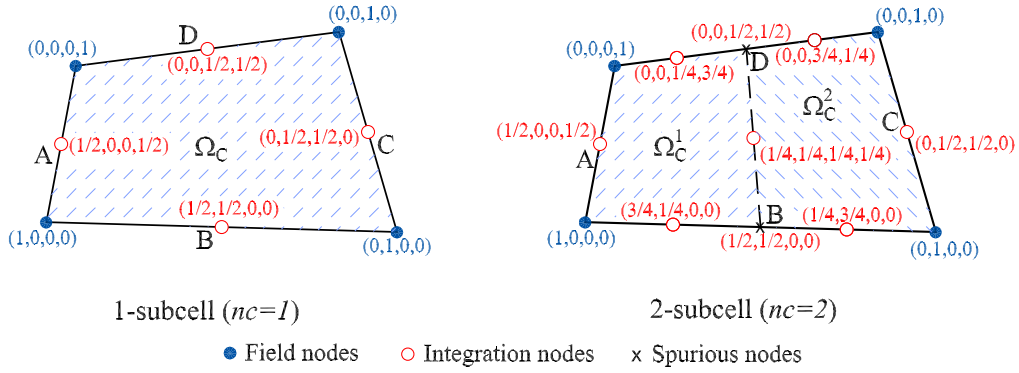

Figure 6.1: Subdivision of an element into nc smoothing cells and the values of shape functions at nodes.

Substituting Φ into Equation (6.42)–(6.43) and applying the divergence theorem, we obtain a smoothed strain and smoothed electric field in the domain Ω_C as follows.

$$\tilde{\boldsymbol{\epsilon}}(\mathbf{x}_C) = \tfrac{1}{A_C} \int_{\Omega_C} \nabla_s \mathbf{u}(\mathbf{x}) d\Omega = \tfrac{1}{A_C} \int_{\Gamma_C} \mathbf{n}_u \mathbf{u}(\mathbf{x}) d\Gamma, \tag{6.46}$$

$$\tilde{\mathbf{E}}(\mathbf{x}_C) = -\tfrac{1}{A_C} \int_{\Omega_C} \nabla \boldsymbol{\phi}(\mathbf{x}) d\Omega = -\tfrac{1}{A_C} \int_{\Gamma_C} \mathbf{n}_\phi \boldsymbol{\phi}(\mathbf{x}) d\Gamma, \tag{6.47}$$

where $\mathbf{n}_u$ and $\mathbf{n}_\phi$ are matrices containing unit outward vector normal to the bound-

ary Γ_C

$$\mathbf{n}_u = \begin{bmatrix} n_x & 0 \\ 0 & n_z \\ n_z & n_x \end{bmatrix}, \quad \mathbf{n}_\phi = [n_x \quad n_z]^T. \tag{6.48}$$

Introducing the finite element approximation of $\mathbf{u}$ and $\boldsymbol{\phi}$ into Equations (6.46) and (6.47) one gets

$$\tilde{\boldsymbol{\epsilon}}(\mathbf{x}_C) = \sum_{i=1}^{nc} \tilde{\mathbf{B}}_{ui}(\mathbf{x}_C)\mathbf{q}_i, \tag{6.49}$$

$$\tilde{\mathbf{E}}(\mathbf{x}_C) = -\sum_{i=1}^{nc} \tilde{\mathbf{B}}_{\phi i}(\mathbf{x}_C)\boldsymbol{\phi}_i, \tag{6.50}$$

in which

$$\tilde{\mathbf{B}}_{ui}(\mathbf{x}_C) = \frac{1}{A_C}\int_{\Gamma_C} \begin{bmatrix} N_i n_x & 0 \\ 0 & N_i n_z \\ N_i n_z & N_i n_x \end{bmatrix} d\Gamma, \tag{6.51}$$

$$\tilde{\mathbf{B}}_{\phi i}(\mathbf{x}_C) = \frac{1}{A_C}\int_{\Gamma_C} \begin{bmatrix} N_i n_x \\ N_i n_z \end{bmatrix} d\Gamma. \tag{6.52}$$

Using one Gauss point to evaluate Equation (6.51) and (6.52) along each line segment of the boundary Γ_i^C of Ω_C, they can be transformed as

$$\tilde{\mathbf{B}}_{ui}(\mathbf{x}_C) = \frac{1}{A_C}\sum_{b=1}^{nb} \begin{bmatrix} N_i(\mathbf{x}_b^G) n_x & 0 \\ 0 & N_i(\mathbf{x}_b^G) n_z \\ N_i(\mathbf{x}_b^G) n_z & N_i(\mathbf{x}_b^G) n_x \end{bmatrix} l_b^C, \tag{6.53}$$

$$\tilde{\mathbf{B}}_{\phi i}(\mathbf{x}_C) = \frac{1}{A_C}\sum_{b=1}^{nb} \begin{bmatrix} N_i(\mathbf{x}_b^G) n_x \\ N_i(\mathbf{x}_b^G) n_z \end{bmatrix} l_b^C, \tag{6.54}$$

where $\mathbf{x}_b^G$ and l_b^C are the midpoint (Gauss point) and the length of Γ_b^C, respectively; nb is the total number of edges of each smoothing cell ($nb = 4$ in this case).

Finally, the linear equations of motion (6.32) can be rewritten as follows

$$\begin{bmatrix} \mathbf{M}_{uu} & 0 \\ 0 & 0 \end{bmatrix} \begin{Bmatrix} \ddot{\mathbf{q}} \\ \ddot{\boldsymbol{\varphi}} \end{Bmatrix} + \begin{bmatrix} \tilde{\mathbf{K}}_{uu} & \tilde{\mathbf{K}}_{u\phi} \\ \tilde{\mathbf{K}}_{u\phi} & \tilde{\mathbf{K}}_{\phi\phi} \end{bmatrix} \begin{Bmatrix} \mathbf{q} \\ \boldsymbol{\varphi} \end{Bmatrix} = \begin{Bmatrix} \mathbf{F} \\ \mathbf{Q} \end{Bmatrix}, \tag{6.55}$$

where

$$\tilde{\mathbf{K}}^e_{uu} = \sum_{C=1}^{nc} \tilde{\mathbf{B}}^T_{uC} \mathbf{c}^E \tilde{\mathbf{B}}_{uC} A_C, \tag{6.56}$$

$$\tilde{\mathbf{K}}^e_{u\phi} = \sum_{C=1}^{nc} \tilde{\mathbf{B}}^T_{uC} \mathbf{e}^T \tilde{\mathbf{B}}_{\phi C} A_C, \tag{6.57}$$

$$\tilde{\mathbf{K}}^e_{\phi\phi} = -\sum_{C=1}^{nc} \tilde{\mathbf{B}}^T_{\phi C} \mathbf{g}^T \tilde{\mathbf{B}}_{\phi C} A_C. \tag{6.58}$$

Equation (6.55) forms the basis of the smoothed piezoelectric finite element method. In this work, four-node quadrilateral element is employed for domain discretization. Two smoothing cells or subcells ($nc = 2$) are used to evaluate Equation (6.56)–(6.58). Further increase of nc will lead to higher computational cost but the accuracy may not be better because this results in stiffer system (Liu, Nguyen, Dai and Lam, 2007). The obtained four-node piezoelectric element with two smoothing cells is named SPQ4 (Smoothed Piezoelectric Quadrilateral 4-node element).

In order to clarify how the cell-based smoothing technique is incorporated into a finite element code, a numerical implementation for computing the element stiffness matrix is briefly presented as follows.

1. Initialize the number of smoothing cell nc
2. Estimate shape function matrix $\mathbf{N}_i$ at field nodes: $\mathbf{N}(\mathbf{x}) = \mathbf{N}(\mathbf{x}_{field})$
3. Create spurious nodes (no associated DOFs) at mid-side edges:
   - Compute $\mathbf{N}_i$ at spurious nodes
   - Update $\mathbf{N}(\mathbf{x}) = [\mathbf{N}(\mathbf{x}_{field});\ \mathbf{N}(\mathbf{x}_{spur})]$
4. Setup a connective matrix (**cells**) for each smoothing cell
5. Calculate and assemble element stiffness matrices to build the system stiffness matrix:

   Loop over all subcells, $ic = 1$ to nc
   - Compute the unit outward normal vector $\mathbf{n}$ on each side of a subcell
   - Compute the area A^{ic} of each subcell

- Loop over 4 sides of each subcell, $iside = 1$ to 4
  - ∘ Loop over Gauss points on each side, $ig = 1$ to 4

    if $iside < 4$ then

    $N(ig) = \frac{1}{2}\{\mathbf{N}(cells(ic, iside), ig) + \mathbf{N}(cells(ic, iside + 1), ig)\}$

    else

    $N(ig) = \frac{1}{2}\{\mathbf{N}(cells(ic, iside), ig) + \mathbf{N}(cells(ic, iside - 3), ig)\}$
  - ∘ End the loop over Gauss points on each side
  - ∘ Compute the gradient matrix $\tilde{\mathbf{B}}_u^{ic}$, $\tilde{\mathbf{B}}_\phi^{ic}$ using Equation (6.53)–(6.54)
- End loop over 4 sides of each subcell
- Compute the stiffness matrices $\tilde{\mathbf{K}}_{uu}^{ic}$, $\tilde{\mathbf{K}}_{u\phi}^{ic}$ and $\tilde{\mathbf{K}}_{\phi\phi}^{ic}$ corresponding to the Ω^{ic} using Equation (6.56)–(6.58)
- Update the smoothed element stiffness matrices and assemble $\tilde{\mathbf{K}}^e \longleftarrow \tilde{\mathbf{K}}^e + \tilde{\mathbf{K}}^{ic}$

End the loop over all nodes.

6.4.2 Node-based strain smoothing approach

Consider a problem domain Ω with a mesh of triangular or quadrilateral elements numbered from 1 to N_e and nodes numbered from 1 to N_n. The basic idea of the following development is to associate new elements (smoothing elements) with each of the nodes of the original mesh. For this process, the problem domain is transformed into smoothing cells associated with nodes such that $\Omega = \Omega^1 \cup \Omega^2 \cup ... \cup \Omega^n$ and $\Omega^i \cap \Omega^j = \emptyset,\ i \neq j$. A new element (smoothing cell) Ω^k associated with a single node k is termed as the node-based element. These elements are created by connecting sequentially the mid-side points of edges emanating from node k to the centroidal points of original elements surrounding node k as shown in Figure 6.2.

Introducing the smoothing operation of the SCNI, the strain and electric fields

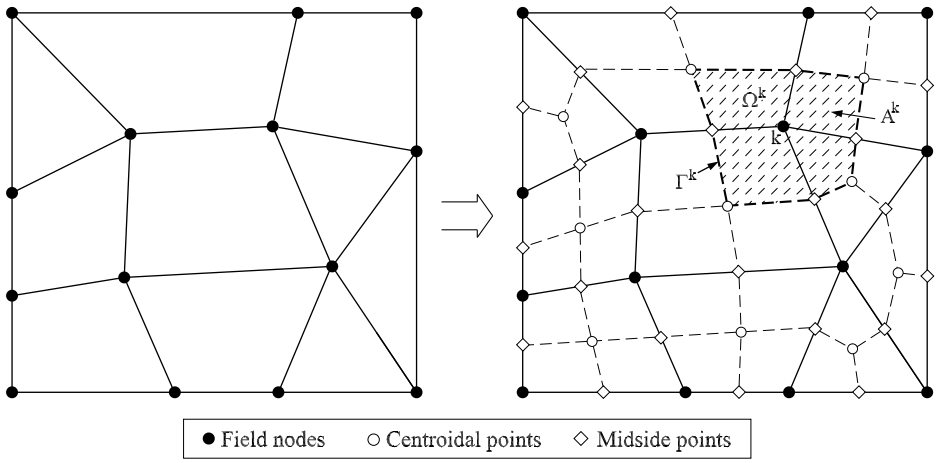

Figure 6.2: Node-based elements: Transformation of an original mesh into smoothing elements associated with nodes. The dashed lines are formed by connecting midside points with centroidal points of original elements and serve as new cell (element) boundaries.

over the smoothing cell Ω^k associated with node k are assumed as follows.

$$\tilde{\boldsymbol{\epsilon}}^k(\mathbf{x}^k) = \int_{\Omega^k} \boldsymbol{\epsilon}(\mathbf{x})\Phi^k(\mathbf{x}-\mathbf{x}^k)d\Omega, \tag{6.59}$$

$$\tilde{\mathbf{E}}^k(\mathbf{x}^k) = \int_{\Omega^k} \mathbf{E}(\mathbf{x})\Phi^k(\mathbf{x}-\mathbf{x}^k)d\Omega, \tag{6.60}$$

where $\boldsymbol{\epsilon}$, $\mathbf{E}$ are respectively the mechanical strain and electric field obtained from displacement compatibility condition as given in Equations (6.26) and (6.27). Φ^k is a smoothing function that satisfies the following properties

$$\Phi^k \geq 0 \qquad \text{and} \qquad \int_{\Omega^k} \Phi^k \mathrm{d}\Omega = 1. \tag{6.61}$$

For simplicity, Φ^k is chosen as a constant function

$$\Phi^k(\mathbf{x}-\mathbf{x}^k) = \begin{cases} 1/A^k & \mathbf{x} \in \Omega^k, \\ 0 & \mathbf{x} \notin \Omega^k. \end{cases} \tag{6.62}$$

where $A^k = \int_{\Omega^k} d\Omega$ is the area of the smoothing cell Ω^k as shown in Figure 6.2.

Substituting Φ^k into Equation (6.59)–(6.60) and applying the divergence theorem, we obtain a smoothed strain and smoothed electric field in the domain Ω^k as follows.

$$\tilde{\boldsymbol{\epsilon}}^k(\mathbf{x}^k) = \tfrac{1}{A^k}\int_{\Omega^k} \nabla_s \mathbf{u}(\mathbf{x})d\Omega = \tfrac{1}{A^k}\int_{\Gamma^k} \mathbf{n}_u^k \mathbf{u}(\mathbf{x})d\Gamma, \tag{6.63}$$

$$\tilde{\mathbf{E}}^k(\mathbf{x}^k) = -\tfrac{1}{A^k}\int_{\Omega^k} \nabla\boldsymbol{\phi}(\mathbf{x})d\Omega = -\tfrac{1}{A^k}\int_{\Gamma^k} \mathbf{n}_\phi^k \boldsymbol{\phi}(\mathbf{x})d\Gamma, \tag{6.64}$$

where $\mathbf{n}_u^k$ and $\mathbf{n}_\phi^k$ are matrices associated with unit outward vector normal to the boundary Γ^k,

$$\mathbf{n}_u^k = \begin{bmatrix} n_x^k & 0 \\ 0 & n_z^k \\ n_z^k & n_x^k \end{bmatrix}, \quad \mathbf{n}_\phi^k = \begin{bmatrix} n_x^k \\ n_z^k \end{bmatrix}, \tag{6.65}$$

and $\mathbf{u}(\mathbf{x})$, $\boldsymbol{\phi}(\mathbf{x})$ are approximated functions as in Equations (6.20)–(6.21).

Introducing the finite element approximation of $\mathbf{u}$ and $\boldsymbol{\phi}$ into Equations (6.63) and (6.64), the smoothed strain and electric field on the smoothing cell Ω^k associated with the node k can be expressed in the following matrix form

$$\tilde{\boldsymbol{\epsilon}}^k(\mathbf{x}^k) = \sum_{i=1}^{nk} \tilde{\mathbf{B}}_u^i(\mathbf{x}^k)\mathbf{q}_i, \tag{6.66}$$

$$\tilde{\mathbf{E}}^k(\mathbf{x}^k) = -\sum_{i=1}^{nk} \tilde{\mathbf{B}}_\phi^i(\mathbf{x}^k)\boldsymbol{\phi}_i, \tag{6.67}$$

in which nk is the number of nodes connecting directly to the node k (i.e. nodes whose shape functions support node k). $\tilde{\mathbf{B}}_{ui}(\mathbf{x}^k)$ and $\tilde{\mathbf{B}}_{\phi i}(\mathbf{x}^k)$ are smoothed gradient matrices for $\mathbf{u}$ and $\boldsymbol{\phi}$ respectively, on the smoothing cell Ω^k

$$\tilde{\mathbf{B}}_u^i(\mathbf{x}^k) = \frac{1}{A^k}\int_{\Gamma^k} \begin{bmatrix} N_i n_x^k & 0 \\ 0 & N_i n_z^k \\ N_i n_z^k & N_i n_x^k \end{bmatrix} d\Gamma, \tag{6.68}$$

$$\tilde{\mathbf{B}}_\phi^i(\mathbf{x}^k) = \frac{1}{A^k}\int_{\Gamma^k} \begin{bmatrix} N_i n_x^k \\ N_i n_z^k \end{bmatrix} d\Gamma. \tag{6.69}$$

When a linear completed displacement field along the boundary Γ^k is used, one Gauss point is sufficient for accurate boundary integration along each line segment Γ_i^k of the boundary Γ^k of Ω^k. Therefore, Equations (6.68)–(6.69) can be evaluated with one-point Gauss quadrature integration as follows.

$$\tilde{\mathbf{B}}_u^i(\mathbf{x}^k) = \frac{1}{A^k}\sum_{b=1}^{nb} \begin{bmatrix} N_i(\mathbf{x}_b^G) n_x^k & 0 \\ 0 & N_i(\mathbf{x}_b^G) n_z^k \\ N_i(\mathbf{x}_b^G) n_z^k & N_i(\mathbf{x}_b^G) n_x^k \end{bmatrix} l_b^k, \tag{6.70}$$

$$\tilde{\mathbf{B}}_\phi^i(\mathbf{x}^k) = \frac{1}{A^k}\sum_{b=1}^{nb} \begin{bmatrix} N_i(\mathbf{x}_b^G) n_x^k \\ N_i(\mathbf{x}_b^G) n_z^k \end{bmatrix} l_b^k, \tag{6.71}$$

where nb is the total number of the line segments of the contour Γ^k, $\mathbf{x}_b^G$ is the midpoint (Gauss point) of each line segments Γ_b^k, whose length and outward unit normal are denoted as l_b^k and $\mathbf{n}^k$, respectively.

Finally, the linear static equation (6.32) can be rewritten as follows

$$\begin{bmatrix} \tilde{\mathbf{K}}_{uu}^k & \tilde{\mathbf{K}}_{u\phi}^k \\ \tilde{\mathbf{K}}_{u\phi}^k & \tilde{\mathbf{K}}_{\phi\phi}^k \end{bmatrix} \begin{Bmatrix} \mathbf{q} \\ \boldsymbol{\varphi} \end{Bmatrix} = \begin{Bmatrix} \mathbf{F} \\ \mathbf{Q} \end{Bmatrix}, \tag{6.72}$$

where

$$\tilde{\mathbf{K}}_{uu}^k = \sum_{i=1}^{nk} \tilde{\mathbf{B}}_u^{iT} \mathbf{c}^E \tilde{\mathbf{B}}_u^i A^k, \tag{6.73}$$

$$\tilde{\mathbf{K}}_{u\phi}^k = \sum_{i=1}^{nk} \tilde{\mathbf{B}}_u^{iT} \mathbf{e}^T \tilde{\mathbf{B}}_\phi^i A^k, \tag{6.74}$$

$$\tilde{\mathbf{K}}_{\phi\phi}^k = -\sum_{i=1}^{nk} \tilde{\mathbf{B}}_\phi^{iT} \mathbf{g}^T \tilde{\mathbf{B}}_\phi^i A^k. \tag{6.75}$$

The stiffness matrix $\tilde{\mathbf{K}}$ of the system is then assembled in a manner similar to that in the conventional FEM such as

$$\tilde{\mathbf{K}} = \sum_{k=1}^{N_n} \tilde{\mathbf{K}}^k, \tag{6.76}$$

where

$$\tilde{\mathbf{K}}^k = \begin{bmatrix} \tilde{\mathbf{K}}_{uu}^k & \tilde{\mathbf{K}}_{u\phi}^k \\ \tilde{\mathbf{K}}_{u\phi}^k & \tilde{\mathbf{K}}_{\phi\phi}^k \end{bmatrix}. \tag{6.77}$$

It can be seen that only values of shape functions at Gauss points along the edges of boundary Γ_i^k are needed for evaluating Equations (6.70)–(6.71). The details for computing values of shape functions are presented in the following section.

6.4.2.1 Construction of linear shape functions

In this approach, a finite element mesh of linear triangular or bilinear quadrilateral elements is considered. It should be noted that the purpose of introducing midside points and centroidal points is to form the linear compatible boundary of

the node-based element and to evaluate the shape functions at the Gauss points. No additional degrees of freedom are associated with these points and the nodal unknowns are the same as in the original FEM mesh. Moreover, the derivations of the smoothed strain and smoothed electric fields of the smoothing cell Ω^k associated with node k transforms the domain integration into boundary integration along the boundary Γ^k of Ω^k. Therefore, only the shape function values at Gauss points along each segment Γ_i^k of the boundary Γ^k are used. Values of shape functions at these points of interest (mid-edge points and centroidal points) for triangular and quadrilateral elements are illustrated in Figure 6.3. Note that the shape function values in Figure 6.3 are denoted in the format $(N_1, N_2, ..., N_{ne})$ where ne is the number of nodes of an element.

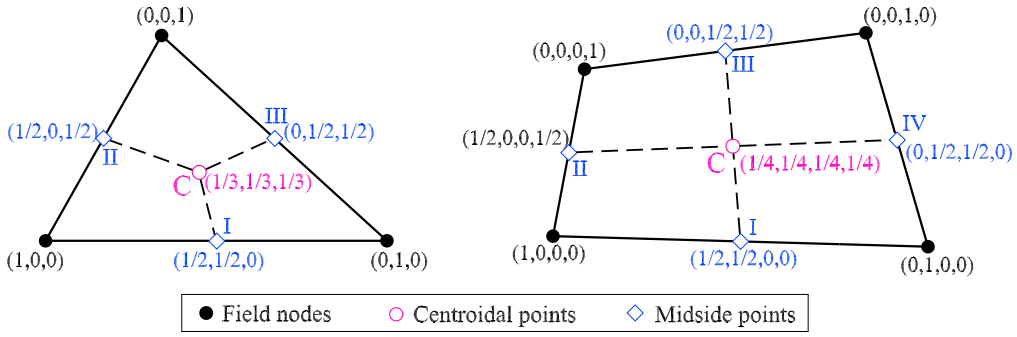

Figure 6.3: Shape function values for a typical linear triangular and bilinear quadrilateral element.

By using an original mesh of linear triangular or bilinear quadrilateral elements, a linear compatible displacement field along the boundary Γ^k of a smoothing cell (node-based element) is obtained. Only one Gauss point at midside point on each segment of Γ^k is required for accurate boundary integration. The shape function values at the Gauss points (e.g. point c) are shown in Figure 6.4.

6.4.2.2 Implementation procedure

In order to clarify how the node-based smoothing technique is incorporated into a finite element code, a numerical implementation for the method is briefly presented as follows.

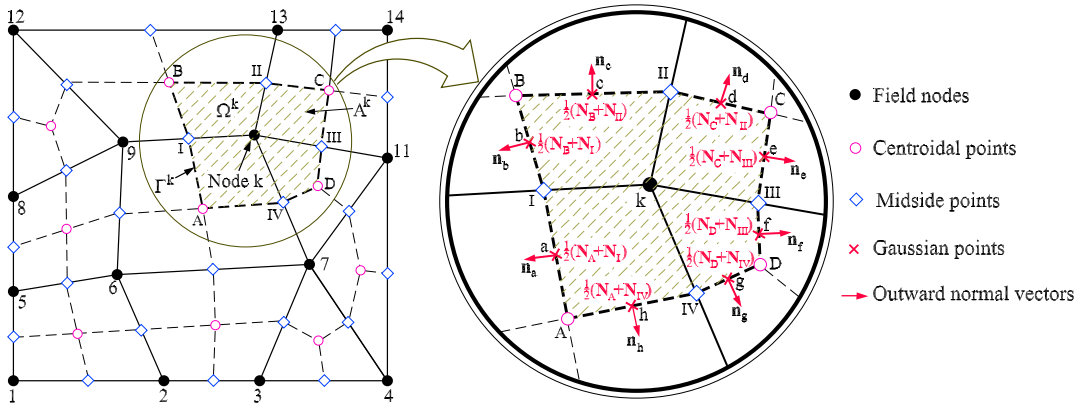

Figure 6.4: Detail of a node-based element (smoothing cell) and values of shape functions at Gauss points (a,b,c,d,e,f,g,h)

1. Discretize the domain into triangular or quadrilateral elements and form the matrices of node coordinates (**coord**) and element connections (**nodes**).

2. Find surrounding cells of each node k and determine the area of each smoothing cell Ω^k associated with node k:

   Loop over all nodes, $k = 1$ to N_n

   Loop over all elements, $j = 1$ to N_e

   if (find $(k == \mathbf{nodes}(j,:))) \geq 1$, add the element j to the list of surrounding cells and compute the area of the surrounding cell j.

   End the loop over all elements.

   End the loop over all nodes.

3. Calculate and assemble element stiffness matrices to build the system stiffness matrix:

   Loop over all nodes, $k = 1$ to N_n

   (a) Determine the connecting points of each smoothing cell Ω^k associated with node k.

   (b) Calculate the outward unit normal vector $\mathbf{n}^k$ on each boundary segment of the smoothing cell Ω^k.

   (c) Evaluate smoothed gradient matrices $\tilde{\mathbf{B}}_u^k$, $\tilde{\mathbf{B}}_\phi^k$ using Equations (6.70)–(6.71).

(d) Compute smoothed element stiffness matrices corresponding to the Ω^k using Equations (6.73)–(6.75).

(e) Assemble the contribution of smoothed element stiffness matrices to form the system stiffness matrix using Equation (6.76).

End the loop over all nodes.

4. Assign boundary conditions.

5. Solve the system equation to obtain nodal kinematics.

6. Post-process strains and stresses at points of interest.

6.5 Numerical examples

In this section, several numerical examples are employed to test and assess the performance of the cell-based as well as node-based smoothing elements as applied to the linear static and free vibration analysis of two-dimensional piezoelectric structures. The elements considered in this section are:

- SPQ4: the cell-based smoothing piezoelectric quadrilateral 4-node element using two smoothing cells.
- NSPE-Q4: the node-based smoothing piezoelectric element based on quadrilateral finite element mesh.
- NSPE-T3: the node-based smoothing piezoelectric element based on triangular finite element mesh.
- FEM-Q4: the standard 4-node quadrilateral piezoelectric finite element using 2×2 Gauss points.
- FEM-T3: the standard 3-node piezoelectric finite element using linear shape functions.

6.5.1 Patch tests

Passing the patch test is a sufficient condition for the convergence of a finite element method. It is an essential check in order to verify that the elements exhibit proper convergence properties, consistency and stability when subjected to constant strain. In this section, a patch test is used to verify that the proposed cell-based (SPQ4) and node-based elements (NSPE-T3, NSPE-Q4) have proper convergence properties. A choice of geometry, mesh and boundary conditions was adapted from the work of Sze et al. (2004), as shown in Figure 6.5.

The following PZT4 material in Sze et al. (2004) is used for the patch test.
$c_{11} = 139 \times 10^3$, $c_{33} = 113 \times 10^3$, $c_{13} = 74.3 \times 10^3$, $c_{55} = 25.6 \times 10^3$ N/mm^2,
$e_{15} = 13.44 \times 10^6$, $e_{31} = -6.98 \times 10^6$, $e_{33} = 13.84 \times 10^6$ pC/mm^2,
$g_{11} = 6.00 \times 10^9$, $g_{33} = 5.47 \times 10^9$ pC/GVmm.

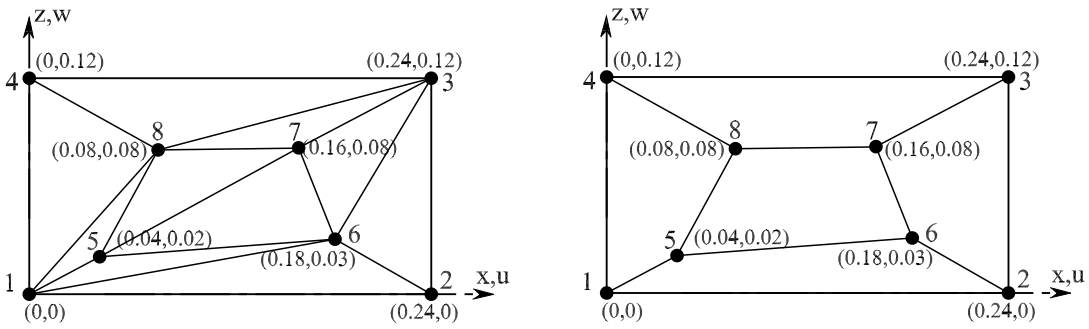

(a) (b)

Figure 6.5: Typical meshes of the patch test: (a) triangular mesh (NSPE-T3 elements); (b) quadrilateral mesh (SPQ4, NSPE-Q4 elements).

The prescribed mechanical displacements and electric potentials are applied at the edges defined by nodes 1, 2, 3 and 4 as follows.

$$u = s_{11}\sigma_0 x, \quad w = s_{13}\sigma_0 z, \quad \phi = b_{31}\sigma_0 z.$$

where $\sigma_0 = 1000$ is an arbitrary stress parameter. s_{11}, s_{13} and b_{31} are material

constants which can be calculated by the following relation

$$\begin{bmatrix} s_{11} & s_{13} & b_{31} \\ s_{13} & s_{33} & b_{33} \\ b_{31} & b_{33} & -f_{33} \end{bmatrix} = \begin{bmatrix} c_{11} & c_{13} & e_{31} \\ c_{13} & c_{33} & e_{33} \\ e_{31} & e_{33} & -g_{33} \end{bmatrix}^{-1}.$$

Under the boundary conditions described above, the corresponding exact stress $\boldsymbol{\sigma}$ and electric displacement $\mathbf{D}$ are given as:

$$\sigma_x = \sigma_0, \quad \sigma_z = \tau_{xz} = D_x = D_z = 0.$$

It is found that the obtained results with SPQ4, NSPE-T3 and NSPE-Q4 elements match well the exact solution as shown in Table 6.1 and hence the proposed elements successfully pass the patch test.

Table 6.1: Results of the patch test

Var.	Models			
	SPQ4	NSPE-T3	NSPE-Q4	Exact
σ_x	1000.0000	1000.0000	1000.0000	1000
σ_z	1.9397×10^{-10}	2.0240×10^{-10}	-8.6968×10^{-14}	0
τ_{xz}	9.4022×10^{-11}	2.2414×10^{-10}	-4.1149×10^{-13}	0
D_x	9.1261×10^{-8}	-1.0658×10^{-8}	-2.2461×10^{-10}	0
D_z	-1.4486×10^{-8}	5.5046×10^{-8}	1.1983×10^{-10}	0
u_5	1.9012×10^{-3}	1.9012×10^{-3}	1.9012×10^{-3}	1.9012×10^{-3}
w_5	-6.0626×10^{-5}	-6.0626×10^{-5}	-6.0626×10^{-5}	-6.0626×10^{-5}
ϕ_5	-3.5557×10^{-7}	-3.5557×10^{-7}	-3.5557×10^{-7}	-3.5557×10^{-7}
u_6	3.0103×10^{-3}	3.0103×10^{-3}	3.0103×10^{-3}	3.0103×10^{-3}
w_6	-9.0939×10^{-5}	-9.0939×10^{-5}	-9.0939×10^{-5}	-9.0939×10^{-5}
ϕ_6	-5.3335×10^{-7}	-5.3335×10^{-7}	-5.3335×10^{-7}	-5.3335×10^{-7}
u_7	2.8519×10^{-3}	2.8519×10^{-3}	2.8519×10^{-3}	2.8519×10^{-3}
w_7	-2.4251×10^{-4}	-2.4251×10^{-4}	-2.4251×10^{-4}	-2.4251×10^{-4}
ϕ_7	-1.4223×10^{-6}	-1.4223×10^{-6}	-1.4223×10^{-6}	-1.4223×10^{-6}
u_8	2.2181×10^{-3}	2.2181×10^{-3}	2.2181×10^{-3}	2.2181×10^{-3}
w_8	-2.4251×10^{-4}	-2.4251×10^{-4}	-2.4251×10^{-4}	-2.4251×10^{-4}
ϕ_8	-1.4223×10^{-6}	-1.4223×10^{-6}	-1.4223×10^{-6}	-1.4223×10^{-6}

6.5.2 Single-layer piezoelectric strip in tension

A piezoelectric strip of size $2a \times 2h$ subjected to uniaxial tension as shown in Figure 6.6 is considered. The material used in this example is PZT-4 ceramic, poled in the $z-$direction. Its mechanical and piezoelectric elastic constants are as follows.

$c_{11} = 12.6 \times 10^{10}$, $c_{33} = 11.5 \times 10^{10}$, $c_{12} = 7.78 \times 10^{10}$,
$c_{13} = 7.43 \times 10^{10}$, $c_{55} = 2.56 \times 10^{10}$ N/m^2,
$e_{15} = 12.7$, $e_{31} = -5.2$, $e_{33} = 15.1$ C/m^2,
$g_{11} = 6.463 \times 10^{-9}$, $g_{33} = 5.611 \times 10^{-9}$ F/m.

Owing to symmetric conditions, only an upper right quadrant of the plate is modeled. Symmetric conditions are imposed on the left and bottom edges as shown in Figure 6.6.

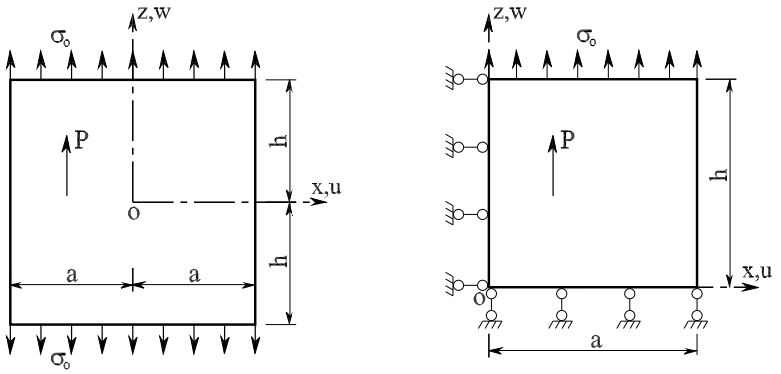

Figure 6.6: Piezo-strip subjected to a uniform tension stress.

In the calculation, we set $a = 5$m, $h = 10$m, $\sigma_o = 10$ N/m^2. To demonstrate the capability of the proposed elements to deal with bad element shapes, the strip is modeled with two types of mesh in this analysis with 5×7 quadrilateral elements as well as triangular elements as shown in Figure 6.7. All corresponding numerical results are compared with the analytic solution given by Ding et al. (1998) and Wang et al. (2003).

All results are plotted together in Figure 6.9–6.11. Note that the computed displacements u are along the bottom side ($z = 0$) while the displacements w and electric potential ϕ distribute along the left edge ($x = 0$). As we can see, the

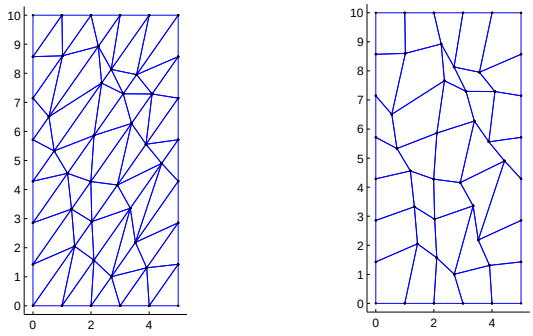

(a) (b)

Figure 6.7: Typical meshes of a piezo-strip in tension: (a) triangular mesh (NSPE-T3, FEM-T3 elements); (b) quadrilateral mesh (NSPE-Q4, SPQ4 elements).

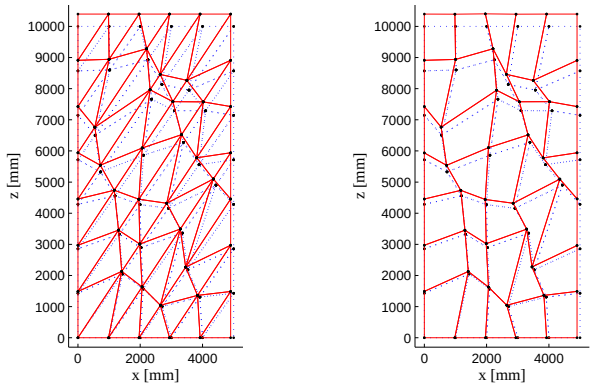

(a) (b)

Figure 6.8: Total deformation of a piezo-strip in tension (scale factor: 5×10^5): (a) triangular mesh; (b) quadrilateral mesh.

present solutions are in excellent agreement with analytic ones. It is also noticed that the performance of NSPE-T3 and SPQ4 elements is slightly better than that of NSPE-Q4 element when compared with exact ones using absolute error, as shown in Figure 6.9b–6.11b.

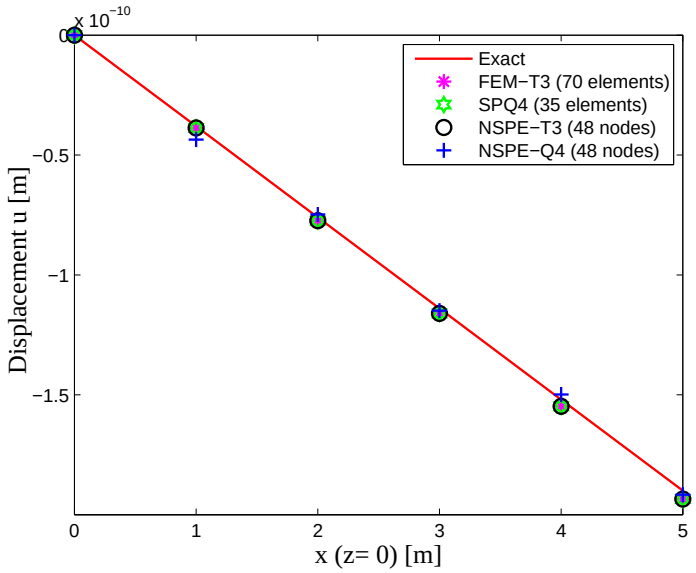

(a)

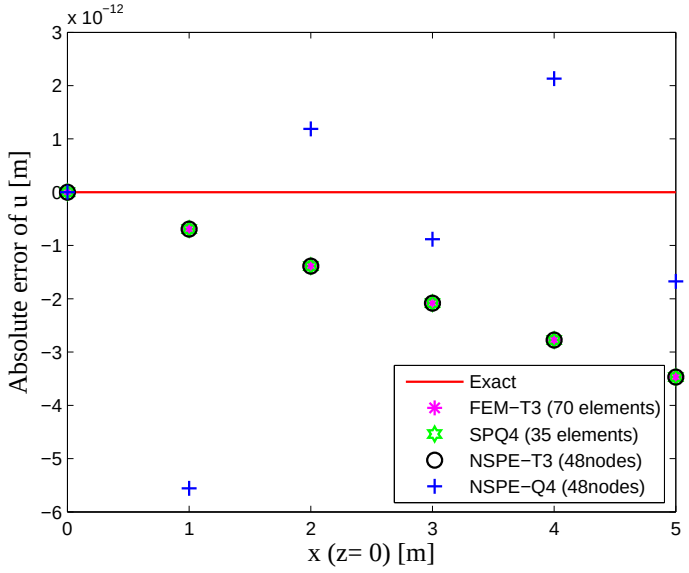

(b)

Figure 6.9: Piezo-strip in tension: Computed and exact $u-$displacements: (a) Distribution of u on the edge $z = 0$; (b) Comparison of the error in $u-$displacement

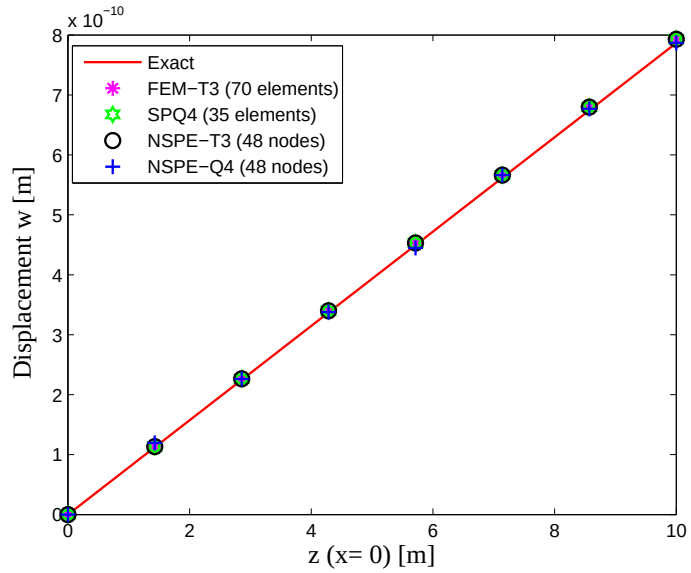

(a)

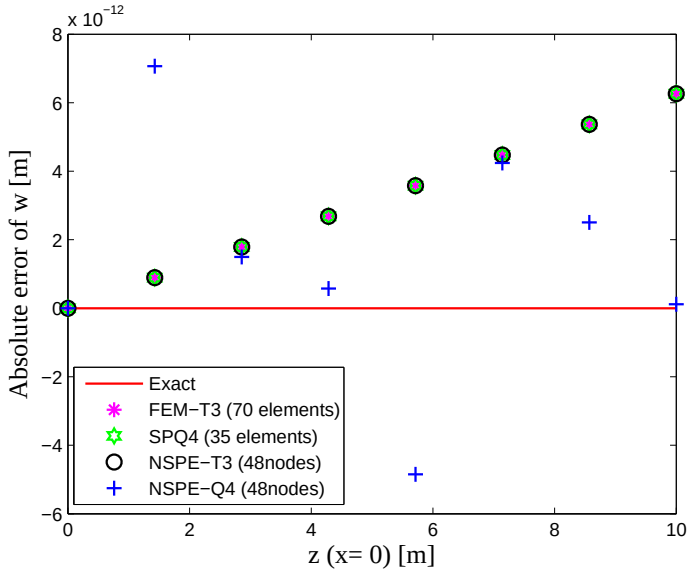

(b)

Figure 6.10: Piezo-strip in tension: Computed and exact $w-$displacements: (a) Distribution of w on the edge $x = 0$; (b) Comparison of the error in $w-$displacement

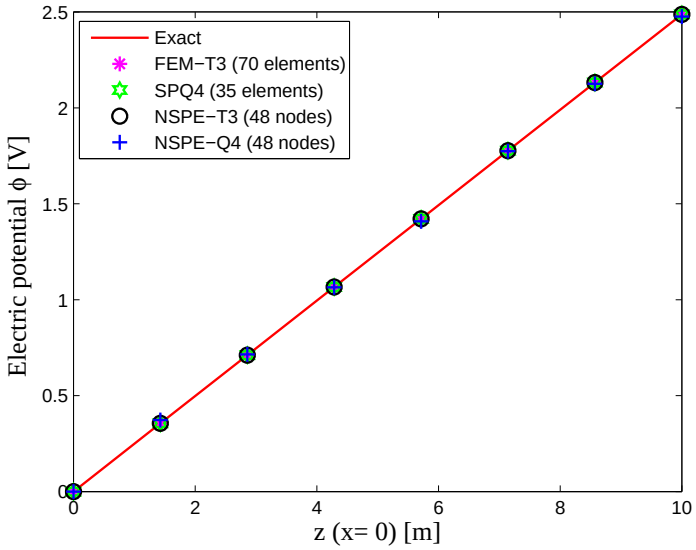

(a)

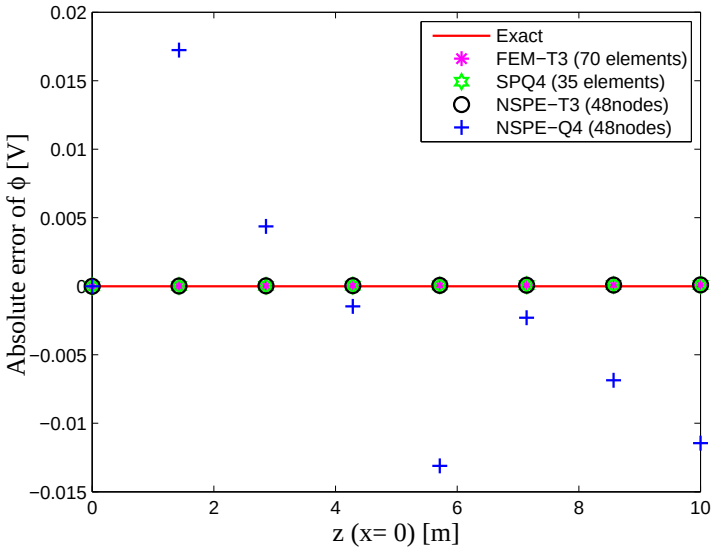

(b)

Figure 6.11: Piezo-strip in tension: Computed and exact electric potential ϕ: (a) Distribution of ϕ on the edge $x = 0$; (b) Comparison of the error in electric potential.

6.5.3 Single-layer piezoelectric strip in shear deformation

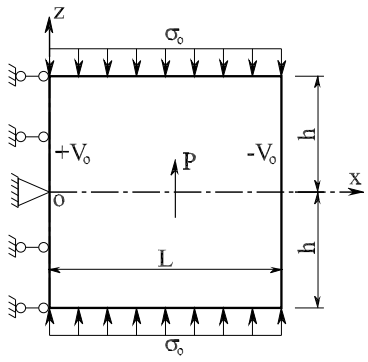

Figure 6.12: Piezo-strip subjected to a uniform stress and a voltage.

In this example, we consider the shear deformation of a 1×1mm single-layer square strip polarized in the $z-$direction. The strip is subjected to a combined loading of pressure σ_0 in the z direction and an applied voltage V_0 as depicted on Figure 6.12. The material PZT-5 is used for this problem and its properties are summarized in Table 6.2.

Table 6.2: Single-layer piezoelectric material properties, dimensions and other constants.

s_{11}	16.4×10^{-6} mm^2/N	d_{31}	-172×10^{-9} mm/V
s_{13}	-7.22×10^{-6} mm^2/N	d_{33}	-374×10^{-9} mm/V
s_{33}	18.8×10^{-6}mm^2/N	d_{15}	584×10^{-9} mm/V
s_{55}	47.5×10^{-6} mm^2/N	g_{11}	1.53105×10^{-8} N/V^2
σ_0	-5.0 N/mm^2	g_{33}	1.505×10^{-8} N/V^2
σ_1	20.0 N/mm^2	V_0	1000V
L	1.0mm	h	0.5mm

The following mechanical and electrical boundary conditions are applied to the sides of the strip

$$\begin{aligned}
\phi_{,z}(x,\pm h) = 0, \quad & \sigma_z(x,\pm h) = \sigma_0, \quad & \tau_{xz}(L,z) &= 0,\\
\tau_{xz}(x,\pm h) = 0, \quad & \phi(L,z) = -V_0, \quad & \sigma_x(L,z) &= 0,\\
\phi(0,z) = +V_0, \quad & u(0,z) = 0, \quad & w(0,0) &= 0.
\end{aligned}$$

The analytical solution for this problem is given by Gaudnzi and Bathe (1995)

$$\begin{aligned}
u &= s_{13}\sigma_0 x,\\
w &= \frac{d_{15}V_0 x}{h} + s_{33}\sigma_0 z,\\
\phi &= V_0\left(1 - 2\frac{x}{L}\right).
\end{aligned}$$

The strip is modelled with two types of mesh in this analysis with 8×8 quadrilateral elements or triangular elements as shown in Figure 6.13.

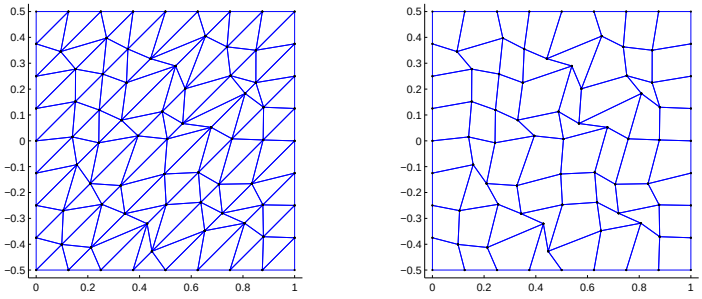

(a) (b)

Figure 6.13: Typical meshes of a piezo-strip in shear: (a) triangular mesh (NSPE-T3, FEM-T3 elements); (b) quadrilateral mesh (NSPE-Q4, SPQ4 elements).

The present numerical results are compared with the standard linear triangular piezoelectric finite element FEM-T3 and the exact solutions given by Gaudnzi and Bathe (1995). The obtained total deformation of the strip is shown in Figure 6.14

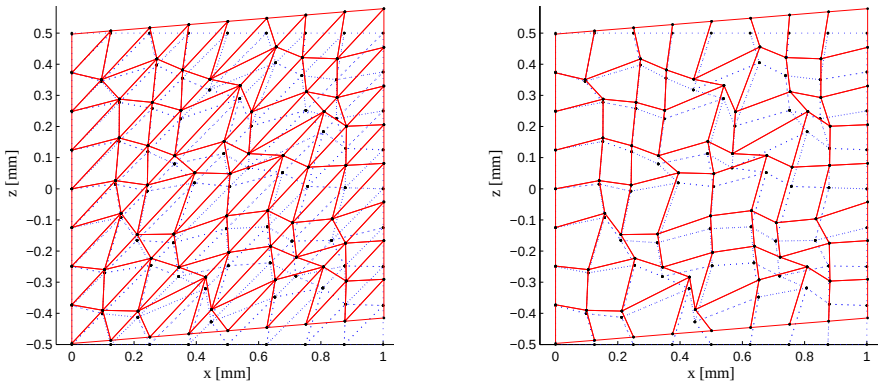

(a) (b)

Figure 6.14: Total deformation of the piezo-strip in shear (scale factor=70): (a) triangular mesh; (b) quadrilateral mesh

Figure 6.15a and Figure 6.16a depict the distribution of the displacements u and w, respectively along the bottom edge ($z = -h$). The distribution of the computed electric potential ϕ along this edge is also demonstrated in Figure 6.17a. It is observed that all the computed displacements and electric potentials for both types of mesh are in excellent agreement with the analytical solutions.

The relative errors (in log scale) of the displacements and electric potentials are illustrated on Figure 6.15b–Figure 6.17b. It can be seen that the node-based NSPE-T3 element achieves the best prediction for displacements (both of u and w) when compared with other numerical solutions. The superior accuracy of the present node-based elements (NSPE-T3, NSPE-Q4) and cell-based element (SPQ4) over the standard FEM-T3 element is evident.

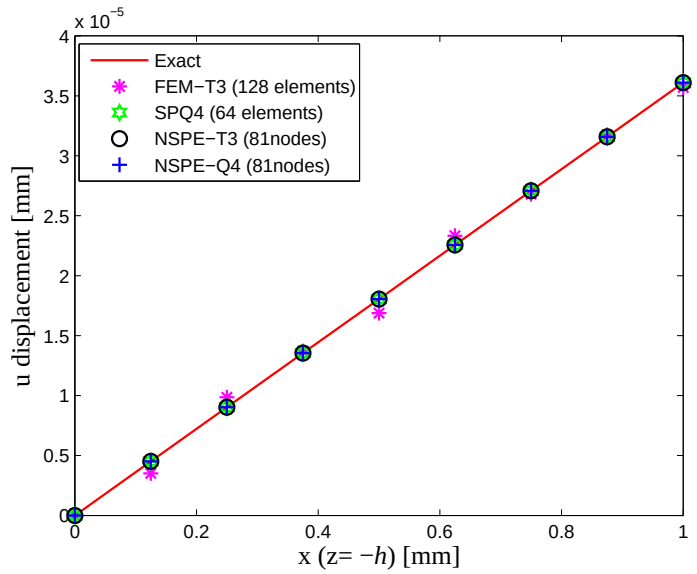

(a)

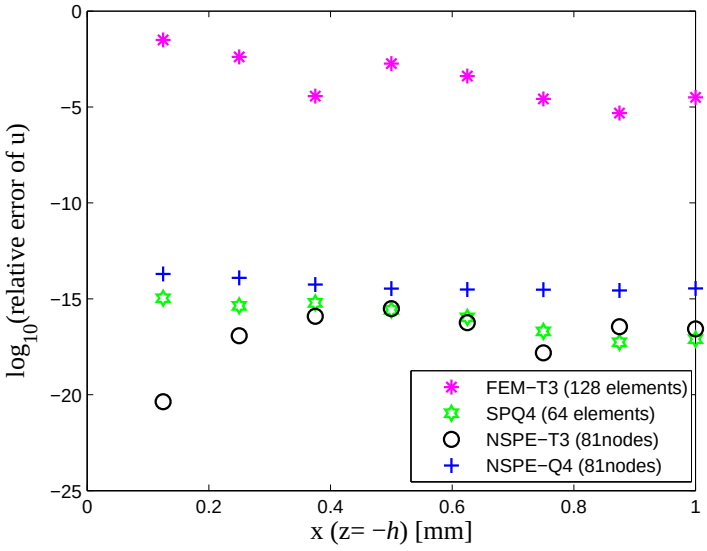

(b)

Figure 6.15: Piezo-strip in shear: Computed and exact $u-$displacements: (a) Distribution of u on the edge $z = -h$; (b) Comparison of the error of $u-$displacement.

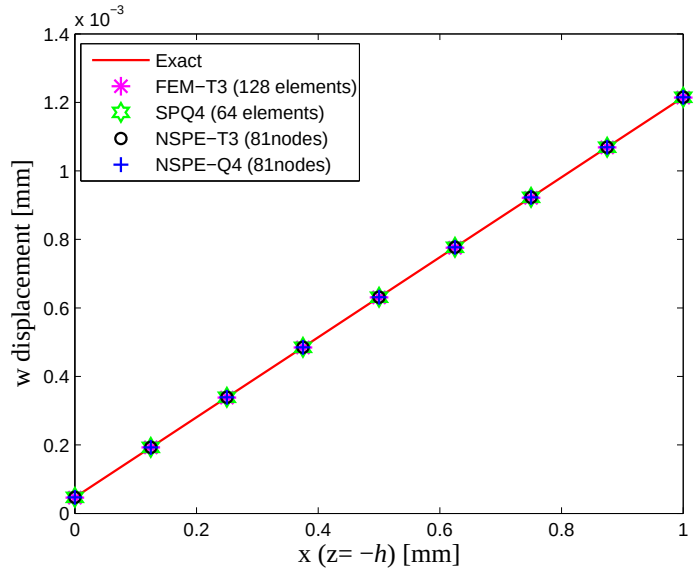

(a)

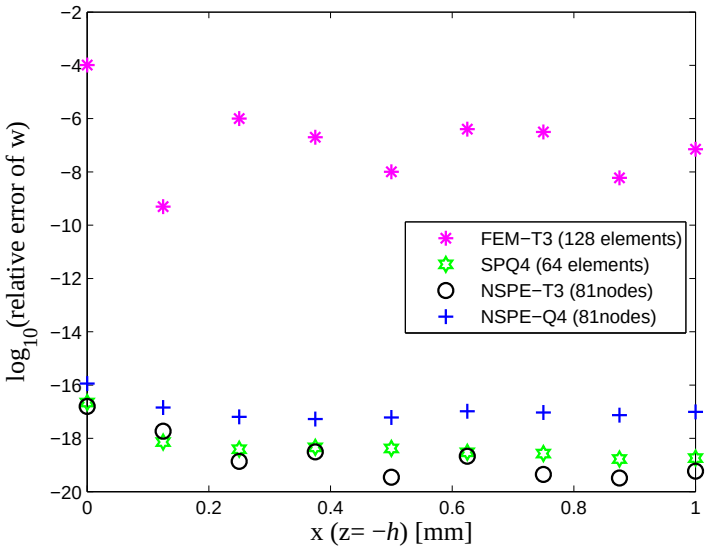

(b)

Figure 6.16: Piezo-strip in shear: Computed and exact $w-$displacements: (a) Distribution of w on the edge $z = -h$; (b) Comparison of the error of $w-$displacement.

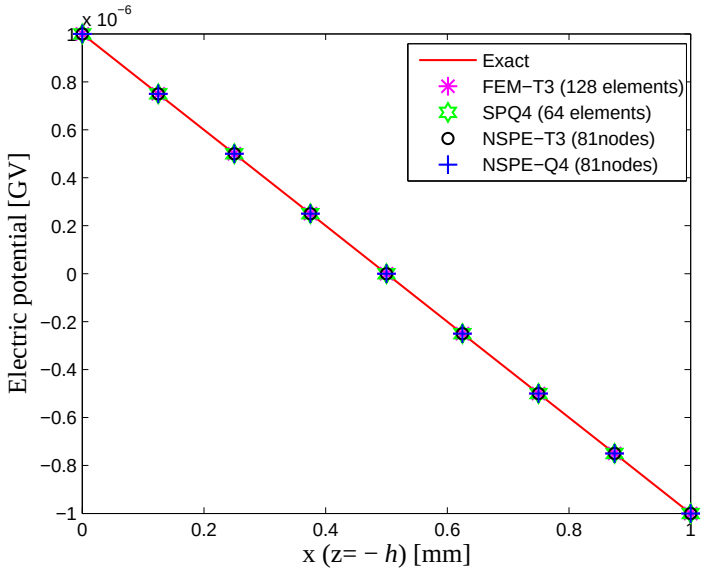

(a)

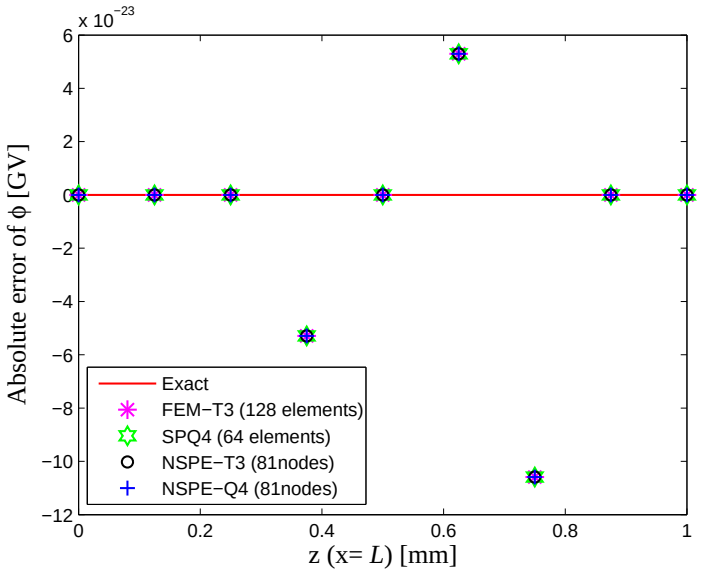

(b)

Figure 6.17: Piezo-strip in shear: Computed and exact electric potential ϕ: (a) Distribution of ϕ on the edge $z = -h$; (b) Comparison of the error of electric potential.

6.5.4 Single-layer piezoelectric strip in bending

The strip with the same material and geometry as in the previous example is considered but with modified boundary conditions for bending situation. In this case, a voltage V_0 is applied on the top and bottom surfaces together with a linear stress applied at the right edge as shown in Figure 6.18.

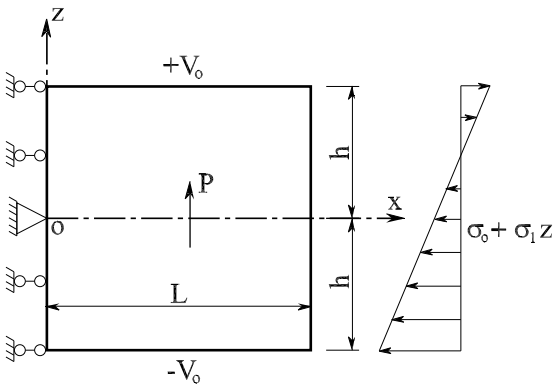

Figure 6.18: Piezo-strip subjected to a linear stress and a voltage.

The following mechanical and electrical boundary conditions are applied to the edges of the strip

$$\begin{aligned}
\phi(x,\pm h) = \pm V_0, \quad \sigma_z(x,\pm h) = 0, \quad \tau_{xz}(x,\pm h) = 0,\\
\phi_{,x}(L,z) = 0, \quad \sigma_x(L,z) = \sigma_0 + \sigma_1 z, \quad \tau_{xz}(L,z) = 0,\\
\phi_{,x}(0,z) = 0, \qquad u(0,z) = 0, \quad w(0,0) = 0.
\end{aligned}$$

The analytical solution is available for this problem and can be found in Gaudnzi and Bathe (1995) or Ohs and Aluru (2001) as follows

$$\begin{aligned}
u &= s_{11}\left(\sigma_0 - \frac{d_{31}V_0}{s_{11}h}\right) + s_{11}\left(1 - \frac{d_{31}^2}{s_{11}g_{33}}\right)\sigma_1 xz,\\
w &= s_{13}\left(\sigma_0 - \frac{d_{33}V_0}{s_{13}h}\right) z + s_{13}\left(1 - \frac{d_{33}d_{31}}{s_{13}g_{33}}\right)\sigma_1\frac{z^2}{2}\\
&\quad -s_{11}\left(1 - \frac{d_{31}^2}{s_{11}g_{33}}\right)\sigma_1\frac{x^2}{2},\\
\phi &= V_0\frac{z}{h} - \frac{d_{31}\sigma_1}{2g_{33}}(h^2 - z^2).
\end{aligned}$$

Two types of mesh as shown in Figure 6.13 are used again in the analysis. The obtained deformation of the strip is shown in Figure 6.19.

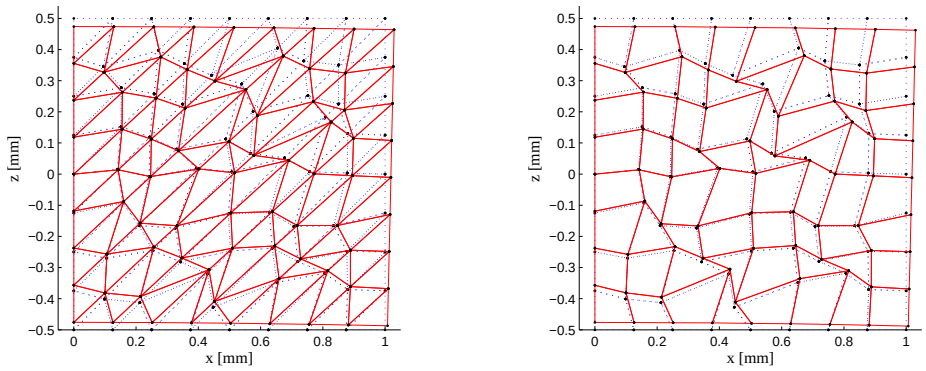

(a) (b)

Figure 6.19: Total deformation of the piezo-strip in bending (scale factor=70): (a) triangular mesh; (b) quadrilateral mesh

Figure 6.20 illustrates the distribution of displacement u and its relative error along the right side ($x = L$) while the vertical displacement w and its relative error along the bottom edge ($z = -h$) are shown in Figure 6.21. The distribution of the computed electric potentials along the right side ($x = L$) and its relative error are demonstrated in Figure 6.22. Both computed displacements and electric potential match well the exact solutions for the node-based NSPE-T3 element as well as for the NSPE-Q4 element. Again, the node-based element NSPE-T3 demonstrates the best performance with respect to displacement fields when compared with the FEM-T3, SPQ4 and NSPE-Q4 elements as can be seen in the Figure 6.20b–Figure 6.21b. For the prediction of electric potential fields, all elements yield virtually identical results which appear indistinguishable from each other as can be seen in Figure 6.22.

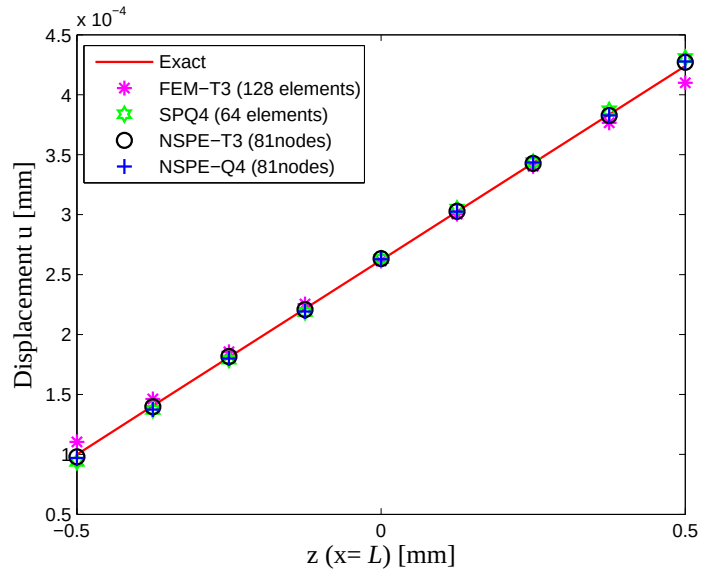

(a)

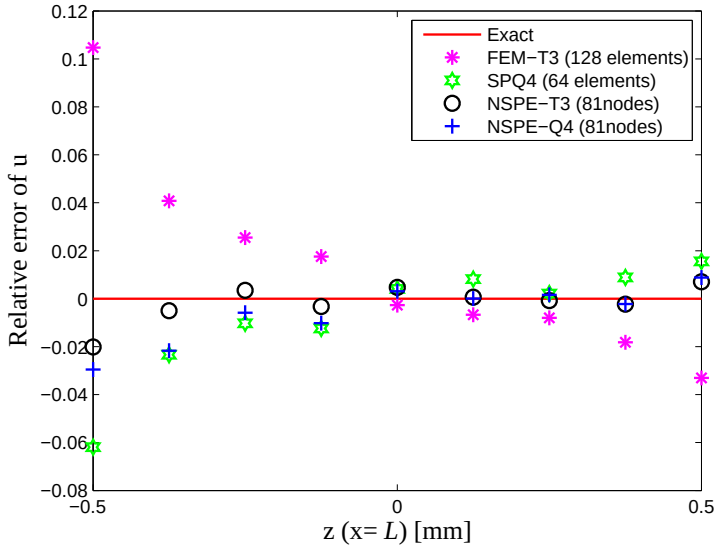

(b)

Figure 6.20: Piezo-strip in bending: Computed and exact $u-$displacements: (a) Distribution of u on the edge $x = L$; (b) Comparison of the error of $u-$displacement.

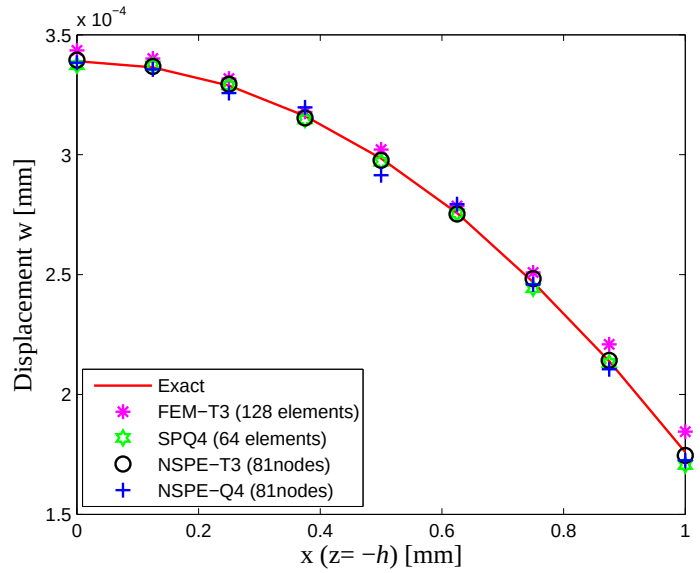

(a)

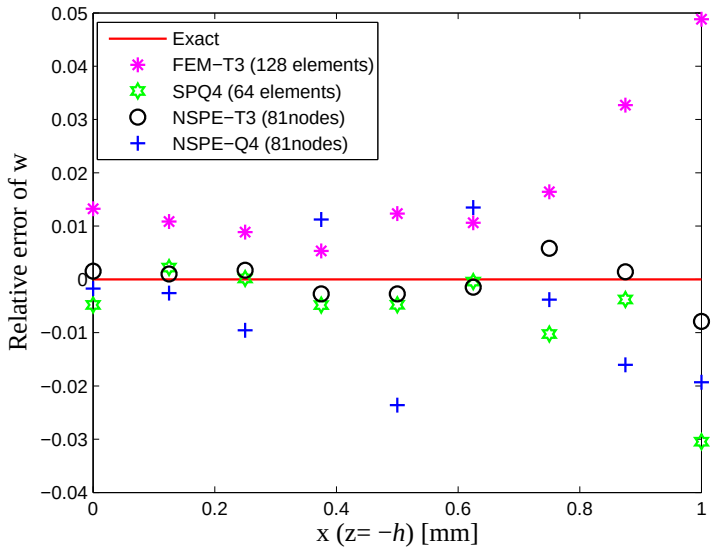

(b)

Figure 6.21: Piezo-strip in bending: Computed and exact $w-$displacements: (a) Distribution of w on the edge $z = -h$; (b) Comparison of the error of $w-$displacement.

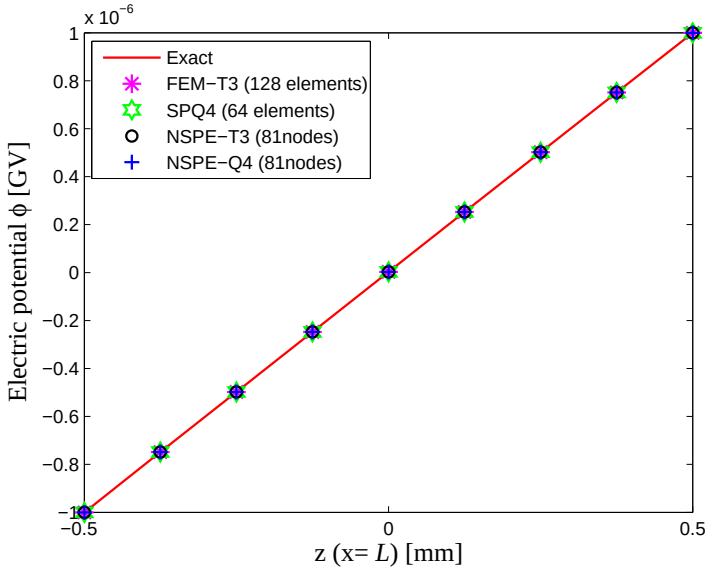

(a)

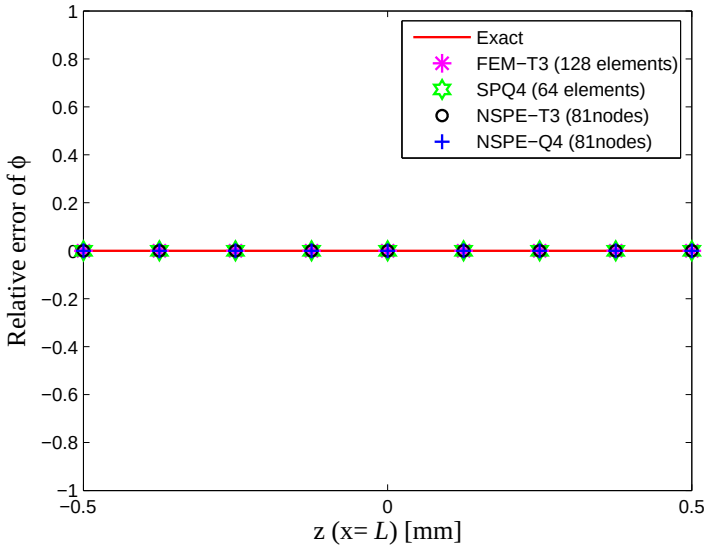

(b)

Figure 6.22: Piezo-strip in bending: Computed and exact electric potential ϕ: (a) Distribution of ϕ on the edge $x = L$; (b) Comparison of the error of electric potential.

6.5.5 Parallel piezoelectric bimorph beam

The example to be discussed here is the two-layer parallel bimorph beam. It consists of a cantilever piezoelectric beam made of two PVDF layers of the same thickness $h_t = h_b = H/2 = 0.2$ mm and a length of $L = 5$ mm, with same polarization orientations as shown in Figure 6.23. The PVDF material properties are summarized as follows.
$E = 2$ GPa, $\nu = 0.29$, $e_{31} = 0.046$ C/m^2, $e_{32} = 0.046$ C/m^2,
$g_{11} = 0.1062 \times 10^{-9}$ F/m, $g_{33} = 0.1062 \times 10^{-9}$ F/m.

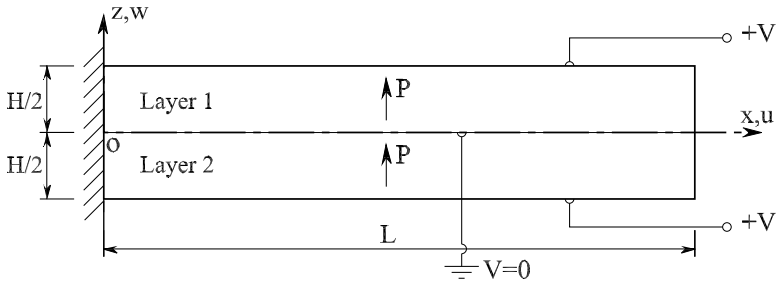

Figure 6.23: Two-layer parallel bimorph cantilever beam.

For the parallel bimorph configuration, a zero voltage ($V = 0$) is applied to the intermediate electrode, while the voltage $V = 1$ is applied to the bottom and top faces of the beam. The loading will generate moments that bend the bimorph.

In this study, the beam is assumed to be in a plane stress state. For an applied electric field V only, the tip deflection δ of the cantilever parallel bimorph can be approximated as in Cambridge (1995)

$$\delta = \frac{2L^2 V d_{31}}{H^2}. \tag{6.78}$$

With $L = 5$ mm and $H = 0.4$ mm, the approximated value of the tip deflection calculated from Equation (6.78) is $\delta = 1.0206 \times 10^{-8}$ m.

The beam is analyzed using 15×2, 25×2, 35×2 and 50×2 uniform meshes. Table 6.3 presents the obtained tip deflections together with mesh-free solutions such as PIM (Liu et al., 2002) and RPIM (Liu et al., 2003) and the analytic solution. Note that the values in parentheses are the relative errors compared with analytic

Table 6.3: Tip deflections of the bimorph beam and comparison with available literatures ($\times 10^{-8}$ m).

Model	Mesh			
	15×2	25×2	35×2	50×2
FEM-T3	0.4967	0.6287	0.6785	0.7084 (-30.589%)
PIM	–	1.098	–	1.111 (8.856%)
RPIM	–	–	–	1.204 (17.970%)
SPQ4	0.814	0.937	0.978	1.003 (-1.724%)
NSPE-Q4	1.0321	1.0287	1.0275	1.0269 (0.617%)
NSPE-T3	1.0263	1.0276	1.0270	1.0264 (0.568%)
Analytic				1.0206

solutions. Numerical results in the Table 6.3 also indicate that the node-based element performance, in terms of rate of convergence and accuracy, with respect to exact solution is excellent.

Figure 6.24 depicts the relative error of the tip deflection for different mesh refinement on a log scale. It is evident that the present NSPE-T3 element, gives more accurate results than those of other numerical solutions cited here where the displacement prediction error for the 50×2 mesh is only 0.568%. On the whole, all the node-based element perform similarly well and better than the cell-based SPQ4 element and the FEM-T3 element.

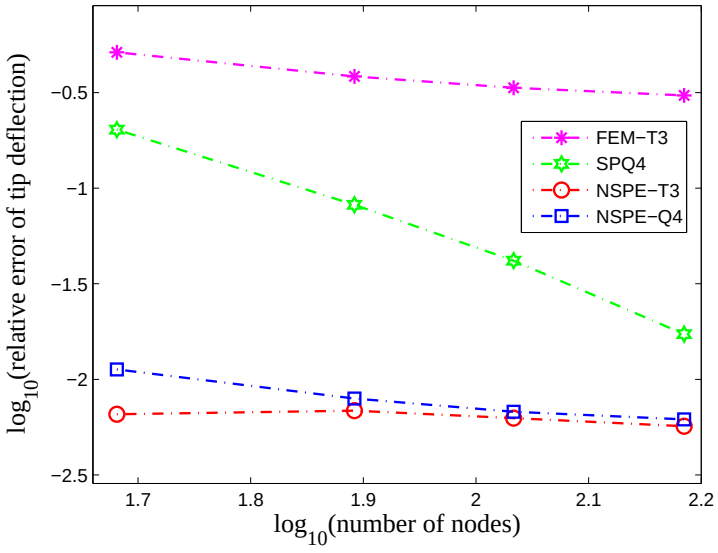

Figure 6.24: Convergence behaviour of tip deflection.

6.5.6 Piezoelectric Cook's membrane

This section deals with a clamped tapered panel with distributed in-plane tip load $F = 1$ similar to the well-known Cook's membrane. The lower surface is subjected to a voltage $V = 0$. The geometry and boundary conditions of the beam are shown in the Figure 6.25. The beam is made of PZT4 material as in Section 6.5.1. The two typical types of mesh with 8×8 quadrilateral elements or

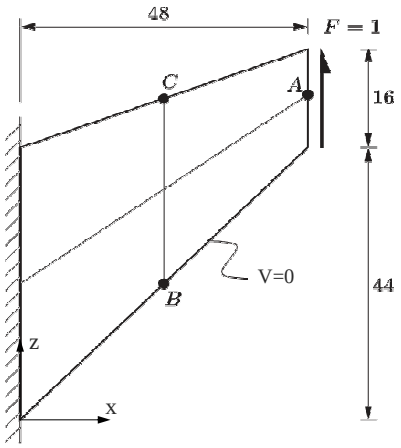

Figure 6.25: Piezoelectric Cook's membrane.

triangular elements are shown in Figure 6.26.

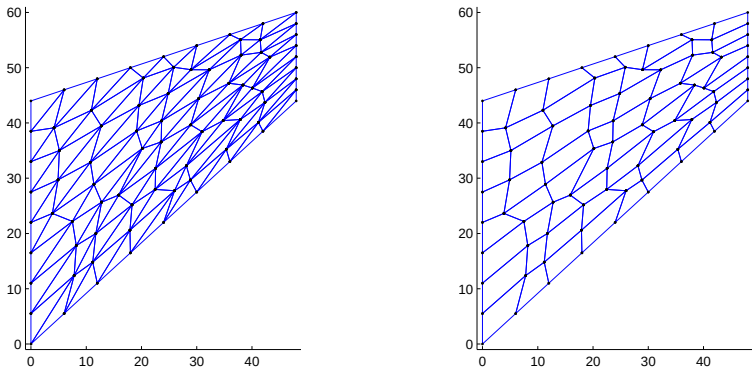

(a) (b)

Figure 6.26: Typical meshes of a piezoelectric Cook's membrane: (a) triangular mesh (NSPE-T3, FEM-T3 elements); (b) quadrilateral mesh (NSPE-Q4 elements).

To the author's best knowledge, there is no analytic solution available for this problem. The present results are compared with the best known values of the displacement, the electric potential, the first principal stress and the electric flux density at node A, B, C according to Long, Loveday and Groenwold (2006). They are summarized as follows.
$w_A = 2.109 \times 10^{-4}$ mm, $\phi_A = 1.732 \times 10^{-8}$ GV,
$\sigma_{1B} = 0.21613$ N/mm^2, $D_C = 22.409$ pC/mm^2.

Table 6.4 presents the obtained results with mesh refinement and relative error (difference) when compared with the best known values of Long, Loveday and Groenwold (2006). It can be seen that with a mesh of 24×24, all the results of node-based elements achieve better accuracy (relative error within 2%) than those of the FEM-T3 element. Figure 6.27a displays the magnitude of the relative error of vertical displacement w_A at point A with various meshes. The accuracy of the node-based element is again found to be better than the SPQ4 and FEM-T3 elements.

Figure 6.27b depicts the magnitude of the relative error of electric potential ϕ_A at point A. Again, the node-based elements is superior to the FEM-T3 elements. It is found that the cell-based SPQ4 element performs slightly better than the node-based elements in this case.

Table 6.4: Computed results of piezoelectric membrane and relative error in comparion with the best known results of Long et al. (2006).

	Mesh	$w_A \times 10^{-4}$ (mm)	$\phi_A \times 10^{-8}$ (GV)	σ_{1B} (N/mm^2)	D_C (pC/mm^2)
NSPE-Q4	4×4	2.2414	2.2294	2.1982E-01	1.8898E+01
	8×8	2.1568	1.9565	2.1423E-01	2.1548E+01
	16×16	2.1204	1.8109	2.1476E-01	2.2133E+01
	24×24	2.1137	1.7680	2.1512E-01	2.2179E+01
		(0.223%)	(2.078%)	(-0.453%)	(-1.026%)
NSPE-T3	4×4	2.2630	2.4646	3.8899E-01	3.2448E+01
	8×8	2.1688	1.9597	2.2729E-01	2.4441E+01
	16×16	2.1227	1.8177	2.1904E-01	2.1828E+01
	24×24	2.1156	1.7622	2.1696E-01	2.1944E+01
		(0.313%)	(1.744%)	(0.398%)	(-2.075%)
SPQ4	4×4	1.8801	1.2703	1.5779E-01	1.0555E+01
	8×8	2.0424	1.5796	1.9397E-01	1.6648E+01
	16×16	2.0910	1.6808	2.0744E-01	1.9785E+01
	24×24	2.1005	1.7033	2.1093E-01	2.0754E+01
		(-0.403%)	(-1.657%)	(-2.392%)	(-7.385%)
FEM-T3	4×4	1.0356	0.64272	1.0975E-01	7.1749E+00
	8×8	1.5383	1.1629	1.6320E-01	7.2903E+00
	16×16	1.8990	1.5186	2.0002E-01	1.5830E+01
	24×24	2.0046	1.6213	2.0955E-01	1.8476E+01
		(-4.950%)	(-6.391%)	(-3.031%)	(-17.551%)
Long et al. (2006)		2.109	1.732	0.2161	22.409

Figure 6.28 presents the magnitude of relative errors of the first principal stress σ_{1B} at point B and the electric flux density D_C at point C. Again, all the node-based elements perform similarly well and achieve better results than those of SPQ4 and FEM-T3 elements.

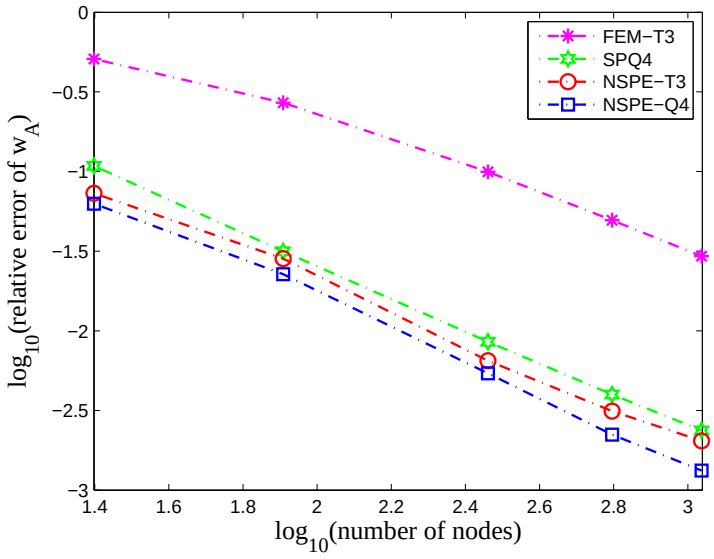

(a)

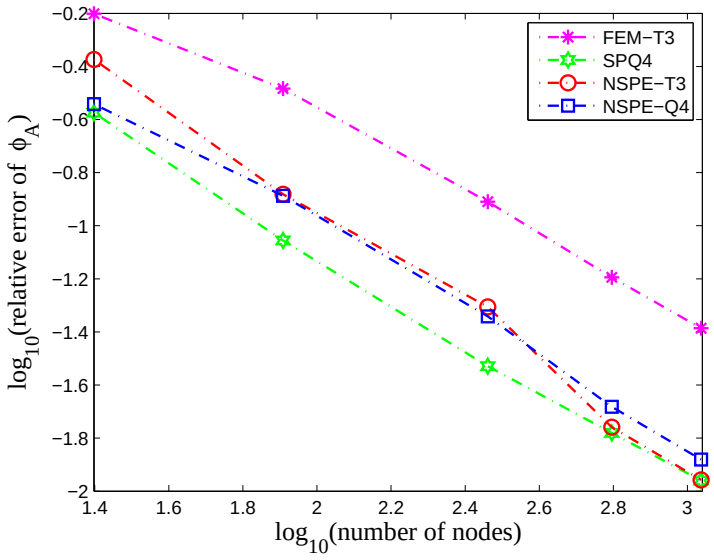

(b)

Figure 6.27: Piezoelectric Cook's membrane: Convergence behaviours: (a) vertical displacement w at point A; (b) electric potential ϕ at point A.

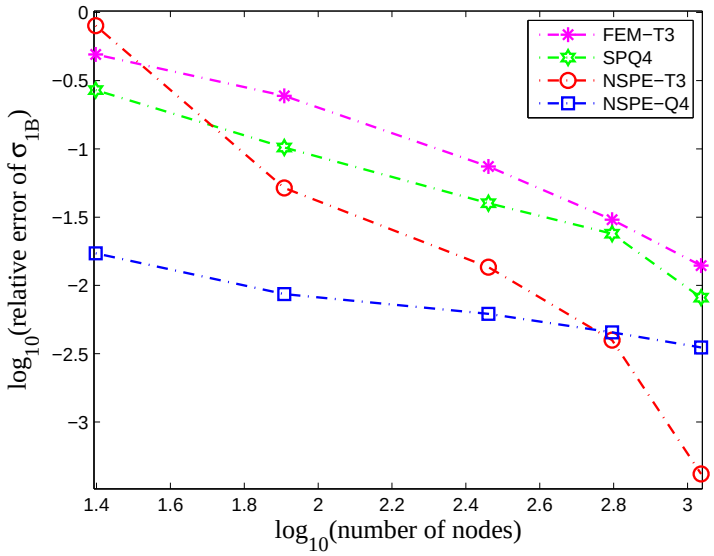

(a)

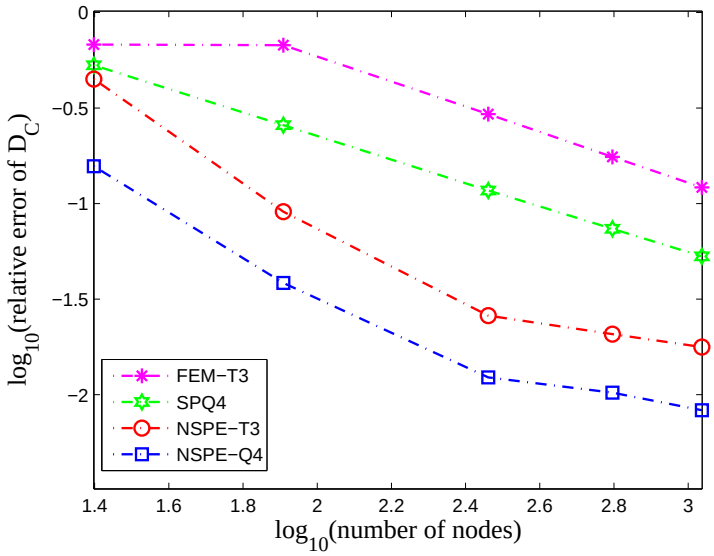

(b)

Figure 6.28: Piezoelectric Cook's membrane: Convergence behaviours: (a) first principal stress σ_{1B} at point B; (b) electric flux density D_C at point C.

6.5.7 Double bimorph optical micro-scanner

A central component of an optical micro-scanner is an adjustable mirror that is used to reflect light beams. It has a variety of applications such as optical scanning, display devices, printer or barcode scanning. This section concerns the modelling of a simple micro-scanner, as depicted in Figure 6.29. The device is composed of two parallel bimorphs bridged by a mirror at their tip center. When a voltage is applied, the bimorphs deflect in opposite directions. This bending moves the edges of the mirror up and down, rotating the mirror with a tilt angle β. The angle of rotation β is larger than the angle at the tip of each bending bimorphs, owing to the mechanical amplification that is achieved in this MEMS device. The direction of the reflected light, therefore, can be changed under different applied voltages.

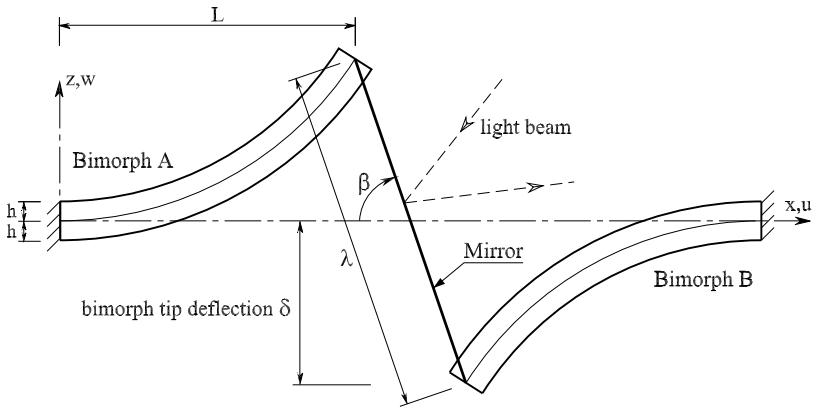

Figure 6.29: A bimorph optical micro-scanner MEMS device.

The two-layer bimorphs are made of PVDF material whose properties are summarized as follows.

$c_{11} = 2.18 \times 10^{-3}$ N/μm^2, $c_{13} = 6.33 \times 10^{-4}$ N/μm^2,
$c_{33} = 2.18 \times 10^{-3}$ N/μm^2, $c_{55} = 7.75 \times 10^{-4}$ N/μm^2,
$e_{31} = 4.6 \times 10^{-8}$ N/(Vμm), $e_{33} = 4.6 \times 10^{-8}$ N/(Vμm),
$g_{11} = 1.062 \times 10^{-10}$ N/V^2, $g_{33} = 1.062 \times 10^{-10}$ N/V^2.

The following boundary conditions apply to the bottom layer of the bimorph beam

$$\begin{aligned}
&\phi^{(1)}(x,-h) = V_0, \quad \sigma_z^{(1)}(x,-h) = 0, \quad \tau_z^{(1)}(x,-h) = 0,\\
&\phi^{(1)}(x,0) = 0, \quad \sigma_z^{(1)}(x,0) = \sigma_z^{(2)}(x,0),\\
&\tau_{xz}^{(1)}(x,0) = \tau_{xz}^{(2)}(x,0),\\
&\phi_{,x}^{(1)}(0,z) = 0, \quad u^{(1)}(0,z) = 0, \quad w^{(1)}(0,z) = 0.\\
&\phi_{,x}^{(1)}(L,z) = 0, \quad \sigma_x^{(1)}(L,z) = 0, \quad \tau_{xz}^{(1)}(L,z) = 0.
\end{aligned}$$

and boundary conditions for the top layer are

$$\begin{aligned}
&\phi^{(2)}(x,0) = \phi^{(1)}(x,0), \quad u^{(2)}(x,0) = u^{(1)}(x,0),\\
&w^{(2)}(x,0) = w^{(1)}(x,0) \quad \phi^{(2)}(x,h) = V_0,\\
&\sigma_z^{(2)}(x,h) = 0, \quad \tau_{xz}^{(2)}(x,h) = 0,\\
&\phi_{,x}^{(2)}(0,z) = 0, \quad u^{(2)}(0,z) = 0, \quad w^{(2)}(0,z) = 0,\\
&\phi_{,x}^{(2)}(L,z) = 0, \quad \sigma_x^{(2)}(L,z) = 0, \quad \tau_{xz}^{(2)}(L,z) = 0.
\end{aligned}$$

Referring to Figure 6.29, each bimorphs have a length $L = 10$ μm and a height $2h = 1$ μm. The length of the mirror is $\lambda = 1$ μm. For sufficiently small rotations, β can be approximated as

$$\beta = \frac{2\delta}{\lambda}. \tag{6.79}$$

A 80×2 uniform mesh (with node-based elements (NSPE-T3, NSPE-Q4), the cell-based element (SPQ4) or the FEM-T3 element) is used to analyse the problem. The tip displacements of the bimorph are calculated for several applied voltages and shown in Table 6.5. All the results are compared with the meshless PCM solution of Ohs and Aluru (2001).

From the tip displacements, the tilt angles of the mirror are determined from Equation (6.79). The tilt angle that varies linearly with applied voltages as expected is shown on Figure 6.30. It can be seen that the results obtained from node-based and cell-based elements are in closer agreement with the meshless PCM solution than FEM-T3 solutions. It is interesting to note that the result of NSPE-T3 element compares very favourably with the meshless PCM solution while the computational cost is lower.

Table 6.5: Tip deflection of the bimorph beam of the micro-scanner MEMS device.

Voltage	FEM-T3	SPQ4	NSPE-Q4	NSPE-T3	PCM
1.00	4.3765E-03	5.1194E-03	4.7828E-03	4.9138E-03	4.9360E-03
2.00	8.7529E-03	1.0239E-02	9.5656E-03	9.8276E-03	9.8720E-03
5.00	2.1882E-02	2.5597E-02	2.3914E-02	2.4569E-02	2.4681E-02
10.00	4.3765E-02	5.1194E-02	4.7828E-02	4.9138E-02	4.9362E-02
15.00	6.5647E-02	7.6791E-02	7.1742E-02	7.3707E-02	7.4043E-02
20.00	8.7529E-02	1.0239E-01	9.5656E-02	9.8276E-02	9.8724E-02
25.00	1.0941E-01	1.2798E-01	1.1957E-01	1.2285E-01	1.2341E-01
50.00	2.1882E-01	2.5597E-01	2.3914E-01	2.4569E-01	2.4681E-01

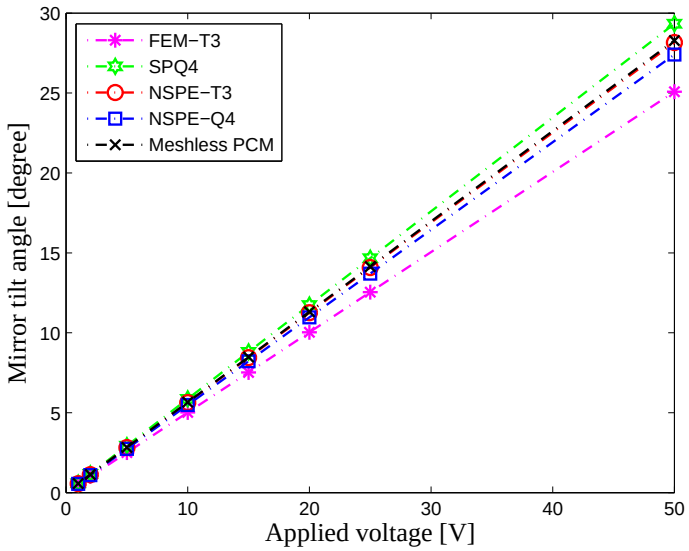

Figure 6.30: Behaviour of the mirror tilt angle under applied voltages.

6.5.8 Infinite piezoelectric plate with a circular hole

The last static analysis problem considered in this section is that of a piezoelectric plate with a central circular cavity subjected to a uniform uniaxial far-field stress σ_∞ in the $z-$direction as shown in Figure 6.31. This example is used to show the efficiency of the developed elements in predicting stresses in a stress concentration problem.

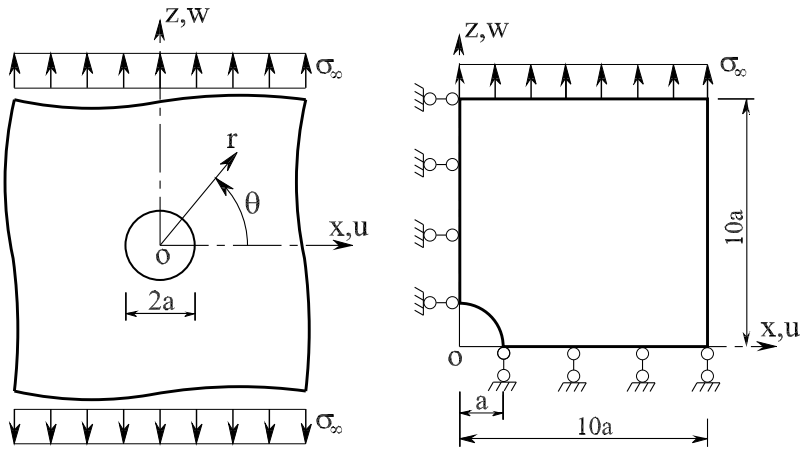

Figure 6.31: An infinite piezo-plate with a circular hole subjected to the far field stress.

The material is PZT-4 ceramic and its mechanical and piezoelectric elastic constants are as follows.

$c_{11} = 12.6 \times 10^{10}$, $c_{33} = 11.5 \times 10^{10}$, $c_{12} = 7.78 \times 10^{10}$,

$c_{13} = 7.43 \times 10^{10}$, $c_{55} = 2.56 \times 10^{10}$ (N/m^2),

$e_{15} = 12.7$, $e_{31} = -5.2$, $e_{33} = 15.1$ (C/m^2),

$g_{11} = 6.463 \times 10^{-9}$, $g_{33} = 5.611 \times 10^{-9}$(F/m).

Owing to symmetric conditions of the geometry and the loading case, only one quadrant of the problem needs to be modeled. According to Saint-Venant's principle, stress disturbance due to the hole extends no more than a few diameters from the hole. Thus, it is reasonable to use a $10a$ by $10a$ domain to model one quadrant of the problem domain. In the analysis, the hole radius a is taken to be 1 and the applied stress $\sigma_\infty = 10$. Two types of mesh used in the calculation are shown in Figure 6.32.

All numerical results are compared with the analytical solutions given by Sosa (1991) as shown in Figure 6.33 –6.36.

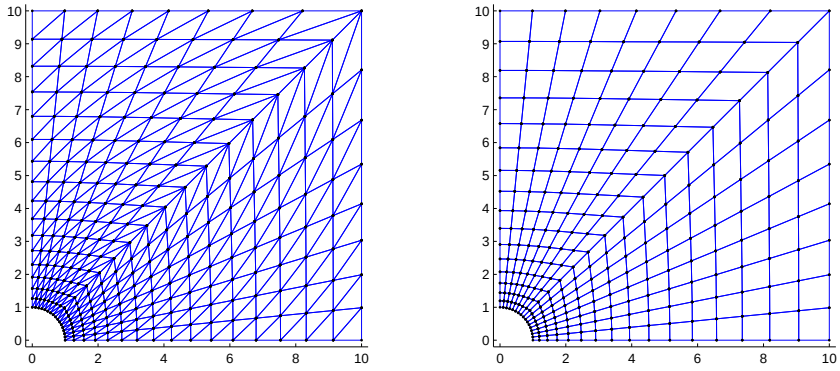

(a) (b)

Figure 6.32: Typical meshes of a quadrant of a piezo-plate with a central circular hole: (a) triangular mesh (NSPE-T3 elements); (b) quadrilateral mesh (NSPE-Q4 elements).

Figure 6.33 and Figure 6.34 describe the distributions of σ_r and σ_θ on the line $\theta = 0$, respectively. It can be seen from Figure 6.34 that σ_θ has maximum value at the intersection of the hole and the $x-$axis as in Sosa's theorical results.

The distributions of σ_r and σ_θ on the line $\theta = \pi/2$ are displayed in Figure 6.35 and Figure 6.36. It is observed from Figure 6.36 that σ_θ approaches zero rapidly when r increases, which indicates that there is a stress concentration region near the hole. The minimum value of σ_θ, obtained where the circle intersects the $z-$axis, agrees well with the theory of piezoelasticity as depicted in Figure 6.36.

It is evident in Figure 6.33–6.36 that the performance of developed elements (SPQ4, NSPE-T3, NSPE-Q4) in predicting stress concentration near the hole are better than those of standard finite elements (FEM-T3 or FEM-Q4)

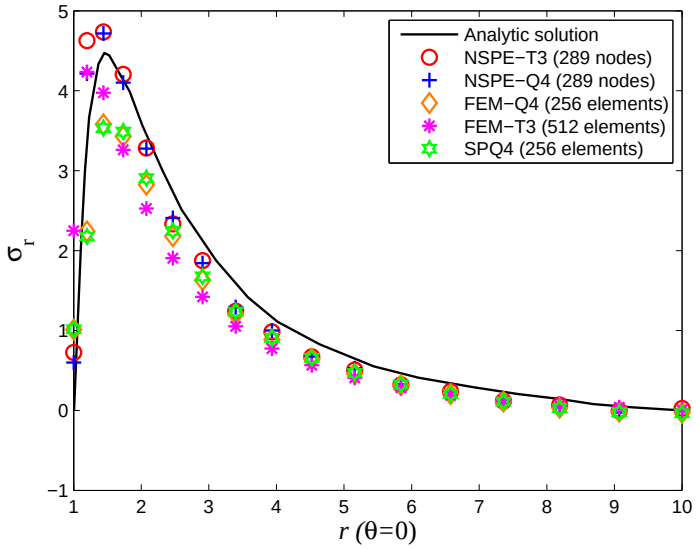

Figure 6.33: Distribution of σ_r along the line $\theta = 0$.

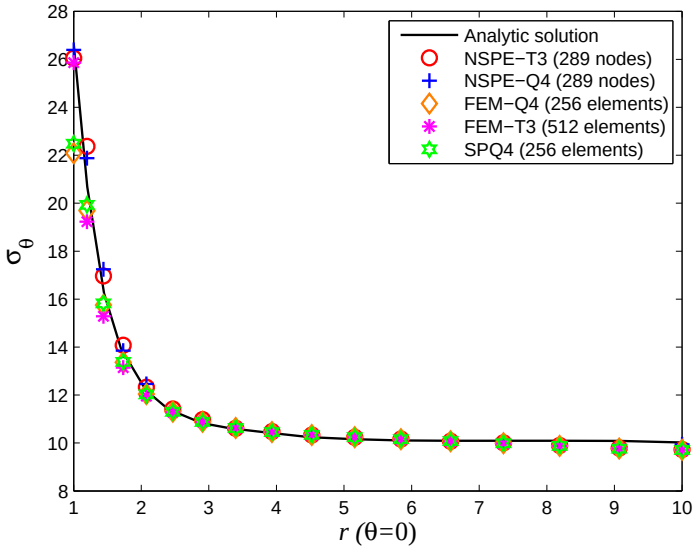

Figure 6.34: Distribution of σ_θ along the line $\theta = 0$.

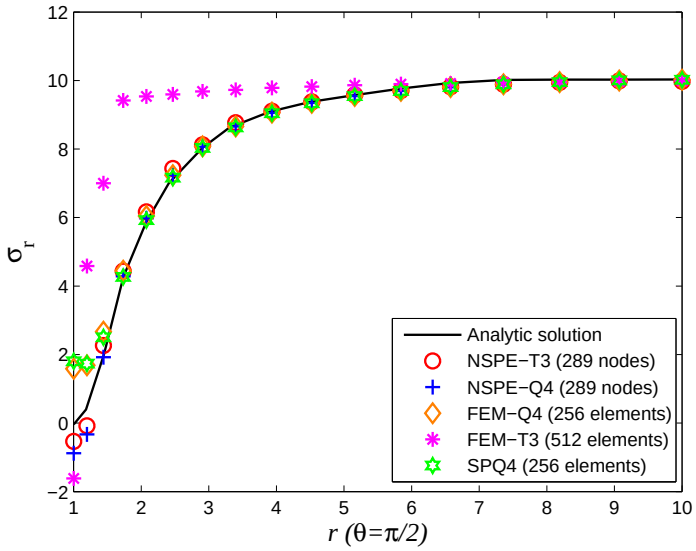

Figure 6.35: Distribution of σ_r along the line $\theta = \pi/2$.

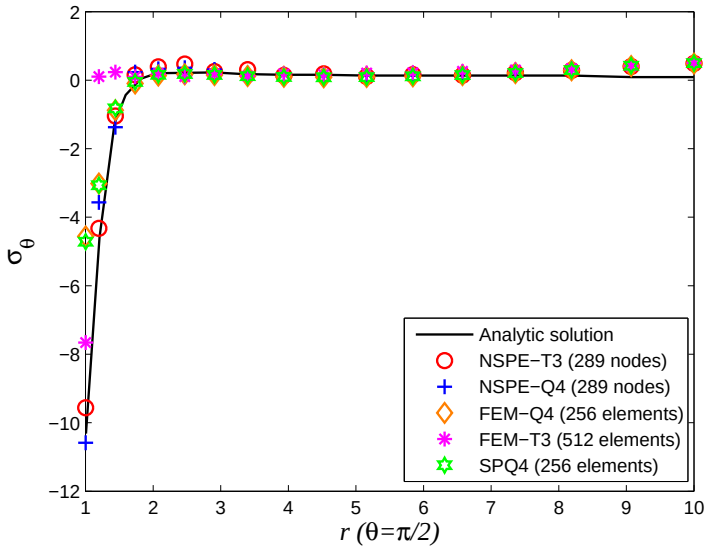

Figure 6.36: Distribution of σ_t along the line $\theta = \pi/2$.

6.5.9 Free vibration of a piezoelectric transducer

This section reports an eigenvalue analysis of a piezoelectric transducer consisting of a piezoelectric wall made of PZT4 material with brass end caps as shown in Figure 6.37. The piezoelectric material is electroded on both the inner and outer surfaces. This problem is similar to the one studied numerically by Liu et al. (2003) and experimentally by Mercer et al. (1987). It is also a typical example described in Section 6.1.1 of ABAQUS/Standard (2004).

The material properties of PZT4 are as follows.

$$
\begin{aligned}
\rho &= 7500\ \mathrm{kgm}^{-3}, \\
\mathbf{c} &= \begin{bmatrix}
115.4 & 74.28 & 74.28 & 0 & 0 & 0 \\
74.28 & 139.0 & 77.84 & 0 & 0 & 0 \\
74.28 & 77.84 & 139.0 & 0 & 0 & 0 \\
0 & 0 & 0 & 25.64 & 0 & 0 \\
0 & 0 & 0 & 0 & 25.64 & 0 \\
0 & 0 & 0 & 0 & 0 & 25.64
\end{bmatrix} \mathrm{GPa}, \\
\mathbf{e} &= \begin{bmatrix}
15.08 & -5.207 & -5.207 & 0 & 0 & 0 \\
0 & 0 & 0 & 12.710 & 0 & 0 \\
0 & 0 & 0 & 0 & 12.710 & 0
\end{bmatrix} \mathrm{Cm}^{-2}, \\
\mathbf{g} &= \begin{bmatrix}
5.872 & 0 & 0 \\
0 & 6.752 & 0 \\
0 & 0 & 6.752
\end{bmatrix} \times 10^{-9} \mathrm{Fm}^{-1},
\end{aligned}
$$

and the material properties of brass are: $\rho = 8500\ \mathrm{kgm}^{-3}$, $E = 10.4 \times 10^{10}$ Pa, $\nu = 0.37$.

The transducer is modelled as an axisymmetric structure with 44 uniform elements as shown in Figure 6.38. The obtained results are compared with those of Liu et al. (2002) using PIM mesh-free method and experimental results reported in Mercer et al. (1987) as given in Table 6.6. The values in parentheses correspond to the relative error compared with experimental results.

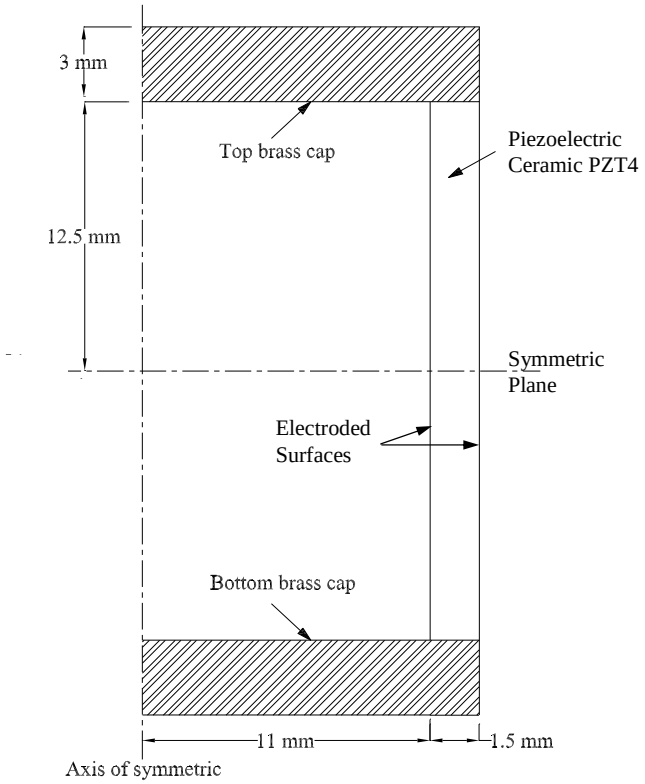

Figure 6.37: Representative sketch of a piezoelectric transducer.

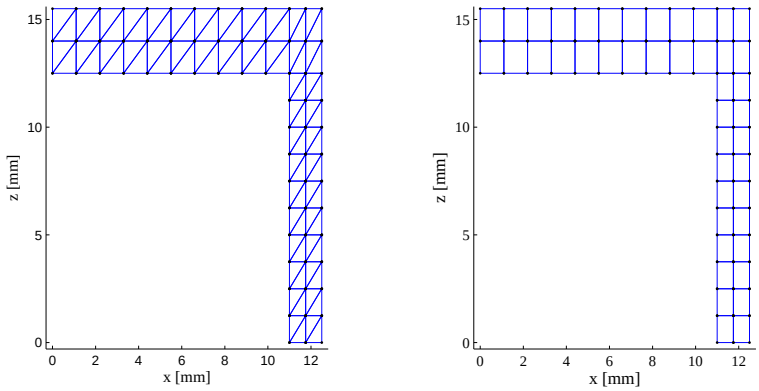

(a) (b)

Figure 6.38: Domain discretization of a piezoelectric transducer: (a) triangular mesh and (b) quadrilateral mesh.

It can be seen that the present solutions of the SPQ4, NSPE-T3 and NSPE-Q4 elements in general indicate good agreement with experimental results and give

Table 6.6: Computed eigenvalues of the transducer and comparison with other solutions.

Model	Mode 1	Mode 2	Mode 3	Mode 4
Experimental	18.6	35.4	54.2	63.3
PIM (44 cells)	19.9	42.8	59.7	66.1
	(6.989%)	(20.904%)	(10.148%)	(4.423%)
FEM-Q4 (44 element)	20.387	43.443	62.874	67.993
	(9.607%)	(22.720%)	(16.003%)	(7.414%)
FEM-T3 (88 element)	20.905	44.181	64.101	72.196
	(12.392%)	(24.805%)	(18.267%)	(14.053%)
NSPE-Q4 (69 nodes)	19.169	42.721	47.642	60.604
	(3.059%)	(20.681%)	(-12.099%)	(-4.259%)
NSPE-T3 (69 nodes)	19.433	42.206	48.086	62.271
	(4.478%)	(19.226%)	(-11.280%)	(-1.626%)
SPQ4 (44 elements)	18.214	41.773	58.642	65.798
	(-2.075%)	(18.003%)	(8.195%)	(3.946%)

smaller relative error than those of PIM, FEM-T3 and FEM-Q4 results. The first four mode shapes are also displayed in Figure 6.39 which appears identical to those depicted in Liu et al. (2003).

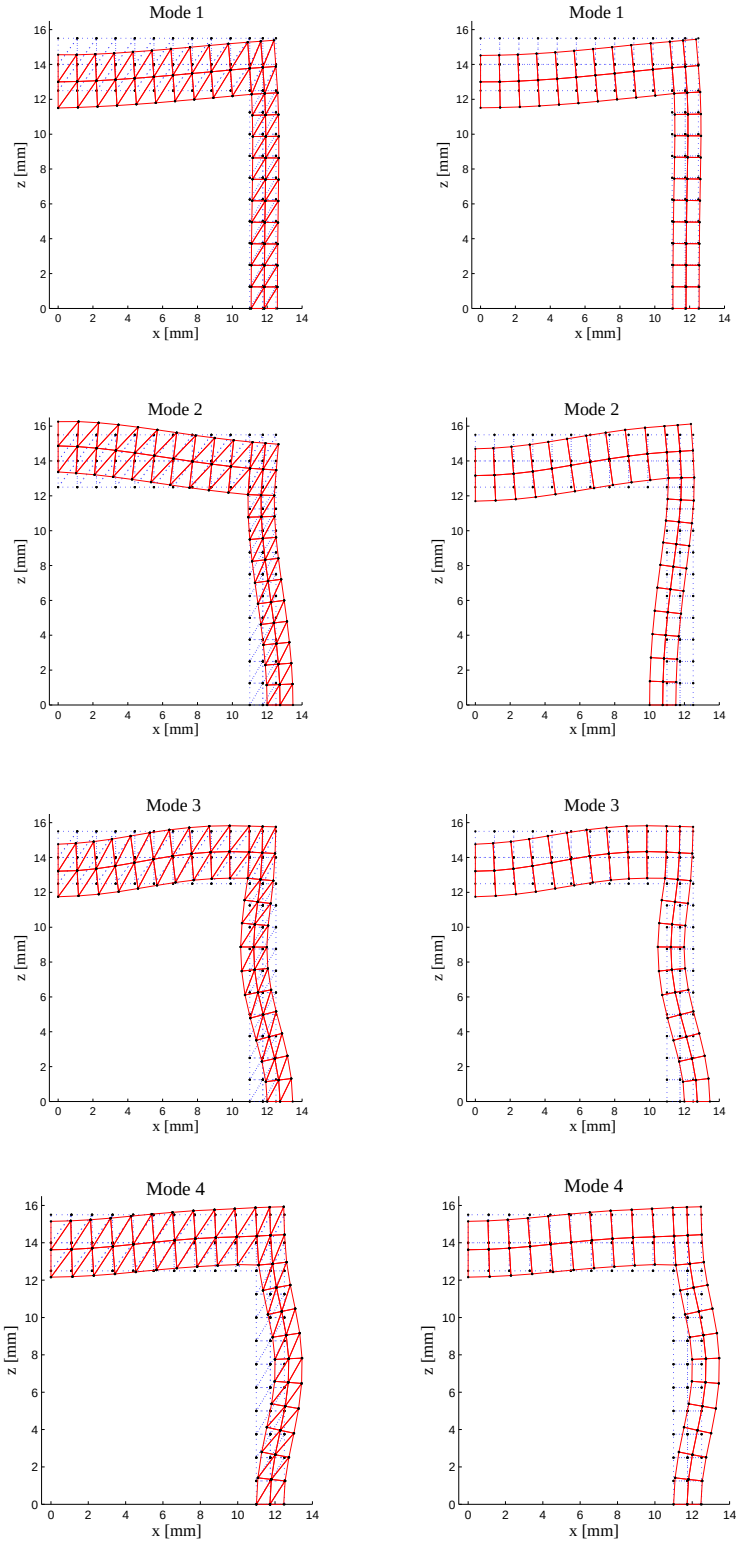

(a) (b)

Figure 6.39: Piezoelectric transducer: the first four mode shapes with (a) triangular mesh and (b) quadrilateral mesh.

6.6 Concluding remarks

This chapter presents the successful development and implementation of a family of novel and robust low-order piezoelectric elements for linear static and frequency analysis of planar piezoelectric structures. The incorporation of the SCNI technique into the finite element method gives the novel elements several advantages: (1) field gradients are to be computed directly from shape functions themselves (i.e. derivatives of shape functions are not required). This property can reduce the requirement on the smoothness of shape functions and low-order shape functions can be used to obtained accurate solutions. (2) the transformation of domain integrations into boundary integrations eliminates coordinate transformation (mapping) and contributes to the preservation of high accuracy of the method when extremely distorted elements are used; (3) the method is straightforward and simple to implement because the constructions of the stiffness matrices of the developed elements are very similar to those of the standard FEM.

The reliability, accuracy and convergence of the novel element formulations are demonstrated through various favourable comparisons with other existing elements as well as analytic solutions. Both the cell-based and node-based approaches are able to offer better results in comparison with the conventional FEM using linear/bilinear shape functions and even more accurate than some mesh-free methods in some cases. Furthermore, the proposed methods allow the elimination of the need for well-shaped element discretisation of the problem domain to obtain accurate solution in the standard FEM. Their performance with respect to analytic solution is excellent even with extreme element distortions.

Among two approaches, the node-based method provides more accurate prediction of the solution than those of the cell-based method with the same degrees of freedom. In addition, the node-based method is more convenient to compute directly nodal stresses while the cell-based method and the standard FEM need to use post-processing to recover these stresses. Therefore the node-based approach is very promising in terms of a simple and practical procedure for stress analysis. Within the two developed node-based elements, the node-based NSPE-T3 element, in general, is better in term of accuracy than the NPSE-Q4 element as shown through many examples.

Chapter 7

Conclusions

7.1 Summary and conclusion

In this thesis, a class of novel and robust low-order displacement-based finite elements for the analysis of composite structures are formulated and presented. The elements are based on the incorporation of the strain smoothing technique of the stabilized conforming nodal integration (SCNI) mesh-free method into the conventional finite element method through the assumed strain technique. The outcome of the present research is the successful creation and implementation of the following novel finite element models:

- Two novel, simple and high-performance low-order quadrilateral flat elements (MISQ20 and MISQ24) for modelling general plate and shell structures which can not only easily be adapted to a particular material type (i.e. composite laminates, isotropic materials or functionally graded materials) but also improve model accuracy and alleviate numerical instabilities for geometrically linear and nonlinear analysis.
- Two novel, simple, accurate and efficient piezoelectric elements (SPQ4 and NSPE-Q4/NSPE-T3) for linear static and free vibration analysis of electromechanical coupling behaviours of planar piezoelectric structures.

The new flat quadrilateral plate/shell elements, MISQ20 and MISQ24, have the following important properties:

- ◇ The elements are formulated based on the equivalent single-layer first-order shear deformation theory and hence they can be used for analysis of moderately thick to thin structures.
- ◇ The evaluation of membrane, bending and geometric stiffness matrices are computed by integration along the boundary of smoothing elements. Therefore the amount of computation required to calculate the element stiffness matrix are reduced when compared with domain integration approach.
- ◇ The elements pass patch tests which imply the convergence of solutions with mesh refinement.
- ◇ The elements are free from membrane and shear locking in the limit of thin plates/shells without any spurious zero-energy modes.
- ◇ The elements are insensitivity to extreme shape distortion and provide good accuracy even with coarse meshes or warping geometries.
- ◇ The elements are simple in formulation and their implementation straightforward. Linear/nonlinear constitutive laws can be incorporated into an existing finite element code with a minimum effort.
- ◇ The elements can be considered as some of the simplest flat quadrilateral elements for analysis of plate/shell structures.
- ◇ The accuracy of the present models is assessed by comparison with analytical or experimental and numerical solutions available in the literature. Highly accurate solutions obtained in all cases show that the elements are reliable and have good predictive capability in the analysis of moderately thick and thin plates/shells of arbitrary geometries.

In the case of coupled analysis of piezoelectric systems, two different approaches are utilized to develop two new smoothing piezoelectric finite elements. The first one is the cell-based element (SPQ4) based on the subdivision of original quadrilateral finite elements into smoothing cells. The second one, the node-based element

(NSPE-T3 or NSPE-Q4), is created by transforming a triangular or quadrilateral mesh into a mesh of new smoothing cells associated with each of the nodes of the original mesh. The significant features of the developed piezoelectric finite element models are summarized as follows.

- ◇ The element field gradients are computed directly from shape functions themselves (i.e. derivatives of shape functions are not required) and no limitation is imposed on the shape of elements in the original mesh.
- ◇ No coordinate transformation or mapping is required in the present formulations and problem domains can be discretized in more flexible ways than the traditional FEM.
- ◇ The transformation of domain integrations into boundary integrations contributes to the preservation of high accuracy of the method in cases of extremely distorted elements and may reduce the computational cost. This also allows the elimination of the need for uniform discretisation of the problem domain to obtain accurate solutions.
- ◇ The element formulations are straightforward and simple to implement because the construction of the element stiffness matrices are very similar to those of the standard FEM.
- ◇ The elements pass patch tests for plane piezoelectric problem which implies convergence of solutions with mesh refinement.
- ◇ The accuracy and reliable of the present elements are justified through various favourable comparisons with other existing elements as well as experimental or analytic solutions.

In conclusion, the present research results in new, simple and efficient finite element formulations, which is a contribution to further knowledge and understanding in the area of computational engineering using finite element analysis. Numerical simulations are studied and demonstrated in a wide range of engineering applications involving analysis of plate/shell structures with various geometric shapes (rectangular, triangular, skew, circular plates; cylindrical, spherical, hyperbolic paraboloid shells, etc.) as well as different type of materials (isotropic,

laminated composite or functionally grade material). The obtained numerical results have provided a definitive and better understanding of the effect of modulus ratios, fibre orientations, different mixed boundary conditions, span-to-thickness ratios and lay-up sequences (i.e. cross-ply, angle-ply, symmetric/unsymmetric laminates) on the behaviour of laminated composite structures regimes in bending, free vibration and buckling analysis. The present method has also been shown to be applicable to other types of composite structures such as piezoelectric materials. Bending analysis and free vibration of planar piezoelectric structures have been investigated in detail through several numerical examples. It is found that the elements offer the advantage of lower computational cost and superior performance in comparison with more conventional finite elements.

7.2 Suggested work

The presently developed framework can be further improved to offer a more valuable model for the analysis of composite structures. The following points are suggested for future research as a possible continuation of this work

- The present method has been successfully formulated for elastic analysis and it is therefore natural to further develop the model to investigate elasto-plastic behaviour of composite structures.
- It is probable that material nonlinearities will occur during the deformation of structures. Therefore, nonlinear material models need to be developed and incorporated in the present formulation to cater for a more realistic structural behavior. Post-buckling analysis to determine the ultimate strength of plate/shell structures can be also investigated.
- It would be interesting to advance a damage model for characterization of damage evolution and propagation in composite structures using the present formulation. Crack and fatigue failures can also be included.
- Another research direction is to extend the models for analysis and design of vibration shape control of FGM or laminated composite plates/shells with piezoelectric coupling.

Appendix A

Determination of transverse shear stresses

A detailed theory for calculating the transverse shear stresses is thoroughly outlined in Rolfes and Rohwer (1997). Only those relationships necessary to obtain the transverse shear stresses are given here.

By solving the local equilibrium equations in the $x-$ and $y-$direction for transverse shear stresses, the following equation is obtained

$$\boldsymbol{\tau}_z = \begin{bmatrix} \tau_{xz}^{(k)} \\ \tau_{yz}^{(k)} \end{bmatrix} = -\int_{\zeta=0}^{\zeta=z} \begin{pmatrix} \sigma_{x,x}^{(k)} + \tau_{xy,y}^{(k)} \\ \sigma_{y,y}^{(k)} + \tau_{xy,x}^{(k)} \end{pmatrix} d\zeta. \tag{A.1}$$

With the assumption of vanishing normal stress, the material law for the k^{th} lamina is

$$\boldsymbol{\sigma}_m^{(k)} = \begin{bmatrix} \sigma_x \\ \sigma_y \\ \tau_{xy} \end{bmatrix}^{(k)} = \bar{\mathbf{Q}}^{(k)}(\boldsymbol{\epsilon}_m + z\boldsymbol{\epsilon}_b), \tag{A.2}$$

where $\bar{\mathbf{Q}}^{(k)}$ are the reduced stiffness of the k^{th} lamina and $\boldsymbol{\epsilon}_m$ and $\boldsymbol{\epsilon}_b$ denote the lamina membrane and bending strains, respectively.

Substituting Equation (A.2) into Equation (A.1) yields

$$\boldsymbol{\tau}_z = -\int_{\zeta=0}^{\zeta=z} \left[\mathbf{B}_1\bar{\mathbf{Q}}^{(k)}(\boldsymbol{\epsilon}_{m,x} + \zeta\boldsymbol{\epsilon}_{b,x}) + \mathbf{B}_2\bar{\mathbf{Q}}^{(k)}(\boldsymbol{\epsilon}_{m,y} + \zeta\boldsymbol{\epsilon}_{b,y})\right] d\zeta, \tag{A.3}$$

in which $\mathbf{B}_1$ and $\mathbf{B}_2$ denote Boolean matrices in the following form

$$\mathbf{B}_1 = \begin{bmatrix} 1 & 0 & 0 \\ 0 & 0 & 1 \end{bmatrix}, \qquad \mathbf{B}_2 = \begin{bmatrix} 0 & 0 & 1 \\ 0 & 1 & 0 \end{bmatrix}. \tag{A.4}$$

Using the elasticity law of the laminate

$$\begin{bmatrix} \mathbf{N} \\ \mathbf{M} \end{bmatrix} = \begin{bmatrix} \mathbf{A} & \mathbf{B} \\ \mathbf{B} & \mathbf{D} \end{bmatrix} \begin{bmatrix} \boldsymbol{\epsilon}_m \\ \boldsymbol{\epsilon}_b \end{bmatrix}, \tag{A.5}$$

where $\mathbf{A}$, $\mathbf{D}$ and $\mathbf{B}$ are the membrane, bending and coupling stiffness, respectively and

$$\mathbf{M} = \begin{bmatrix} M_x \\ M_y \\ M_{xy} \end{bmatrix}, \qquad \mathbf{N} = \begin{bmatrix} N_x \\ N_y \\ N_{xy} \end{bmatrix}. \tag{A.6}$$

Since the influence of the membrane forces on the transverse shear stresses is very small, the membrane forces $\mathbf{N}$ can be neglected and the laminate strains can be expressed by only the moments as follows.

$$\boldsymbol{\epsilon}_m = -\mathbf{A}^{-1}\mathbf{B}\boldsymbol{\epsilon}_b, \tag{A.7}$$

$$\boldsymbol{\epsilon}_b = -\mathbf{D}^{*-1}\mathbf{M}, \tag{A.8}$$

where

$$\mathbf{D}^* = (\mathbf{D} - \mathbf{B}^T\mathbf{A}^{-1}\mathbf{B}). \tag{A.9}$$

Substituting Equation (A.7)–(A.9) into Equation (A.3) the transverse shear stresses are obtained as

$$\boldsymbol{\tau}_z = -\mathbf{B}_1\mathbf{F}(z)\mathbf{M}_{,x} - \mathbf{B}_2\mathbf{F}(z)\mathbf{M}_{,y}, \tag{A.10}$$

where

$$\mathbf{F}(z) = \left(\mathbf{a}(z)\mathbf{A}^{-1}\mathbf{B} - \mathbf{b}(z)\right)\mathbf{D}^{*-1}, \tag{A.11}$$

in which $\mathbf{a}(z)$ and $\mathbf{b}(z)$ are partial membrane and coupling stiffnesses of the laminate, respectively. They are defined as

$$\mathbf{a}(z) = \int_{\zeta=0}^{\zeta=z} \bar{\mathbf{Q}} d\zeta, \qquad \mathbf{b}(z) = \int_{\zeta=0}^{\zeta=z} \bar{\mathbf{Q}}\zeta d\zeta. \tag{A.12}$$

Further assuming cylindrical bending around the $x-$ axis yields

$$\mathbf{M}_{,x} = \begin{bmatrix} M_{x,x} \\ 0 \\ 0 \end{bmatrix}, \tag{A.13}$$

and around the $y-$ axis provides

$$\mathbf{M}_{,y} = \begin{bmatrix} 0 \\ M_{y,y} \\ 0 \end{bmatrix}. \tag{A.14}$$

Then, the derivatives of the moments can be related to the shear forces as

$$R_{xz} = -M_{x,x}, \tag{A.15}$$

$$R_{yz} = -M_{y,y}. \tag{A.16}$$

With the aid of the above relations, the moment derivatives in Equation (A.10) are replaced by transverse shear forces, leading to

$$\boldsymbol{\tau}_z = \begin{bmatrix} F_{11} & F_{32} \\ F_{31} & F_{22} \end{bmatrix} \begin{bmatrix} R_{xz} \\ R_{yz} \end{bmatrix} = \mathbf{f}(z)\mathbf{R}. \tag{A.17}$$

where the transverse shear force $\mathbf{R}$ can be calculated using the material law

$$\mathbf{R} = \bar{\mathbf{G}}\boldsymbol{\gamma}, \tag{A.18}$$

in which $\bar{\mathbf{G}}$ is the improved transverse shear stiffness matrix given as

$$\bar{\mathbf{G}} = \left[\int \mathbf{f}^T \mathbf{G}^{-1} \mathbf{f} dz \right]^{-1}, \tag{A.19}$$

where $\mathbf{G}$ is the shear moduli matrix.

Appendix B

Assumed strain smoothing finite elements for FGM Reissner-Mindlin plates

B.1 Material properties and thermal analysis

Consider a functionally graded material (FGM) plate of thickness h made of two-constituent material such as ceramic and metal. The material property is assumed to vary through the thickness direction with the following power-law distribution:

$$V(z) = (V_t - V_b)V_c + V_b, \tag{B.1}$$

$$V_c = \left(\frac{1}{2} + \frac{z}{h}\right)^n, \quad (n \geq 0, \ -\frac{h}{2} \leq z \leq \frac{h}{2}). \tag{B.2}$$

where V denote a generic material property, V_t, V_b represent the material properties at the top (ceramic) and bottom (metal) faces of the plate, respectively, z is the thickness coordinate, V_c is the volume fraction and n is the volume fraction exponent. The variation of the volume fraction through the thickness for different value of n is plotted in Figure B.1.

For all cases of FGM plates being exposed in a temperature field, the temperature is assumed to be constant in the plane of the plate and varies only through the thickness direction. The temperature distribution across the thickness can be

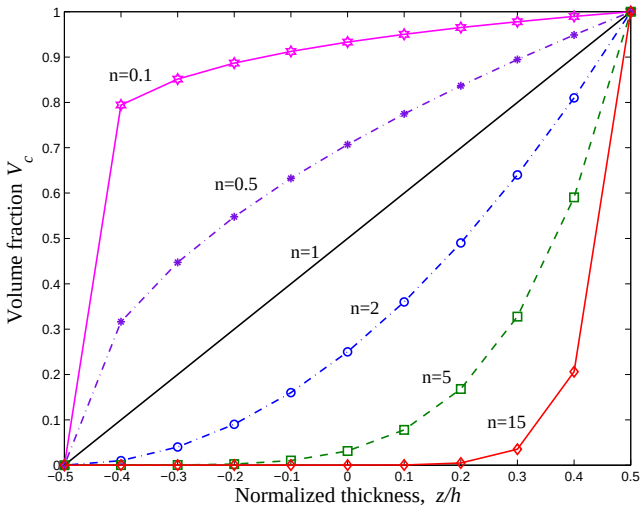

Figure B.1: Variation of the volume fraction V_c versus the normalized thickness.

obtained by solving the one-dimensional steady heat transfer equation:

$$-\frac{d}{dt}\left(\lambda(z)\frac{dT}{dz}\right) = 0 \tag{B.3}$$

with the thermal boundary conditions

$$T = T_t \text{ at } z = h/2, \qquad T = T_b \text{ at } z = -h/2.$$

The solution of Equation (B.3) is then obtained as

$$T(z) = T_t - \frac{T_t - T_b}{\int_{-h/2}^{h/2}(dz/\lambda(z))}\int_z^{h/2}\frac{d\xi}{\lambda(\xi)} \tag{B.4}$$

where the thermal conductivity $\lambda(z)$ varies according to the power-law distribution of Equation (B.1). The thermal effects are often introduced at the constitutive level and are described in the next section.

B.2 Assumed strain smoothing finite element formulation for FGM Reissner-Mindlin plates

Based on the Reissner-Mindlin theory, the displacement fields are expressed as

$$u(x,y,z) = -z\theta_x(x,y), \quad v(x,y,z) = -z\theta_y(x,y), \quad w(x,y,z) = w(x,y). \tag{B.5}$$

The in-plane strain vector is defined as

$$\boldsymbol{\epsilon}_b = [\theta_{x,x} \quad \theta_{y,y} \quad \theta_{x,y} + \theta_{y,x}]^T, \tag{B.6}$$

and the transverse shear strain is

$$\boldsymbol{\gamma} = [\theta_x - w_{,x} \quad \theta_y - w_{,y}]^T. \tag{B.7}$$

Under a given temperature distribution T with a thermal coefficient of expansion $\alpha(z)$, the thermal strain vector in the plate is given by

$$\boldsymbol{\epsilon}_{th} = [\alpha(z)\,(T(z) - T_0) \quad \alpha(z)\,(T(z) - T_0) \quad 0]^T. \tag{B.8}$$

Then, the constitutive relations are expressed as

$$\boldsymbol{\sigma} = \mathbf{B}(z)(\boldsymbol{\epsilon} - \boldsymbol{\epsilon}_{th}), \qquad \boldsymbol{\tau} = \mathbf{S}(z)\boldsymbol{\gamma}, \tag{B.9}$$

where $\boldsymbol{\sigma} = [\sigma_x, \sigma_y, \sigma_{xy}]^T$ and $\boldsymbol{\tau} = [\tau_x, \tau_y]^T$ are the total in-plane and shear stresses, respectively.

The grading matrices $\mathbf{B}(z)$ and $\mathbf{S}(z)$ are defined as

$$\mathbf{B}(z) = \frac{E(z)}{1-\nu^2}\begin{bmatrix} 1 & \nu & 0 \\ \nu & 1 & 0 \\ 0 & 0 & \frac{1-\nu}{2} \end{bmatrix}, \quad \mathbf{S}(z) = \frac{E(z)}{1-\nu^2}\begin{bmatrix} \frac{1-\nu}{2} & 0 \\ 0 & \frac{1-\nu}{2} \end{bmatrix} \tag{B.10}$$

In the Reissner-Mindlin model, the total potential energy under the thermal load and the mechanical pressure load p can be written as

$$\Pi(\theta_x, \theta_y, w) = \frac{1}{2}\int_\Omega \boldsymbol{\epsilon}_b^T \mathbf{D}_b \boldsymbol{\epsilon}_b d\Omega + \frac{k_s}{2}\int_\Omega \boldsymbol{\gamma}^T \mathbf{D}_s \boldsymbol{\gamma} d\Omega + \frac{1}{2}\int_\Omega \mathbf{m}_{th}\boldsymbol{\epsilon}_b d\Omega - \int_\Omega pw d\Omega, \tag{B.11}$$

where $k_s = 5/6$ is the shear correction factor and the elasticity matrices are given as

$$\mathbf{D}_b = \int_{-h/2}^{h/2} \mathbf{B}(z) z^2 dz, \qquad \mathbf{D}_s = \int_{-h/2}^{h/2} \mathbf{S}(z) dz, \tag{B.12}$$

and the vector of the thermal moments is

$$\mathbf{m}_{th} = \int_{-h/2}^{h/2} \mathbf{B}(z)\boldsymbol{\epsilon}^{th} z dz = \frac{1}{1-\nu}\begin{bmatrix} \int_{-h/2}^{h/2} \alpha(z)E(z)(T(z)-T_0)z dz \\ \int_{-h/2}^{h/2} \alpha(z)E(z)(T(z)-T_0)z dz \\ 0 \end{bmatrix} \tag{B.13}$$

Consider a bounded domain $\Omega = \sum_{i=1}^{n_e} \Omega^e$ of a FGM plate which is discretized into n_e finite elements. The finite element solution $\mathbf{u}$ of a displacement-based 4-node quadrilateral model is approximated as

$$\mathbf{u} = \left\{ \begin{array}{c} w \\ \theta_x \\ \theta_y \end{array} \right\} = \sum_{i=1}^{4} \mathbf{N}_i \mathbf{q}_i, \tag{B.14}$$

where $\mathbf{N}_i$ is the bilinear shape function, $\mathbf{q}_i = [w_i \;\; \theta_{xi} \;\; \theta_{yi}]^T$ is the nodal displacement vectors of the element.

The corresponding approximation of the smoothed bending strain and the assumed natural shear strains can be expressed in the following forms

$$\tilde{\boldsymbol{\epsilon}}_b = \tilde{\mathbf{B}}_b \mathbf{q}, \quad \boldsymbol{\gamma} = \bar{\mathbf{B}}_s \mathbf{q}, \tag{B.15}$$

where $\tilde{\mathbf{B}}_{bi}$ and $\bar{\mathbf{B}}_{si}$ were already defined in Equation (3.54) and Equation (3.59) of Chapter 3 as follows.

$$\tilde{\mathbf{B}}_{bi} = \frac{1}{A_C} \sum_{b=1}^{4} \begin{pmatrix} 0 & N_i(\mathbf{x}_b^G) n_x & 0 \\ 0 & 0 & N_i(\mathbf{x}_b^G) n_y \\ 0 & N_i(\mathbf{x}_b^G) n_y & N_i(\mathbf{x}_b^G) n_x \end{pmatrix} l_b, \tag{B.16}$$

$$\bar{\mathbf{B}}_{si} = \mathbf{J}^{-1} \begin{pmatrix} N_{i,\xi} & b_i^{11} N_{i,\xi} & b_i^{12} N_{i,\xi} \\ N_{i,\eta} & b_i^{21} N_{i,\eta} & b_i^{22} N_{i,\eta} \end{pmatrix}. \tag{B.17}$$

By minimizing Equation (B.11), the finite element formulations for thermoelastic static analysis of Reissner-Mindlin FGM plates can be obtained as follows.

$$\tilde{\mathbf{K}} \mathbf{q} = \tilde{\mathbf{F}}, \tag{B.18}$$

where $\tilde{\mathbf{K}}$ is the element stiffness matrix and $\tilde{\mathbf{F}}$ is the element load vector, which are given as

$$\tilde{\mathbf{K}} = \sum_{C=1}^{nc} \tilde{\mathbf{B}}_{bC}^T \mathbf{D}_b \tilde{\mathbf{B}}_{bC} A_C + \int_\Omega \bar{\mathbf{B}}_s^T \mathbf{D}_s \bar{\mathbf{B}}_s d\Omega, \tag{B.19}$$

$$\tilde{\mathbf{F}} = \int_\Omega p \mathbf{N} d\Omega + \sum_{C=1}^{nc} \mathbf{m}_{th} \tilde{\mathbf{B}}_{bC} A_C, \tag{B.20}$$

in which the number of smoothing cells nc is chosen as $nc = 2$.

Bibliography

[1] ABAQUS/Standard (2004). *Example Problems Manual v6.5-1.*

[2] Allik, H. and Hughes, T. J. R. (1970). Finite element method for piezoelectric vibration, *International Journal for Numerical Methods in Engineering* **2**: 151–157.

[3] Allman, D. J. (1984). A compatible triangular element including vertex rotations for plane elasticity analysis, *Computers and Structures* **19**: 1–8.

[4] Andrade, L. G., Awruch, A. M. and Morsch, I. B. (2007). Geometrically nonlinear analysis of laminate composite plates and shells using the eight-node hexahedral element with one-point integration, *Composite Structures* **79**: 571–580.

[5] ANSYS (1998). *ANSYS User's Manual v5.5.*

[6] Argyris, J. and Tenek, L. (1994). Linear and geometrically nonlinear bending of isotropic and multilayered composite plates by the natural mode method, *Computer Methods in Applied Mechanics and Engineering* **113**: 207–251.

[7] Auricchio, F. and Sacco, E. (1999). A mixed-enhanced finite-element for the analysis of laminated composite plates, *International Journal for Numerical Methods in Engineering* **44**: 1481–1504.

[8] Ayad, R. and Rigolot, A. (2002). An improved four-node hybrid-mixed element based upon Mindlin's plate theory, *International Journal for Numerical Methods in Engineering* **55**: 705–731.

[9] Bathe, K. J. (1996). *Finite Element Procedures*, Prentice-Hall: New Jersey.

[10] Bathe, K. J. and Dvorkin, E. N. (1985). A four node plate bending element based on Mindlin-Reissner plate theory and a mixed interpolation, *International Journal for Numerical Methods in Engineering* **21**: 367–383.

[11] Bathe, K. J., Iosilevich, A. and Chapelle, D. (2000). An evaluation of the MITC shell elements, *Computers and Structures* **75**: 1–30.

[12] Batoz, J. L., Bathe, K. J. and Ho, L. W. (1980). A study of three-node triangular plate bending elements, *International Journal for Numerical Methods in Engineering* **15**: 1771–1812.

[13] Batoz, J. L. and Lardeur, P. (1989). A discrete shear triangular nine dof element for analysis of thick to very thin plate, *International Journal for Numerical Methods in Engineering* **28**: 533–560.

[14] Batoz, J. L. and Tahar, M. B. (1982). Evaluation of a new quadrilateral thin plate bending element, *International Journal for Numerical Methods in Engineering* **18**: 1655–1677.

[15] Beissel, S. and Belytschko, T. (1996). Nodal integration of the element-free Galerkin method., *Computer Methods in Applied Mechanics and Engineering* **139**: 49–74.

[16] Belytschko, T., Krongauz, Y., Organ, D., Fleming, M. and Krysl, P. (1996). Meshless methods: An overview nd recent developments, *Computer Methods in Applied Mechanics and Engineering* **139**: 3–47.

[17] Belytschko, T. and Leviathan, I. (1994). Physical stabilization of the 4-node shell with one-point quadrature, *Computer Methods in Applied Mechanics and Engineering* **113**: 321–350.

[18] Belytschko, T. and Tsay, C. S. (1983). A stabilization procedure for the quadrilateral plate element with one point quadrature, *International Journal for Numerical Methods in Engineering* **19**: 405–419.

[19] Belytschko, T., Tsay, C. S. and Liu, W. K. (1981). A stabilization matrix for the bilinear Mindlin plate element, *Computer Methods in Applied Mechanics and Engineering* **29**: 313–327.

[20] Belytschko, T., Wong, B. L. and Stolarski, H. (1989). Assumed strain stabilization procedure for the 9-node Lagrange shell element, *International Journal for Numerical Methods in Engineering* **28**: 385–414.

[21] Benjeddou, A. (2000). Advances in piezoelectric finite element modeling of adaptive structural elements: a survey, *Computers and Structures* **76**: 347–363.

[22] Bisegna, P. and Maceri, F. (1996). An exact three-dimensional solution for simply supported rectangular piezoelectric plate, *ASME Journal of Applied Mechanics* **63**: 628–638.

[23] Bonet, J. and Kulasegaram, S. (1999). Correction and stabilization of smooth particle hydrodynamics methods with applications in metal forming simulation, *International Journal for Numerical Methods in Engineering* **47**: 1189–1214.

[24] Brezzi, F., Bathe, K. J. and Fortin, M. (1989). Mixed-Interpolated elements for Reissne-Mindlin plates, *International Journal for Numerical Methods in Engineering* **28**: 1787–1801.

[25] Cambridge, M. (1995). *Product Catalogue: Piezo Systems Inc.*, cambridge ma edn.

[26] Cannarozzi, A. A. and Ubertini, F. (2001). Some hybrid variational methods for linear electroelasticity problems, *International Journal of Solids and Structures* **38**: 2573–2596.

[27] Cantin, G. and Clough, R. W. (1968). A curved cylindrical shell finite element, *AIAA Journal* **6**: 1057–1062.

[28] Carrera, E. and Boscolo, M. (2007). Classical and mixed finite elements for static and dynamic analysis of piezoelectric plates, *International Journal for Numerical Methods in Engineering* **70**: 1135–1181.

[29] Cazzani, A., Garusi, E., Tralli, A. and Atluri, S. N. (2005). A four-node hybrid assumed-strain finite element for laminated composite plate, *CMC: Computers, Materials & Continua* **2**: 23–38.

[30] Cen, S., Long, Y. Q. and Yao, Z. H. (2002). A new hybrid-enhanced displacement-based element for the analysisof laminated composite plates, *Computers and Structures* **80**: 819–833.

[31] Cen, S., Long, Y.-Q., Yao, Z.-H. and Chiew, S.-P. (2006). Application of the quadrilateral area co-ordinate method: A new element for Mindlin-Reissner plate, *International Journal for Numerical Methods in Engineering* **66**: 1–45.

[32] Chakrabarti, A., Sengupta, S. K. and Sheikh, A. H. (2004). Analysis of skew composite plates using a new triangular element based on higher order shear deformation theory, *IE(I) Journal-CV* **85**: 77–83.

[33] Chakrabarti, A. and Sheikh, A. H. (2003). Buckling of Laminated Composite Plates by a New Element Based on Higher Order Shear Deformation Theory, *Mechanics of Composite Materials and Structures* **10**(4): 303–317.

[34] Chapelle, D. and Bathe, K. J. (1998). Fundamental considerations for the finite element analysisof shell structures, *Computers and Structures* **66**: 19–36.

[35] Chen, J. S., Wu, C. T. and You, Y. (2001). A stabilized conforming nodal integration for Galerkin meshfree method, *International Journal for Numerical Methods in Engineering* **50**: 435–466.

[36] Chen, W. J. and Cheung, Y. K. (2000). Refined quadrilateral element based on Mindlin/Reissner plate theory, *International Journal for Numerical Methods in Engineering* **47**: 605–627.

[37] Chen, W. J. and Cheung, Y. K. (2001). Refined 9-Dof triangular Mindlin plate elements, *International Journal for Numerical Methods in Engineering* **51**: 1259–1281.

[38] Choi, C.-K. and Lee, P.-S. (1999). Defect-free 4-node flat shell element: NMS-4F element, *Structural Engineering and Mechanics* **8**: 207–231.

[39] Choi, C.-K. and Lee, T.-Y. (2003). Efficient remedy for membrane locking of 4-node flat shell elements by non-conforming modes, *Computer Methods in Applied Mechanics and Engineering* **192**: 1961–1971.

[40] Cook, R. D. (1994). Four-node 'flat' shell element: drilling degrees of freedom, membrane-bending coupling, warped geometry and behaviour, *Computers and Structures* **50**: 549–555.

[41] Cook, R. D., Malkus, D. S., Plesha, M. E. and Witt, R. J. (2002). *Concepts and applications of finite element analysis*, New York: Wiley.

[42] Corradi, L. and Vena, P. (2003). Limit analysis of orthotropic plates, *International Journal of Plasticity* **19**: 1543–1566.

[43] Crawley, E. F. and Luis, J. D. (1987). Use of piezoelectric actuators as elements of intelligent strucutures, *AIAA Journall* **25**: 1373–1385.

[44] Croce, L. D. and Venini, P. (2004). Finite elements for functionally graded reissner-mindlin plates, *Computer Methods in Applied Mechanics and Engineering* **193**: 705–725.

[45] Darilmaz, K. and Kumbasar, N. (2006). An 8-node assumed stress hybrid element for analysis of shell, *Computers and Structures* **84**: 1990–2000.

[46] Ding, H., Wang, G. and Chen, W. (1998). A boundary integral formulation and 2D fundamental solutions for piezoelectric media, *Computer Methods in Applied Mechanics and Engineering* **158**: 65–80.

[47] Duddeck, H. (1962). Die Biegetheorie der flachen hyperbolischen Paraboloidschale $z = \bar{c}xy$, *Archive of Applied Mechanics (Ingenieur Archiv)* **31**: 44–78.

[48] Dvorkin, E. N. and Bathe, K. J. (1984). A continuum mechanics based four-node shell element for general non-linear analysis, *Engineering Computations* **1**: 77–78.

[49] Falzon, B. G., Hitchings, D. and Besant, T. (1999). Fracture mechanics using a 3d composite element, *Composite Structures* **45**(1): 29–39.

[50] Fares, M. E. and Zenkour, A. M. (1999). Buckling and free vibration of non-homogeneous composite cross-ply laminated plates with various plate theories, *Composite Structures* **44**: 279–287.

[51] Ferreira, A. J. M. and Fasshauer, G. E. (2007). Analysis of natural frequencies of composite plates by an RBF-pseudospectral method, *Composite Structures* **79**(2): 202–210.

[52] Ferreira, A. J. M., Jorge, R. M. N. and Roque, C. M. C. (2005). Free vibration analysis of symmetric laminated composite plates by FSDT and radial basis functions, *Computer Methods in Applied Mechanics and Engineering* **194**: 4265–4278.

[53] Gal, E. and Levy, R. (2006). Geometrically nonlinear analysis of shell structures using a flat triangular shell finite element, *Archives of Computational Methods in Engineering* **13**(3): 331–388.

[54] Gaudnzi, P. and Bathe, K. J. (1995). An iterative finite element procedure for the analysis of piezoelectric continua, *Journal of Intelligent Material Systems and Structures* **6**: 266–273.

[55] Ge, Z. and Chen, W. J. (2002). A refined discrete triangular Mindlin element for laminated composite plates, *Structural Engineering and Mechanics* **14**: 575–593.

[56] Ghugal, Y. M. and Shimpi, R. P. (2002). A review of refined shear deformation theories of isotropic and anisotropic laminated plates, *Journal of Reinforced Plastics and Composites* **21, No. 9**: 775–813.

[57] Groenwold, A. A. and Slander, N. (1995). An efficient 4-node 24 DOF thick shell finite element with 5-point quadrature, *Engineering Computations* **12**: 723–747.

[58] Gruttmann, F. and Wagner, W. (2005). A linear quadrilateral shell element with fast stiffness computation, *Computer Methods in Applied Mechanics and Engineering* **194**: 4279–4300.

[59] Haldar, S. and Sengupta, D. (2003). Free vibration analysis of composite right angle triangular plate using a shear flexible element, *Journal of Reinforced Plastics and Composites* **22**(3): 229–255.

[60] Han, F., Pan, E., Roy, A. K. and Yue, Z. Q. (2006). Responses of piezoelectric, transversely isotropic, functionally graded and multilayered half spaces to uniform circular surface loading, *CMES: Computer Modeling in Engineering & Sciences* **14**(1): 15–30.

[61] Hu, H. T. and Tzeng, W. L. (2000). Buckling analysis of skew laminate plates subjected to uniaxial inplane loads, *Thin-Walled Structures* **38**: 53–77.

[62] Huang, Y. Q. and Li, Q. S. (2004). Bending and buckling analysis of antisymmetric laminates using the moving least square differential quadrature method, *Computer Methods in Applied Mechanics and Engineering* **193**(33–35): 3471–3492.

[63] Hughes, T. J. R. and Brezzi, F. (1989). On drilling degrees of freedom, *Computer Methods in Applied Mechanics and Engineering* **72**: 105–121.

[64] Hughes, T. J. R., Brezzi, F., Masud, A. and Harari, I. (1989). Finite element with drilling degrees of freedom: Theory and numerical evaluations, *Proceedings of the fifth international symposium on numerical methods in engineering*, Computational mechanics publications, Ashurst, U.K, pp. 3–17.

[65] Hughes, T. J. R., Cohen, M. and Haroun (1978). Reduced and selective integration techniques in finite element analysis of plates, *Nuclear Engineering Design* **46**: 203–222.

[66] Hughes, T. J. R. and Liu, W. K. (1981). Nonlinear finite element analysis of shells: Part II. Two-dimensional shells, *Computer Methods in Applied Mechanics and Engineering* **27**: 167–182.

[67] Hughes, T. J. R., Taylor, R. L. and Kalcjai, W. (1977). (simple and efficient element for plate bending), *International Journal for Numerical Methods in Engineering* **11**: 1529–1543.

[68] Hughes, T. J. R. and Tezduar, T. E. (1981). Finite elements based upon Mindlin plate theory with particular reference to the four-node bilinear isoparametic element, *Journal of Applied Mechanics* **48**: 587–596.

[69] Ibrahimbegovic, A. (1992). Plate quadrilateral finite elements with incompatible modes, *Communications in Applied Numerical Methods* **8**: 497–504.

[70] Ibrahimbegovic, A. (1993). Quadrilateral finite elements for analysis of thick in thin plates, *Computer Methods in Applied Mechanics and Engineering* **110**: 195–209.

[71] Ibrahimbegovic, A. and Frey, F. (1994). Stress resultant geometrically nonlinear shell theory with drilling rotations. Part III: Linearized kinematics, *International Journal for Numerical Methods in Engineering* **37**: 3659–3683.

[72] Ibrahimbegovic, A., Taylor, R. L. and Wilson, E. L. (1990). A robust quadrilateral membrane finite element with drilling degrees of freedom, *International Journal for Numerical Methods in Engineering* **30**: 445–457.

[73] Ikeda, T. (1996). *Fundamentals of Piezoelectricity*, Oxford Science Publications.

[74] Im, S. and Atluri, S. N. (1989). Effect of a piezo-actuator on a finitely deformed beam subjected to general loading, *AIAA Journal* **27**: 1801–1807.

[75] Jayasankar, S., Mahesh, S., Narayanan, S. and Padmanabhan, C. (2007). Dynamic analysis of layered composite shells using nine node degenerate shell elements, *Journal of Sound and Vibration* **299**: 1–11.

[76] Jensen, L. R., Rauhe, J. C. and Stegmann, J. (2002). *Finite elements for geometric nonlinear analysis of composite laminates and sandwich structures*, Master's thesis, Institue of Mechanical Engineering, Aalborg University.

[77] Jian, W. S., Akihiro, N. and Hiroshi, K. (2004). Vibration analysis of fully clamped arbitrary laminated plate, *Composite Structures* **63**: 115–122.

[78] Kant, T. and Kommineni, J. R. (1992). c^0 finite element geometrically nonlinear analysis of fibre reinforced composite and sandwich laminates based on a higher-order theory, *Computers & Structures* **45**: 511–520.

[79] Katili, I. (1993a). A new discrete Kirchhoff-Mindlin element based on Mindlin-Reissner plate theory and assumed shear strain fields – Part I: An extended DKT element for thick-plate bending analysis, *International Journal for Numerical Methods in Engineering* **36**: 1859–1883.

[80] Katili, I. (1993b). A new discrete Kirchhoff-Mindlin element based on Mindlin-Reissner plate theory and assumed shear strain fields – Part II: An extended DKQ element for thick-plate bending analysis, *International Journal for Numerical Methods in Engineering* **36**: 1885–1908.

[81] Khdeir, A. A. (1989). Comparison between shear deformable and Kirchhoff theories for bending, buckling and vibration of antisymmetric angle-ply laminated plates, *Composite Structures* **13**: 159–172.

[82] Khdeir, A. A. and Librescu, L. (1988). Analysis of symmetric cross-ply elastic plates using a higher-order theory. Part II: buckling and free vibration, *Composite Structures* **9**: 259–277.

[83] Kim, K.-D., Chang-Soo, L. and Sung-Cheon, H. (2007). A 4-node corotational ANS shell element for laminated composite strucutres, *Composite Strucutres* **80**(2): 234–252.

[84] Kim, K. D., Lomboy, G. R. and Voyiadjis, G. Z. (2003). A 4-node assumed strain quasi-conforming shell element with 6 degrees of freedom, *International Journal for Numerical Methods in Engineering* **58**: 2177–2200.

[85] Kumar, L. R., Datta, P. K. and Prabhakara, D. L. (2003). Tension buckling and dynamic stability behaviour of laminated composite doubly curved panels subjected to partial edge loading, *Composite Structures* **60**: 171–181.

[86] Kumbasar, N. and Aksu, T. (1995). A finite element formulation for moderately thick shells of general shape, *Computers and Structures* **54**: 49–57.

[87] Lanhe, W., Hua, L. and Daobin, W. (2005). Vibration analysis of generally laminated composite plates by the moving least squares differential quadrature method, *Composite Structures* **68**: 319–330.

[88] Lardeur, P. and Batoz, J. L. (1989). Composite plate analysis using a new discrete shear triangular finite element, *International Journal for Numerical Methods in Engineering* **27**: 343–359.

[89] Lee, P.-S. and Bathe, K.-J. (2004). Development of MITC isotropic triangular shell finite elements, *Computers & Structures* **82**(11-12): 945–962.

[90] Li, S. and Liu, W. K. (2002). Meshfree and particle methods and their applications, *Applied Mechanics Reviews* **55**: 1–34.

[91] Liew, K. M. (1996). Solving the vibration of thick symmetric laminates by Reissner/Mindlin plate theory and the p-Ritz method, *Journal of Sound and Vibration* **198**: 343–360.

[92] Liew, K. M. and Huang, Y. Q. (2003). Bending and buckling of thick symmetric rectangular laminates using the moving least-squares differential quadrature method, *International Journal of Mechanical Sciences* **45**(1): 95–114.

[93] Liew, K. M., Huang, Y. Q. and Reddy, J. N. (2003). Vibration analysis of symmetrically laminated plates based on FSDT using the moving least squares differential quadrature method, *Computer Methods in Applied Mechanics and Engineering* **192**: 2203–2222.

[94] Liew, K. M., Lim, H. K., Tan, M. J. and He, X. Q. (2002). Analysis of laminated composite beams and plates with piezoelectric patches using the element-free Galerkin method, *Computational Mechanics* **29**: 486–497.

[95] Lines, M. E. and Glass, A. M. (1977). *Principles and Applications of Ferroelectric and Related Materials*, Clarendon Press, Oxford.

[96] Liu, G. R., Dai, K. Y., Lim, K. M. and Gu, Y. T. (2002). A point interpolation mesh free method for static and frequency analysis of two-dimensional piezoelectric structures, *Computational Mechanics* **29**: 510–519.

[97] Liu, G. R., Dai, K. Y., Lim, K. M. and Gu, Y. T. (2003). A radial point interpolation method for simulation of twoo-dimensional piezoelectric structures, *Smart Materials and Strucutres* **12**: 171–180.

[98] Liu, G. R., Dai, K. Y. and Nguyen, T. T. (2007). A smoothed finite element method for mechanics problems, *Computational Mechanics* **39**(6): 859–877.

[99] Liu, G. R., Nguyen, T. T., Dai, K. Y. and Lam, K. Y. (2007). Theoretical aspects of the smoothed finite element method (SFEM), *International Journal for Numerical Methods in Engineering* **71**: 902–930.

[100] Liu, G. R. and Zhang, G. Y. (2008). Upper bound solution to elasticity problems: A unique property of the linearly conforming point interpolation method (LC-PIM)., *International Journal for Numerical Methods in Engineering* **74**: 1128–1161.

[101] Liu, J., Riggs, H. R. and Tessler, A. (2000). A four-node, shear-deformable shell element developed via explicit Kirchhoff constraints, *International Journal for Numerical Methods in Engineering* **49**: 1065–1086.

[102] Liu, K. K., Law, E. S., Lam, D. and Belytschko, T. (1986). Resultant-stress degenerated-shell element, *Computer Methods in Applied Mechanics and Engineering* **55**: 259–300.

[103] Liu, L., Chua, L. P. and Ghista, D. N. (2007). Mesh-free radial basis function method for static, free vibration and buckling analysis of shear deformable composite laminates, *Composite Structures* **78**: 58–69.

[104] Liu, M. L. and To, C. W. S. (2003). Free vibration analysis of laminated composite shell structures using hybrid strain based layerwise finite elements, *Finite Elements in Analysis and Design* **40**: 83–120.

[105] Long, C. S., Geyer, S. and Groenwold, A. A. (2006). A numerical study of the effect of penalty parameters for membrane elements with independent rotation fields and penalized equilibrium, *Finite Element in Analysis and Design* **42**: 757–765.

[106] Long, C. S., Loveday, P. W. and Groenwold, A. A. (2006). Planar four node piezoelectric elements with drilling degrees of freedom, *International Journal for Numerical Methods in Engineering* **65**: 1820–1830.

[107] Loy, C. T., Lam, K. Y., Hua, L. and Liu, G. R. (1999). Vibration of antisymmetric angle-ply laminated cylindrical panels with different boundary conditions, *The Quarterly Journal of Mechanics and Applied Mathematics* **52**(1): 55–71.

[108] Mackerle, J. (2003). Smart materials and structures - an finite element approach - an addendum: a bibliography (1997-2002), *Modelling and Simulation in Materials Science and Engineering* **11**: 707–744.

[109] MacNeal, R. H. (1978). A simple quadrilateral shell element, *Computers and Structures* **8**: 175–183.

[110] MacNeal, R. H. (1982). Derivation of element stiffness matrices by assumed strain distributions, *Nuclear Engineering and Design* **70**: 3–12.

[111] MacNeal, R. H. and Harder, R. L. (1985). A proposed standard test problems to test finite element accuracy, *Finite Element in Analysis and Design* **1**: 3–20.

[112] Mai-Duy, N., Khennane, A. and Tran-Cong, T. (2007). Computation of laminated composite plates using integrated radial basis function networks, *CMC: Computers, Materials & Continua* **5**: 63–77.

[113] Malkus, D. S. and Hughes, T. J. R. (1978). Mixed finite element methods-reduced and selective integration techniques: a unification of concepts, *Computer Methods in Applied Mechanics and Engineering* **15**: 63–81.

[114] Matsunaga, H. (1991). Vibration and stability of cross-ply laminated composite plates accorsing to a global higher-order plate theory, *Composite Structures* **145**: 429–442.

[115] Matsunaga, H. (2007). Vibration and stability of cross-ply laminated composite shallow shells subjected to in-plane stress, *Composite Structures* **78**: 377–391.

[116] Mercer, C. D., Reddy, B. D. and Eve, R. A. (1987). Finite Element Method for Piezoelectric Media, *Technical Report 92*, UCT/CSIR Applied Mechanics Research Unit Technical Report, Univers.

[117] Nguyen-Van, H., Mai-Duy, N. and Tran-Cong, T. (2007a). A simple and accurate four-node quadrilateral element using stabilized nodal integration for laminated plates, *CMC: Computers, Materials & Continua* **6**(3): 159–176.

[118] Nguyen-Van, H., Mai-Duy, N. and Tran-Cong, T. (2007b). Analysis of laminated composite plate/shell structures using a stabilized nodal-integrated quadrilateral element, *in* P. A. Mendis, D. T. Cao and T. Ngo (eds), *The 1st International Conference on Modern Design, Construction & Maintenance of Structures*, Vol. 2, Construction Publishing House, pp. 85–92. ISBN 978-0-646-48404-4.

[119] Nguyen-Van, H., Mai-Duy, N. and Tran-Cong, T. (2008a). A node-based element for analysis of planar piezoelectric structures, *CMES: Computer Modeling in Engineering & Sciences* **36**(1): 65–96.

[120] Nguyen-Van, H., Mai-Duy, N. and Tran-Cong, T. (2008b). A smoothed four-node piezoelectric element for analysis of two-dimensional smart structures, *CMES: Computer Modeling in Engineering & Sciences* **23**(3): 209–222.

[121] Nguyen-Van, H., Mai-Duy, N. and Tran-Cong, T. (2008c). Analysis of piezoelectric solids with an efficient node-based smoothing element, *The 8th World Congress on Computational Mechanics (WCCM8), Venice, Italy*, CIMNE (ISBN 978-84-96736-55-9).

[122] Nguyen-Van, H., Mai-Duy, N. and Tran-Cong, T. (2008d). Free vibration of laminated plate/shell structures based on FSDT with a stabilized nodal-integrated quadrilateral element, *Journal of Sound and Vibration* **313**(1-2): 205–223.

[123] Nguyen-Van, H., Mai-Duy, N. and Tran-Cong, T. (2009). An improved quadrilateral flat element with drilling degrees of freedom for shell structural analysis., *CMES: Computer Modeling in Engineering & Sciences* **49**(2): 81–112.

[124] Nguyen-Xuan, H., Rabczukb, T., Bordas, S. and Debongnie, J. F. (2008). A smoothed finite element method for plate analysis, *Computer Methods in Applied Mechanics and Engineering* **197**(13–16): 1184–1203.

[125] Noor, A. K. (1975). Stability of Multilayered Composite Plates, *Fibre Science and Technology* **8**(2): 81–89.

[126] Noor, A. K. and Mathers (1975). Shear-flexible finite element method of laminated composite plate, *Technical report*, NASA.

[127] Ohs, R. R. and Aluru, N. R. (2001). Meshless analysis of piezoelectric devices, *Computational Mechanics* **27**: 23–36.

[128] Pagano, N. J. (1970). Exact solutions for rectangular bi-directional composites and sandwich plates, *Journal of Composite Materials* **4**: 20–34.

[129] Palazotto, A. N. and Dennis, S. T. (1992). *Nonlinear analysis of shell strucures*, AIAA education series, Wahsington DC.

[130] Park, T., Kim, K. and Han, S. (2006). Linear static and dynamic analysis of laminated composite plates and shell using a 4-node quasi-conforming shell element, *Composite Part B: Engineering* **37**: 237–248.

[131] Phan, N. D. and Reddy, J. N. (1985). Analysis of laminated composite plates using a higher-order shear deformation theory, *International Journal for Numerical Methods in Engineering* **21**: 2201–2219.

[132] Pica, A., Wood, R. D. and Hinton, E. (1980). Finite element analysis of geometrically nonlinear plate behavior using a mindlin formulation, *Computational Mechanics* **11**: 203–215.

[133] Pimpinelli, G. (2004). An assumed strain quadrilateral element with drilling degrees of freedom, *Finite Element in Analysis and Design* **41**: 267–283.

[134] Prusty, B. G. and Satsangi, S. K. (2001). Finite element buckling analysis of laminated composite stiffened shells, *International Journal of Crashworhiness* **6**: 471–484.

[135] Putcha, N. S. and Reddy, J. N. (1986). A refined mixed shear flexible finite element for non-linear analysis of laminated plates, *Computers & Structures* **22**: 529–538.

[136] Rattanawangcharoen, N., Varma, V., Shah, A. H. and Bai, H. (2005). A finite element model for vibration analysis of laminated composite cylindrical panels, *Mechanics of Advanced Materials and Structures* **12**: 265–274.

[137] Ray, M. C., Bhattacharya, R. and Samanta, B. (1998). Exact solutions for dynamic analysis of composite plates with distributed piezoelectric layers, *Computers and Structures* **66**(6): 737–743.

[138] Reddy, J. N. (1984a). Exact solutions of moderately thick laminated shells, *ASCE Journal of Engineering Mechanics* **110**: 794–809.

[139] Reddy, J. N. (1984b). Solutions of moderately thick laminated shells, *Journal of Engineering Mechanics* **110**: 794–809.

[140] Reddy, J. N. (2000). Analysis of functionally graded plates, *International Journal for Numerical Methods in Engineering* **47**: 663–684.

[141] Reddy, J. N. (2004a). *An introduction to nonlinear finite element analysis*, Oxford University Press.

[142] Reddy, J. N. (2004b). *Mechanics of laminated composite plates and shells-Theory and analysis*, CRC Press.

[143] Reddy, J. N. and Arciniega, R. A. (2004). Shear deformation plate and shell theories: from Stavsky to present, *Mechanics of Advanced Materials and Structures* **11**: 535–582.

[144] Reddy, J. N. and Khdeir, A. A. (1989). Buckling and vibration of laminated composite plates using various plate theories, *AIAA Journal* **27**(12): 1808–1817.

[145] Reddy, J. N. and Phan, P. H. (1985). Stability and vibration of isotropic, orthotropic and laminated plates according to a higher order shear deformation theory, *Journal of Sound and Vibration* **89**: 157–170.

[146] Rolfes, R. and Rohwer, K. (1997). Improved transverse shear stresses in composite finite elements based on first order shear deformation theory, *International Journal for Numerical Methods in Engineering* **40**: 51–60.

[147] Samtech (2003). *Samcef User's Manual v10.1.*

[148] Sauer, R. (1998). *Eine einheitliche Finite-Element-Formulierung fur Stab- und Schalentragwerke mit endlichen Rotationen*, Bericht 4, Institut fur Baustatik, Universitat Karlsruhe (TH).

[149] Schoop, H. (1989). A simple nonlinear flat element for large displacement structures, *Computers & Structures* **32**: 379–385.

[150] Sciuva, M. D. and Carrera, E. (1990). Static buckling of moderately thick, anisotropic, laminated and sandwich cylindrical shell panels, *AIAA Journal* **28**: 1782–1793.

[151] Shen, I. Y. (1995). Bending and torsional vibration vibration control of composite beam through intelligent constrained-layer damping treatments, *Smart Materials and Strucutres* **4**(1): 340–355.

[152] Simo, J. C., Fox, F. D. and Rifai, M. S. (1989). On a stress resultant geometrically exact shell model. Part II: The linear theory; Computational aspects, *International Journal for Numerical Methods in Engineering* **73**: 53–92.

[153] Singh, G., Raveendranath, P. and Rao, G. V. (2000). An accurate four-node shear flexible composite plate element, *International Journal for Numerical Methods in Engineering* **47**: 1605–1620.

[154] Sladek, J., Sladek, V., Zhang, C., Garcia-Sanche, F. and Wunsche, M. (2006). Meshless Local Petrov-Galerkin Method for Plane Piezoelectricity, *CMC: Computers, Materials & Continua* **4**(2): 109–117.

[155] Sladek, J., Sladek, V., Zhang, C., Solek, P. and Starek, L. (2007). Fracture Analyses in Continuously Nonhomogeneous Piezoelectric Solids by the MLPG, *CMES: Computer Modeling in Engineering & Sciences* **19**(3): 247–262.

[156] Soh, A. K., Cen, S., Long, Y. Q. and Long, Z. F. (2001). A new twelve DOF quadrilateral element for analysis of thick and thin plates, *European Journal of Mechanics - A/Solids* **20**: 299–326.

[157] Soh, A. K., Long, Z. F. and Cen, S. (1999). A new nine d.o.f triangular element for analysis of thick and thin plates, *Computers and Mechanics* **24**: 408–417.

[158] Soldatos, K. (1987). Influence of thickness shear deformation on free vibrations of rectangular plates, cylindrical panels and cylinders of antisymmetric angle-ply construction, *Journal of Sound and Vibration* **119**: 111–137.

[159] Somashekar, B. R., Prathap, G. and Babu, R. (1987). A field consistent four-noded laminated anisotropic plate/shell element, *Computers and Structures* **25**: 345–353.

[160] Sosa, H. (1991). Plane problems in piezoelectric media with defects, *International Journal of Solids and Structures* **28**: 491–505.

[161] Spilker, R. L., Jakobs, D. M. and Engelmann, B. E. (1985). Efficient hybrid stress isoparametric elements for moderately thick and thin multiplayer plates, *Hybrid and Mixed Finite Element Method* **73**: 113–122.

[162] Stricklin, J. A., Haisler, W. E. and Tisdale, P. R. (1969). A rapidly converging triangular plate elment, *AIAA Journal* **7**: 180–181.

[163] Striz, A. G., Cho, K. N. and Bert, C. W. (1991). Free vibration of laminated rectangular plates analyzed by higher-order individual-layer theory, *Journal of Sound and Vibration* **145**: 429–442.

[164] Sze, K. Y. and Pan, Y. S. (1999). Hybrid finite element models for piezoelectric materials, *Journal of Sound and Vibration* **226**: 519–547.

[165] Sze, K. Y., Yang, X.-M. and Yao, L.-Q. (2004). Stabilized plane and axisymmetricpiezoelectric finite element models, *Finite Elements in Analysis and Design* **40**: 1105–1122.

[166] Sze, K. Y. and Yao, L. Q. (2000). Modelling smart structures with segmented piezoelectric sensors and actuators, *Journal of Sound and Vibration* **235**: 495–520.

[167] Taylor, R. L. (1987). Finite element analysis of linear shell problems, *in* J. Whiteman (ed.), *Proceeding of the Mathematics in Finite Element and Applications*, Academic Press, New York.

[168] Taylor, R. L. and Auricchio, F. (1993). Linked interpolation for reissner-mindlin plate elements. part i–a simple triangle, *International Journal for Numerical Methods in Engineering* **36**: 3057–3066.

[169] To, C. W. S. and Liu, M. L. (2001). Geometrically nonlinear analysis of layerwise anisotropic shell structures by hibrid strain based lower order elements, *Finite Element in Analysis and Design* **37**: 1–34.

[170] To, C. W. S. and Wang, B. (1998). Hybrid strain-based three-node flat triangular laminated composite shell elements, *Finite Element in Analysis and Design* **28**: 177–207.

[171] To, C. W. S. and Wang, B. (1999). Hybrid strain based geometrically nonlinear laminated composite triangular shell finite elments, *Finite Element in Analysis and Design* **33**: 83–124.

[172] Tzou, H. S. and Tiersten, H. F. (1994). Elastic analysis of laminated composite plates in cylindrical bending due to piezoelectric actuators, *Smart Materials and Strucutres* **3**: 255–265.

[173] Valchoutsis, S. (1992). Shear correction factors for plates and shells, *International Journal for Numerical Methods in Engineering* **33**: 1537–1552.

[174] Vaziri, R., Olson, M. D. and Anderson, D. L. (1992). Finite element analysis of fibrous composite structures: A plasticity approach, *Computer & Structures* **44**(1-2): 103–116.

[175] Vaziri, R., Quan, X. and Olson, M. D. (1996). Impact analysis of laminated composite plates and shells by super finite elements, *International Journal of Impact Engineering* **18**(7-8): 765–782.

[176] Wagner, W., Gruttmann, F. and Sprenger, W. (2001). A finite element formulation for the simulation of propagating delaminations in layered composite structures, *International Journal for Numerical Methods in Engineering* **51**(11): 1337–1359.

[177] Wang, D. and Chen, J. S. (2004). Locking-free stabilized conforming nodal integration for meshfree Mindlin-Reissner plate formulation, *Computer Methods in Applied Mechanics and Engineering* **193**: 1065–1083.

[178] Wang, D. and Chen, J. S. (2007). A hermite reproducing kernel approximation for thin plate analysis with sub-domain stabilized conforming integration, *International Journal for Numerical Methods in Engineering* **74**: 368–390.

[179] Wang, D., Dong, S. B. and Chen, J. S. (2006). Extended meshfree analysis of transverse and inplane loading of a laminated anisotropic plate of general planform geometry, *International Journal of Solids and Structures* **43**: 144–171.

[180] Wang, J., Liew, K. M., Tan, M. J. and Rajendran, S. (2002). Analysis of rectangular laminated composite plates via FSDT meshless method, *International Journal of Mechanical Sciences* **44**(7): 1275–1293.

[181] Wang, Q., Wang, G., Liu, Z. and Ding, H. (2003). The boundary contour method for piezoelectric media with linear elements, *International Journal for Numerical Methods in Engineering* **56**: 1847–1860.

[182] Wang, S. (1997). Free vibration analysis of skew fibre-reinforced composite laminates based on first-order shear deformation plate theory, *Computer & Structures* **63**: 525–538.

[183] Whitney, J. M. (1969). Bending-extensional coupling in laminated plates under transverse load, *Journal of Composite Materials* **3**: 398–411.

[184] Whitney, J. M. (1970). The effect of boundary conditions on the response of laminated composites, *Journal of Composite Materials* **4**: 192–203.

[185] Whitney, J. M. (1973). Shear correction factors for orthotropic laminates under static load, *Journal of Applied Mechanics* **40**: 302–304.

[186] Wilt, T. E., Saleeb, A. F. and Chang, T. Y. (1990). Mixed element for laminated plates and shells, *Computers and Structures* **37**: 597–611.

[187] Wu, C. C., Sze, K. Y. and Huang, Y. Q. (2001). Numerical solutions on fracture of piezoelectric materials by hybrid element, *International Journal of Solids and Structures* **38**: 4315–4329.

[188] Wu, C. P. and Chen, W. Y. (1994). Vibration and stability of laminated plates based on a local higher-order plate theory, *Journal of Sound and Vibration* **177**: 503–520.

[189] Xiang, Y., Kitipornchai, S. and Liew, K. M. (1996). Buckling and vibration of thick laminates on pasternak foundations, *Journal of engineering mechanics-ASCE* **122**(1): 54–63.

[190] Xiang, Y. and Reddy, J. N. (2003). Natural vibration of rectangular plates with an internal line hinge using the first order shear deformation plate theory, *Journal of Sound and Vibration* **263**(2): 285–297.

[191] Xiang, Y. and Zhang, L. (2005). Free vibration analysis of stepped circular mindlin plates, *Journal of Sound and Vibration* **280**(3-5): 633–655.

[192] Yang, H. T. Y., Saigal, S., Masud, A. and Kapania, R. K. (2000). A survey of recent shell element, *International Journal for Numerical Methods in Engineering* **47**(1-3): 101–127.

[193] Yoo, J. W., Moran, B. and Chen, J. S. (2004). Stabilized conforming nodal integration in the natural-element method, *International Journal for Numerical Methods in Engineering* **60**: 861–890.

[194] Zaghloul, S. A. and Kennedy, J. B. (1975). Nonlinear behavior of symmetrically laminated plates, *ASME Journal of Applied Mechanics* **42**: 234–236.

[195] Zemcik, R., Rolfes, R., Rose, M. and Temer, J. (2007). High-performance four-node shell element with piezoelectric coupling for the analysis of smart laminated structures, *International Journal for Numerical Methods in Engineering* **70**: 934–961.

[196] Zhang, Y. X. and Kim, K. S. (2004). Two simple and efficient displacement-based quadrilateral elements for the analysis of the composite laminated plates, *International Journal for Numerical Methods in Engineering* **61**: 1771–1796.

[197] Zhang, Y. X. and Kim, K. S. (2005). Linear and geometrically nonlinear analysis of plates and shells by a new refined non-conforming triangular plate/shell element, *Computational Mechanics* **36**: 331–342.

[198] Zhang, Y. X. and Kim, K. S. (2006). Geometrically nonlinear analysis of laminated composite plates by two new displacement-based quadrilateral plate elements, *Composite Structures* **72**: 301–310.

[199] Zhang, Y. X. and Yang, C. H. (2009). Recent developments in finite element analysis for laminated composite plates, *Composite Structures* **88**(1): 147–157.

[200] Zhao, X., Liu, G. R., Dai, K. Y., Zhong, Z. H., Li, G. Y. and Han, X. (2008). Geometric nonlinear analysis of plates and cylindrical shells via a linearly conforming radial point interpolation method, *Computational Mechanics* **42**: 133–144.

[201] Zhen, W. and Wanji, C. (2006). Free vibration of laminated composite and sandwich plates using global-local higher-order theory., *Journal of Sound and Vibration* **298**: 333–349.

[202] Zienkiewicz, O. C. (1977). *The Finite Element Method*, McGraw-Hill, NewYork.

[203] Zienkiewicz, O. C. and Taylor, R. L. (2000). *The Finite Element Method*, Vol. 2: Solid Mechanics, 5th edn, Butterworth Heinemann-Oxford.

[204] Zienkiewicz, O. C., Taylor, R. L. and Too, J. M. (1971). Reduced integration technique in general analysis of plates and shells, *International Journal for Numerical Methods in Engineering* **3**: 275–290.

[205] Zienkiewicz, O. C., Xu, Z., Zeng, L. F., Samuelson, A. and Wiberg, N. E. (1993). Linked interpolation for Reissner-Mindlin plate elements. Part I–A simple quadrilateral, *International Journal for Numerical Methods in Engineering* **36**: 3043–3056.